Constitutive Models for Geomaterials Considering Structural Changes and Anisotropy(Dissertation_全文)

AUTHOR(S):

Kimoto, Sayuri

Constitutive Models for Geomaterials Considering Structural Changes and Anisotropy

December 2002

Sayuri KIMOTO

Constitutive Models for Geomaterials Considering Structural Changes and Anisotropy

December 2002

Sayuri KIMOTO

Abstract

In order to accurately predict the deformation of geomaterials in numerical simulations, structural changes and anisotropy need to be incorporated into the constitutive model. In the present study, constitutive models for clay and soft rock, considering structural changes and anisotropy, are proposed. The ability of the model is evaluated with respect to the localization of both shear and compressive strain and to the unstable behavior during consolidation.

The main subject of this dissertation can be divided into two parts, namely, a description of structural changes and a description of anisotropy. In order to describe the structural changes, the static yield function and the overconsolidation boundary surface are assumed to shrink with the viscoplastic deformation. The proposed elasto-viscoplastic model is able to reproduce the results of undrained triaxial tests on Osaka Pleistocene clay well. From an evaluation of the instability of the model, it is found that an unstable region exists not only around the failure line, but also away from the failure line in the proposed model.

A finite element analysis of undrained and partially drained compression tests under plane strain conditions is conducted to study the effect of structural changes on strain localization. It is seen in the results that the strain localization is promoted by the collapse of the soil structure and that the structural parameters affect the geometry of the shear bands. In the analysis of the partially drained compression tests, the localization of the compressive strain is reproduced. Furthermore, one-dimensional consolidation are simulated. The proposed model can effectively reproduce certain types of unstable behavior during consolidation, such as stagnation, or a temporary increase in pore water pressure, and a sudden increase in the settlement rate.

Next, an elasto-plastic constitutive model for soft rock and an elasto-viscoplastic constitutive model for clay are extended to the anisotropic models by replacing the stress tensor with a transformed stress tensor determined by the structural tensor. The proposed model can describe the initial structural anisotropy specified by the sedimentation plane. The model is applied to the experimental results of sedimentary soft rock sampled in different directions, and well reproduces the anisotropic behavior with respect to strength and dilatancy. Finally, the effect of anisotropy on strain localization is discussed by means of a simulation of the compression tests under plane strain conditions. The formation of shear bands depends on the anisotropic parameters.

Acknowledgements

Six years ago, I entered the Laboratory of Soil Mechanics in the Department of Civil Engineering at Kyoto University. Since that time, I have been through the Master and the Doctoral programs in the laboratory. Throughout those years, the greatest opportunity I had was to be a student of Professor Fusao Oka. First and foremost, I am sincerely grateful to Professor Fusao Oka, my supervisor, for his continuous and ever-present support, guidance, and encouragement. His flexible ideas and vast knowledge were a matter of great importance to this thesis. It has really been a privilege for me to study under him and to be one of his students.

I would like to express sincere thanks to Professor Masashi Kamon and Professor Takeshi Tamura, both of the Department of Civil Engineering at Kyoto University, for their thorough review of my thesis and their valuable suggestions. My sincere appreciation is also extended to Dr. Toshihisa Adachi, presently the Principal Director of the Geo-Research Institute and a professor emeritus of Civil Engineering at Kyoto University, for his useful suggestions regarding the study of soft rock. I extend my appreciation to Associate Professor Takeshi Kodaka for his valuable support in the Laboratory of Soil Mechanics over the years. I also want to thank Research Associate Shinichiro Nakashima for his kind assistance in the completion of this thesis.

I offer my sincere thanks to my laboratory mates. I extend my gratitude to Dr. Kim Yong-Seong, a former doctoral course student and now a member of the Water Resources Research Institute in Korea, for his valuable support. I also acknowledge Mr. Chih-Wei Lu, a doctoral course student, for his friendship and encouragement through the completion of this thesis. Special thanks are also due to Mr. Yosuke Higo, a doctoral course student, for his support which made it possible to achieve this thesis. I also want to express my sincere gratitude to all the other members of the laboratory for always giving me a helping hand, which encouraged me to complete this thesis.

Above all, my deepest gratitude goes to my parents. Every part of my life has been strengthened and enriched by their tremendous love and support. Without the constant support of my family, this thesis could not have been completed.

Contents

List of Figures

List of Tables

Chapter 1

INTRODUCTION

1.1 Background and Objectives

Natural deposits are affected by the chemical bonding or the cementation between soil particles during the sedimentation process. Under the effect called 'aging', aggregations and a linkage between assemblages are formed in the soil structure. The process by which a structure is formed is affected by the chemical properties of the material, the temperature, and the secondary consolidation. However, this process has not yet been clarified. Moreover, the internal soil particles are arranged in one direction, generally in a vertical direction, because of gravity. Natural deposits exhibit anisotropy due to the arrangement of the microstructure.

The properties of a soil structure make predicting the deformation of the geomaterials difficult. The ability of a non-linear computational analysis to provide realistic simulations of the behavior of soil depends directly on the capability of the constitutive model used for describing the mechanical response of the soil skeleton. Many constitutive models for geomaterials have been proposed and studied during the last three decades. Generally, the models are developed for remolded clay in which the soil structure has been degraded. The effect of the structure, however, cannot be negligible. It is well known that the characteristics of the strength and the deformation of remolded soils are different from those of intact soils. Types of unstable behavior such as the generation of pore water pressure after the construction of the embankment, and secondary creep, caused by structural changes, have been reported by many researchers. For example, the unpredictable settlement of Kansai International Airport is considered to be related to the degradation of the soil structure in the Pleistocene clay layer due to the large load which the soils have never

had to bear. In order to predict such unstable phenomena by a numerical simulation, the effect of the soil structure has to be taken into account in the constitutive model.

Changes in the microstructure also affect the strain localization. In the macroscopic localized zone, the breaks down of natural microstructure with an increasing deformation are clearly observed (Pusch 1970). Strain localization is generally considered to be important as a presage of failure. It has recently been recognized that strain localization may occur during compressive deformation, particularly for porous materials with a large confining stress, and the localized compressive deformation may cause a large displacement.

It is well known that the mechanical behavior of geomaterials exhibits anisotropy due to the anisotropic microstructure formed during the sedimentation process. Studies of microstructure of clays have shown that clay particles tend to become oriented perpendicular to the major principal stress during one-dimensional consolidation. The orientation of soil particles causes anisotropy behavior. Anisotropy has been confirmed in the shape of the yield curve obtained from experiments on clay and soft rock (Tavenas and Leroueil 1977), and by the directional character of the mechanical response to the load. Although the mechanical behavior of anisotropy has been studied, an appropriate model has not been proposed which can describe the anisotropic behavior of natural deposits.

The present study is concerned with the numerical modeling of the structural changes and the anisotropy of geomaterials, namely, clay and soft rock. The elasto-viscoplastic constitutive model for clay is extended to consider the effect of structural changes and anisotropy. In the proposed model, structural changes are expressed as strain-softening with an increasing viscoplastic strain, so that the model can describe the instability not only around the failure stress, but also during the compressive deformation. The effect of structural changes on strain localization during undrained and partially drained compression is evaluated. Furthermore, the model is applied to a one-dimensional consolidation analysis in order to evaluate the property of the proposed model during compressive deformation. The elasto-plastic constitutive model for rock and the elasto-viscoplastic constitutive model are extended to express anisotropic behavior based on the transformed stress concept. By comparing the analytical and the experimental results, the ability of the model is evaluated. The effect of anisotropy on strain localization is also studied using the model for clay considering anisotropy.

As mentioned above, the main subject of this dissertation can be roughly divided into two parts, namely, an expression for structural changes and an expression for anisotropy in constitutive models. Firstly, the elasto-viscoplastic model, which considers structural changes, will be presented. Then, the effect of the structure on shear localization will be examined under both undrained and partially drained conditions. The performance of the proposed model during the consolidation process, particularly the ability of predicting unstable behavior will also be evaluated.

Secondly, the elasto-plastic model will be extended to consider anisotropic behavior. The model is applied to drained triaxial tests on soft rock. In addition, the effect of anisotropy on strain localization is studied.

1.2 Scope and Organization

The dissertation consists of seven chapters, and the outline for each chapter is as follows:

In Chapter 2, an extended elasto-viscoplastic constitutive model for clay is proposed which takes into account of structural changes. The proposed model can describe unstable behavior not only around the failure stress, but also during compressive deformation. A structural collapse is expressed as the shrinking of both the overconsolidation boundary surface and the static yield surface with an increasing viscoplastic deformation. The static yield function is continuously transformed when stress path crosses the boundary between the overconsolidated region and the normally consolidated region, so that calculations can be conducted continuously between both regions. We apply the proposed model to Osaka Pleistocene clay, which shows the typical behavior of structural soil. In addition, the instability of the model is evaluated for both undrained and drained creep conditions.

In Chapter 3, the effect of structural changes on strain localization is evaluated through numerical simulations of compression under plane strain conditions. Simulations are performed under both undrained and partially drained conditions in order to examine the effect on the compressive deformation as well as the shear deformation.

In Chapter 4, the effect of structural changes on one-dimensional consolidation behavior is examined. As a result, the model can reproduce the unstable phenomena well during consolidation, such as a temporary increase in the strain rate and pore water generation.

In Chapter 5, the modeling of the anisotropy of the geomaterials is studied. An elasto-plastic constitutive model for soft rock is extended to consider the anisotropy based on the transformed stress method proposed by Boehler (1977). Simulations of drained triaxial compression tests are performed, and the simulation results are compared to the experimental tests on Tomuro stone sampled in different directions.

In Chapter 6, the elasto-viscoplastic constitutive model for clay is extended to an anisotropic model in a similar way to that used in Chapter 5. The effect of the anisotropy on strain localization is studied through a numerical simulation of undrained compression under plane strain conditions.

In Chapter 7, the conclusions of this dissertation and the recommendations for future work are given.

Chapter 2

ELASTO-VISCOPLASTIC CONSTITUTIVE MODEL FOR CLAY CONSIDERING STRUCTURAL CHANGES

2.1 Introduction

It is generally known that the natural clay and the reconstituted clay exhibit different behavior in the laboratory tests such as triaxial tests and oedometer tests. The natural clay, namely, the undisturbed clay, provides the apparent peak strength and then exhibits brittle behavior, while the reconstituted clay gives a smaller strength than the undisturbed clay even at a smaller void ratio and it shows strain-hardening behavior. We consider the difference is due to the microstructure of soils.

Fig.2.1 shows the schematic pictures of the soil structure for the undisturbed clay and the reconstituted clay. The natural microstructural pattern is characterized by a network of small aggregates connected by links of particles, as shown in Fig.2.1(a). Pusch (1970) investigated the microstructural changes in soft sensitive clay, and showed that the links break down with an increasing shear deformation, and then, the majority of the links is broken in the residual strength while the aggregate are still intact. In contrast, the links are mostly broken down in the reconstituted clay (Shigematsu 2002), as shown in Fig.2.1(b).

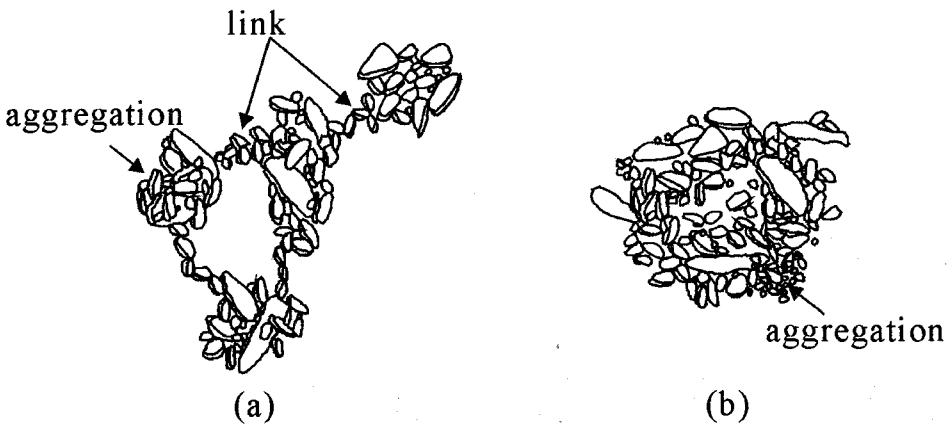

Figure 2.1: Schematic pictures of the clay structure for the undisturbed clay (Pusch 1970) (a), and the reconstituted clay (b)

Some models which consider the effect of soil structures have been proposed. Di Prisco, Matiotti, and Nova (1992) formulated a constitutive model which could describe the mechanical behavior of grouted sand specimens. The tensile strength parameter decreases with an increasing plastic strains, so that the model can describe the degradation of the strength. Asaoka, Nakano, and Noda (2000) introduced the superloading yield surface concept to the original Cam-clay model in order to describe some aspects of the mechanical behavior of highly structured soils. Furthermore, Oka, Adachi, and Yashima (1998) extended the elasto-plastic constitutive model for soft rock in order to describe the negative dilatancy with strain softening behavior by considering the change in the initial volumetric component of stress history tensor and the shrinkage of the overconsolidation boundary surface.

In the present study, an elasto-viscoplastic model for water-saturated clay proposed by Adachi and Oka (1982) is extended to consider the concept of soil structures. The model is based on Perzyna type of viscoplasticity theory (Perzyna 1963) and a Cam-clay model. Since it has been pointed out that the original model could not describe an accelerating creep process or a creep rupture, Adachi, Oka, and Mimura (1987a) introduced a second material function, Φ_2, in order to reproduce unstable soil behavior such as accelerating creep under undrained conditions. Furthermore, Adachi, Oka, and Mimura (1987b) modified the original model by controlling the viscoplastic parameter with a stress ratio, so that the model can describe undrained creep ruptures around the failure stress ratio.

These modified models can express unstable behavior only when the stress ratio ap-

proaches the failure stress ratio. On the other hand, unstable behavior during the consolidation process, whereby the stress paths depart from the failure line, has been observed. Bishop and Lovenbury (1969) and Leroueil et al. (1985) conducted drained creep tests on undisturbed clay, and observed creep failure and a temporary rise in the strain rate with an increasing pore water pressure. Mitchell (1986) pointed out that the observed pore pressure stagnation or its continuous increase during consolidation might be caused by the structural breakdown of sensitive clay.

We propose the model which describes the viscoplastic strain-softening which is related to the structural changes in the present study. Structural changes are described as shrinking of both the overconsolidation boundary surface and the static yield surface with the evolution of the viscoplastic strain. In the following, the developed model will firstly be presented. Simulations of undrained triaxial compression tests for both normally consolidated and overconsolidated clays are performed in order to evaluate the performance of the proposed model. Next, the model is applied to the experimental results of undrained triaxial compression tests for Osaka Pleistocene clay. Finally, the instability of the proposed constitutive equation will be evaluated for both undrained creep and secondary compression.

2.2 Elasto-viscoplastic Model for Clay

In the present study, the concept of Terzaghi's effective stress for water-saturated soil is used as

$$\sigma_{ij} = \sigma'_{ij} + u_w \delta_{ij} \tag{2.1}$$

where σ_{ij} is the total stress tensor, σ'_{ij} is the effective stress tensor, u_w is the pore water pressure, and δ_{ij} is Kronecker's delta. It is assumed that the strain rate tensor consists of an elastic strain rate tensor and a viscoplastic strain rate tensor, so that

$$\dot{\varepsilon}_{ij} = \dot{\varepsilon}^e_{ij} + \dot{\varepsilon}^{vp}_{ij} \tag{2.2}$$

2.2.1 Elastic Strain Rate

Elastic strain rate $\dot{\varepsilon}^e_{ij}$ can be broken down into

$$\dot{\varepsilon}^e_{ij} = \dot{e}^e_{ij} + \frac{1}{3}\dot{\varepsilon}^e_v \delta_{ij} \tag{2.3}$$

where $\dot{e}^e_{ij}$ is the deviatoric component of the elastic strain rate tensor and $\dot{\varepsilon}^e_v$ is the elastic volumetric strain rate ($\dot{\varepsilon}^e_v = \dot{\varepsilon}^e_{11} + \dot{\varepsilon}^e_{22} + \dot{\varepsilon}^e_{33}$).

The elastic deviatoric strain rate is given by

$$\dot{e}^e_{ij} = \frac{1}{2G}\dot{S}_{ij} \tag{2.4}$$

where G is the elastic shear coefficient, S_{ij} is the deviatoric stress tensor ($S_{ij} = \sigma'_{ij} - \sigma'_m \delta_{ij}$), and the superimposed dot denotes the time differentiation. σ'_m denotes the mean effective stress ($\sigma'_m = \frac{1}{3}\sigma'_{kk}$). The elastic shear coefficient G is assumed to be proposional to $\sqrt{\sigma'_m}$ as

$$G = G_0\sqrt{\frac{\sigma'_m}{\sigma'_{m0}}} \tag{2.5}$$

in which G_0 is the value of G when $\sigma'_m = \sigma'_{m0}$.

Considering a proportional relation between void ratio e and the logarithm of σ'_m in the isotropic swelling process, the following incremental relation is obtained:

$$de^e = -\kappa\frac{d\sigma'_m}{\sigma'_m} \tag{2.6}$$

where de^e is the elastic component of the void ratio increment and $d\sigma'_m$ denotes the increment in mean effective stress. κ is the swelling index determined by the slope of the volumetric unloading curve on the natural logarithmic scale. The elastic volumetric strain increment can be given as

$$\begin{aligned} d\varepsilon^e_v &= -\frac{de^e}{1+e_0} \\ &= \frac{\kappa}{1+e_0}\frac{d\sigma'_m}{\sigma'_m} \end{aligned} \tag{2.7}$$

in which e_0 is the initial void ratio. Hence, the elastic volumetric strain rate is obtained as the following:

$$\dot{\varepsilon}^e_v = \frac{\kappa}{1+e_0}\frac{\dot{\sigma}'_m}{\sigma'_m} \tag{2.8}$$

2.2.2 Overconsolidation Boundary Surface

In the constitutive model for overconsolidated soils proposed by Adachi and Oka, it is assumed that an overconsolidation (OC) boundary surface exists which delineates the OC region ($f_b < 0$) from the normal consolidated (NC) region ($f_b \geq 0$). In previous papers (Adachi and Oka 1984; Oka 1992; Oka et al. 1999), a similar OC boundary surface was used in an elasto-plastic model for sand and overconsolidated clay. The OC boundary surface was introduced to control the value of $\tilde{M}^*$ in the plastic potential function and the yield function.

$$f_b = \bar{\eta}^*_{(0)} + M^*_m \ln\left(\sigma'_m/\sigma'_{mb}\right) = 0 \tag{2.9}$$

where $\bar{\eta}^*_{(0)}$ is the relative stress ratio defined by

$$\bar{\eta}^*_{(0)} = \left\{ \left(\eta^*_{ij} - \eta^*_{ij(0)} \right) \left(\eta^*_{ij} - \eta^*_{ij(0)} \right) \right\}^{1/2} \tag{2.10}$$

in which (0) denotes the state at the end of the consolidation, in other words, the initial state before deformation occurs. η^*_{ij} is the stress ratio tensor ($\eta^*_{ij} = \frac{S_{ij}}{\sigma'_m}$) and M^*_m is the value of $\eta^* = \sqrt{\eta^*_{ij}\eta^*_{ij}}$ when the volumetric strain increment changes from compression to swelling. σ'_{mb} controls the size of the surface and σ'_{mbi} is the initial value of σ'_{mb}, which is defined as the isotropic consolidation yield stress. Regarding the structured soil, which has been affected by chemical bonding, secondary consolidation, etc., namely, the aging effect, the consolidation yield stress exceeds the largest stress that the soil has ever suffered. That is called quasi-overconsolidated soil. Therefore, it is appropriate to define the quasi-overconsolidation ratio as the ratio of consolidation yield stress σ'_{mbi} to the mean effective stress at the end of consolidation σ'_{m0}, that is, $OCR^* = \sigma'_{mbi}/\sigma'_{m0}$.

The OC boundary surface described in Eq.(2.9) can be written as follows in the triaxial stress state of $(\sigma'_{11}, \sigma'_{33}, \sigma'_{33})$:

$$f_b = \left| \left(\frac{q}{\sigma'_m} \right) - \left(\frac{q}{\sigma'_m} \right)_{(0)} \right| + M_m \ln \frac{\sigma'_m}{\sigma'_{mb}} = 0 \tag{2.11}$$

in which q is the deviator stress ($q = \sigma'_{11} - \sigma'_{33}$) and $M_m = \sqrt{\frac{3}{2}} M^*_m$. This is schematically shown in Fig.2.2.

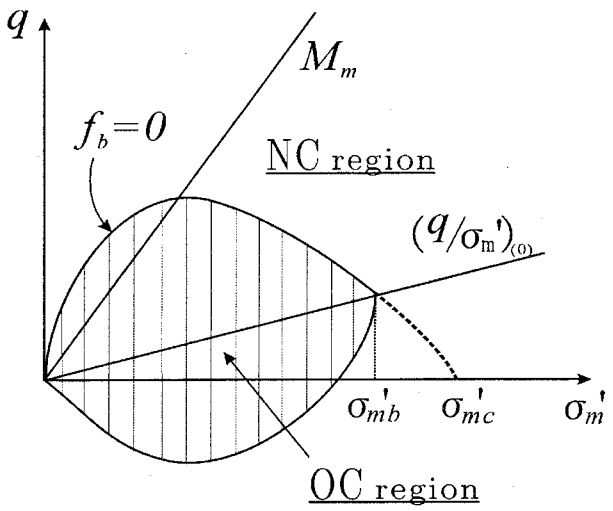

Figure 2.2: Overconsolidation boundary surface under triaxial conditions

Originally, the hardening rule for the OC boundary surface was defined with respect to the viscoplastic volumetric strain as

$$\sigma'_{mb} = \sigma'_{mbi} \exp\left(\frac{1+e_0}{\lambda - \kappa} \varepsilon^{vp}_v \right) \tag{2.12}$$

where λ and κ are the compression and the swelling index which are determined by the slope of the volumetric loading and unloading, respectively, on the natural logarithmic scale, and e_0 is the initial void ratio.

In order to describe the degradation of the material caused by structural changes, strain-softening with the viscoplastic strain is introduced in addition to the hardening with the viscoplastic volumetric strain as

$$\sigma'_{mb} = \sigma'_{ma} \exp\left(\frac{1+e_0}{\lambda-\kappa}\varepsilon_v^{vp}\right) \tag{2.13}$$

in which σ'_{ma} is assumed to decrease with an increasing viscoplastic strain as

$$\sigma'_{ma} = \sigma'_{maf} + (\sigma'_{mai} - \sigma'_{maf}) \exp(-\beta z) \tag{2.14}$$

where z is an accumulation of the second invariant of the viscoplastic strain rate.

$$z = \int_0^t \dot{z} dt \tag{2.15}$$

$$\dot{z} = \left(\dot{\varepsilon}_{ij}^{vp} \dot{\varepsilon}_{ij}^{vp}\right)^{\frac{1}{2}} \tag{2.16}$$

σ'_{mai} and σ'_{maf} are the initial and the final values of σ'_{ma} respectively. Assuming that the value of σ'_{mb} coincides with consolidation yield stress σ'_{mbi} before the viscoplastic deformation occurs, namely, $\varepsilon_v^{vp} = z = 0$,

$$\sigma'_{mbi} = \sigma'_{mai} \tag{2.17}$$

is obtained. β is a parameter which denotes the degradation rate of σ'_{ma}. Hence, two independent parameters, σ'_{maf} and β, are introduced to describe the soil structures. The ratio of σ'_{maf} to σ'_{mai}, namely,

$$n = \sigma'_{maf}/\sigma'_{mai} \tag{2.18}$$

provides the degree for a possible collapse of the structure at the initial state.

2.2.3 Static Yield Function

The mechanical behavior of clay at its static equilibrium state is assumed to be described by the original Cam-clay model (Adachi and Oka 1982). The following static yield function is used:

$$f_y = \bar{\eta}^*_{(0)} + \tilde{M}^* \ln \frac{\sigma'_m}{\sigma'^{(s)}_{my}} = 0 \tag{2.19}$$

$$\bar{\eta}^*_{(0)} = \left\{\left(\eta^*_{ij} - \eta^*_{ij(0)}\right)\left(\eta^*_{ij} - \eta^*_{ij(0)}\right)\right\}^{1/2} \tag{2.20}$$

In the above equation, $\sigma'^{(s)}_{my}$ denotes the mean effective stress in the static equilibrium state, where stress may be reached after an infinite period of time. Accordingly, $f_y = 0$ represents the static state in which no viscoplastic deformation occurs.

Considering volumetric strain hardening, the hardening rule of $\sigma'^{(s)}_{my}$ was originally given as follows:

$$\sigma'^{(s)}_{my} = \sigma'^{(s)}_{myi} \exp\left(\frac{1+e_0}{\lambda-\kappa}\varepsilon^{vp}_v\right) \tag{2.21}$$

In a similar way for OC boundary surface f_b, strain-softening is defined in order to express the effect of a structural collapse through changes in $\sigma'^{(s)}_{my}$ with the viscoplastic strain.

$$\sigma'^{(s)}_{my} = \{n + (1-n)\exp(-\beta z)\}\,\sigma'^{(s)}_{myi} \exp\left(\frac{1+e_0}{\lambda-\kappa}\varepsilon^{vp}_v\right) \tag{2.22}$$

$$= \frac{\left\{\sigma'_{maf} + (\sigma'_{mai} - \sigma'_{maf})\exp(-\beta z)\right\}}{\sigma'_{mai}} \sigma'^{(s)}_{myi} \exp\left(\frac{1+e_0}{\lambda-\kappa}\varepsilon^{vp}_v\right) \tag{2.23}$$

The decrease in $\sigma'^{(s)}_{my}$, defined by Eq.(2.23), leads to the shrinking of the static yield function according to the structural collapse.

2.2.4 Viscoplastic Potential Function

The viscoplastic potential function is given as follows:

$$f_p = \bar{\eta}^*_{(0)} + \tilde{M}^* \ln\frac{\sigma'_m}{\sigma'_{mp}} = 0 \tag{2.24}$$

where $\tilde{M}^*$ is assumed to be constant in the NC region. The value of $\tilde{M}^*$ varies with the current stress and σ'_{mc} in the OC region as

$$\tilde{M}^* = \begin{cases} M^*_m & : \ f_b \geq 0 \\ -\dfrac{\sqrt{\eta^*_{ij}\eta^*_{ij}}}{\ln(\sigma'_m/\sigma'_{mc})} & : \ f_b < 0 \end{cases} \tag{2.25}$$

where σ'_{mc} denotes the mean effective stress at the intersection of the overconsolidation boundary surface and the σ'_m axis as

$$\sigma'_{mc} = \sigma'_{mb} \exp\frac{\sqrt{\eta^*_{ij(0)}\eta^*_{ij(0)}}}{M^*_m} \tag{2.26}$$

In the case of isotropic consolidation, σ'_{mc} equals σ'_{mb}. The overconsolidation boundary surface, f_b, the static yield function, f_y, and the viscoplastic potential function, f_p, for $\eta^*_{ij(0)} = 0$, are illustrated in the σ'_m-$\sqrt{S_{ij}S_{ij}}$ space in Fig.2.3 for the NC region and in Fig.2.4

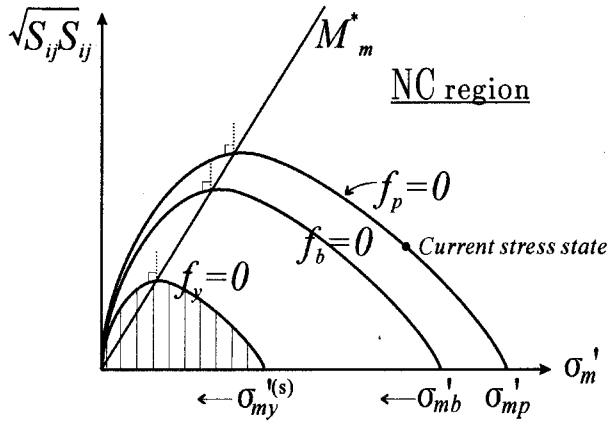

Figure 2.3: OC boundary surface, static yield function, and potential function in the NC region

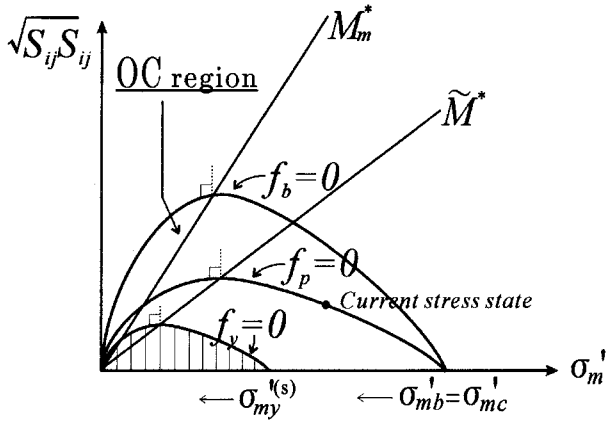

Figure 2.4: OC boundary surface, static yield function, and potential function in the OC region

for the OC region, respectively. σ'_{mb} and $\sigma'^{(s)}_{my}$ decrease with an increasing viscoplastic strain. Although the inside of the static yield function is defined as the elastic region, the initial value of $\sigma'^{(s)}_{myi}$, which is included in parameter C_0 introduced later, is assumed to be very small, so that the current stress state is always outside of the static yield function. The static yield function as well as the potential surface is transformed smoothly between the OC and the NC regions, so that calculations can be conducted continuously without interruption.

2.2.5 Viscoplastic Flow Rule

Viscoplastic strain rate tensor $\dot{\varepsilon}^{vp}_{ij}$ is given as the following equation based on Perzyna's overstress type of viscoplastic theory (Perzyna 1963):

$$\dot{\varepsilon}^{vp}_{ij} = \gamma \left\langle \Phi_1 \left(f_y \right) \right\rangle \frac{\partial f_p}{\partial \sigma'_{ij}} \tag{2.27}$$

where the symbol $\langle\rangle$ is defined as

$$< \Phi_1(f_y) >= \begin{cases} \Phi_1(f_y) & ; \quad f_y > 0 \\ 0 & ; \quad f_y \leq 0 \end{cases} \tag{2.28}$$

in which $f_y = 0$ denotes the static yield function, $f_p = 0$ is the viscoplastic potential function, and Φ_1 denotes a material function for rate sensitivity. Herein, the value of f_y is assumed to be positive for any stress state in this model, in other words, the stress state always exists outside of the static yield function, so that the viscoplastic deformation always occurs.

Based on the experimental results of the strain-rate constant triaxial tests (Adachi and Oka 1984), material function Φ_1 is defined as

$$\begin{aligned}
\gamma\Phi_1(f_y) &= C' \exp\{m' f_y\} \\
&= C' \exp\left\{ m' \left(\bar{\eta}^*_{(0)} + \tilde{M}^* \ln \frac{\sigma'_m}{\sigma'^{(s)}_{my}} \right) \right\} \\
&= C' \exp\left\{ m' \left(\bar{\eta}^*_{(0)} + \tilde{M}^* \ln \frac{\sigma'_{mai}}{\sigma'^{(s)}_{myi}} \frac{\sigma'_m}{\left\{ \sigma'_{maf} + (\sigma'_{mai} - \sigma'_{maf}) \exp(-\beta z) \right\} \exp(A_3 \varepsilon_v^{vp})} \right) \right\} \\
&= C' \exp\left(m' \tilde{M}^* \ln \frac{\sigma'_{mai}}{\sigma'^{(s)}_{myi}} \right) \exp\left\{ m' \left(\bar{\eta}^*_{(0)} + \tilde{M}^* \ln \frac{\sigma'_m}{\sigma'_{ma} \exp(A_3 \varepsilon_v^{vp})} \right) \right\} \\
&= C_0 \exp\left\{ m' \left(\bar{\eta}^*_{(0)} + \tilde{M}^* \ln \frac{\sigma'_m}{\sigma'_{ma} \exp(A_3 \varepsilon_v^{vp})} \right) \right\}
\end{aligned} \tag{2.29}$$

where,

$$A_3 = \frac{1 + e_0}{\lambda - \kappa} \tag{2.30}$$

When we assume $\sigma'_{mai} = \sigma'_{mbi}$,

$$\gamma\Phi_1(f_y) = C_0 \exp\left\{ m' \left(\bar{\eta}^*_{(0)} + \tilde{M}^* \ln \frac{\sigma'_m}{\sigma'_{mb}} \right) \right\} \tag{2.31}$$

Substituting Eq.(2.31) into Eq.(2.27) gives the viscoplastic strain rate as

$$\dot{\varepsilon}_{ij}^{vp} = C_0 \exp\left\{ m' \left(\bar{\eta}^*_{(0)} + \tilde{M}^* \ln \frac{\sigma'_m}{\sigma'_{mb}} \right) \right\} \frac{\partial f_p}{\partial \sigma'_{ij}} \tag{2.32}$$

Finally the viscoplastic deviatoric strain rate and the viscoplastic strain rate are obtained as follows:

$$\begin{aligned}
\dot{e}_{ij}^{vp} &= C_0 \exp\left\{ m' \left(\bar{\eta}^*_{(0)} + \tilde{M}^* \ln \frac{\sigma'_m}{\sigma'_{mb}} \right) \right\} \frac{\partial f_p}{\partial S_{ij}} \\
&= C_0 \exp\left\{ m' \left(\bar{\eta}^*_{(0)} + \tilde{M}^* \ln \frac{\sigma'_m}{\sigma'_{mb}} \right) \right\} \frac{\eta^*_{ij} - \eta^*_{ij(0)}}{\bar{\eta}^*_{(0)}}
\end{aligned} \tag{2.33}$$

$$\begin{aligned}\dot{\varepsilon}_v^{vp} &= C_0 \exp\left\{m'\left(\bar{\eta}^*_{(0)} + \tilde{M}^* \ln\frac{\sigma'_m}{\sigma'_{mb}}\right)\right\}\frac{\partial f_p}{\partial \sigma_{kk}} \\ &= C_0 \exp\left\{m'\left(\bar{\eta}^*_{(0)} + \tilde{M}^* \ln\frac{\sigma'_m}{\sigma'_{mb}}\right)\right\}\left(\tilde{M}^* - \frac{\eta^*_{ij}(\eta^*_{ij} - \eta^*_{ij(0)})}{\bar{\eta}^*_{(0)}}\right) \end{aligned} \tag{2.34}$$

2.3 Determination of Material Parameters

Given below are the ten material parameters for the proposed equations.

- Initial void ratio e_0, compression index λ, and swelling index κ
- Elastic shear modulus G_0
- Compression yield stress σ'_{mbi}
- Stress ratio at maximum compression M^*_m
- Viscoplastic parameters m' and C_0
- Structural parameters σ'_{maf} and β

The procedure for determining these parameters is as follows. Initial void ratio e_0 can be obtained from tests for physical properties. Compression index λ and swelling index κ are given by the slope of the isotropic consolidation and the swelling tests, respectively. Compression yield stress σ'_{mbi} is assumed to be determined from the yield point of the isotropic consolidation tests.

Elastic shear modulus G_0 can be determined from the initial slope of the undrained triaxial compression tests as

$$G_0 = \frac{1}{3}\frac{\Delta q}{\Delta \varepsilon_{11}} \tag{2.35}$$

or the drained triaxial compression tests as

$$G_0 = \frac{1}{3}\frac{\Delta q}{\Delta e_{11}} \tag{2.36}$$

where Δq is the increment in the deviator stress, namely, $q = \sigma'_{11} - \sigma'_{33}$, $\Delta\varepsilon_{11}$ is the increment in the axial strain, and Δe_{11} is the increment in the deviatoric strain, namely, $e_{11} = \varepsilon_{11} - \varepsilon_v/3$.

Other material parameters are determined from undrained triaxial compression tests. The stress ratio at maximum compression M^*_m is defined as the stress ratio whereby maximum compression occurs in the drained compression tests. For clay, however, it has

been assumed to equal the stress ratio at the critical state. Herein, M_m^* is determined from the stress ratio at the residual state in the undrained triaxial compression tests.

Viscoplastic parameter m' can be determined from undrained triaxial compression tests with different strain rates. From Eq.(2.33), viscoplastic deviatoric strain rate $\dot{e}_{11}^{vp}$ in triaxial stress state is obtained as

$$\dot{e}_{11}^{vp} = \sqrt{\frac{2}{3}} C_0 \exp\left\{ m' \left(\sqrt{\frac{2}{3}} \frac{q}{\sigma'_m} + \tilde{M}^* \ln \frac{\sigma'_m}{\sigma'_{mb}} \right) \right\} \tag{2.37}$$

Considering the undrained conditions, and assuming that the elastic strain rate is negligible, we obtain $\dot{e}_{11}^{vp} = \dot{\varepsilon}_{11}$. When undrained triaxial tests with different strain rates $\dot{\varepsilon}_{11}^{(1)}$ and $\dot{\varepsilon}_{11}^{(2)}$ are performed, the following equations are obtained at the point where the mean effective stress takes the same value, $\sigma_m'^{(0)}$, in the stress path (see Fig.2.5).

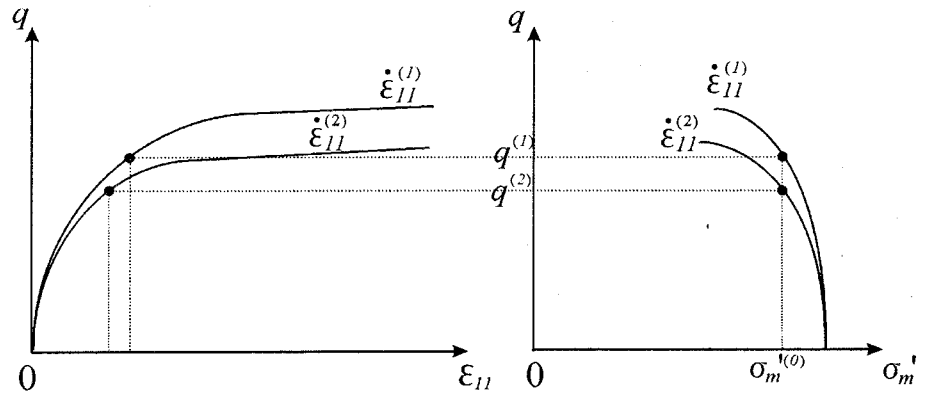

Figure 2.5: Determination of parameter m'

$$\frac{\dot{\varepsilon}_{11}^{(1)}}{\dot{\varepsilon}_{11}^{(2)}} = \exp\left\{ m' \sqrt{\frac{2}{3}} \left(\left(\frac{q}{\sigma'_m} \right)^{(1)} - \left(\frac{q}{\sigma'_m} \right)^{(2)} \right) \right\} \tag{2.38}$$

$$m' = \sqrt{\frac{3}{2}} \frac{\ln \dot{\varepsilon}_{11}^{(1)} - \ln \dot{\varepsilon}_{11}^{(2)}}{(\frac{q}{\sigma'_m})^{(1)} - (\frac{q}{\sigma'_m})^{(2)}} \tag{2.39}$$

When m' is determined, viscoplastic parameter C_0 is obtained from Eq.(2.37). The determination of structural parameters σ'_{maf} and β will be discussed in the next section.

2.4 Numerical Simulation of Undrained Triaxial Tests

The ability of a non-linear computational analysis to provide realistic simulations of the behavior of soil depends directly on the capability of the constitutive model used to describe the mechanical response of the soil skeleton. In this section, simulations of

undrained triaxial tests are conducted to investigate the performance of the model including dilatancy characteristics and stress-strain relations in both NC and OC regions. In particular the effects of structural parameters σ'_{maf} and β will be studied.

Table 2.1: Material parameters for NC clay

Parameters	NC clay
Elastic shear modulus G_0(kPa)	31600
Compression index λ	0.508
Swelling index κ	0.0261
Initial void ratio e_0	1.70
Compression yield stress $\sigma'_{mbi}(=\sigma'_{mai})$ (kPa)	580
Stress ratio at maximum compression M^*_m	1.09
Viscoplastic parameter m'	18.5
Viscoplastic parameter C_0 (1/s)	1.3×10^{-13}

2.4.1 Characteristics of Normally Consolidated Clay

Numerical simulations of undrained triaxial compression tests are conducted using a numerical approximation, namely, the Runge-Kutta method, by giving incompressive strain rates of $(\dot{\varepsilon}_{11}, \dot{\varepsilon}_{22}, \dot{\varepsilon}_{33}) = \left(\dot{\varepsilon}_{11}, -\frac{1}{2}\dot{\varepsilon}_{11}, -\frac{1}{2}\dot{\varepsilon}_{11}\right)$ under the triaxial stress state. A strain rate of $\dot{\varepsilon}_{11}$=0.005%/min is provided for all calculations. The effects of structural parameters σ'_{maf} and β, which are introduced in the present study, are examined in the NC region.

At first, parametric studies on the changes in σ'_{maf} are performed. β is set to be 10 in all calculations. The remaining soil parameters are listed in Table 2.1. Fig.2.6 provides the stress-strain relations and the effective stress paths obtained from the simulations. From Fig.2.6, it is confirmed that parameter σ'_{maf} controls the degree of the decline in peak stress. In the original model, which corresponds to the case of σ'_{maf} = 580 (=σ'_{mai}), the stress state remains constant in a residual state. The smaller the value of σ'_{maf} becomes, the lower the residual stress becomes. Fig.2.7 shows the effect of β in the NC region. The material parameters used in the calculations are the same as those listed in Table 2.1. In the calculations, σ'_{maf} is set to be 300 kPa. Fig.2.7 confirms that β determines the rate of the degradation of strain-softening. The larger the β value becomes, the faster the stress state reaches the residual state.

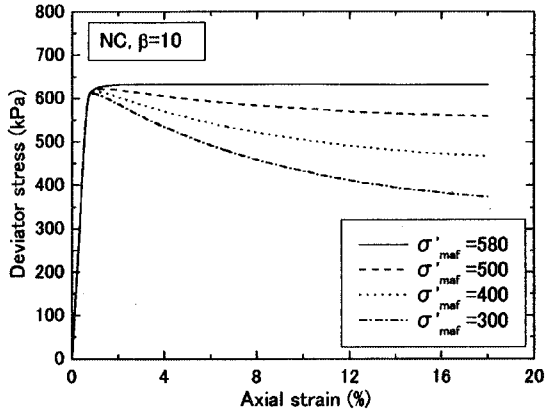

(a) Stress-strain relations

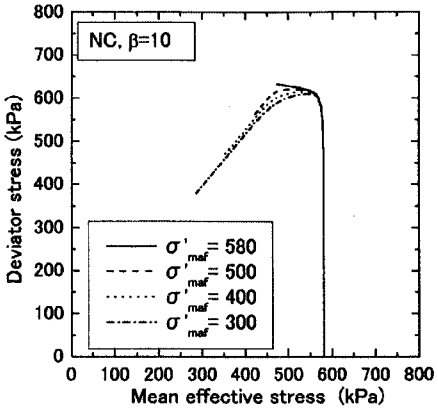

(b) Stress paths

Figure 2.6: Effects of parameter σ'_{maf} in the NC region

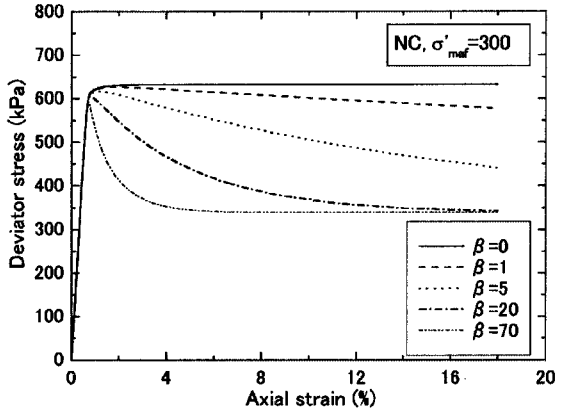

(a) Stress-strain relations

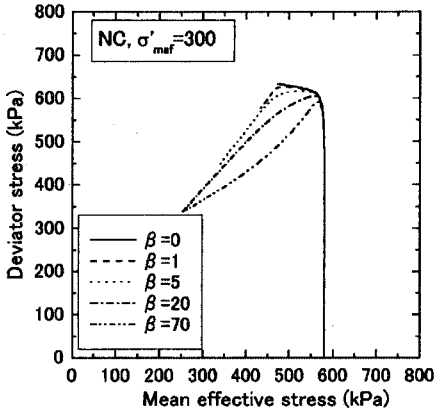

(b) Stress paths

Figure 2.7: Effects of parameter β in the NC region

2.4.2 Characteristics of Overconsolidated Clay

Similarly parametric studies for σ'_{maf} and β are conducted in the overconsolidated regions of OCR=2.0 and 5.9. The material parameters for the overconsolidated soils are listed in Table ??. The parametric studies of σ'_{maf} and β for OCR=2.0 are shown in Figs.2.8 and 2.9, respectively. The effects of the structural parameters are similar to those obtained in the NC region. The parametric studies of the structural parameters for OCR=5.9 are shown in Figs.2.10 and 2.11, respectively. These results reveals that structural parameter σ'_{maf} provides the residual state of the soil, which is related to the degree of initial structure, while β controls the rate of collapse of the structure.

It should be noted that $\dot{e}^{vp}_{ij}$ and $\dot{\varepsilon}^{vp}_{v}$ take a small value in the OC region in the case of $\eta^*_{ij(0)} = 0$. It is because $\tilde{M}^* = -\frac{\sqrt{\eta^*_{ij}\eta^*_{ij}}}{\ln(\sigma'_m/\sigma'_{mb})}$ is obtained from Eqs.(??) and (??). Conclu-

Table 2.2: Material parameters for OC clay

Parameters	**OCR=2.0**	**OCR=5.9**
Elastic shear modulus G_0(kPa)	22500	13000
Compression index λ	0.508	
Swelling index κ	0.0261	
Initial void ratio e_0	1.70	
Compression yield stress σ'_{mbi} (kPa)	580	
Stress ratio at maximum compression M^*_m	1.09	
Viscoplastic parameter m'	18.5	
Viscoplastic parameter C_0 (1/s)	4.0×10^{-13}	1.0×10^{-10}

Conclusively,

$$\bar{\eta}^*_{(0)} + \tilde{M}^* \ln \frac{\sigma'_m}{\sigma'_{mb}} = 0 \tag{2.40}$$

is approved in Eq.(2.32) when $\eta^*_{ij(0)} = 0$ in the OC region. In Figs.2.8(b)~2.11(b), the stress paths depart from the OC boundary surface before softening occurs, and accordingly, strain-softening occurs in the NC region in the calculations. Consequently, σ'_{maf} can be determined from the residual stress; β is then determined by a curve fitting method during strain-softening from the undrained triaxial tests.

2.4.3 Application to Osaka Pleistocene Clay

In this section, the model is applied to Osaka Pleistocene clay, namely, Kyuhoji clay and Tsurumi clay. These are sampled from the upper Pleistocene layer called Ma12, which is distributed widely in the western and eastern part of Osaka at a depth of 20-40 meters (Shigematsu 2002). These are marine clays containing diatoms, and exhibit sensitive behavior, which is due to the effect of structures formed during the sedimentation process.

Fig.2.12 compares the undrained compression test results between undisturbed, namely, natural and reconstituted samples for Kyuhoji clay (Yashima et al. 1999). Both of undisturbed and reconstituted clays were sheared with an axial strain rate of 0.005%/min after isotropically consolidation with a confining pressure of 392 kPa, which is a little larger than the compression yield stress of 340 kPa. The initial void ratio of the undisturbed clay is larger than that of the reconstituted clay, specifically, 1.41 for the undisturbed clay

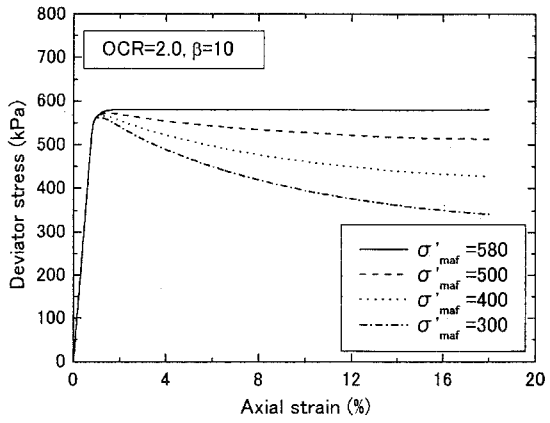

(a) Stress-strain relations

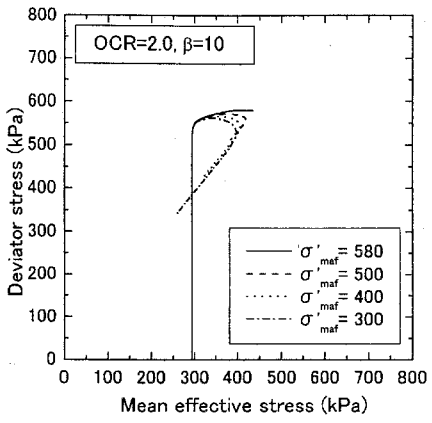

(b) Stress paths

Figure 2.8: Effects of parameter σ'_{maf} in the OC region (OCR=2.0)

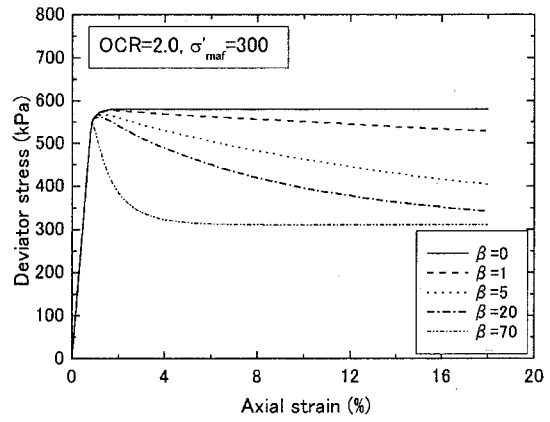

(a) Stress-strain relations

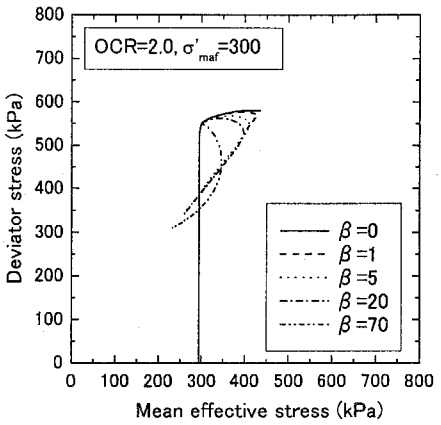

(b) Stress paths

Figure 2.9: Effects of parameter β in the OC region (OCR=2.0)

and 1.02 for the reconstituted clay. The undisturbed clay exhibits larger strength and the deviator stress decreases after the peak stress in Fig.2.12. Fig.2.13 shows the results of simulations. The material parameters used in the simulations are shown in Table 2.3. The structural parameter σ'_{maf} is set to be 280 kPa for the undisturbed clay, and β is set to be 10 for the undisturbed clay and 0 for reconstituted clay. β=0 provides the original model which does not describe structural changes. The values of C_0 contains $\sigma'^{(s)}_{myi}$ concerning the degree of initial structures in the derivation (Eq.(2.29)). Since the degree of the initial structure of the reconstituted clay is considered lower than the undisturbed clay, the larger value of C_0 is given for the reconstituted clay. Fig.2.13 confirms that the proposed model can describe the difference of the behavior between the high structured and the low structured soils.

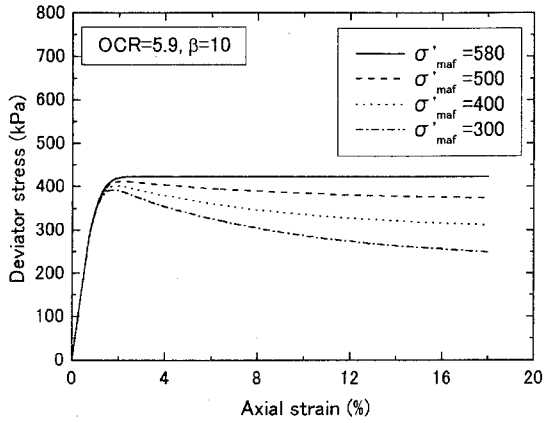

(a) Stress-strain relations

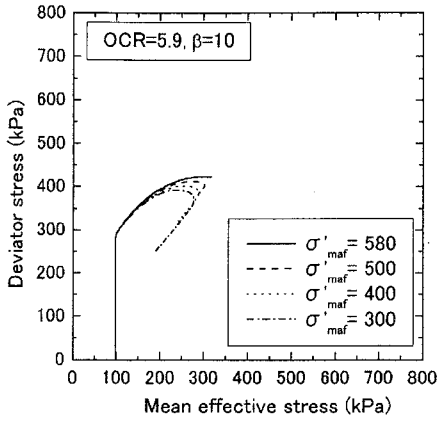

(b) Stress paths

Figure 2.10: Effects of parameter σ'_{maf} in the OC region (OCR=5.9)

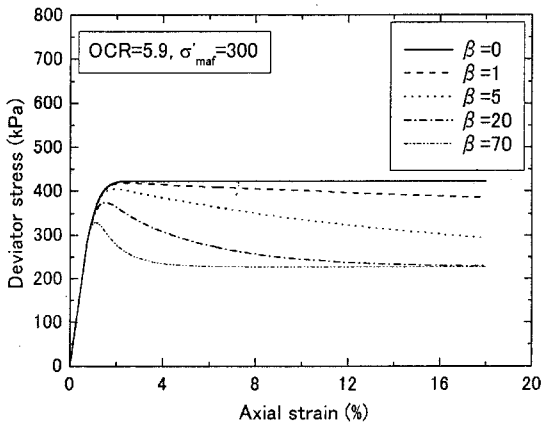

(a) Stress-strain relations

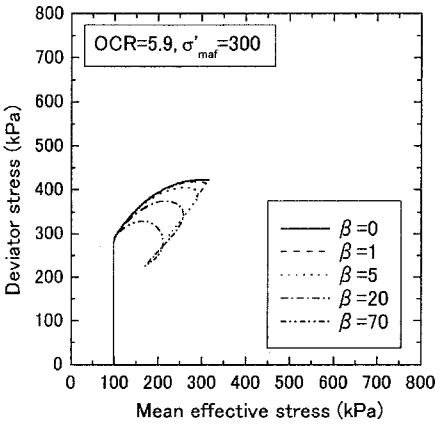

(b) Stress paths

Figure 2.11: Effects of parameter β in the OC region (OCR=5.9)

Fig.2.14 shows the undrained triaxial compression test results for Tsurumi clay, which contains more diatoms than Kyuhoji clay (Yashima et al. 1999). The axial strain rate is 0.005%/min, and the overconsolidation ratios are 1.0 (NC), 2.0, and 5.9. The ratios are determined based on an isotropic yield stress of 580 kPa. Fig.2.15 provides the simulation results by the proposed model considering the soil structure. In the calculations, a constant strain rate of 0.005%/min is adopted. The material parameters used in the calculations are listed in Table 2.4. Figs.2.14 and 2.15 confirm that the model can well describe the strain-softening behavior for the NC clay and the heavily overconsolidated clay, that is, OCR=5.9, in both the stress-strain relations and the stress paths. In the case of OCR=2.0, the mean effective stress decreases after the peak stress in the stress path of the experimental results (Fig.2.14(b)), while it increases after the peak stress in

Table 2.3: Material parameters for Kyuhoji clay

Parameters	**Undisturbed**	**Reconstituted**
Elastic shear modulus G_0(kPa)	8333	6330
Compression index λ	0.327	
Swelling index κ	0.028	
Initial void ratio e_0	1.41	1.02
Compression yield stress $\sigma'_{mbi}(=\sigma'_{mai})$ (kPa)	392	
Stress ratio at maximum compression M^*_m	1.22	
Viscoplastic parameter m'	21.5	
Viscoplastic parameter C_0 (1/s)	4.5×10^{-11}	2.5×10^{-8}
Structural parameter σ'_{maf} (kPa)	280	392
Structural parameter β	10	0

the simulation (Fig.2.15(b)). The reason is that the viscoplastic volumetric strain is assumed to be negative, namely, viscoplastic expansion, above the line of M^*_m outside the OC boundary surface.

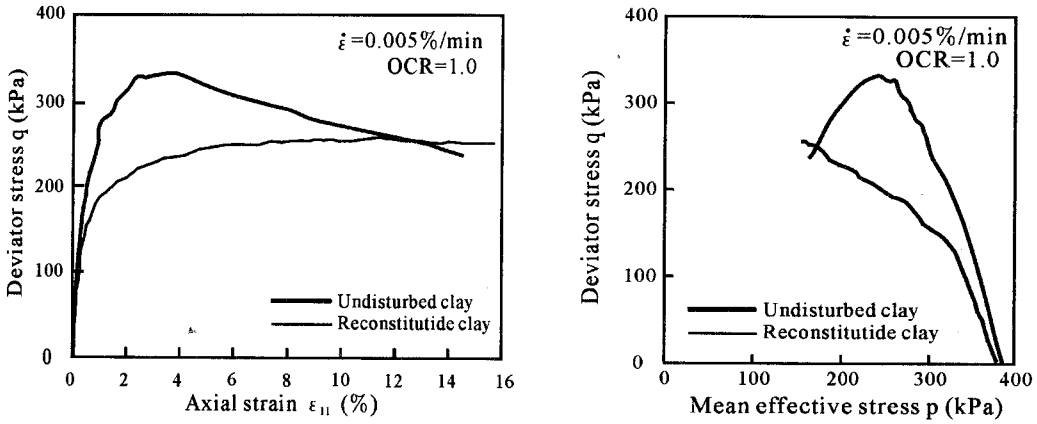

(a) Stress-strain relations (b) Stress paths

Figure 2.12: Experimental results of Kyuhoji clay (Yashima et al. 1999)

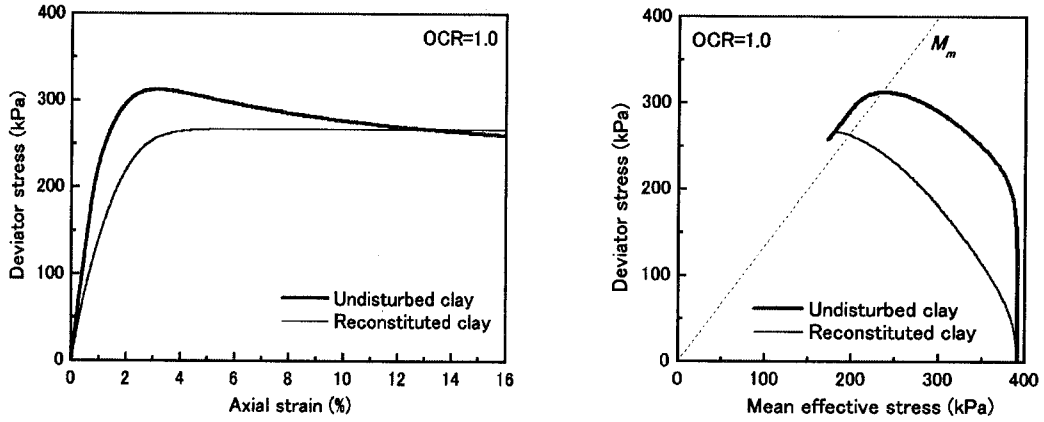

(a) Stress-strain relations (b) Stress paths

Figure 2.13: Simulation results of undrained triaxial tests for Kyuhoji clay

Table 2.4: Material parameters for Tsurumi clay

Parameters	NC	OCR=2.0	OCR=5.9
Elastic shear modulus G_0(kPa)	36100	22500	13000
Compression index λ	0.508		
Swelling index κ	0.0261		
Initial void ratio e_0	1.70		
Compression yield stress $\sigma'_{mbi}(=\sigma'_{mai})$ (kPa)	580		
Stress ratio at maximum compression M^*_m	1.09		
Viscoplastic parameter m'	18.5		
Viscoplastic parameter C_0 (1/s)	1.3×10^{-13}	4.0×10^{-13}	1.0×10^{-10}
Structural parameter σ'_{maf} (kPa)	300	290	370
Structural parameter β	20	45	40

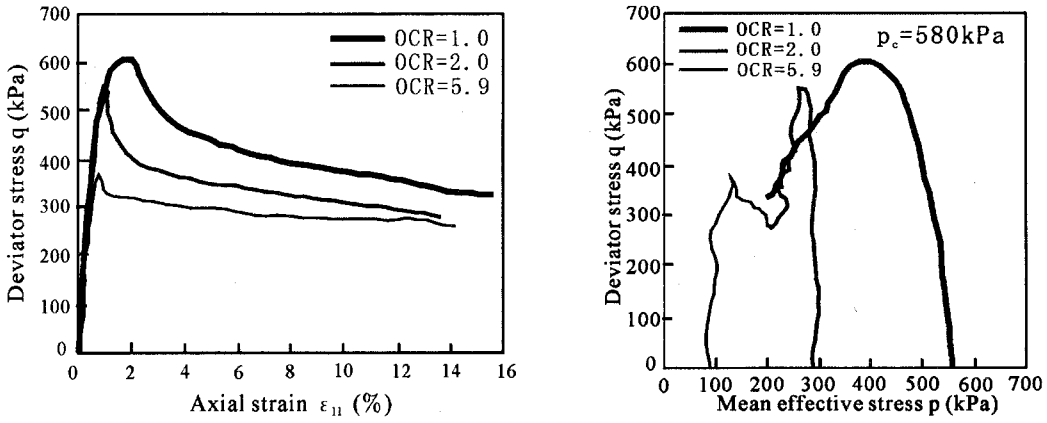

(a) Stress-strain relations (b) Stress paths

Figure 2.14: Experimental results of Tsurumi clay (Yashima et al. 1999)

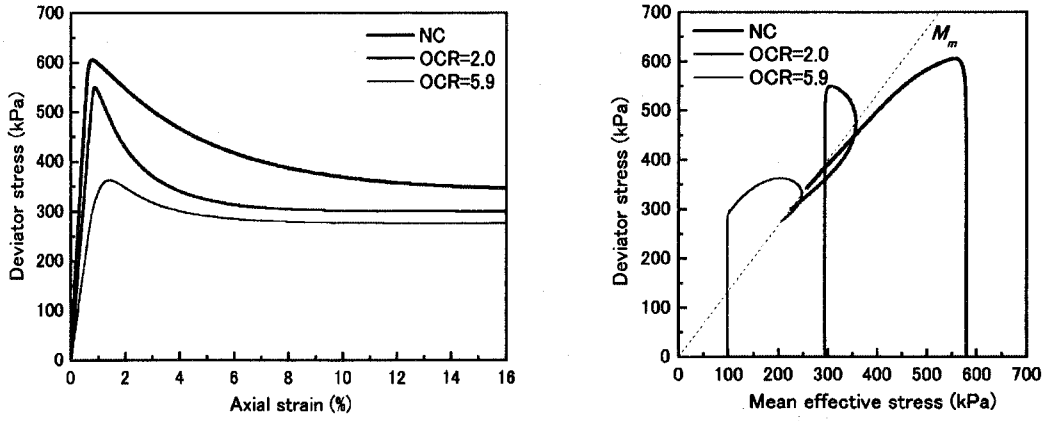

(a) Stress-strain relations (b) Stress paths

Figure 2.15: Simulation results of undrained triaxial tests for Tsurumi clay

2.5 Instability of the Model

The objective of this section is to clarify the instability of the proposed model. The instability is discussed in the sense of Liapunov, that is to say, the instability is evaluated based on whether or not the values approach the solutions at an infinite time, when slightly different initial values for the solutions are provided. Firstly, the instability is evaluated for the undrained creep conditions. Secondly, it is evaluated for constant stress conditions, namely, the secondary consolidation.

2.5.1 Instability During Undrained Creep

Under conventional undrained creep conditions, the volumetric deformation does not occur and the deviatoric stress is kept constant. Since the deviatoric elastic strain rate is zero under creep conditions, the total strain rate is equal to the deviatoric viscoplastic strain rate as

$$\dot{\varepsilon}_{ij} = \dot{e}_{ij} + \frac{1}{3}\dot{\varepsilon}_v \delta_{ij} = \dot{e}_{ij} = \dot{e}_{ij}^{vp} \tag{2.41}$$

From Eq.(2.33), the second invariant of the deviatoric viscoplastic strain rate is expressed as

$$I_2 = I_2^p = \sqrt{\dot{e}_{ij}^{vp}\dot{e}_{ij}^{vp}} = C \exp\left[m'\left\{\eta^* + M^*\left(\ln\frac{\sigma'_m}{\sigma'_{ma}} - y_m^*\right)\right\}\right] \tag{2.42}$$

$$dy_m^* = \frac{1+e_0}{\lambda-\kappa} d\varepsilon_v^{vp} \tag{2.43}$$

$$\eta^* = \frac{\sqrt{2J_2}}{\sigma'_m} \tag{2.44}$$

where $\eta^*_{ij(0)}$=0 and $\tilde{M}^* = M^*$(=const.) are adopted for the normally consolidated specimen under isotropic conditions. In order to express the degradation of the soil structure, the diminution of σ'_{ma} is given in the following equations, as previously mentioned:

$$\sigma'_{ma} = \sigma'_{maf} + \sigma'_{mab}\exp(-\beta z) \tag{2.45}$$

$$\dot{z} = \sqrt{\dot{\varepsilon}_{ij}^{vp}\dot{\varepsilon}_{ij}^{vp}}, \quad z = \int_0^t \dot{z}dt \tag{2.46}$$

$$\sigma'_{mab} = \sigma'_{mai} - \sigma'_{maf}$$

A stress-dilatancy relation is obtained as

$$\dot{\varepsilon}_v^{vp} = (M^* - \eta^*)\, I_2^p \tag{2.47}$$

Since $\dot{\varepsilon}_v^{vp} = -\dot{\varepsilon}_v^e$ is satisfied under undrained conditions, the rate of mean effective stress $\dot{\sigma}'_m$ can be related to volumetric viscoplastic strain rate $\dot{\varepsilon}_v^{vp}$ as

$$\frac{\dot{\sigma}'_m}{\sigma'_m} = \frac{1+e_0}{\kappa}\dot{\varepsilon}_v^e = -\frac{1+e_0}{\kappa}\dot{\varepsilon}_v^{vp} \tag{2.48}$$

The rate of change in stress rate $\dot{\eta}^*$ is expressed as

$$\dot{\eta}^* = -\eta^*\frac{\dot{\sigma}'_m}{\sigma'_m} = \frac{1+e_0}{\kappa}\eta^*\left(M^* - \eta^*\right) I_2^p \tag{2.49}$$

Differentiating Eq.(2.46), with respect to time, gives

$$\dot{\sigma}'_{ma} = -\beta\dot{z}\sigma'_{mb}\exp\left(-\beta z\right) \tag{2.50}$$

$$\dot{z} = \sqrt{\dot{\varepsilon}_{ij}^{vp}\dot{\varepsilon}_{ij}^{vp}} = \sqrt{I_2^{p2} + \dot{\varepsilon}_v^{vp2}} = \sqrt{1 + \left(M^* - \eta^*\right)^2} I_2^p \tag{2.51}$$

Consequently, we obtain the differentiation of the second invariant of the deviatoric viscoplastic strain rate with respect to time as

$$\begin{aligned}
\dot{I}_2 &= m'\left\{\dot{\eta}^* + M^*\left(\frac{\dot{\sigma}'_m}{\sigma'_m} - \frac{\dot{\sigma}'_{ma}}{\sigma'_{ma}} - \dot{y}_m^*\right)\right\} I_2 \\
&= m'\left\{-\frac{1+e_0}{\kappa}(M^* - \eta^*)\left(\frac{\lambda}{\lambda-\kappa}M^* - \eta^*\right) + \frac{\beta\sigma'_{mab}\exp\left(-\beta z\right)}{\sigma'_{ma}}M^*\sqrt{1+(M^*-\eta^*)^2}\right\}[I_2 \\
&= m' a_1\left(\eta^*, z\right)\left[I_2\right]^2
\end{aligned} \tag{2.52}$$

where

$$\begin{aligned}
a_1\left(\eta^*, z\right) = &- \frac{1+e_0}{\kappa}(M^* - \eta^*)\left(\frac{\lambda}{\lambda-\kappa}M^* - \eta^*\right) \\
&+ \frac{\beta\sigma'_{mab}\exp\left(-\beta z\right)}{\sigma'_{ma}}M^*\sqrt{1+(M^*-\eta^*)^2}
\end{aligned} \tag{2.53}$$

For simplicity, Eq.(2.52) is rewritten as

$$\dot{y} = a_1 y^2 \tag{2.54}$$

where

$$y = I_2 \tag{2.55}$$

By integrating the differential equation under the initial conditions whereby $y = y_0$ when $t = 0$, the solution of Eq.(2.54) is obtained as

$$y = \frac{y_0}{\left(1 - a_1 t y_0\right)} \tag{2.56}$$

Let us consider two solutions, y_1 and y_2, for two slightly different initial values for y. At $t = t_0$, $y_{02} = y_{01} + \varepsilon$ in which y_{01} and y_{02} are positive initial values for y and ε is a small

positive constant. At time t, the difference between the two solutions can be evaluated by the following equation:

$$|y_1 - y_2| = \frac{\varepsilon}{|(1 - a_1 t y_{01})(1 - a_1 t(y_{01} + \varepsilon))|} \tag{2.57}$$

If a_1 is negative, the difference becomes zero when $t \to \infty$. This means that the solution is asymptotically stable in the sense of Liapunov. If a_1 is positive, on the other hand, the difference between the two slightly different solutions becomes infinite at a finite time. This indicates that the solution is unstable when a_1 is positive. The positive sign of function $a_1(\eta^*, z)$ in Eq.(2.52) leads to a positive value for the time differentiation of the strain rate, namely, the acceleration of strain in a local sense.

In the case that β equals to zero in Eq.(2.53), which corresponds to the original model, the sign of a_1 depends only on the stress ratio, and $\dot{I}_2$ always denotes a negative in the region of $M^* > \eta^*$. In contrast, the unstable region can not be captured by the current stress in the present model, that is, depending on the stress-strain history, specifically, z and σ'_{ma}. The model shows instability even at low stress ratios. Since the second term in function $a_1(\eta^*, z)$ decreases with an increasing z, the possibility that the will be unstable at the current stress ratio under undrained creep conditions, can be evaluated by replacing 0 with z in Eq.(2.53) as

$$a_1(\eta^*, 0) = \beta(1-n)M^*\sqrt{1 + (M^* - \eta^*)^2} - \frac{1+e_0}{\kappa}(M^* - \eta^*)\left(\frac{\lambda}{\lambda - \kappa}M^* - \eta^*\right) \tag{2.58}$$

In Eq.(2.53), n is the ratio of the final value of σ'_{ma} to the initial value, namely, $\sigma'_{maf}/\sigma'_{mai}$.

When the material parameters are set at, $e_0 = 1.70$, $\lambda = 0.508$, $\kappa = 0.0261$, and $M^* = 1.09$, unstable condition $a_1(\eta^*, 0) > 0$ can be written as

$$\beta > \frac{103(1.09 - \eta^*)(1.15 - \eta^*)}{1.09(1+n)\sqrt{1 + (1.09 - \eta^*)^2}} \tag{2.59}$$

Fig.2.16 shows the unstable region where Eq.(2.59) holds for $\eta^* = 0, 0.5$, and 1.0. If the sets of material parameters for n and β do not satisfy Eq.(2.59), the material cannot be unstable at a stress ratio of η^*. The large value of β and the small value of n lead to the unstable condition.

For the purpose of evaluating the sign of instability index $\dot{I}_2$ during a q =constant undrained creep condition, numerical simulations of undrained creep tests under a triaxial

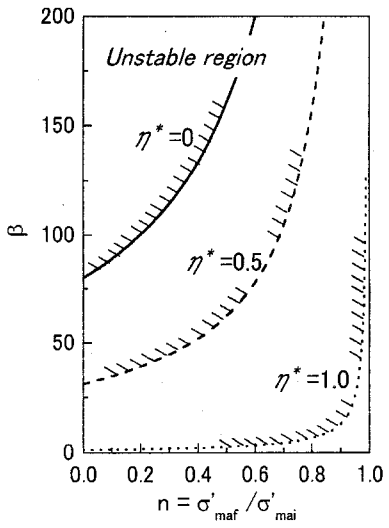

Figure 2.16: Region of parameters n and β satisfying $a_1 > 0$ (Undrained creep)

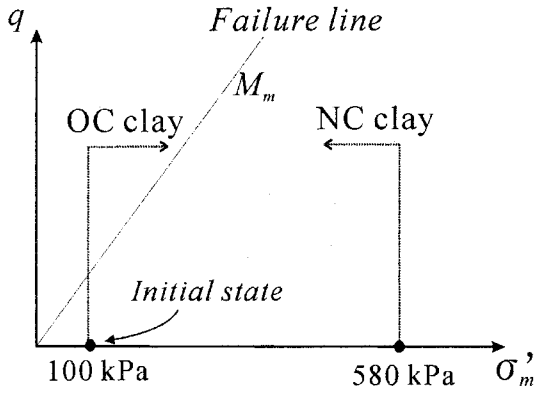

Figure 2.17: Stress paths of undrained creep for NC and OC clays

compression stress state are conducted with the Runge-Kutta method. The initial effective stress levels are 580 kPa for normally consolidated clay and 100 kPa for overconsolidated clay, as illustrated in Fig.2.17. The material parameters for Tsurumi clay are used in the calculations listed in Table 2.4 except structural parameters of σ'_{maf} and β. Material parameter n is set to be 0.5 in all calculations, and β is set to be 20, 40, and 80 for both NC and OC clay. The deviator stress levels are applied in a second for each case and kept constant until the sign of the index, $\dot{I}_2$, becomes positive.

Figs.2.18 and 2.19 show the obtained unstable regions during undrained creep for normally consolidated and overconsolidated clay at the initial state, respectively. In the case of the original model, $\dot{I}_2$ becomes positive only in the region of $M^* < \eta^* < \lambda M^*/(\lambda - \kappa)$, as shown in Fig.2.19, while in the present model, the unstable regions change with the value of β and expand around the failure line.

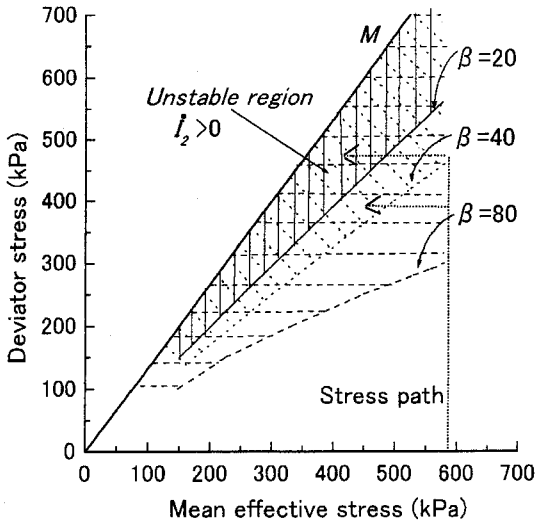

Figure 2.18: Unstable regions during undrained creep simulations ($\eta^* < M^*$)

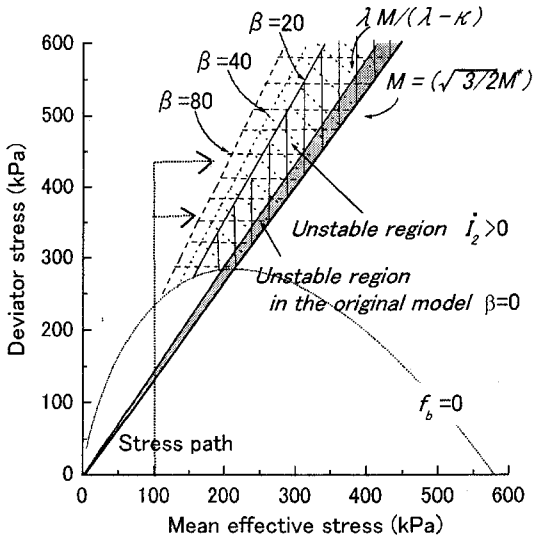

Figure 2.19: Unstable regions during undrained creep simulations ($\eta^* > M^*$)

In the process of deriving Eq.(2.52), M^* is assumed to be constant. In the overconsolidation boundary surface, $f_b < 0$, however, dilatancy coefficient M^* changes with the current stress. The viscoplastic deviatoric strain rate $\dot{e}_{11}^{vp}$ takes a constant value in the OC region when $\eta_{ij(0)}^* = 0$ under a triaxial stress state since Eq.(2.40) is satisfied. Accordingly $\dot{I}_2 = 0$ holds in the overconsolidation region. In other words, no unstable region exists in the overconsolidation region, as seen in Fig.2.19.

2.5.2 Instability During Secondary Consolidation

Let us consider the secondary consolidation in which stress is kept constant under drained conditions. The elastic deformation does not occur in this case. The differentiation of the second invariant of the deviatoric strain rate with respect to time under constant stress yields

$$\begin{aligned}
\dot{I}_2 &= m'M^* \left(-\frac{\dot{\sigma}'_{ma}}{\sigma'_{ma}} - \dot{y}_m^* \right) I_2 \\
&= m'M^* \left\{ -\frac{1+e_0}{\lambda-\kappa} \left(M^* - \eta_c^*\right) + \frac{\beta\sigma'_{mab} \exp\left(-\beta z\right)}{\sigma'_{ma}} \sqrt{1 + (M^* - \eta_c^*)^2} \right\} \left[I_2\right]^2 \\
&= m'M^* a_2\left(z\right) \left[I_2\right]^2
\end{aligned} \tag{2.60}$$

in which

$$a_2\left(z\right) = -\frac{1+e_0}{\lambda-\kappa} \left(M^* - \eta_c^*\right) + \frac{\beta\sigma'_{mab} \exp\left(-\beta z\right)}{\sigma'_{ma}} \sqrt{1 + (M^* - \eta_c^*)^2} \tag{2.61}$$

where η_c^* denotes the creep stress ratio.

The differentiation of the volumetric strain with respect to time is expressed as

$$\begin{aligned}\ddot{\varepsilon}_v &= (M^* - \eta_c^*)\,\dot{I}_2 \\ &= m'M^*\,(M^* - \eta_c^*)\left\{-\frac{1+e_0}{\lambda-\kappa}\,(M^* - \eta_c^*) + \frac{\beta\sigma'_{mab}\exp(-\beta z)}{\sigma'_{ma}}\sqrt{1+(M^* - \eta_c^*)^2}\right\}[I_2]^2 \\ &= m'M^*\,(M^* - \eta_c^*)\,a_2(z)\,[I_2]^2 \end{aligned} \tag{2.62}$$

The condition of instability for the deviatoric strain is given as $a_2(z) > 0$; for the volumetric strain, the condition of instability is

$$a_2(z) > 0 \quad and \quad M^* > \eta_c^* \tag{2.63}$$

Note that if $a_2(z) < 0$ is satisfied in Eq.(2.61), $M^* > \eta_c^*$ should also be satisfied. Then, it follows that $\ddot{\varepsilon}_v < 0$ is obtained when $a_2(z) < 0$. The condition of Eq.(2.63) is related to unstable behavior of the compressive deformation. It cannot be described in the original model since

$$\ddot{\varepsilon}_v = -m'M^*\,(M^* - \eta_c^*)^2\,\frac{1+e_0}{\lambda-\kappa} < 0 \tag{2.64}$$

is obtained by setting β at zero in Eq.(2.62).

The condition $a_2(z) > 0$ yields

$$\frac{\beta(1-n)\exp(-\beta z)}{n+(1-n)\exp(-\beta z)} > \frac{\frac{1+e_0}{\lambda-\kappa}(M^* - \eta_c^*)}{\sqrt{1+(M^* - \eta_c^*)^2}} = c_c \tag{2.65}$$

where $n = \sigma'_{maf}/\sigma'_{mai}$. The left side of Eq.(2.65) decreases with an increasing z; the state becomes stable even if the initial condition is unstable in the secondary consolidation. Supposing z equals zero in the initial state, the condition of instability Eq.(2.65) yields

$$\beta > \frac{c_c}{(1-n)} \tag{2.66}$$

The region of n and β which satisfies Eq.(2.66) for η^*=0, 0.5, and 1.0 is schematically shown in Fig.2.20. The material parameters are set to be the same as those for undrained creep, namely, e_0=1.70, λ=0.508, κ=0.0261, and M^*=1.09. If a set of parameters exists in the unstable region shown in Fig.2.20, the soil becomes unstable at a stress ratio of η_c^*. This presents a description of an accelerating creep of volumetric strain at a constant stress, namely, the secondary consolidation.

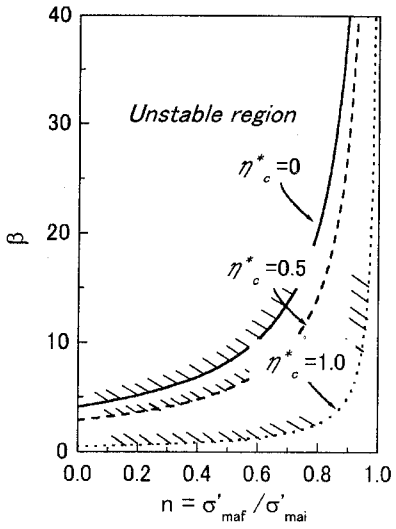

Figure 2.20: Region of parameters n and β satisfying $a_2 > 0$ (Secondary consolidation)

2.6 Summary

In this chapter, an elasto-viscoplastic constitutive model was developed to consider the effect of the structural changes in soils. The proposed model has been applied to undrained triaxial tests on Kyuhoji clay and Tsurumi clay which are typical structured clays. The model can well reproduce the stress-strain relations and the stress paths in undrained triaxial tests in the NC region and heavily consolidated region. In the slightly overconsolidated state, however, the stress path after the peak stress cannot be adequately described. Furthermore, the instability of the proposed model was evaluated during both undrained creep and secondary consolidation. Unstable regions were found to exist around the failure line in both NC and OC regions in the undrained creep simulation, which is related to the creep failure and the strain-softening behavior around the failure stress ratio in undrained compression tests. The model also exhibits instability in the secondary consolidation in which the stress remains constant. It is related to types of unstable behavior during consolidation, such as a sudden increase in strain rate or pore water generation. It should be noted that the instability depends not only on the present stress state, but also on the strain history in the proposed model.

Chapter 3

EFFECT OF STRUCTURAL CHANGES ON STRAIN LOCALIZATION

3.1 Introduction

The problem of strain localization in geomaterials has been studied in the context of experimental, theoretical, and numerical approaches over the last three decades. The conditions for strain localization have been captured in a bifurcation analysis by Rice (1976). Rudnicki and Rice (1975) discussed the localization of deformation as a result of an instability in the constitutive description. They showed that faulting or shear banding may be considered a type of constitutive instability in the sense of a bifurcation appearing in the deformation rate field. Furthermore, Olsson (1999) and Issen and Rudnicki (2000) recognized that the approach of Rudnicki and Rice (1975) could be applied to explain not only shear bands, but also the origin of compaction bands, which are formed perpendicularly to the maximum compressive stress. They discussed the possibility of predicting compaction bands using a set of material parameters.

Strain localization is considered to be affected by both the instability of material and the geometric instability of the deformation. The former is related to the strain-softening characteristics of the material due to the degradation of the microstructure. The latter is the macroscopic instability which is caused by boundary conditions. Both probably affect each other in the strain localization phenomenon.

The objective of this chapter is to study the effect, considering structural changes in the constitutive model, on both shear and compressive localization. We have performed finite element analyses for both undrained and partially drained compression tests for saturated clay under plane strain conditions, and have discussed deformation characteristics including the distribution of both shear and volumetric type of strain, effective stress, and pore water pressure.

Firstly, finite element formulations are presented. Secondly, numerically simulated results of undrained compression are shown. Finally, numerical simulations of partially drained compression tests are presented to discuss the compressive deformation.

3.2 Finite Element Formulation for Strain Localization Analysis

In this section, a finite element formulation for two-phases mixtures based on the finite deformation theory, is presented. Governing equations of the coupling problem, involving the soil skeleton and pore water, are obtained through the application of the two-phase mixture theory by Biot (1962). For a simple and practical formulation, both the grain particles and the fluid are assumed to be incompressible.

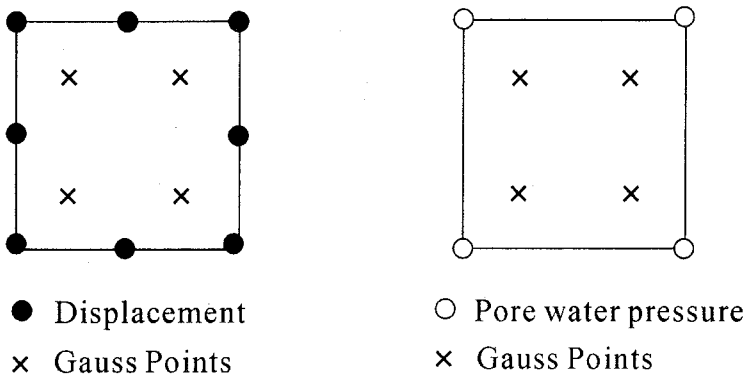

Figure 3.1: Finite elements and Gauss integration points

In the formulations, an updated Lagrangian method with the objective Jaumann rate of Cauchy stress is used for a weak form of the equilibrium equation. An eight-node quadrilateral element with a reduced Gaussian two-point integration is used for the displacement to eliminate shear locking and to reduce the appearance of a spurious hourglass mode. The pore water pressure is defined at the four corner nodes (see Fig.3.1).

3.2.1 Equilibrium Equation

Based on the definition of Terzaghi's effective stress, the total stress tensor is expressed as

$$T_{ij} = T'_{ij} + u_w \delta_{ij} \tag{3.1}$$

$$\dot{T}_{ij} = \dot{T}'_{ij} + \dot{u}_w \delta_{ij} \tag{3.2}$$

where T_{ij} is the total Cauchy stress tensor, T'_{ij} is the effective Cauchy stress tensor, u_w is the pore water pressure, and δ_{ij} is Kronecker's delta. The superimposed dot denotes the time differentiation.

Nominal stress rate tensor $\dot{S}_{ij}$, and the effective nominal stress tensor are given by

$$\dot{S}_{ij} = \dot{T}_{ij} + L_{kk} T_{ij} - T_{ik} L_{jk} \tag{3.3}$$

$$\dot{S}'_{ij} = \dot{T}'_{ij} + L_{kk} T'_{ij} - T'_{ik} L_{jk} \tag{3.4}$$

in which L_{ij} denotes velocity gradient tensor. Substituting Eqs.(3.1) and (3.2) into Eq.(3.3) gives the relation between $\dot{S}_{ij}$ and $\dot{S}'_{ij}$ as

$$\dot{S}_{ij} = \dot{S}'_{ij} + \dot{u}_w \delta_{ij} + B_{ij} \tag{3.5}$$

$$B_{ij} = L_{kk} u_w \delta_{ij} - u_w \delta_{ik} L_{jk} \tag{3.6}$$

The weak form of the equilibrium for the whole fluid-solid mixture is

$$\int_V \dot{S}_{ij,j} \delta v_i dV = 0 \tag{3.7}$$

where δv_i is the component of the virtual velocity vector. Considering the relation,

$$\left(\dot{S}_{ij} \delta v_i\right)_{,j} = \dot{S}_{ij,j} \delta v_i + \dot{S}_{ij} \delta v_{i,j} \tag{3.8}$$

Eq.(3.7) yields

$$\int_V \left(\dot{S}_{ij} \delta v_i\right)_{,j} dV - \int_V \dot{S}_{ij} \delta v_{i,j} dV = 0 \tag{3.9}$$

From the Gauss principle, the first term on the left-hand side of Eq.(3.9) can be written as

$$\int_V \left(\dot{S}_{ij} \delta v_i\right)_{,j} dV = \int_\Gamma \left(\dot{S}_{ij} \delta v_i\right) n_j d\Gamma \tag{3.10}$$

The second term on the left-hand side of Eq.(3.9) yields

$$\int_V \dot{S}_{ij} \delta v_{i,j} dV = \int_V \dot{S}_{ij} \delta L_{ij} dV \tag{3.11}$$

Substituting Eqs.(3.10) and (3.11) into Eq.(3.9) yields

$$\int_{\Gamma} \left(\dot{S}_{ij}\delta v_i\right) n_j d\Gamma - \int_V \dot{S}_{ij}\delta L_{ij} dV = 0 \tag{3.12}$$

Cauchy's stress principle gives

$$\hat{S}_{ti} = \dot{S}_{ij} n_j \tag{3.13}$$

Replacing Eq.(3.12) with Eqs.(3.5) and (3.13) yields

$$\int_V \dot{S}'_{ij}\delta L_{ij} dV + \int_V \dot{u}_w \delta_{ij}\delta L_{ij} dV + \int_V B_{ij}\delta L_{ij} dV = \int_{\Gamma} \hat{S}_{ti}\delta v_i d\Gamma \tag{3.14}$$

In Eq.(3.14), the following relation is approved:

$$\delta_{ij}\delta L_{ij} = \delta L_{kk} = \delta D_{kk} \tag{3.15}$$

in which D_{ij} is the stretching tensor. Substituting Eq.(3.15) into Eq.(3.14) yields

$$\int_V \dot{S}'_{ij}\delta L_{ij} dV + \int_V \dot{u}_w \delta D_{kk} dV + \int_V B_{ij}\delta L_{ij} dV = \int_{\Gamma} \hat{S}_{ti}\delta v_i d\Gamma \tag{3.16}$$

From the symmetry of the effective Cauchy stress tensor,

$$\dot{T}'_{ij} D_{ij} = \frac{1}{2}\dot{T}'_{ij}(L_{ij} + L_{ji}) = \dot{T}'_{ij} L_{ij} \tag{3.17}$$

is obtained.

Finally, a weak form of the equilibrium equation is given in an incremental form by substituting Eqs.(3.4) and (3.17) into Eq.(3.16), in other words,

$$\int_V \dot{T}'_{ij}\delta D_{ij} dV + \int_V A_{ij}\delta L_{ij} dV + \int_V L_{kk} T'_{ij}\delta L_{ij} dV + \int_V \dot{u}_w \delta D_{kk} dV + \int_V B_{ij}\delta L_{ij} dV = \int_{\Gamma} \hat{S}_{ti}\delta v_i d\Gamma \tag{3.18}$$

where

$$A_{ij} = -T'_{ik} L_{jk} \tag{3.19}$$

For the discretization of the weak form of the equilibrium equation, the following relations are defined.

$$\{v\} = [N]\{v^*\}, \quad \{\delta v\} = [N]\{\delta v^*\} \tag{3.20}$$

where $\{v\}$ is the velocity vector in an element, $\{v^*\}$ is the nodal velocity vector, and $[N]$ is the shape function of the eight-node quadrilateral element.

$$\{D\} = [B]\{v^*\}, \quad \{\delta D\} = [B]\{\delta v^*\} \tag{3.21}$$

where $\{D\}$ is the vector form of the stretching tensor and $[B]$ is the matrix which transforms the nodal velocity vector into the stretching vector.

$$trD = D_{ii} = \{B_v\}^T \{v^*\}, \quad \delta D_{ii} = \{B_v\}^T \{\delta v^*\} \tag{3.22}$$

where $\{B_v\}$ is the vector which transforms the nodal velocity into the trace of D.

$$\{L\} = [B_M] \{v^*\}, \quad \{\delta L\} = [B_M] \{\delta v^*\} \tag{3.23}$$

where $\{L\}$ is the velocity gradient vector and $[B_M]$ is the matrix which transforms the nodal velocity vector into the velocity gradient vector.

$$\dot{u}_w = \{N_h\}^T \{\dot{u}_w^*\} \tag{3.24}$$

where $\dot{u}_w$ is the pore pressure rate, $\{\dot{u}_w^*\}$ is the nodal pore pressure rate vector, and $\{N_h\}$ is the shape function of the four-node quadrilateral element.

For the finite deformation theory, the Jaumann rate of Cauchy stress tensor $\hat{T}'_{ij}$ is used in the formulation. The Jaumann rate of Cauchy stress tensor $\hat{T}'_{ij}$ is the objective tensor defined as

$$\hat{T}'_{ij} = \dot{T}'_{ij} - W_{ik}T'_{kj} + T'_{ik}W_{kj} \tag{3.25}$$

where W_{ij} is the spin tensor.

The relation between the Jaumann rate of Cauchy stress $\hat{T}'_{ij}$ and the stretching tensor D_{ij} is obtained as

$$\hat{T}'_{ij} = C^e_{ijkl}D^e_{kl} = C^e_{ijkl}(D_{kl} - D^{vp}_{kl}) \tag{3.26}$$

in which C^e_{ijkl} is the elastic tangential stiffness matrix, D^e_{ij} is the elastic stretching tensor, and D^{vp}_{ij} is the viscoplastic stretching tensor. The viscoplastic stretching tensor D^{vp}_{ij} is given as

$$D^{vp}_{ij} = \gamma \langle \Phi_1 (f_y) \rangle \frac{\partial f_p}{\partial T'_{ij}} \tag{3.27}$$

To evaluate the viscoplastic stretching tensor D^{vp}_{ij}, the tangent modulus method (Pierce et al. 1984) is adopted to obtain stable solutions.

Based on Eq.(3.26), the relation between the Jaumann rate vector of Cauchy stress $\left\{\hat{T}'\right\}$ and stretching vector $\{D\}$ are obtained in the matrix form as

$$\left\{\hat{T}'\right\} = [C] \{D\} - \{Q\} \tag{3.28}$$

where $[C]$ is the tangential stiffness matrix and $\{Q\}$ is the relaxation stress vector. Using the definition for $\left\{\hat{T}'\right\}$ (Eq.(3.25)), Eq.(3.28) can be written as

$$\left\{\dot{T}'\right\} = [C] \{D\} - \{Q\} + \{W^*\} \tag{3.29}$$

where $\{W^*\}$ is the vector defined as $\{W^*\} = \{WT - TW\}$.

Substituting Eqs.(3.20)~(3.29) into Eq.(3.18) and dividing by $\{\delta v^*\}^T$ produce

$$[K]\{v^*\} - \int_V [B]^T \{Q\}\, dV + \int_V [B]^T \{W^*\}\, dV + [K_L]\{v^*\} + [K_v]\{\dot{u}_w^*\} = \left\{\dot{F}\right\} \quad (3.30)$$

in which

$$[K] = \int_V [B]^T [C][B] dV \quad (3.31)$$

$$[K_L] = \int_V [B_M]^T [D_s'][B_M] dV + \int_V [B_M]^T [U][B_M] dV + \int_V [B_M]^T \{T'\}\{B_v\}^T dV \quad (3.32)$$

$$[K_v] = \int_V \{B_v\}\{N_h\}^T dV \quad (3.33)$$

$$\left\{\dot{F}\right\} = \int_\Gamma [N]^T \left\{\hat{S}_t\right\} d\Gamma \quad (3.34)$$

in the above equations, the matrix form of A_{ij} is defined as

$$[A] = [D_s'][B_M]\{v^*\} \quad (3.35)$$

and the matrix form of B_{ij} is defined as

$$[B] = [U][B_M]\{v^*\} \quad (3.36)$$

The relation between nodal velocity vector $\{v^*\}$ and the displacement increment vector of node $\{\Delta u^*\}$ is given by Euler's approximation as

$$\{v^*\} = \frac{\{\Delta u^*\}}{\Delta t} \quad (3.37)$$

For the water pressure, the following equation is obtained with the finite difference method:

$$\{\dot{u}_w^*\} = \frac{\{u_w^*\}_{t+\Delta t} - \{u_w^*\}_t}{\Delta t} \quad (3.38)$$

Substituting Eqs.(3.37) and (3.38) into Eq.(3.30) yields the discretization of the equilibrium equation as

$$\begin{aligned} \left[[K] + [K_L]\right]\{\Delta u^*\} + [K_v]\{u_w^*\}_{t+\Delta t} &= \Delta t \left\{\dot{F}\right\} + [K_v]\{u_w^*\}_t \\ &+ \Delta t \int_V [B]^T \{Q\}\, dV - \Delta t \int_V [B]^T \{W^*\}\, dV \end{aligned} \quad (3.39)$$

3.2.2 Continuity Equation

Boundary surface Γ of closed domain V can be broken down into two parts, namely,

$$\Gamma = \Gamma_p + \Gamma_v \tag{3.40}$$

in which Γ_p is the boundary where the pore water increment is predicted and Γ_v is the boundary where the velocity is predicted.
On boundary Γ_p,

$$u_w = \bar{u}_w \tag{3.41}$$

On boundary Γ_v,

$$v_i = \bar{v}_i \tag{3.42}$$

The equilibrium equation of the fluid phase gives

$$\frac{k}{\gamma_w} u_{w,ii} + D_{ii} = 0 \tag{3.43}$$

where k is the coefficient of permeability and γ_w is the density of the pore water.

Considering the test function of $\hat{u}_w$, we obtain the weak form of the continuity equation as

$$\int_V \left(\frac{k}{\gamma_w} u_{w,ii} + D_{ii} \right) \hat{u}_w dV = \frac{k}{\gamma_w} \int_V u_{w,ii} \hat{u}_w dV + \int_V D_{ii} \hat{u}_w dV = 0 \tag{3.44}$$

Using the relation,

$$u_{w,ii} \hat{u}_w = \left(u_{w,i} \hat{u}_w \right)_{,i} - u_{w,i} \hat{u}_{w,i} \tag{3.45}$$

Eq.(3.44) can be rewritten as

$$\frac{k}{\gamma_w} \int_V \left(\hat{u}_w u_{w,i} \right)_{,i} dV - \frac{k}{\gamma_w} \int_V \hat{u}_{w,i} u_{w,i} dV + \int_V \hat{u}_w D_{ii} dV = 0 \tag{3.46}$$

Using the Gauss principle, Eq.(3.46) yields

$$\frac{k}{\gamma_w} \int_\Gamma \hat{u}_w u_{w,i} n_i d\Gamma - \frac{k}{\gamma_w} \int_V \hat{u}_{w,i} u_{w,i} dV + \int_V \hat{u}_w D_{ii} dV = 0 \tag{3.47}$$

Next, the following vectors and matrixes are defined for the discretization:

$$u_w = \{N_h\}^T \{u_w^*\}, \quad \hat{u}_w = \{N_h\}^T \{\hat{u}_w^*\} \tag{3.48}$$

$$\{u_{w,i}\} = [N_{h,i}]^T \{u_w^*\} = [B_h] \{u_w^*\}, \quad \{\hat{u}_{w,i}\} = [B_h] \{\hat{u}_w^*\} \tag{3.49}$$

$$[N_{h,i}] = \nabla \{N_h\} \tag{3.50}$$

$$D_{ii} = trD = \{B_v\}^T \{v^*\} \tag{3.51}$$

Substituting Eqs.(3.48)~(3.51) into Eq.(3.47) yields

$$\frac{k}{\gamma_w}\int_\Gamma \{\hat{u}_w^*\}^T \{N_h\} \{n\}^T [B_h] \{u_w^*\} \, d\Gamma - \frac{k}{\gamma_w}\int_V \{\hat{u}_w^*\}^T [B_h]^T [B_h] \{u_w^*\} \, dV + \int_V \{\hat{u}_w^*\}^T \{N_h\} \{B_v\}^T \{v^*\} \, dV = 0 \tag{3.52}$$

where $\{n\}$ is the unit vector normal to the boundary surface Γ.

Considering arbitration of the test function, we get the following equation by dividing Eq.(3.52) by $\{\hat{u}_w^*\}^T$, namely,

$$\frac{k}{\gamma_w}\int_\Gamma \{N_h\} \{n\}^T [B_h] d\Gamma \{u_w^*\} - \frac{k}{\gamma_w}\int_V [B_h]^T [B_h] dV \{u_w^*\} + \int_V \{N_h\} \{B_v\}^T dV \{v^*\} = 0 \tag{3.53}$$

Substituting Eq.(3.37) into Eq.(3.53) yields the discretization of the continuity equation as

$$[K_v]^T \{\Delta u^*\} - \Delta t \left([K_h] + [V]\right) \{u_w^*\}_{t+\Delta t} = 0 \tag{3.54}$$

where

$$[K_h] = \frac{k}{\gamma_w}\int_V [B_h]^T [B_h] dV \tag{3.55}$$

$$[K_v]^T = \int_V \{N_h\} \{B_v\}^T dV \tag{3.56}$$

$$[V] = -\frac{k}{\gamma_w}\int_\Gamma \{N_h\} \{n\}^T [B_h] d\Gamma \tag{3.57}$$

Combining Eqs.(3.39) and (3.54) gives the governing equation for the finite element formulation as

$$\begin{bmatrix} [K] + [K_L] & [K_v] \\ [K_v]^T & -\Delta t \left([K_h] + [V]\right) \end{bmatrix} \begin{Bmatrix} \Delta u^* \\ u^*_{w,t+\Delta t} \end{Bmatrix}$$

$$= \begin{Bmatrix} \Delta t \left\{\dot{F}\right\} + [K_v] \{u_w^*\}_t + \Delta t \int_V [B]^T \{Q\} \, dV - \Delta t \int_V [B]^T \{W^*\} \, dV \\ 0 \end{Bmatrix} \tag{3.58}$$

3.3 Numerical Simulation of Undrained Compression Tests

The shearing of a clay specimen is simulated under globally undrained plane strain conditions with displacement control. The finite element mesh and the boundary conditions for the simulations are shown in Fig.3.2.

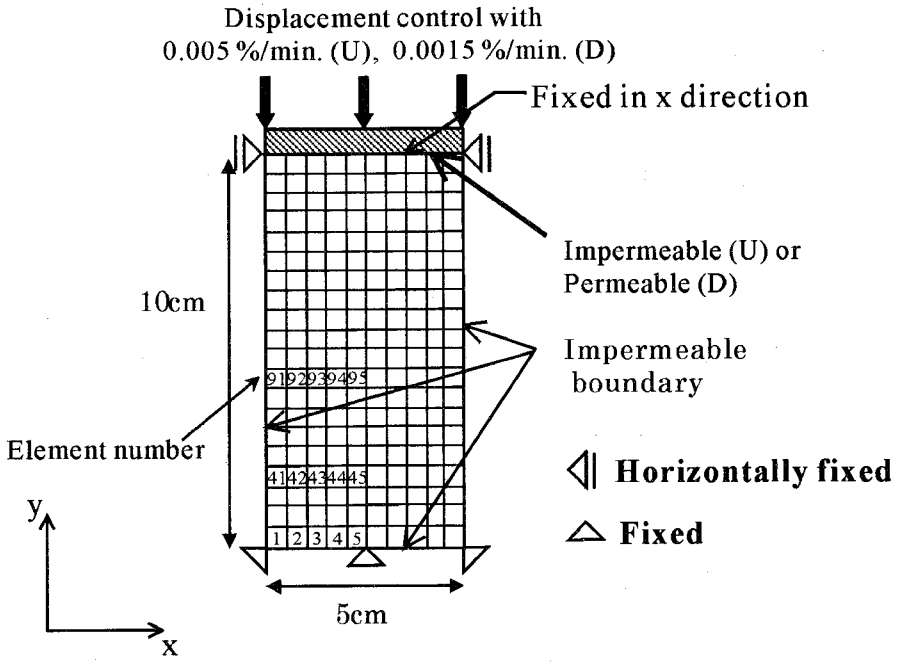

Figure 3.2: Finite element meshes and boundary conditions

The specimen is 5 cm in width by 10 cm in height, and consists of two hundred square elements deforming in plane strain. All the boundaries of the specimen are set to be impermeable in this problem. A constant axial (y-direction) displacement of 0.005%/min is applied to the nodes of the top surface, and a horizontal (x-direction) displacement of nodes on both top and bottom surfaces is constrained as a trigger for strain localization.

Table 3.1: Material parameters β (Undrained conditions)

	NC	OC
Without structural changes	β=0	β=0
With structural changes	β=5, 20, 40	β=40
With Φ_2	G_2=10	

Simulations are performed with both NC and OC clays, which are compared among the models with and without consideration given to structural changes, and with a material function of Φ_2; the patterns of the analyses are listed in Table 3.1.

The initial conditions and the material parameters used in the analysis are listed in Tables 3.2 and 3.3. The material parameters are the same as those used for the simulations

for Tsurumi clay in Chapter 2. In all the computations, the time increment for each step is 6 s, and the increment of the average strain for a step is determined as $\Delta\varepsilon_{11} = 0.0005\%$.

Table 3.2: Initial conditions for the simulations

Initial value	**NC**	**OC**
Initial mean effective stress $\sigma'_{m(0)}$ (kPa)	580	98
Coefficient of earth pressure K_0	1.0	
OCR	1.0	5.9

Table 3.3: Material parameters used in the analysis

Parameters	**NC**	**OCR=5.9**
Coefficient of permeability $k_0(m/s)$	0.8×10^{-9}	
Elastic shear modulus G_0(kPa)	36100	13000
Compression index λ	0.508	
Swelling index κ	0.0261	
Initial void ratio e_0	1.70	
Compression yield stress σ'_{mbi} (kPa)	580	
Stress ratio at maximum compression M^*_m	1.09	
Viscoplastic parameter m'	18.5	
Viscoplastic parameter C_0 (1/s)	1.3×10^{-13}	1.0×10^{-10}
Structural parameter σ'_{maf} (kPa)	300	370
Structural parameter β	0, 5, 20, 40	0, 40

Simulations of the undrained triaxial compression tests with an axial strain rate of 0.005%/min are shown in Figs.3.3 and 3.4 for NC and OC clays, and for the model with Φ_2 in Fig.3.5, respectively, to confirm the properties of the material parameters.

3.3.1 Analysis of Normally Consolidated Clay

3.3.1.1 Structural Parameter (β=0 and 20)

Starting from NC clay, we now compare the results of β=0, that is, the original model, with β=20, namely, the model which considers structural changes. The results for $\beta = 0$

are shown in Figs.3.6~3.12, and the results for β=20 are shown in Figs.3.13~3.19. Fig.3.6 shows the relation between the average vertical stress on the top surface and the average axial strain (Fig.3.6(a)), and the average stress paths (Fig.3.6(b)) for β=0. The average vertical stress was calculated as the mean value of the nodal force in the y-direction along the top surface, and the average mean effective stress was calculated as the mean value of all the elements. In the same way, the average stress-strain relation and the average stress path for β=20 are shown in Figs.3.13(a) and (b). The calculation diverged at an axial strain of around 13% for β=20. Simulations show that the model considering structural changes can describe the degradation of shear strength, while the stress remains nearly constant in the original model of β=0. The average vertical stress attains its peak value at an average axial strain of around 0.57% as seen in Fig.3.13(a).

The stress paths for element 1~5 (at the bottom of the specimen, see Fig.3.2), element 41~45 and element 91~95 (at the center of the specimen) are shown in Fig.3.7 for β=0, and in Fig.3.14 for β=20, respectively. These figures confirm that the stress paths reach the failure line more slowly for the top and bottom elements (element 1-5) than for the center of the specimen because of a lower generation of pore pressure. At the same depth, the stress path reaches the failure line of M_m^* the fastest along the side of the element in both cases.

The deformed meshes at axial strains of 0.6%, 1.0%, 2.0%, 5.0%, 10.0%, and 15.0% for β=0 and β=20 are shown in Figs.3.8 and 3.15. These figures demonstrate that when β=20, a more apparent localization is provided than when β=0. In particular, it is obvious that the horizontal displacement is apparent at the center of the specimen in Fig.3.15.

Figs.3.9 and 3.16 show the distribution of accumulated viscoplastic shear strain $\gamma^p \equiv \int \sqrt{de_{ij}^{vp} de_{ij}^{vp}}$. The lighter region indicates the larger deformation. These figures confirm that shear localization is apparent in the case of β=20, in which the localization starts near the edges of the specimen. Then, four bands proceed from the four edges. In the case of β=20, a small deformation remains at the center. The angle of shear bands will be discussed later.

Figs.3.10 and 3.17 show the distribution of accumulated viscoplastic volumetric strain. The volumetric strain localization is also distributed more apparently in the case of considering structural changes. Viscoplastic volumetric compression develops along the shear

bands in both cases, and a viscoplastic expansion occurs at the center of the specimen.

Figs.3.11 and 3.18 show the distribution of mean effective stress for β=0 and β=20. Fig.3.18 shows a more inhomogeneous distribution than Fig.3.11. The distribution of mean effective stress relates to that of the viscoplastic volumetric strain since calculations are performed under globally undrained conditions. Along shear band where viscoplastic compression occurs, the mean effective stress takes the small value as shown in Fig.3.18.

Figs.3.12 and 3.19 show the distribution of excess pore water pressure for β=0 and β=20. A higher pore water pressure is generated at the top and the bottom of the specimen in the case of β=0, whereas pore water pressure is highly generated in the center in the case of β=20. The distribution of pore water pressure is relatively homogeneous, however, compared to the viscoplastic strain and the mean effective stress. This may be due to the migration of pore water pressure.

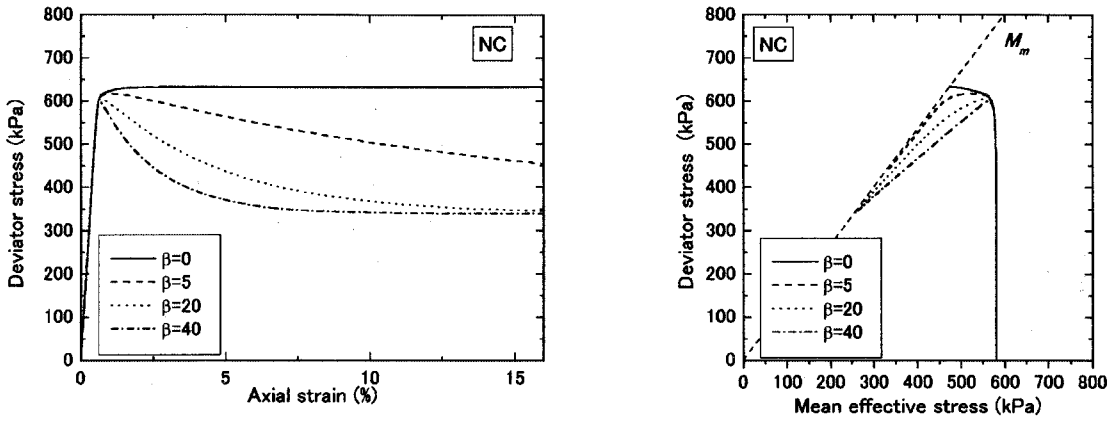

(a) Stress-strain relations (b) Stress paths

Figure 3.3: Simulations of undrained triaxial tests for NC clay

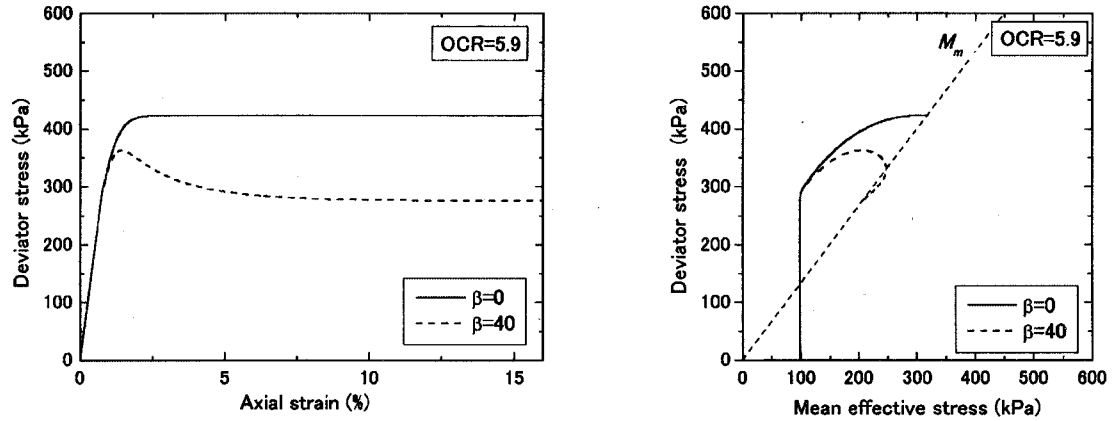

(a) Stress-strain relations (b) Stress paths

Figure 3.4: Simulations of undrained triaxial tests for OC clay

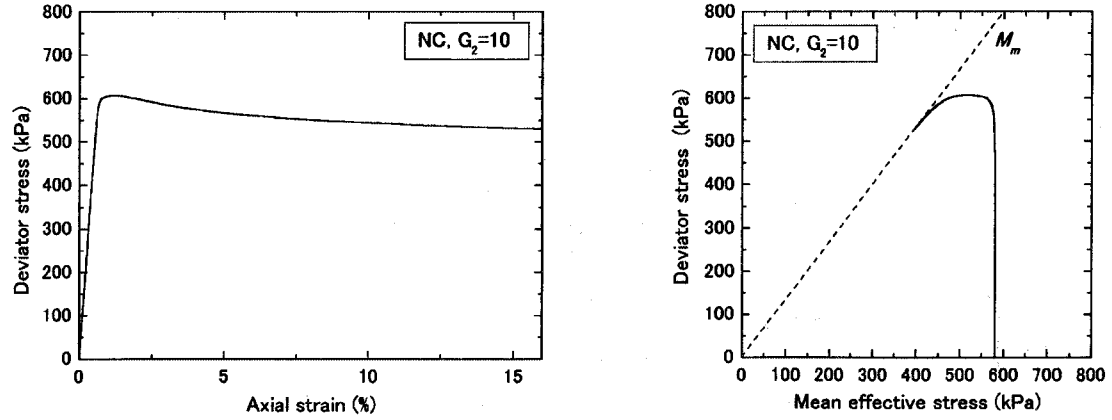

(a) Stress-strain relations (b) Stress paths

Figure 3.5: Simulations of undrained triaxial tests with material function Φ_2 for NC clay

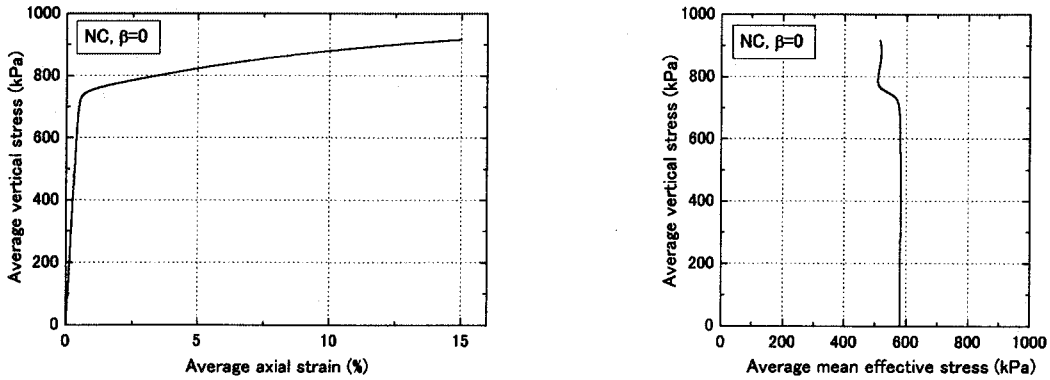

(a) Stress-strain relations (b) Stress paths

Figure 3.6: Undrained compression test for NC clay (β=0)

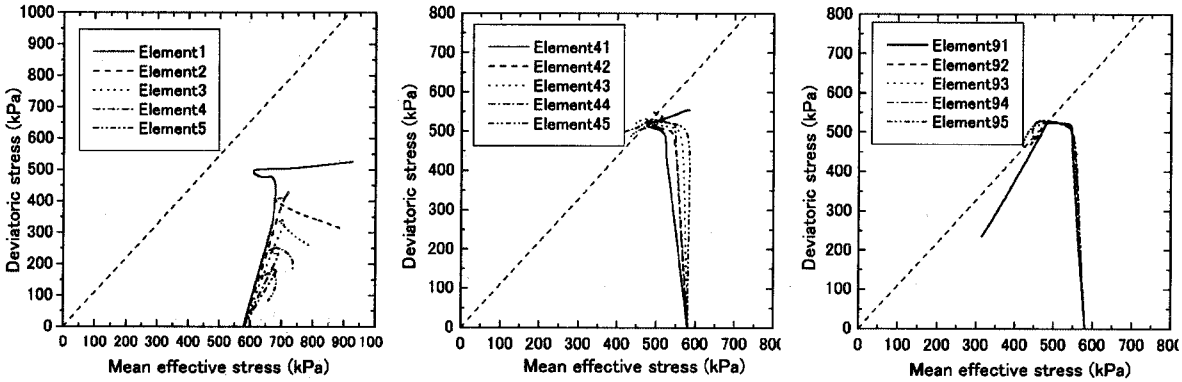

(a) Element 1-5 (b) Element 41-45 (c) Element 91-95

Figure 3.7: Stress paths of each element for NC clay (β=0, Undrained)

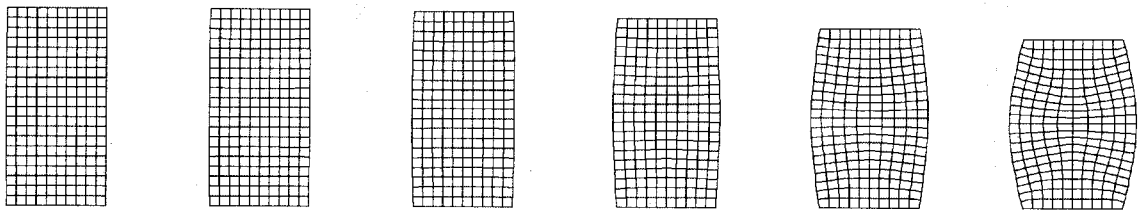

0.6 % 1.0 % 2.0 % 5.0 % 10.0 % 15.0 %

Figure 3.8: Deformed meshes for NC clay (β=0, Undrained))

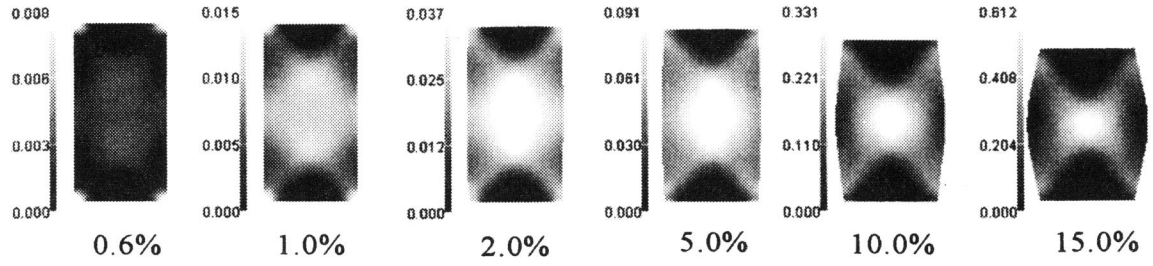

Figure 3.9: Distribution of viscoplastic deviatoric strain for NC clay (β=0, Undrained)

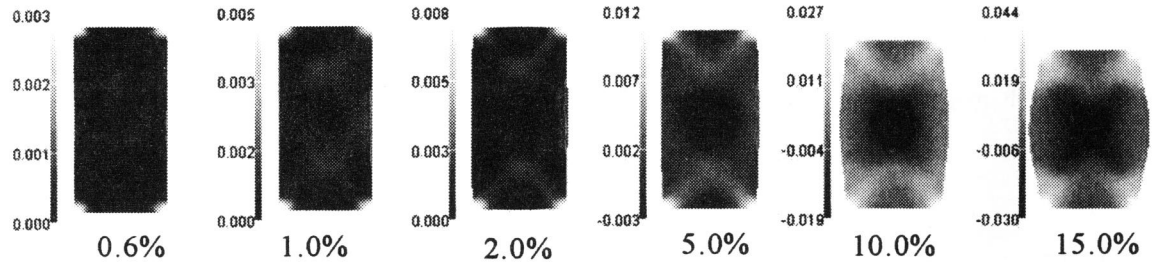

Figure 3.10: Distribution of viscoplastic volumetric strain for NC clay (β=0, Undrained)

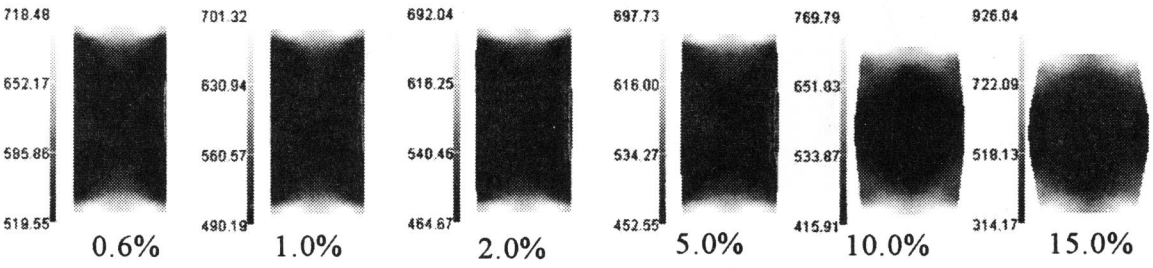

Figure 3.11: Distribution of mean effective stress (kPa) for NC clay (β=0, Undrained)

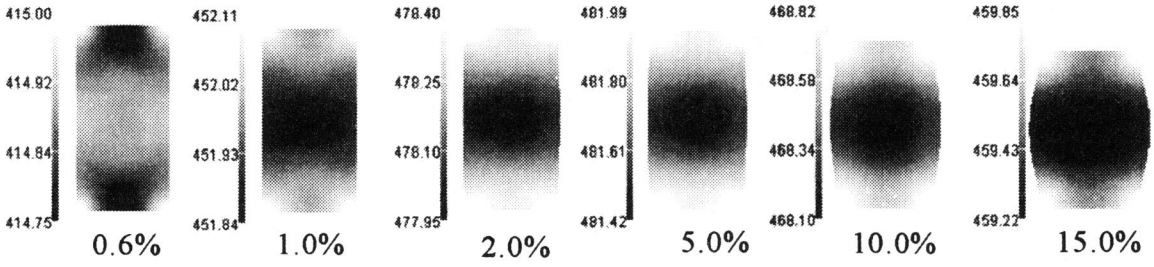

Figure 3.12: Distribution of pore water pressure (kPa) for NC clay (β=0, Undrained)

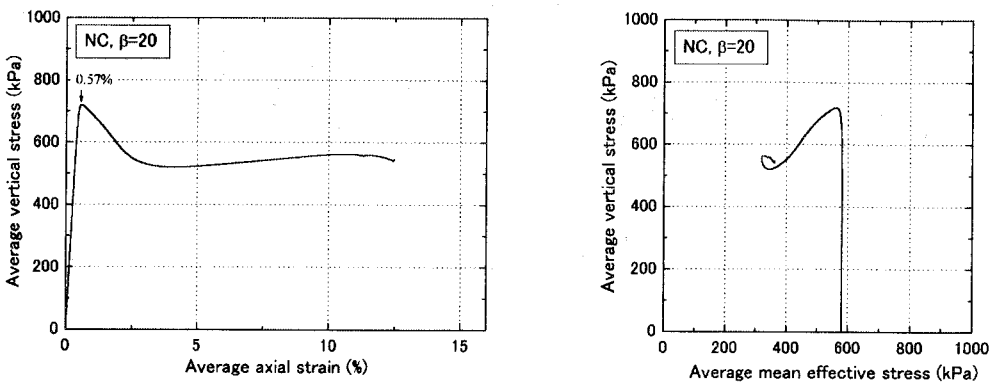

(a) Stress-strain relations (b) Stress paths

Figure 3.13: Undrained compression test for NC clay (β=20)

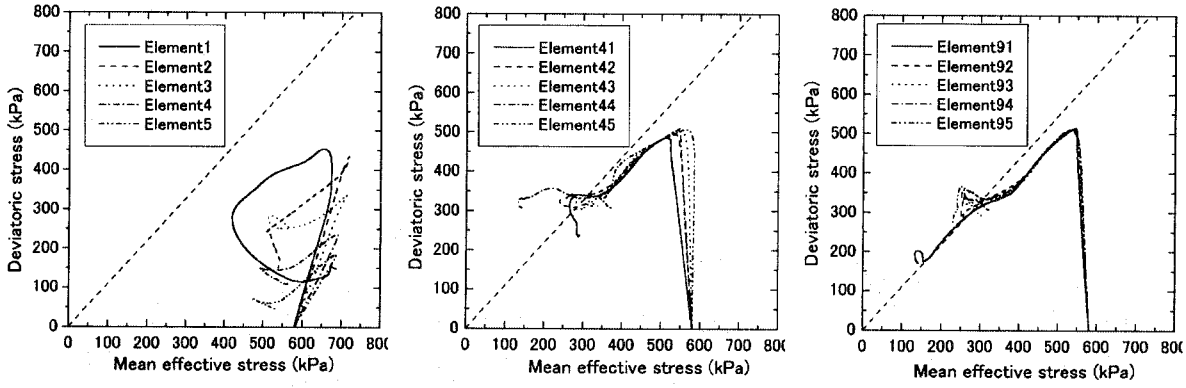

(a) Element 1-5 (b) Element 41-45 (c) Element 91-95

Figure 3.14: Stress paths of each element for NC clay (β=20, Undrained)

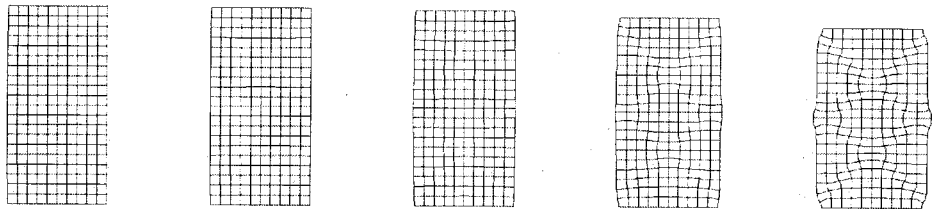

0.6 % 1.0 % 2.0 % 5.0 % 10.0 %

Figure 3.15: Deformed meshes for NC clay (β=20, Undrained))

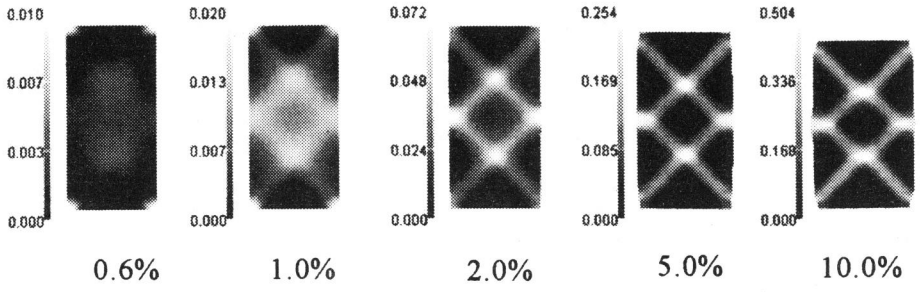

Figure 3.16: Distribution of viscoplastic deviatoric strain for NC clay (β=20, Undrained)

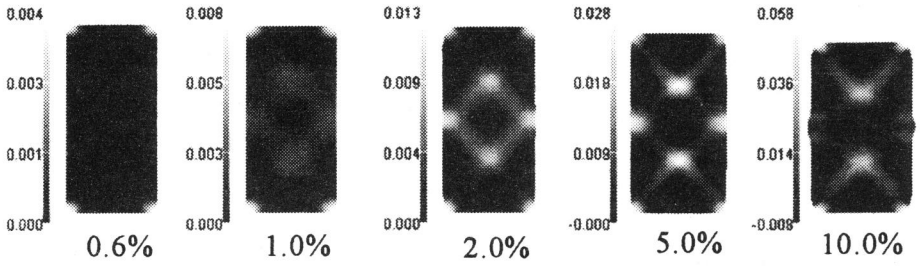

Figure 3.17: Distribution of viscoplastic volumetric strain for NC clay (β=20, Undrained)

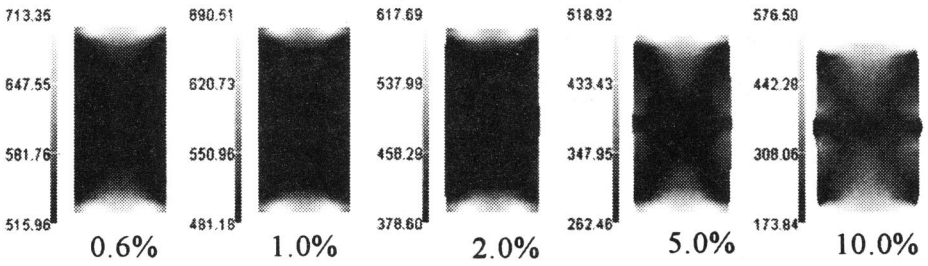

Figure 3.18: Distribution of mean effective stress (kPa) for NC clay (β=20, Undrained)

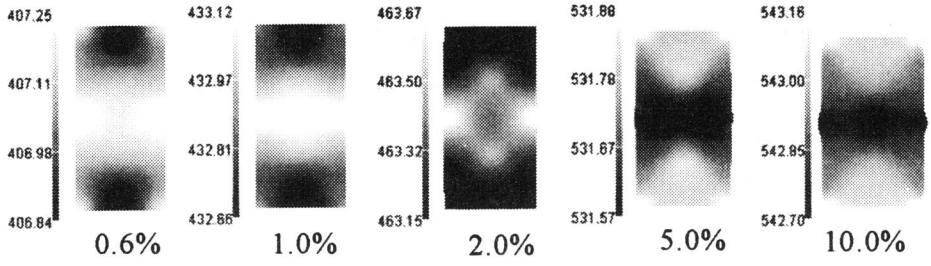

Figure 3.19: Distribution of pore water pressure (kPa) for NC clay (β=20, Undrained)

3.3.1.2 Structural Parameter (β=5, 20, and 40)

Let us compare the calculations of different values for structural parameter β, namely, β=5, 20, and 40. As mentioned in the previous chapter, parameter β controls the rate of collapse for the structure; a larger value for β leads to a rapid decrease in the shear stress.

The calculation results for β=5 are shown in Figs.3.20~3.26: Fig.3.20 shows the average stress-strain relation and the average stress path, Fig.3.21 shows the stress paths of the elements, Fig.3.22 presents the deformed mesh, Fig.3.23 shows the distribution of viscoplastic deviatoric strain γ^p, Fig.3.24 for the distribution of viscoplastic volumetric strain, Fig.3.25 presents the distribution of mean effective stress, Fig.3.26 for the distribution of pore water pressure. The calculation results for β=40 are shown in Figs.3.27 ~3.33 in the same way. The calculation for β=40 diverged at an axial strain of 9.0%. Calculations for β=20 have been already presented in Figs.3.13~3.19.

Comparisons of the average stress-strain relations in Figs.3.13(a), 3.20(a), and 3.27(a) confirm that a larger value for β promotes the rapid degradation of the shear strength. The peak strength is obtained at an axial strain of 0.57% for β=20 and 0.53% for β=40, while the apparent peak is not obtained for β=5. From the comparisons among the stress paths in Figs.3.13(b), 3.20(b), and 3.27(b), the average vertical stress declines at the small value for the stress ratio when β=20 and 40, since the vertical stress decreases at the early stage where the level of pore water pressure is small. Comparisons of the deformed mesh in Figs.3.15, 3.22, and 3.29 demonstrate that the specimen is horizontally compressed at the center of the depth for β=40.

Let us compare the distribution of accumulated viscoplastic deviatoric strain in Figs.3.16, 3.23, and 3.30. The pronounced shear bands are observed at an axial strain of 1.0% for β=40 (see Fig.3.30), at an axial strain of 2.0% for β=20 (see Fig.3.16), and at an axial strain of 5~10% for β=5 (see Fig.3.23). Hence, with the larger value for β, shear localization appears at a smaller average axial strain. The angles of shear bands will be discussed in a later section.

Figs.3.17, 3.24, and 3.31 show the distribution of the viscoplastic volumetric strain. We confirm that the difference between the maximum and minimum value is the largest for β=40.

Figs.3.18, 3.25, and 3.32 show the distribution of mean effective stress for $\beta = 20, 5,$ and 40, respectively. The localization of the mean effective stress becomes apparent at a small axial strain in the case of β=40. Fig.3.19, 3.26, and 3.33 show the distribution of the excess pore water pressure for β=20, 5, and 40, respectively.

3.3.1.3 Analysis with Material Function Φ_2

For comparison, we conducted calculations using the model with material function Φ_2 proposed by Adachi, Oka, and Mimura (1987a) . Material function Φ_2 is a strain-softening term which describes softening when the stress approaches the failure line. The viscoplastic strain rate is given as

$$\dot{\varepsilon}_{ij}^{vp} = \gamma \langle \Phi_1 (f_y) \rangle \Phi_2(\xi) \frac{\partial f_p}{\partial \sigma'_{ij}} \tag{3.59}$$

in which

$$\Phi_2(\xi) = 1 + \xi \tag{3.60}$$

$$\xi = \frac{\bar{\eta}^*_{(0)} M^*_f}{G^*_2 \left\{ M^*_f - \frac{\eta^*_{mn}(\eta^*_{mn} - \eta^*_{mn(0)})}{\bar{\eta}^*_{(0)}} \right\}} \tag{3.61}$$

where $\bar{\eta}^*_{(0)}$ is the relative stress ratio defined by

$$\bar{\eta}^*_{(0)} = \left\{ \left(\eta^*_{ij} - \eta^*_{ij(0)} \right) \left(\eta^*_{ij} - \eta^*_{ij(0)} \right) \right\}^{1/2} \tag{3.62}$$

M^*_f is the failure stress rate, set to be 1.09, and G^*_2 is a viscoplastic parameter, set to be 10 in the calculation. The other material parameters are set to be the same as those listed in Table 3.3 for NC clay. The increment of time and the axial strain for each step are also set to be the same.

The computed results are shown in Figs.3.34~3.40. As shown in Fig.3.34, the calculation diverged before the axial strain reached 7%, since the model rapidly became unstable around the failure line. The geometry of the shear bands is different from that obtained by the proposed model.

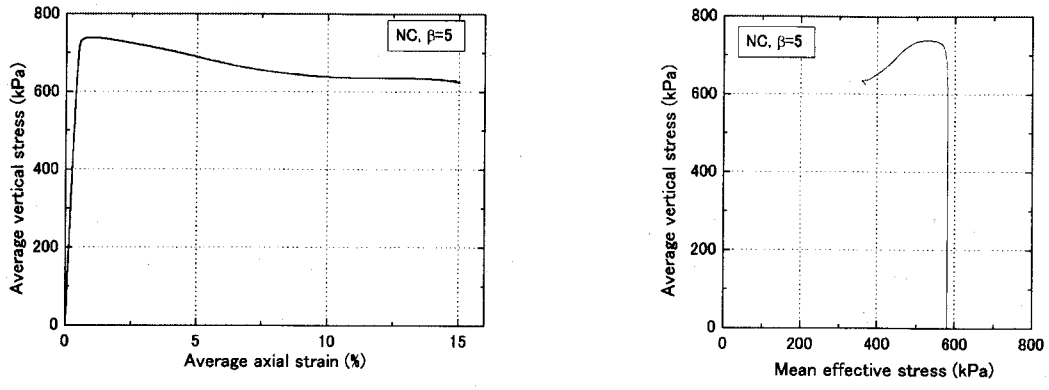

(a) Stress-strain relations (b) Stress paths

Figure 3.20: Undrained compression test for NC clay (β=5)

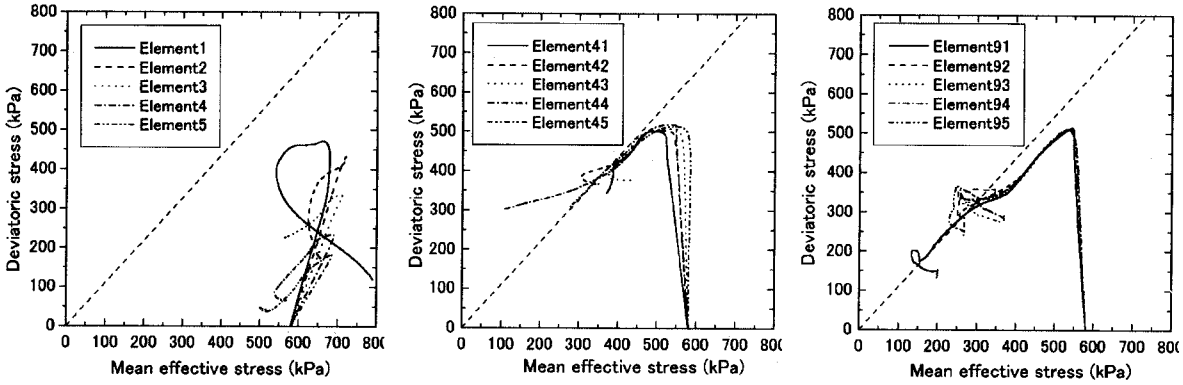

(a) Element 1-5 (b) Element 41-45 (c) Element 91-95

Figure 3.21: Stress paths of each element for NC clay (β=5, Undrained)

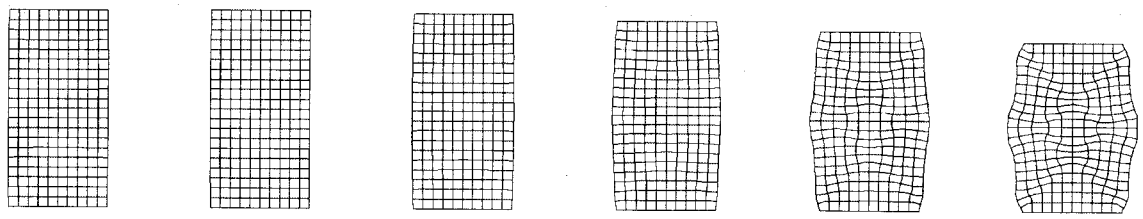

0.6 % 1.0 % 2.0 % 5.0 % 10.0 % 15.0 %

Figure 3.22: Deformed meshes for NC clay (β=5, Undrained))

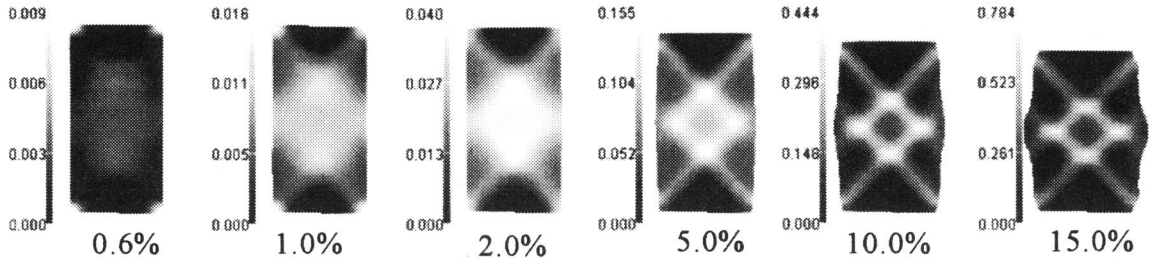

Figure 3.23: Distribution of viscoplastic deviatoric strain for NC clay (β=5, Undrained)

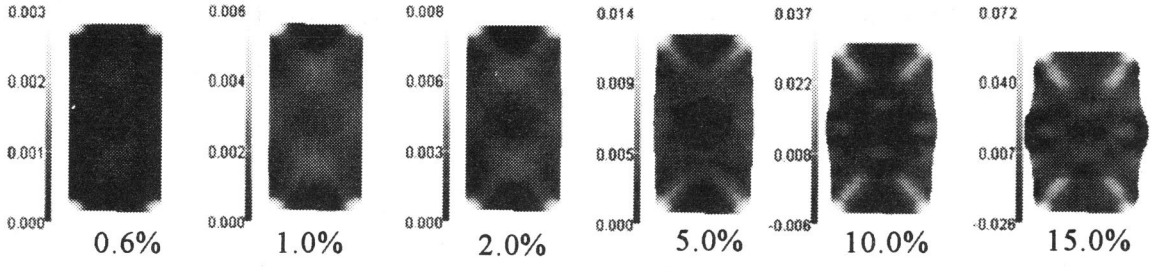

Figure 3.24: Distribution of viscoplastic volumetric strain for NC clay (β=5, Undrained)

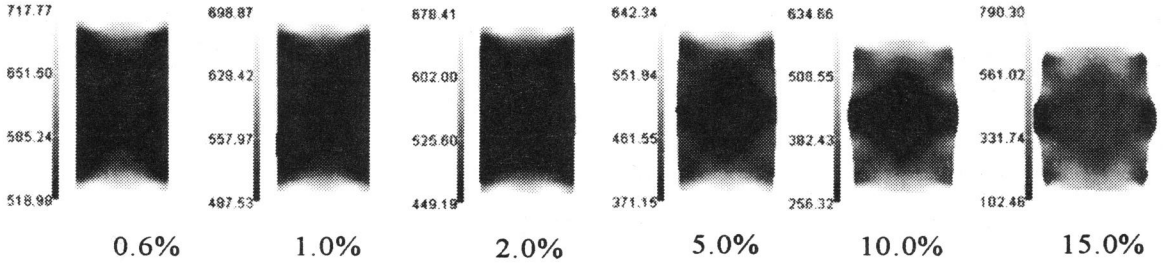

Figure 3.25: Distribution of mean effective stress (kPa) for NC clay (β=5, Undrained)

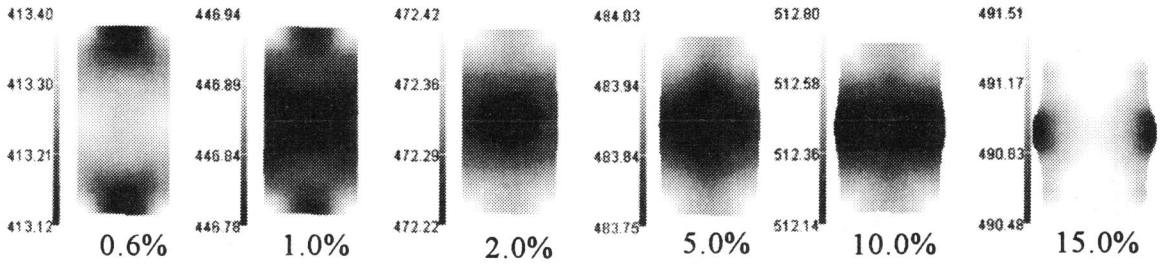

Figure 3.26: Distribution of pore water pressure (kPa) for NC clay (β=5, Undrained)

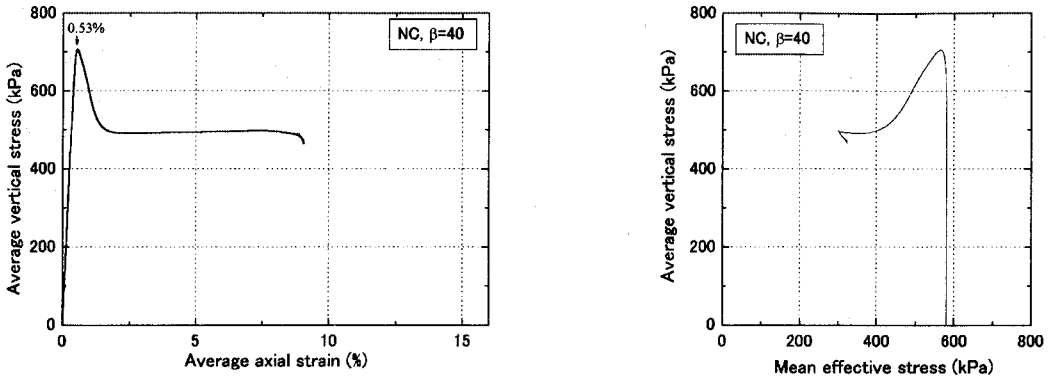

(a) Stress-strain relations (b) Stress paths

Figure 3.27: Undrained compression test for NC clay (β=40)

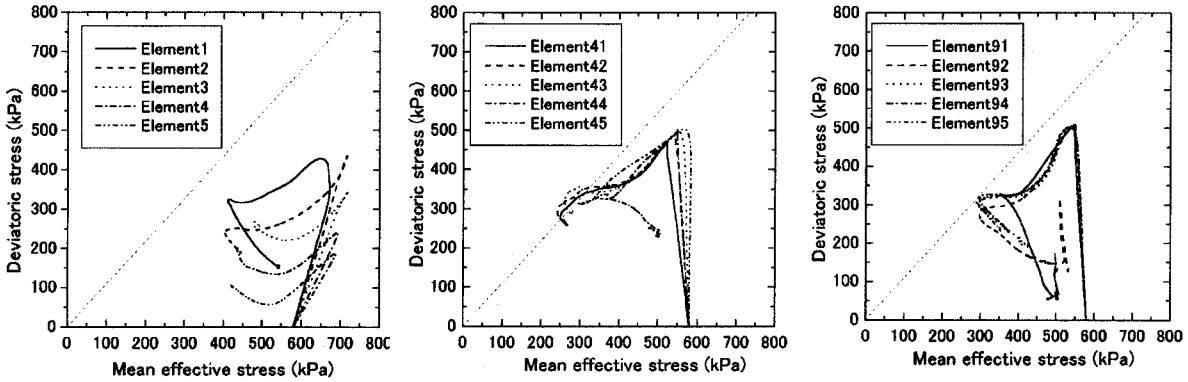

(a) Element 1-5 (b) Element 41-45 (c) Element 91-95

Figure 3.28: Stress paths of each element for NC clay (β=40, Undrained)

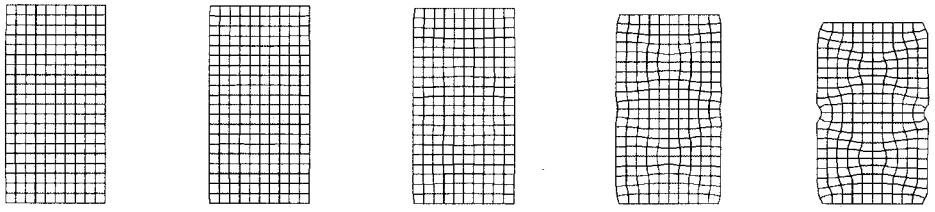

0.6 % 1.0 % 2.0 % 5.0 % 9.0 %

Figure 3.29: Deformed meshes for NC clay (β=40, Undrained))

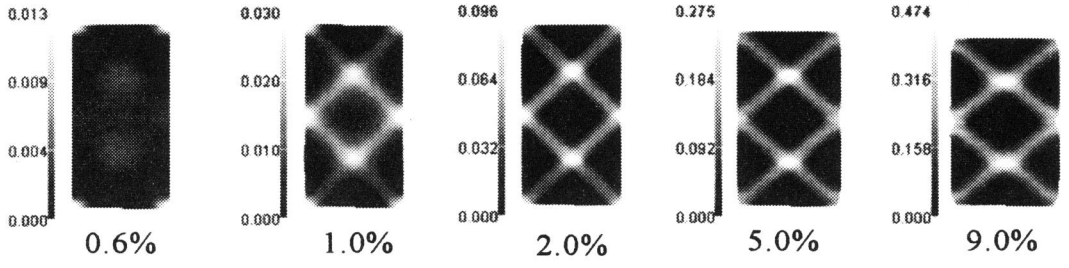

Figure 3.30: Distribution of viscoplastic deviatoric strain for NC clay (β=40, Undrained)

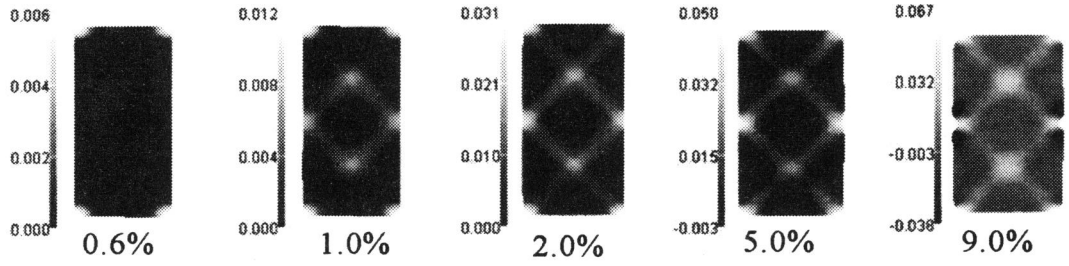

Figure 3.31: Distribution of viscoplastic volumetric strain for NC clay (β=40, Undrained)

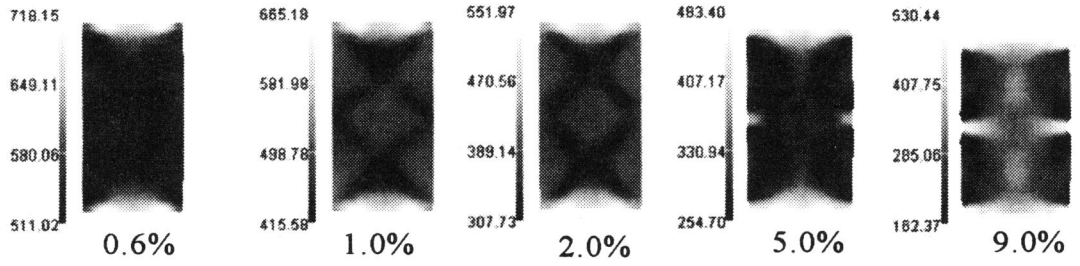

Figure 3.32: Distribution of mean effective stress (kPa) for NC clay (β=40, Undrained)

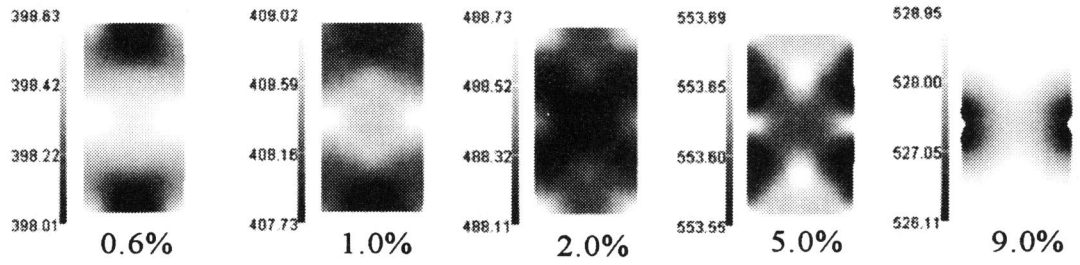

Figure 3.33: Distribution of pore water pressure (kPa) for NC clay (β=40, Undrained)

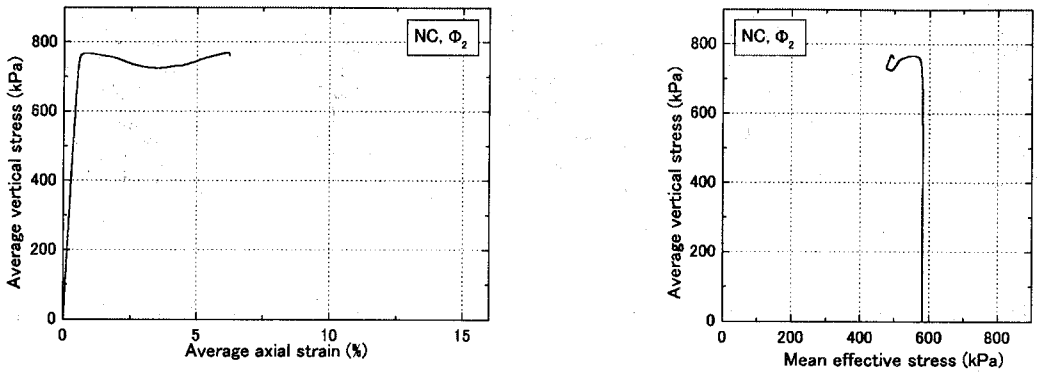

(a) Stress-strain relations (b) Stress paths

Figure 3.34: Undrained compression test for NC clay (with Φ_2)

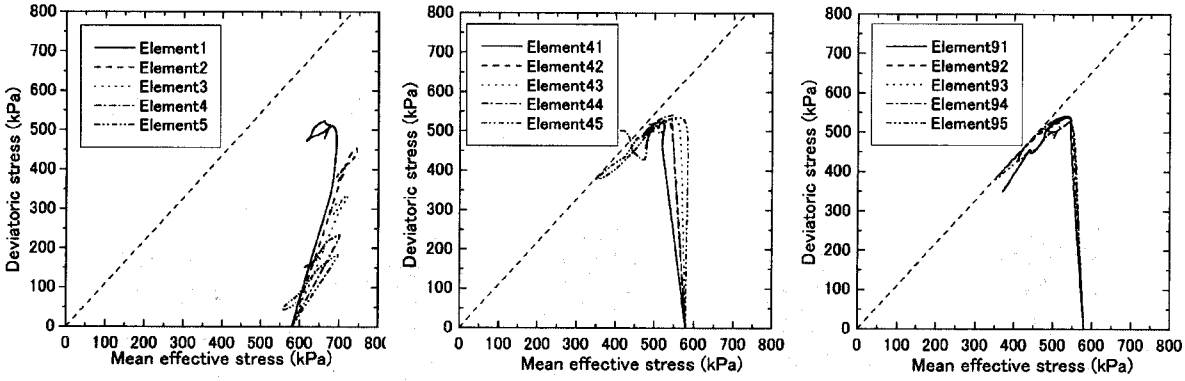

(a) Element 1-5 (b) Element 41-45 (c) Element 91-95

Figure 3.35: Stress paths of each element for NC clay (with Φ_2, Undrained)

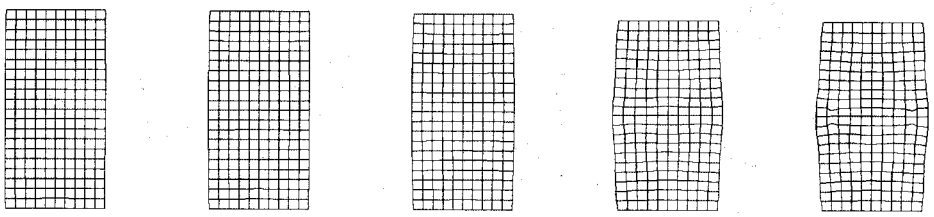

0.6 % 1.0 % 2.0 % 5.0 % 6.0 %

Figure 3.36: Deformed meshes for NC clay (with Φ_2, Undrained))

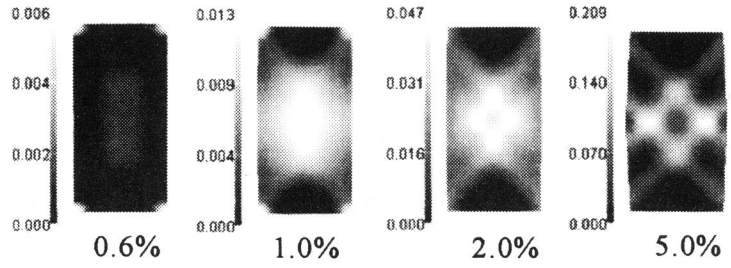

Figure 3.37: Distribution of viscoplastic deviatoric strain for NC clay (with Φ_2, Undrained)

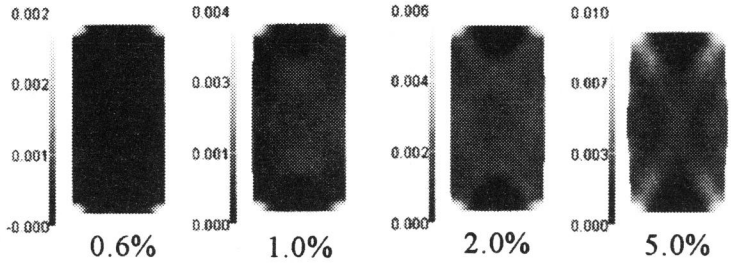

Figure 3.38: Distribution of viscoplastic volumetric strain for NC clay (with Φ_2, Undrained)

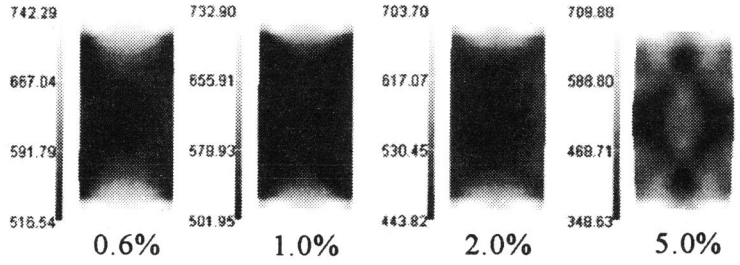

Figure 3.39: Distribution of mean effective stress (kPa) for NC clay (with Φ_2, Undrained)

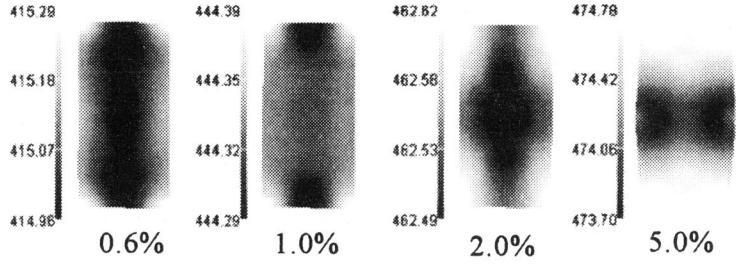

Figure 3.40: Distribution of pore water pressure (kPa) for NC clay (with Φ_2, Undrained)

3.3.2 Analysis of Overconsolidated Clay

Herein, we will discuss the calculated results for the overconsolidated clay of OCR=5.9, and then compare the results for $\beta = 0$ and β=40. Results are shown in Figs.3.41~3.48 for $\beta = 0$, Figs.3.49~3.56 for $\beta = 40$. Figs.3.41(a) and (b) show the average stress-strain relation and the average stress path for $\beta = 0$, while Fig.3.42 shows the stress paths for each element. Figs.3.49(a) and (b) show the average stress-strain relation and the average stress path for $\beta = 40$, while Fig.3.50 shows the stress paths for each element. Note that the calculation diverged at an axial strain of around 10% in some elements, that is, along the edge and the center of the specimen, specifically, elements 1 and 91~95 for $\beta = 0$, where the viscoplastic strain is concentrated, which is confirmed in the deviatoric stress-average strain relations for the elements in Fig.3.43. When $\beta = 40$, the calculation firstly diverged around the average axial strain of 4% at the center of the specimen, namely, at element 94 and 95 as confirmed in Fig.3.51(c).

Let us compare the average vertical stress-average axial strain relations in Fig.3.41(a) and Fig.3.49(a). In the case of $\beta = 40$, the degradation of the shear strength can be described, while the average vertical stress continues to increase when $\beta = 0$. The deformed meshes at axial strains of 0.6%, 1.0%, 2.0%, 5.0%, 10.0%, and 15.0% are shown in Figs.3.44 and 3.52 for β=0 and β= 40, respectively. The figures confirm that the model considering structural changes demonstrates a more apparent localization zone in a similar way to the NC clay. Figs.3.45 and 3.53 compare the distribution of the accumulated viscoplastic deviatoric strain γ^p of $\beta = 0$ and $\beta = 40$. The shear bands show different geometries. In the case of $\beta = 0$, shear bands developed from the four edges of the specimen, while in the case of $\beta = 40$, they developed similarly from the four edges, and appeared to double at an axial strain of 5%.

Figs.3.46 and 3.54 compare the distribution of accumulated viscoplastic volumetric strain for $\beta = 0$ and $\beta = 40$. Note that viscoplastic volumetric expansion occurs in the shear zone, while viscoplastic volumetric compression occurs in the shear bands in the NC region as shown before. The localization is more apparent when β=40.

Figs.3.47 and 3.55 provide the distribution of mean effective stress for β =0 and β =40. Figs.3.48 and 3.56 show the distribution of excess pore water pressure for β =0 and β =40. These figures show localization associated with the distribution of viscoplastic strain.

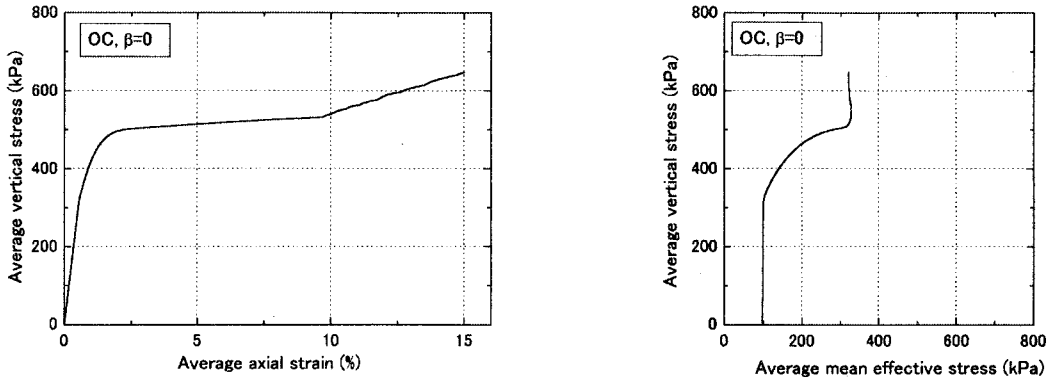

(a) Stress-strain relations (b) Stress paths

Figure 3.41: Undrained compression test for OC clay (β=0)

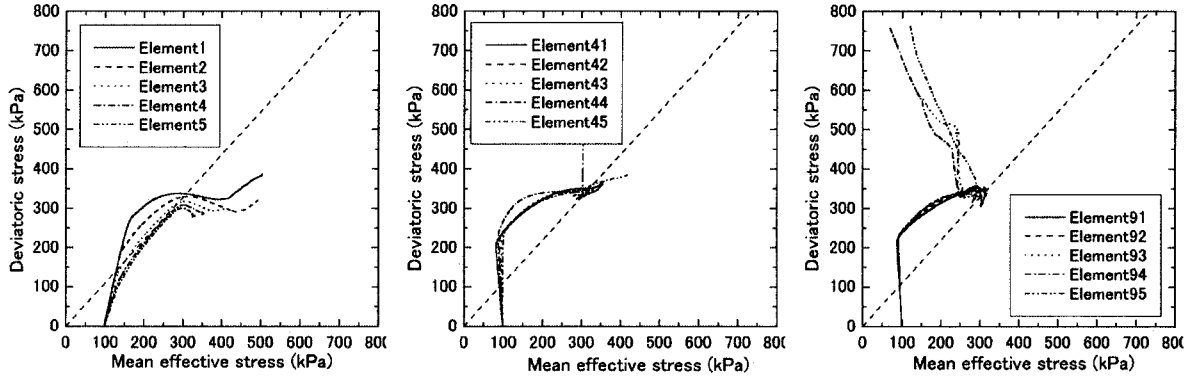

(a) Element 1-5 (b) Element 41-45 (c) Element 91-95

Figure 3.42: Stress paths of each element for OC clay (β=0, Undrained)

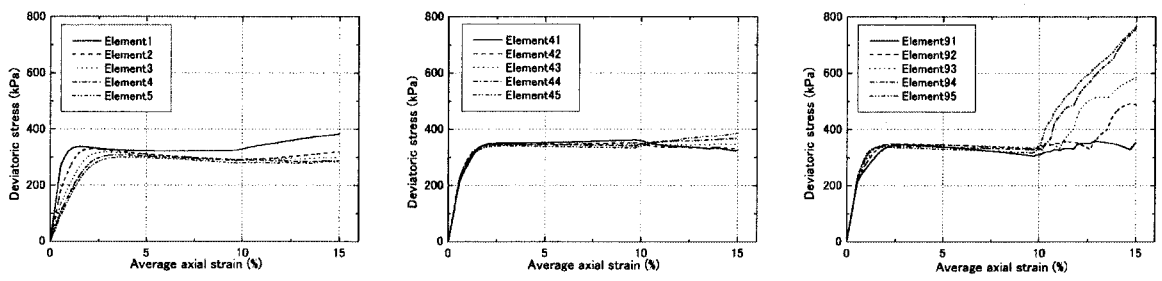

(a) Element 1-5 (b) Element 41-45 (c) Element 91-95

Figure 3.43: Deviatoric stress-average strain relations of each element for OC clay (β=0, Undrained)

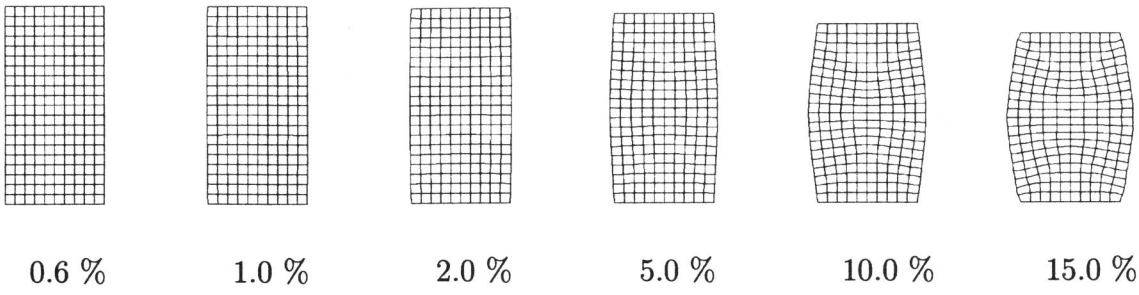

Figure 3.44: Deformed meshes for OC clay (β=0, Undrained))

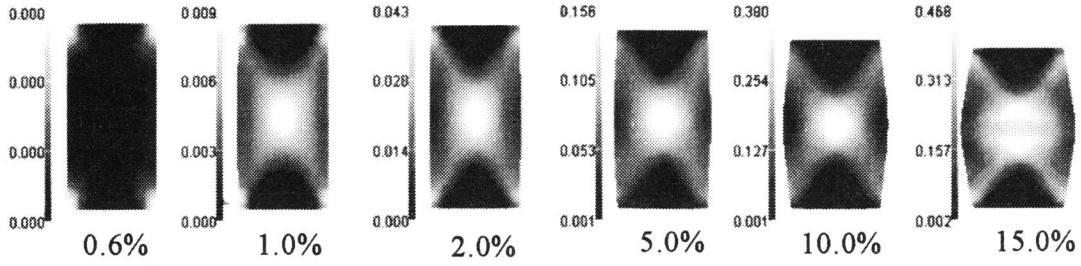

Figure 3.45: Distribution of viscoplastic deviatoric strain for OC clay (β=0, Undrained)

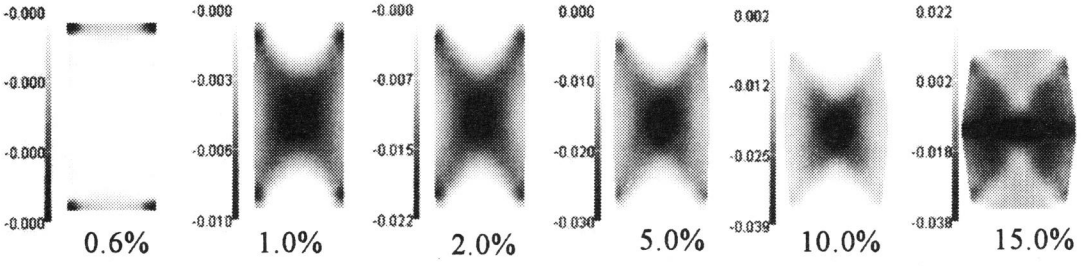

Figure 3.46: Distribution of viscoplastic volumetric strain for OC clay (β=0, Undrained)

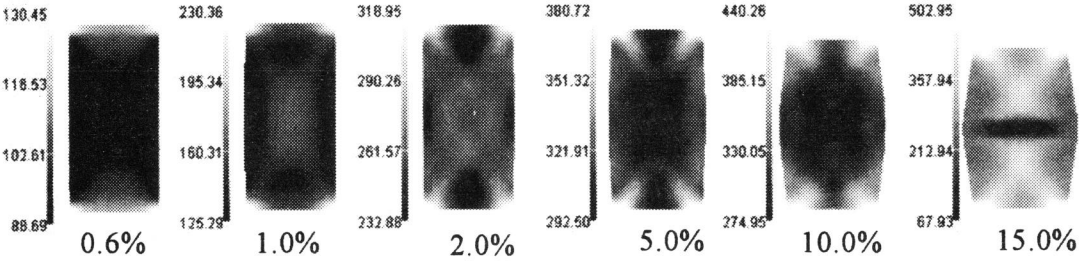

Figure 3.47: Distribution of mean effective stress (kPa) for OC clay (β=0, Undrained)

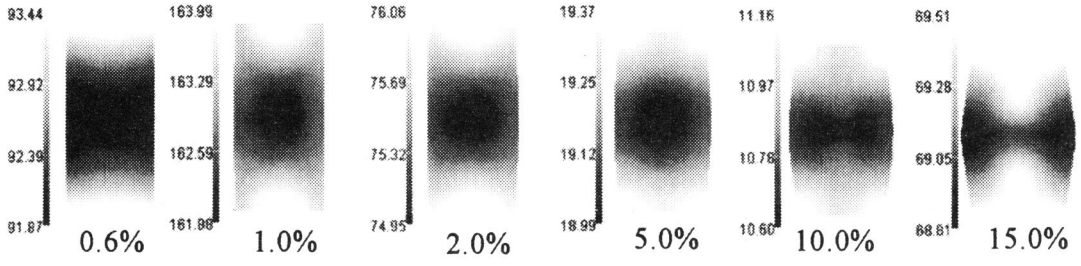

Figure 3.48: Distribution of pore water pressure (kPa) for OC clay (β=0, Undrained)

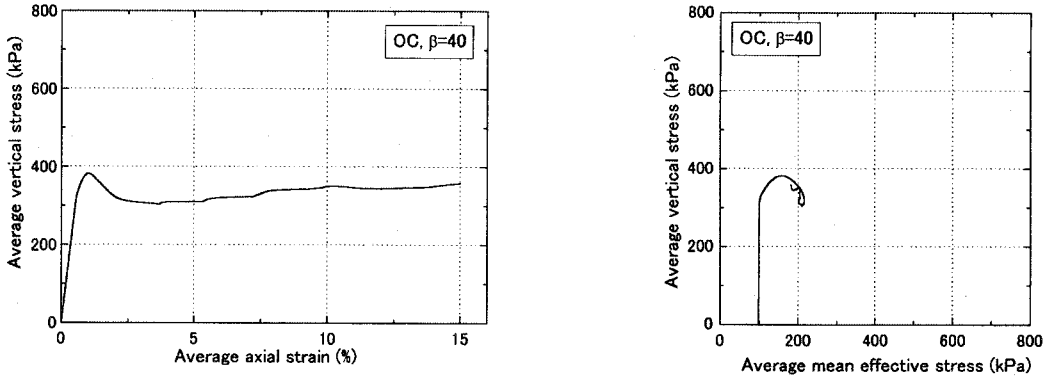

(a) Stress-strain relations (b) Stress paths

Figure 3.49: Undrained compression test for OC clay (β=40)

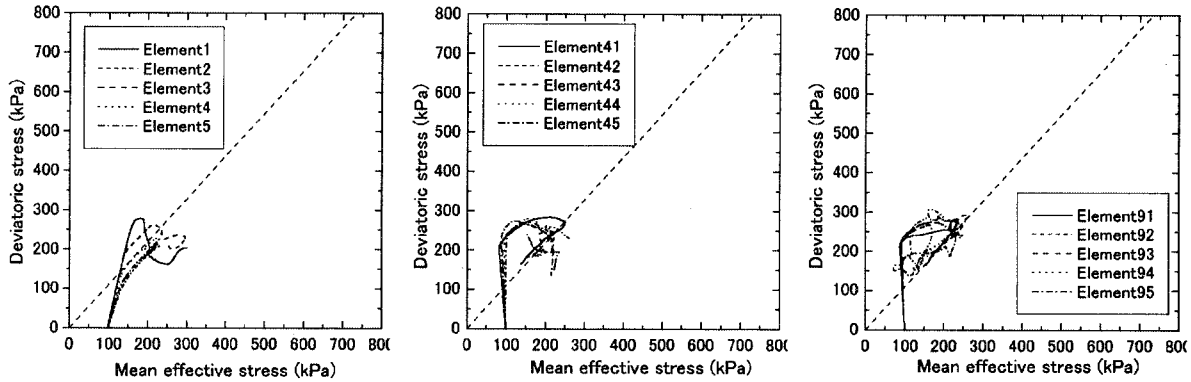

(a) Element 1-5 (b) Element 41-45 (c) Element 91-95

Figure 3.50: Stress paths of each element for OC clay (β=40, Undrained)

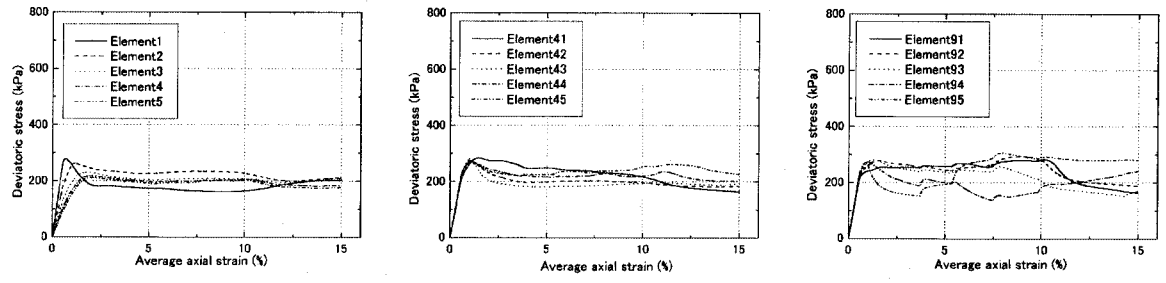

(a) Element 1-5 (b) Element 41-45 (c) Element 91-95

Figure 3.51: Deviatoric stress-average strain relations of each element for OC clay (β=40, Undrained)

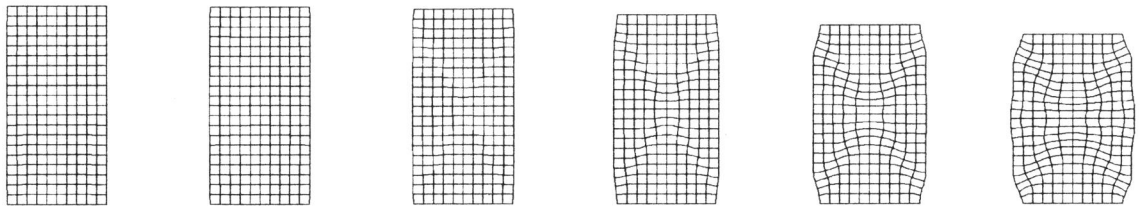

0.6 % 1.0 % 2.0 % 5.0 % 10.0 % 15.0 %

Figure 3.52: Deformed meshes for OC clay (β=40, Undrained))

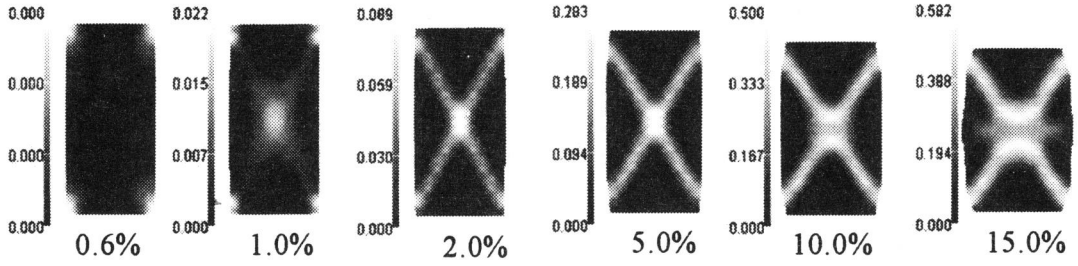

Figure 3.53: Distribution of viscoplastic deviatoric strain for OC clay (β=40, Undrained)

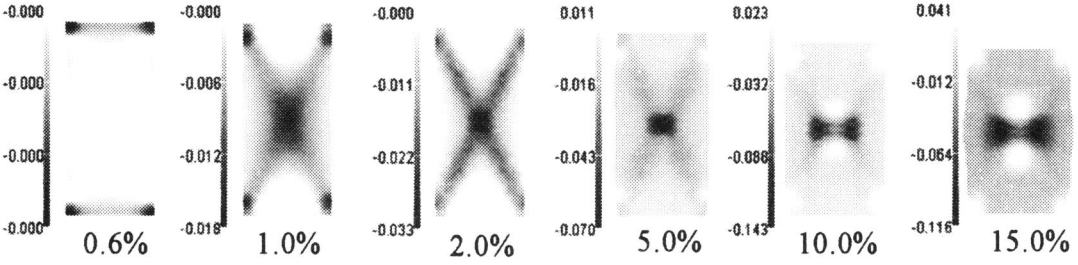

Figure 3.54: Distribution of viscoplastic volumetric strain for OC clay (β=40, Undrained)

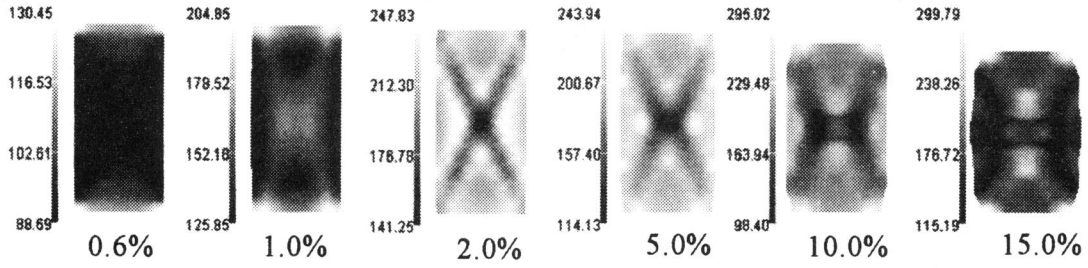

Figure 3.55: Distribution of mean effective stress (kPa) for OC clay (β=40, Undrained)

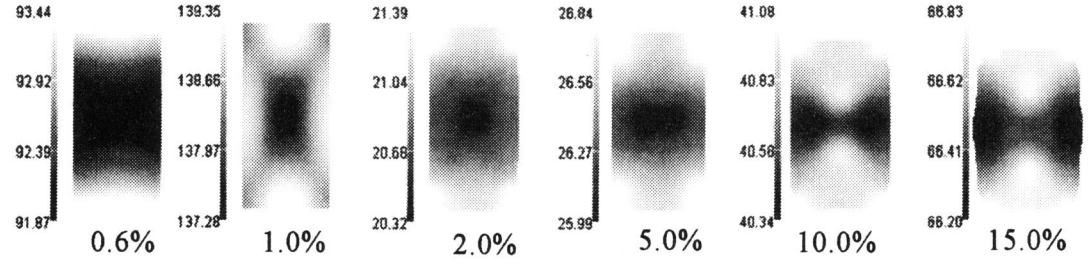

Figure 3.56: Distribution of pore water pressure (kPa) for OC clay (β=40, Undrained)

3.4 Numerical Simulation of Partially Drained Compression Tests

In this section, we show the simulation of partially drained compression tests. The finite element mesh is the same as that used in the previoius section, as shown in Fig.3.2. The boundary surface is also the same except that the top surface of the specimen is set to be permeable in order to permit pore water to go out of the specimen. A constant axial strain rate of 0.0015%/min is given, the time increment for each step is 10 s, and the increment of the average strain is determined as $\Delta\varepsilon_{11} = 0.00025\%$. Note that a small value of excess pore water pressure, at the most 15 kPa, is generated in all the simulations. This implies that the specimen is compressed in partially drained conditions.

The initial conditions and the material parameters for NC and OC clays are the same as those used in the previous section listed in Tables 3.2 and 3.3. Numerical analyses are conducted with and without structural changes as shown in Table 3.4.

Table 3.4: Material Parameters β (Partially drained conditions)

	NC	OC
Without structural changes	β=0	β=0
With structural changes	β=20	β=40

3.4.1 Analysis of Normally Consolidated Clay

Let us see the calculations for NC clay. Simulation results are shown in Figs.3.57~3.63 for β =0, namely, the original model and Figs.3.64~3.70 for β =20, namely, the model considering structural changes. Fig.3.57 shows the average vertical stress-average axial strain and average stress path for β =0, and Fig.3.58 shows the stress paths of the top, the center, and the bottom elements of the specimen for β =0. Similarly, Figs.3.64 and 3.65 show the results for β =20. Average vertical stress increases continuously in the case of β =0, while it temporarily decreases and begins to increase again in the case of β =20.

Figs.3.59 and 3.66 compare the deformed meshes for β =0 and β =20. Figs.3.60 and 3.67 compare the distribution of accumulated viscoplastic deviatoric strain γ^p. In the case of β =0, the distributions almost show symmetry for upper and lower parts at every

stage. In the case of β =20, viscoplastic strain develops in the upper part, and shear bands are more apparent in the upper part, namely, near the permeable boundary, than in the lower part, in particular, at axial strains of 2.0%, 5.0%, and 10.0%. A similar tendency is observed for the distribution of viscoplastic volumetric strain, as shown in Figs.3.61 and 3.68. Hence, the concentration of viscoplastic strain at the permeable surface is more apparent in the model considering structural changes. The angles of the shear bands are evaluated later.

Figs.3.62 and 3.69 show the distribution of mean effective stress for β=0 and β=20; they confirm that the localized zone is more apparent in the case of β =20. Figs.3.63 and 3.70 show the distribution of pore water pressure for β=0 and β=20. We confirm that the difference of pore water pressure between the top and the bottom of the specimen is larger for β=40.

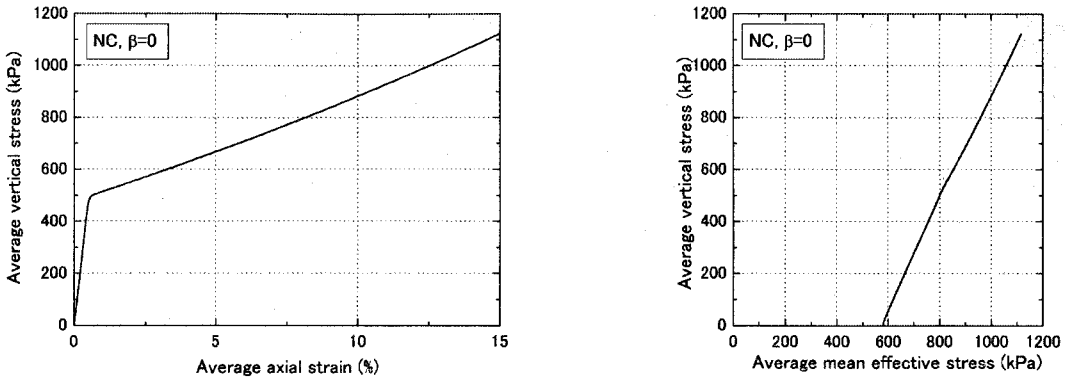

(a) Stress-strain relations (b) Stress paths

Figure 3.57: Partially drained compression test for NC clay (β=0)

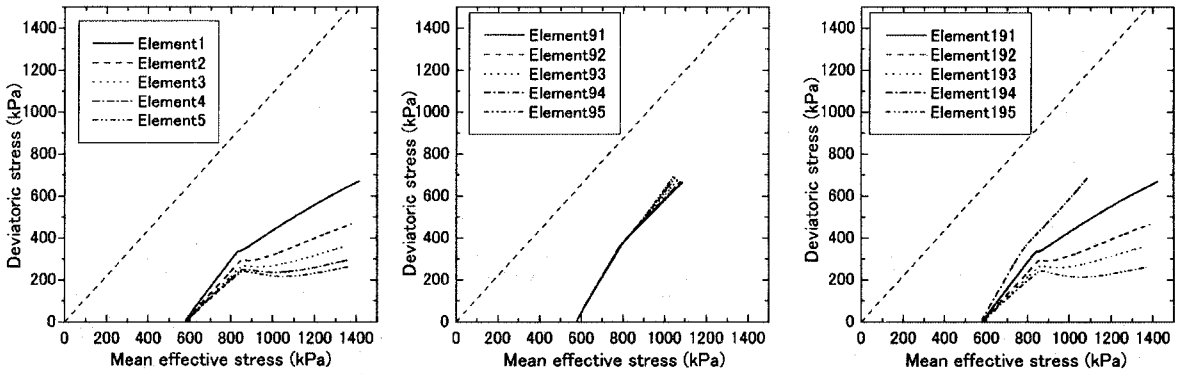

(a) Element 1-5 (b) Element 91-95 (c) Element 191-195

Figure 3.58: Stress paths of each element for NC clay (β=0, Drained)

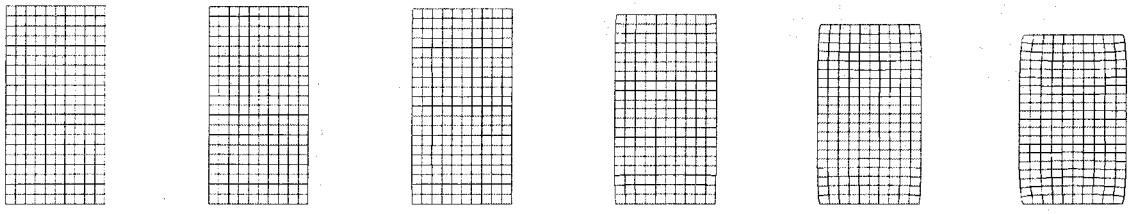

0.6 % 1.0 % 2.0 % 5.0 % 10.0 % 15.0 %

Figure 3.59: Deformed meshes for NC clay (β=0, Drained))

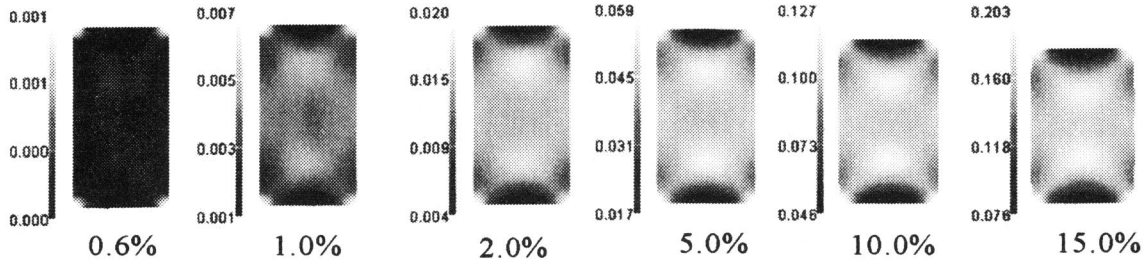

Figure 3.60: Distribution of viscoplastic deviatoric strain for NC clay (β=0, Drained)

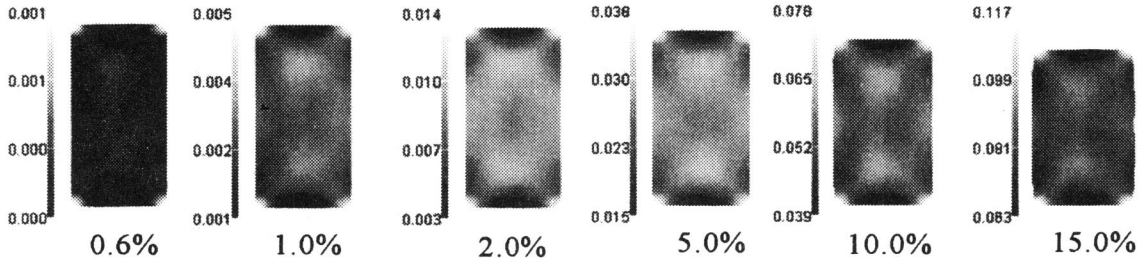

Figure 3.61: Distribution of viscoplastic volumetric strain for NC clay (β=0, Drained)

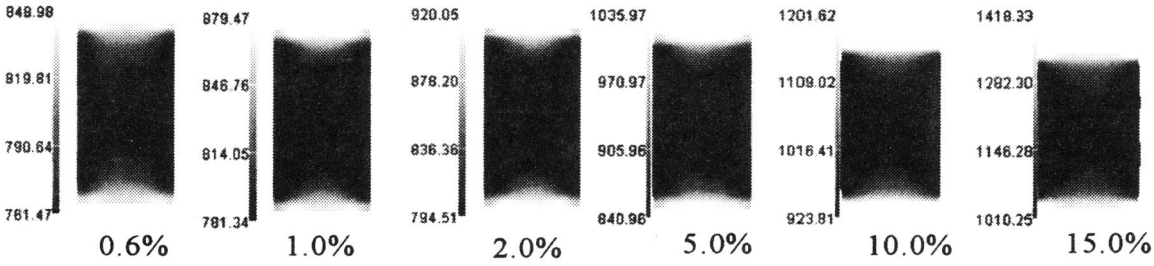

Figure 3.62: Distribution of mean effective stress (kPa) for NC clay (β=0, Drained)

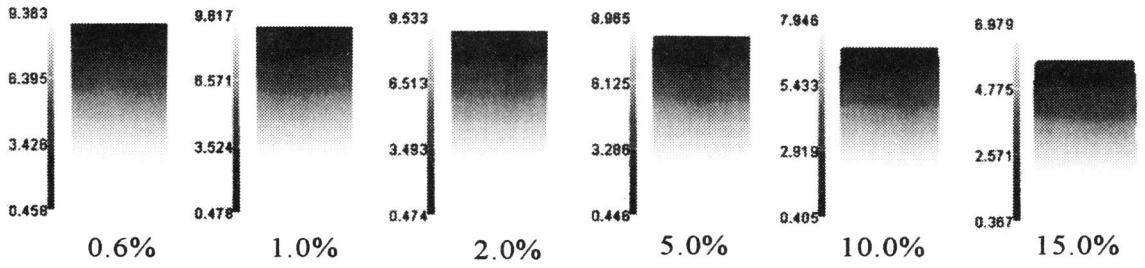

Figure 3.63: Distribution of pore water pressure (kPa) for NC clay (β=0, Drained)

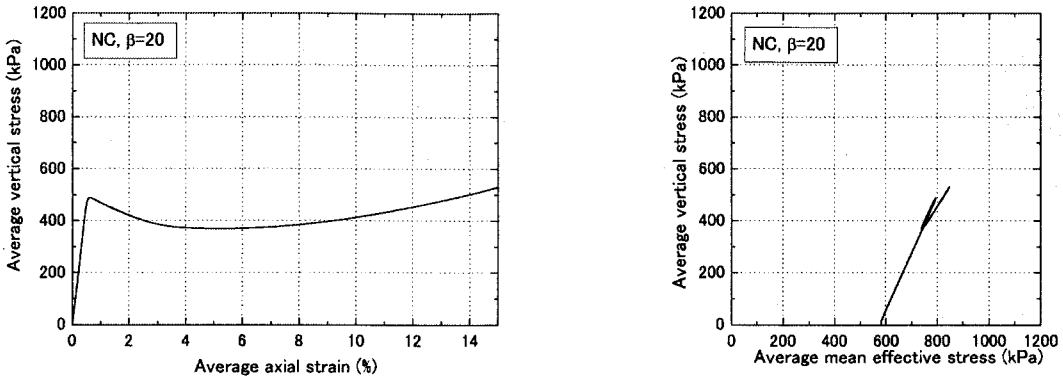

(a) Stress-strain relations (b) Stress paths

Figure 3.64: Partially drained compression test for NC clay (β=20)

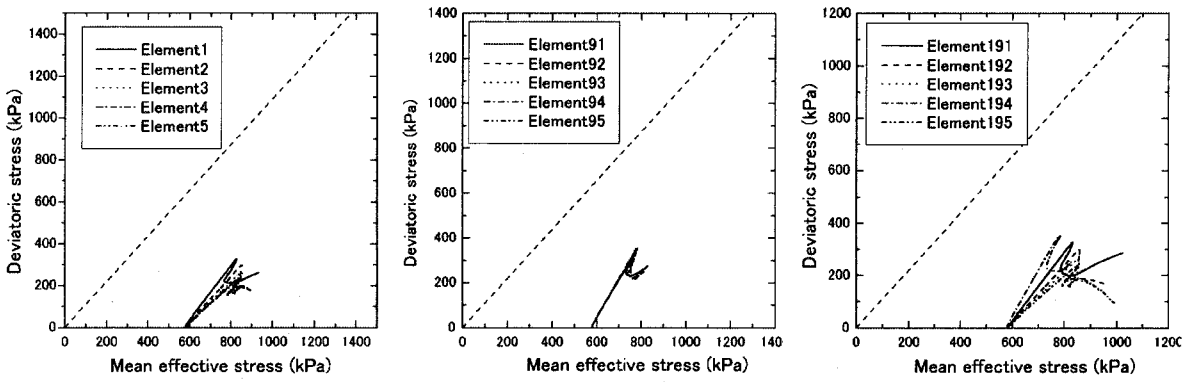

(a) Element 1-5 (b) Element 91-95 (c) Element 191-195

Figure 3.65: Stress paths of each element for NC clay (β=20, Drained)

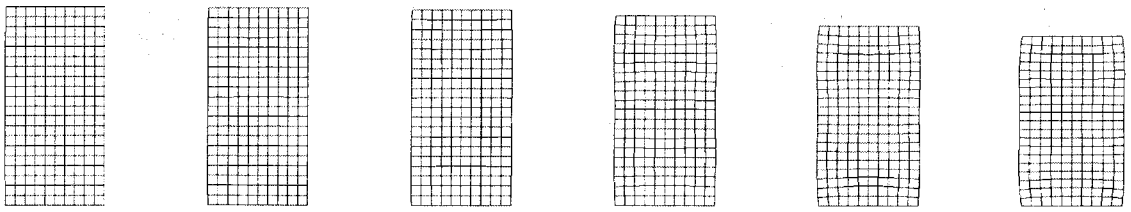

0.6 % 1.0 % 2.0 % 5.0 % 10.0 % 15.0 %

Figure 3.66: Deformed meshes for NC clay (β=20, Drained))

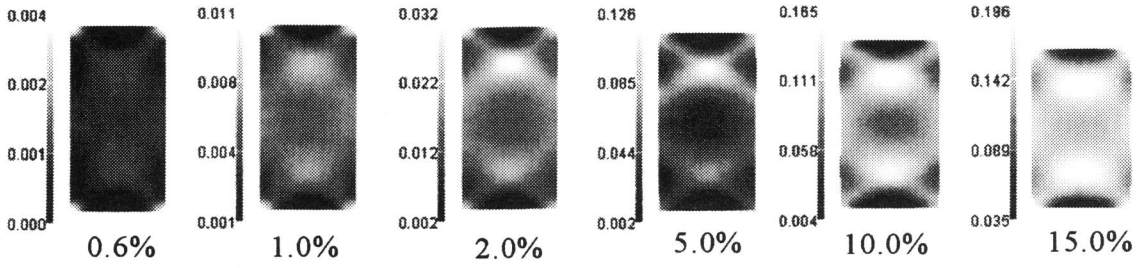

Figure 3.67: Distribution of viscoplastic deviatoric strain for NC clay (β=20, Drained)

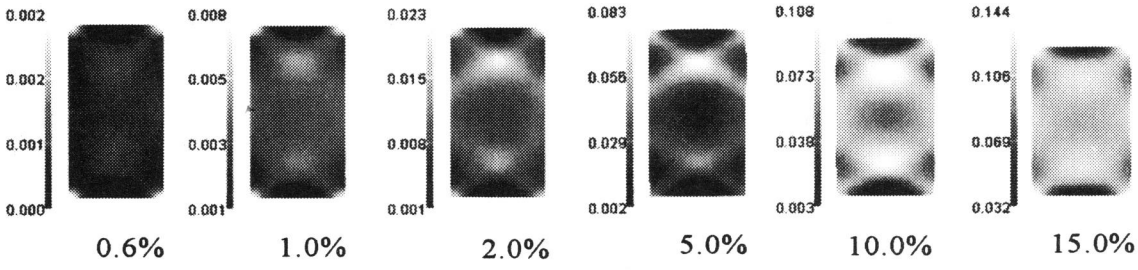

Figure 3.68: Distribution of viscoplastic volumetric strain for NC clay (β=20, Drained)

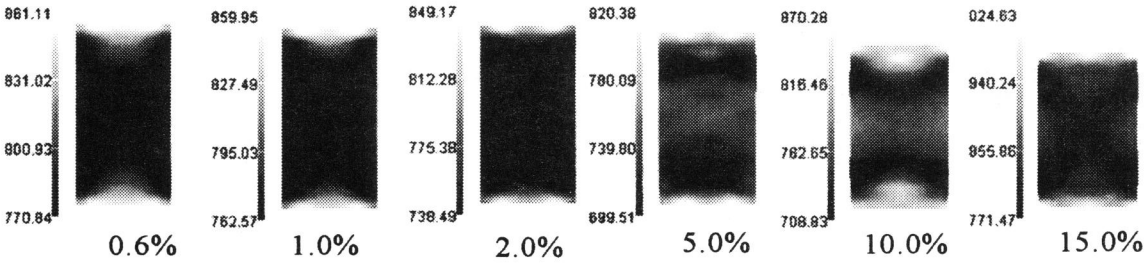

Figure 3.69: Distribution of mean effective stress (kPa) for NC clay (β=20, Drained)

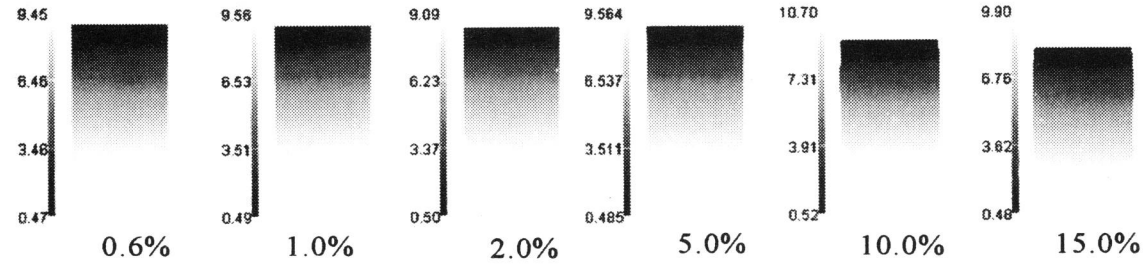

Figure 3.70: Distribution of pore water pressure (kPa) for NC clay (β=20, Drained)

3.4.2 Analysis of Overconsolidated Clay

Let us look at the calculations for the OC clay. Figs.3.71~3.77 provide the results for β=0 and Figs.3.78~3.84 for β=40. The average stress-strain relation, the average stress path, and stress paths of the elements for β=0 are shown in Figs.3.71(a), (b), and 3.72. Figs.3.78(a), (b), and 3.79 show the results of β=40 in the same way. The model which considers structural changes describes the degradation of shear strength.

The deformed meshes are shown in Figs.3.73 and 3.80 for β=0 and β=40, respectively. It appears that the specimen exhibits asymmetric deformation at the upper and the lower parts in the case of β=40. For the lower parts, the horizontal (x-direction) displacement on the side of the lateral specimen is larger than the upper parts at axial strains of 5.0%, 10.0% and 15.0% shown in Fig.3.80.

Distribution of accumulated viscoplastic shear strain for β =0 andβ=40 is shown in Figs.3.74, and 3.81. It should be noticed that viscoplastic shear strain is larger, and shear localization is more apparent in lower parts than upper parts of the specimen especially after axial strain of 5.0% in the case of β =40 as shown in Fig.3.81, while, in the case of β =0, the distribution appears to be almost symmetric for the upper and lower part of the specimen. It seems that the expansion due to positive dilatancy can be diminished by compression due to drainage near the permeable surface. As a result, the deformation is concentrated in the lower part of the specimen.

Figs.3.75 and 3.82 show the distribution of viscoplastic volumetric strain for β =0 and β=40, respectively. Viscoplastic compression occurs in the shear zone for both cases. Figs.3.76 and 3.83 compare the distribution of the mean effective stress for β =0 and β=40. Figs.3.77 and 3.84 show the distribution of pore water pressure for β =0 and β=40. For both, localization is apparent in the case of β =40.

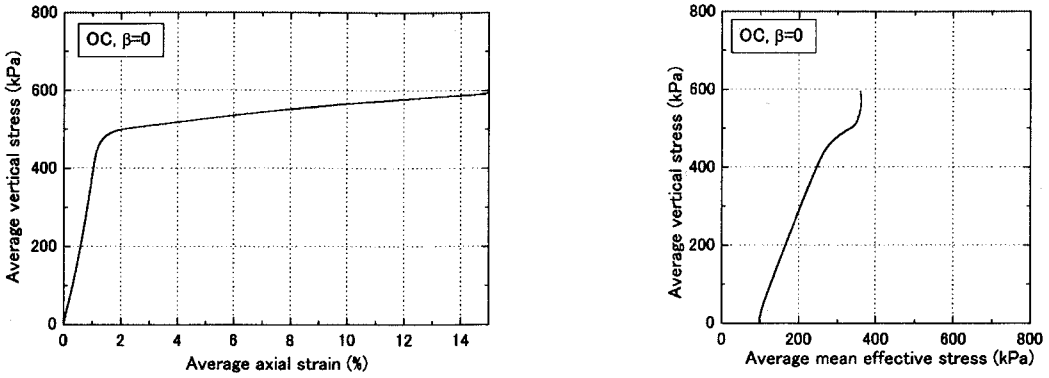

(a) Stress-strain relations (b) Stress paths

Figure 3.71: Partially drained compression test for OC clay (β=0)

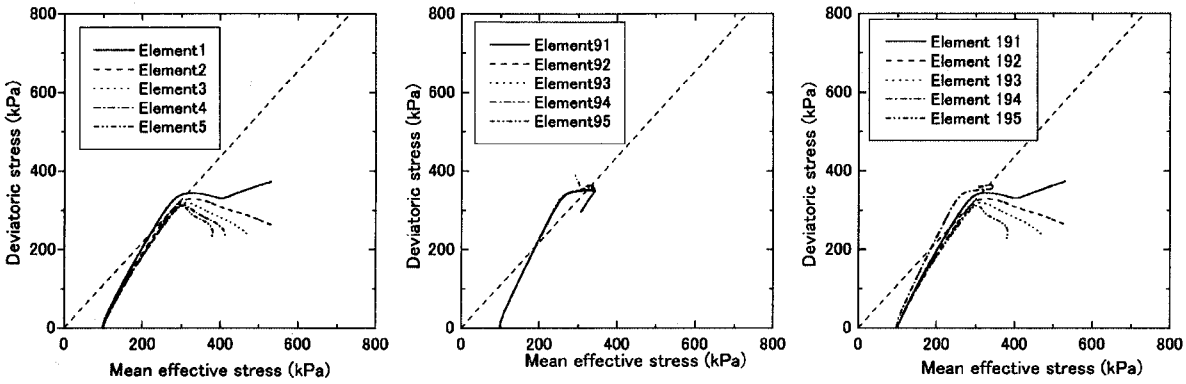

(a) Element 1-5 (b) Element 91-95 (c) Element 191-195

Figure 3.72: Stress paths of each element for OC clay (β=0, Drained)

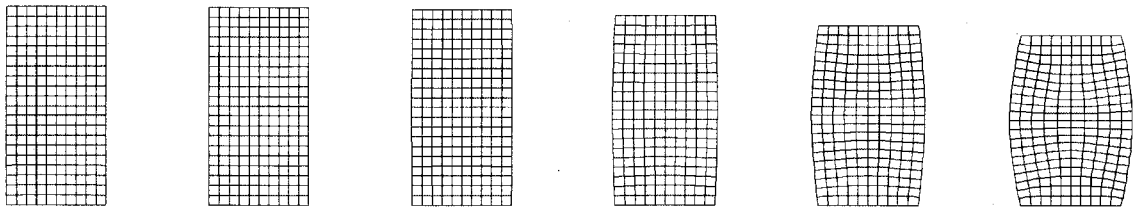

0.6 % 1.0 % 2.0 % 5.0 % 10.0 % 15.0 %

Figure 3.73: Deformed meshes for OC clay (β=0, Drained))

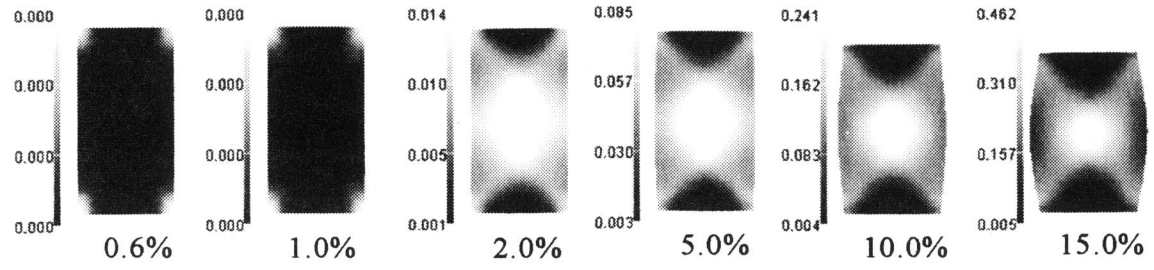

Figure 3.74: Distribution of viscoplastic deviatoric strain for OC clay (β=0, Drained)

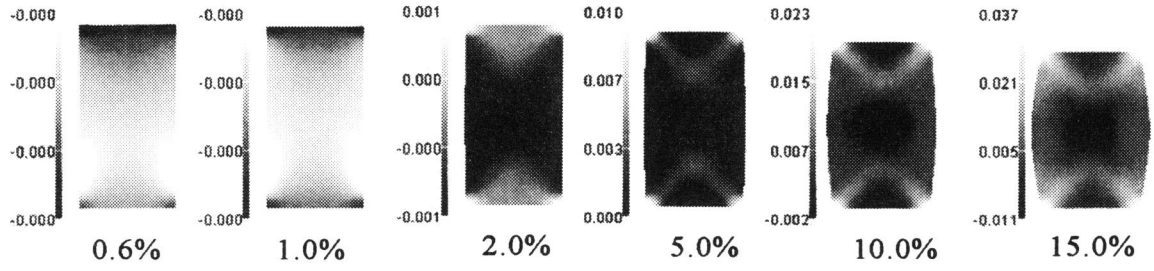

Figure 3.75: Distribution of viscoplastic volumetric strain for OC clay (β=0, Drained)

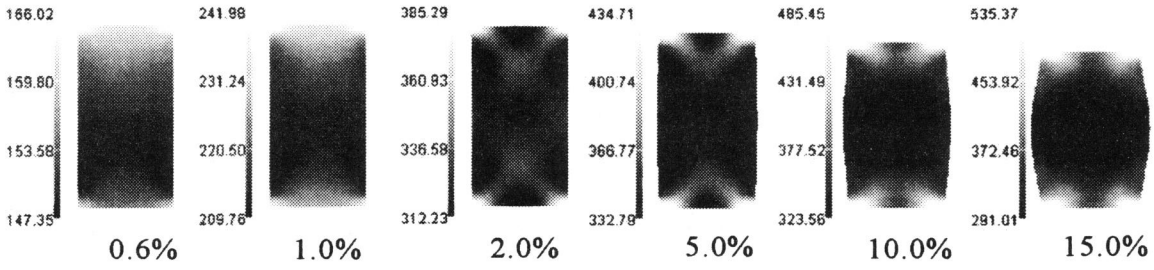

Figure 3.76: Distribution of mean effective stress (kPa) for OC clay (β=0, Drained)

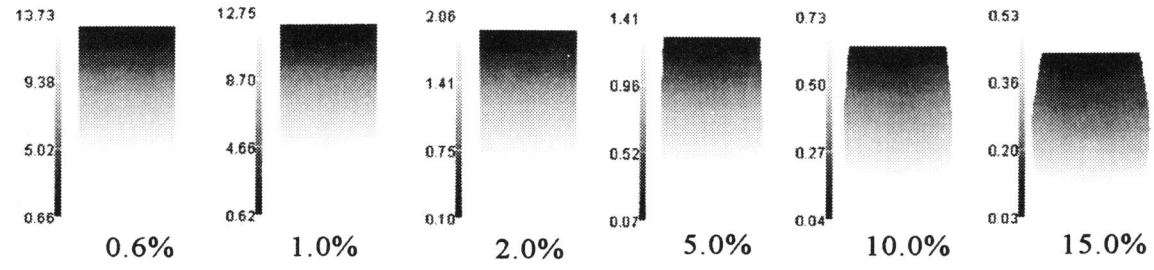

Figure 3.77: Distribution of pore water pressure (kPa) for OC clay (β=0, Drained)

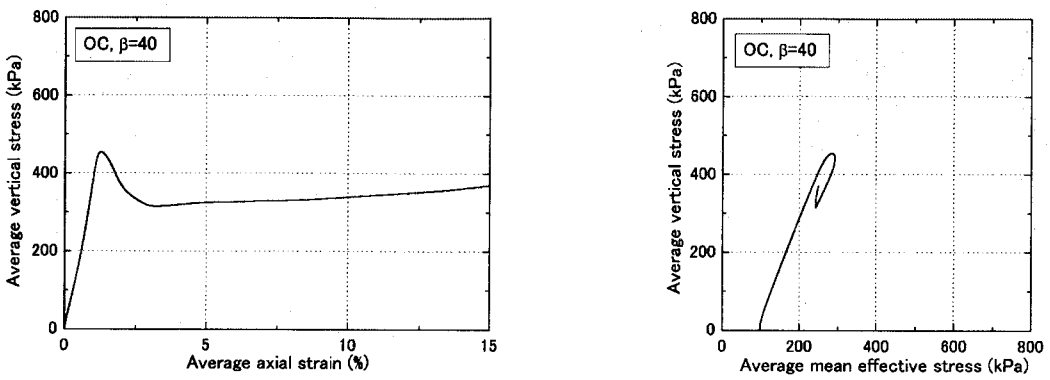

(a) Stress-strain relations (b) Stress paths

Figure 3.78: Partially drained compression test for OC clay (β=40)

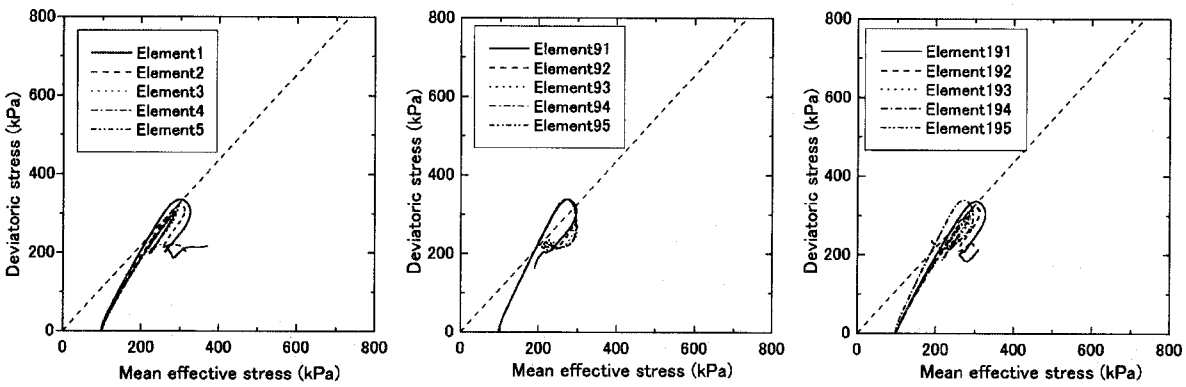

(a) Element 1-5 (b) Element 91-95 (c) Element 191-195

Figure 3.79: Stress paths of each element for OC clay (β=40, Drained)

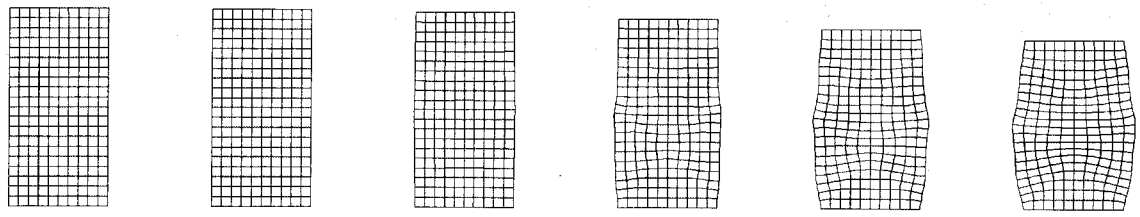

0.6 % 1.0 % 2.0 % 5.0 % 10.0 % 15.0 %

Figure 3.80: Deformed meshes for OC clay (β=40, Drained))

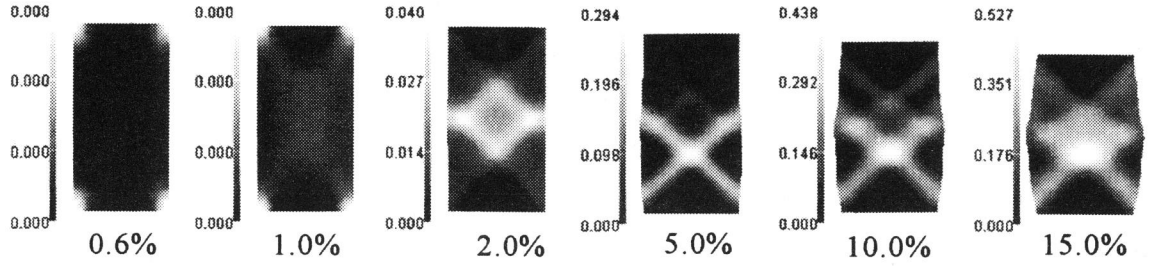

Figure 3.81: Distribution of viscoplastic deviatoric strain for OC clay (β=40, Drained)

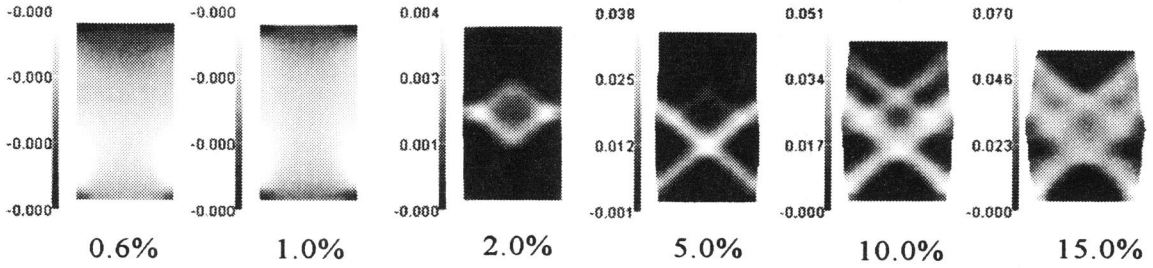

Figure 3.82: Distribution of viscoplastic volumetric strain for OC clay (β=40, Drained)

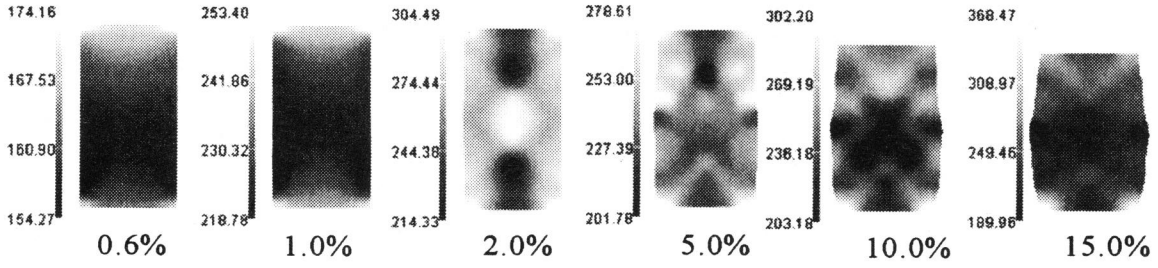

Figure 3.83: Distribution of mean effective stress (kPa) for OC clay (β=40, Drained)

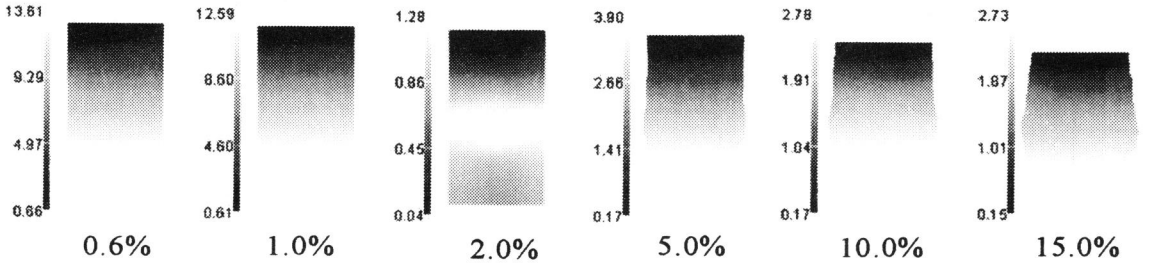

Figure 3.84: Distribution of pore water pressure (kPa) for OC clay (β=40, Drained)

3.4.3 Angles of Shear Bands

Fig.3.85 compares the directions of the shear bands for the NC clay during undrained compression. The angles are obtained from the distribution of viscoplastic deviatoric strain γ^p at an axial strain of 5%. The angles are estimated as 44.1° for β=0 , 44.4° for β=5, 42.3° for β=20, 41.7° for β=40, and 44.7° for the model with Φ_2. It appears that a larger value for β gives a smaller value for the angle of the shear band. The angles are smaller for the proposed model than for that obtained from the model with material function Φ_2 by 3∼4 degrees.

Fig.3.86 demonstrates the angles of shear bands for the OC clay during undrained compression. The angles are calculated from the distribution of γ^p in the same way. The angles are estimated at 52.7° for β=0 and at 55.4° for β=40. The values of angles for OC clays are larger than those for the NC clay. A larger value for β results in a larger value for the angle. This is the opposite tendency to that of the NC clay.

Figs.3.87 and 3.88 show the estimated angles of the shear bands for NC and OC clays in drained compression, namely, 42° for β=0 and 40° for β=0 for the NC clay (see Fig.3.87), and 44° for β=0 and 42° for β=42 for the OC clay (see Fig.3.88). In the case of β=20 for the NC clay, and β=40 for OC clay, the most pronounced shear bands are considered. The angles are relatively small compared to those obtained during undrained compression for both NC and OC clays. Angles for the OC clays are larger than those for the NC clay in the same way as that under undrained conditions. A larger value for β leads to a smaller value for the angle for both NC and OC clays. It seems that localization of viscoplastic compressive strain results in small angle of shear bands.

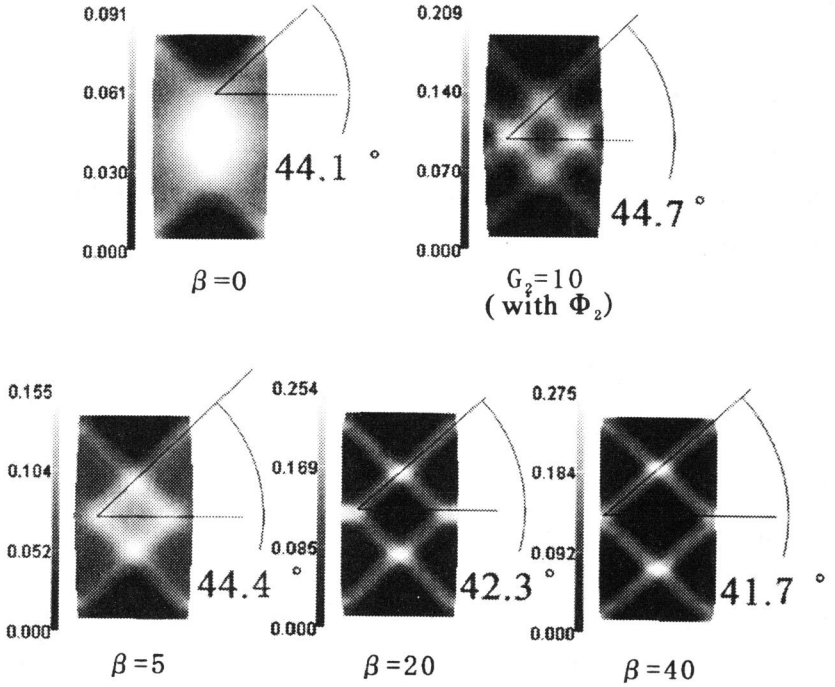

Figure 3.85: Angles of shear bands for NC clay (Undrained)

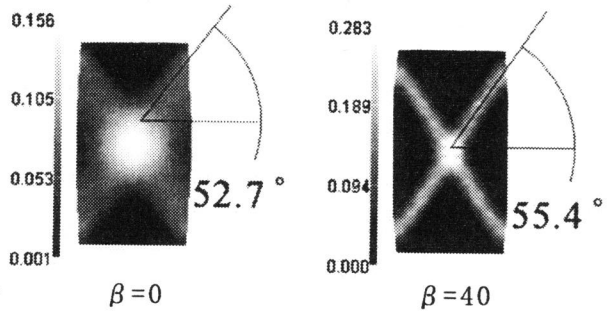

Figure 3.86: Angles of shear bands for OC clay (Undrained)

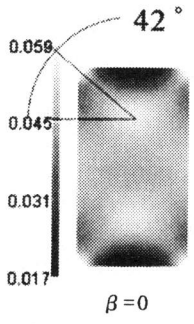

Figure 3.87: Angles of shear bands for NC clay (Drained)

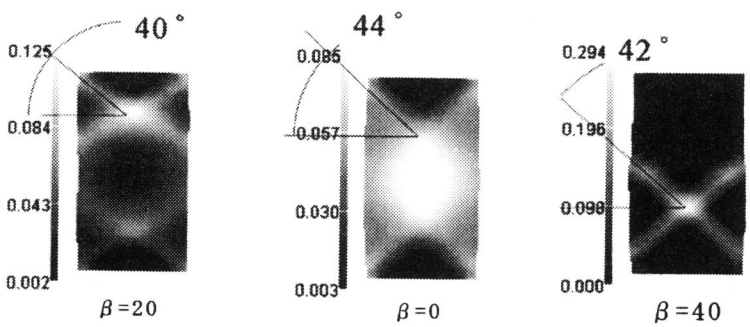

Figure 3.88: Angles of shear bands for OC clay (Drained)

3.5 Summary

The effect of structural changes on strain localization was studied in this chapter. Numerical simulations of behavior under undrained and drained compression conditions were conducted under plane strain conditions with displacement control. The obtained conclusions are summarized as follows:

1. In every case of the analysis, specifically for NC and OC clays in both undrained and partially drained conditions, the numerical results using the constitutive model which considers structural changes provide more apparent strain localization than those obtained from the original model.

2. During undrained compression for the NC clay, the angles of the shear bands depend on the value of structural parameter β; a larger β value provides a smaller value for the angle of the shear band.

3. During undrained compression for the OC clay, viscoplastic expansion occurs in the shear bands, while viscoplastic compression occurs in the NC clay. The angles of the shear bands are larger than those of the NC clay.

4. During drained compression, the deformation is concentrated on the upper parts of the specimen for the NC clay and on the lower parts for the OC clay apparently when structural changes are considered. This is one phenomenon of the localization of compressive strain.

5. During drained compression, the angles of the shear bands are smaller, namely, the shear bands are inclined, than those of the undrained compression. We believe that the shear bands decline as the compressive strain proceeds.

Chapter 4

EFFECT OF STRUCTURAL CHANGES ON CONSOLIDATION ANALYSIS

4.1 Introduction

Many researchers have reported that the behavior which appears to be associated with the collapse of the soil structure can be recognized during the consolidation process. Bishop and Lovenbury (1969) conducted constant stress creep tests under drained conditions on undisturbed clay, and observed a sudden increase in the strain rate (see Fig.4.1). They concluded that the phenomenon was a form of instability which appears to be associated with a modification of the soil structure. Leroueil, Kabbaj, Tavenas, and Bouchard (1985) and Kabbaj et al. (1985) carried out oedometer creep tests on Champlain sea clays, and reported similar behavior, that is, a temporary increase in the settlement rate under a constant load (see Fig.4.2). Concerning field cases, anomalous pore pressure behavior during the consolidation of soft clay has been reported by many researchers. Mitchell (1986) related that pore pressure stagnation or a continuous increase after all fill placement occurred because of a structural breakdown during compression. Furthermore, Leroueil (1988) and Kabbaj, Tavenas, and Leroueil (1988) observed pore water increases after the completion of the construction of test embankments, reflecting the fact that the effective stress temporarily diminished in the stress-strain curve (see Fig.4.3).

The prediction of these phenomena by numerical methods has been studied since the 1980s. Kabbaj, Oka, Leroueil, and Tavenas (1985) analyzed one-dimensional creep tests

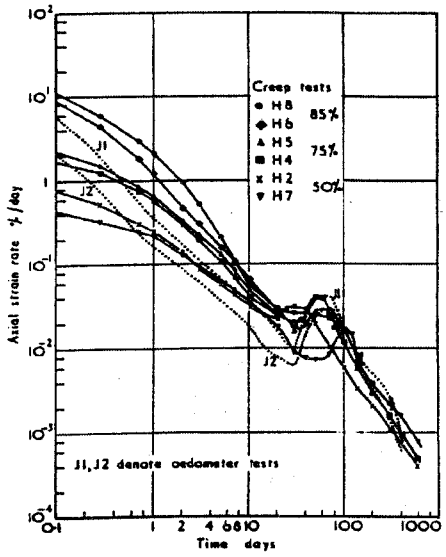

Figure 4.1:

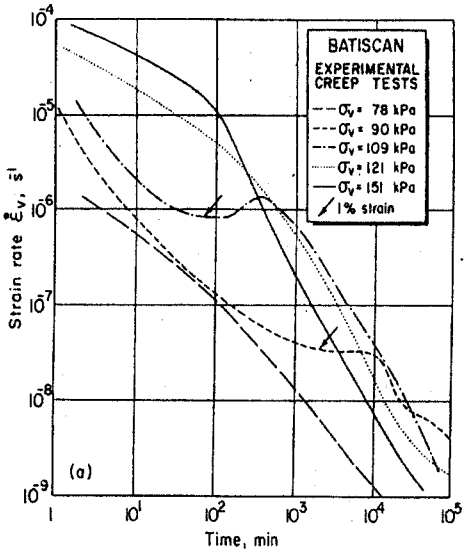

Figure 4.2:

Figure 4.1: Sudden increase in strain rate during drained creep tests on Pancone clay (Bishop 1969)

Figure 4.2: Sudden increase in strain rate during oedometer tests on Batiscan clay (Kabbaj et al. 1985)

by the finite-difference method using an elasto-viscoplastic constitutive model (Oka 1981), in which different values for the viscoplastic parameters were chosen with the strain rate. They showed that the strain rate remained momentarily constant during creep simulations around the preconsolidation pressure, whereas the experimental results showed a temporary increase in the strain rate. Asaoka, Nakano, Noda, and Kaneda (2000) also conducted analyses of one-dimensional consolidation using an elasto-plastic model with a super-subloading surface concept for the structured soil. They proved that the inhomogeneity of pore water pressure, stress, and void ratio distributions caused by softening could be reproduced. Oka, Tavenas, and Leroueil (1991) conducted a finite element analysis on a sensitive clay foundation beneath an embankment using an elasto-viscoplastic constitutive model, in which volumetric strain-softening terms were introduced. The analytical results were in better agreement with the observations than the model without softening terms, while the actual increase in pore water in the test embankment could not be reproduced.

In this chapter, the finite element analysis of one-dimension consolidation is conducted using the elasto-viscoplastic constitutive model proposed in the previous chapter, which takes into account the effect of structural changes, in order to study the performance of the model with respect to unstable behavior during consolidation. The ability to predict unstable behavior during consolidation is evaluated with reference to pore water generation and the changes in strain rate with time, and also to the distribution of axial

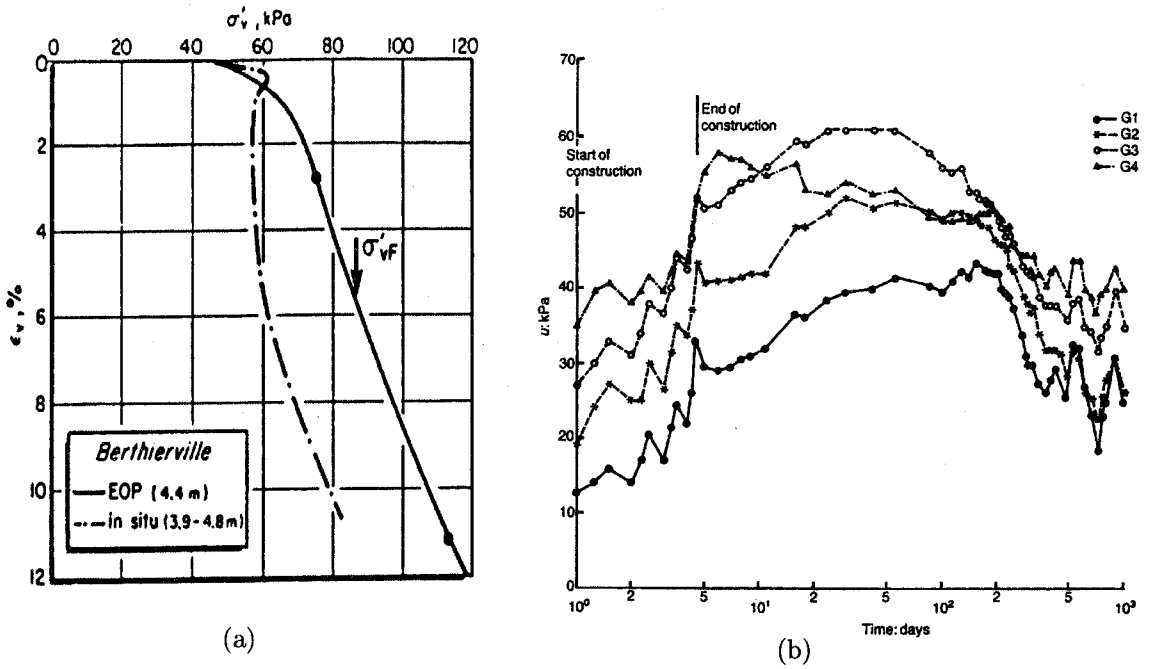

Figure 4.3: A stress-strain curve (a), and variation in pore pressure (b) obtained at the Berthierville test embankment (Leroueil 1988 and Kabbaj et al. 1988)

strain in the soil layer.

4.2 Finite Element Formulation

For a boundary value problem related to the soil-water coupled consolidation problem, the finite element method based on Biot's two-phase mixture theory (Biot 1962) is adopted. Both the grain particles and the fluid are assumed to be incompressive for simple formulations. The infinitesimal strain is valid in this problem since large deformations are not expected. A four-node quadrilateral element with a reduced Gaussian two-point integration is used for the displacement, and the pore water pressure is defined at the center of each element based on Akai and Tamura (1978).

The effective stress tensor σ'_{ij} and its rate form $\dot{\sigma}'_{ij}$ are defined as

$$\sigma_{ij} = \sigma'_{ij} + u_w \delta_{ij} \tag{4.1}$$

$$\dot{\sigma}_{ij} = \dot{\sigma}'_{ij} + \dot{u}_w \delta_{ij} \tag{4.2}$$

where σ_{ij} is the stress tensor and u_w is the pore water pressure.

For the discretization of the equilibrium equation of the solid-fluid mixture, the boundary Γ of closed domain V can be separated into two parts, namely,

$$\Gamma = \Gamma_T + \Gamma_u \tag{4.3}$$

in which Γ_T and Γ_u are the boundaries where the stress rate component and the deformation rate are predicted.

On boundary Γ_T,

$$\dot{\sigma}_{ij} n_j = \dot{\bar{T}}_i \tag{4.4}$$

where n_i is the ith component of the unit vector normal n to the surface.

Applying the principle of virtual work to the equilibrium equation in the incremental form gives the following:

$$\int_V \dot{\sigma}_{ij} \delta\dot{\varepsilon}_{ij} dV = \int_V \dot{\sigma}'_{ij} \delta\dot{\varepsilon}_{ij} dV + \int_V \dot{u}_w \delta_{ij} \delta\dot{\varepsilon}_{ij} dV = \int_\Gamma \dot{\bar{T}}_i \delta\dot{u}_i d\Gamma \tag{4.5}$$

in which $\dot{\sigma}_{ij}$ is the stress rate tensor, $\dot{\sigma}'_{ij}$ is the effective stress rate tensor, $\dot{u}_w$ is the rate of the pore water pressure, $\delta\dot{\varepsilon}_{ij}$ is the virtual strain rate tensor, and $\delta\dot{u}_i$ is the virtual displacement rate vector. The body force is disregarded here.

Next, the equations in matrix form are used in the finite element formulation; the following vectors and matrixes are defined. Total stress rate vector $\{\dot{\sigma}\}$, effective stress rate vector $\{\dot{\sigma}'\}$, and strain rate vector $\{\dot{\varepsilon}\}$ are

$$\{\dot{\sigma}\} = \begin{Bmatrix} \dot{\sigma}_{xx} \\ \dot{\sigma}_{yy} \\ \dot{\sigma}_{xy} \end{Bmatrix}, \quad \{\dot{\sigma}'\} = \begin{Bmatrix} \dot{\sigma}'_{xx} \\ \dot{\sigma}'_{yy} \\ \dot{\sigma}'_{xy} \end{Bmatrix}, \quad \{\dot{\varepsilon}\} = \begin{Bmatrix} \dot{\varepsilon}_{xx} \\ \dot{\varepsilon}_{yy} \\ \dot{\gamma}_{xy} \end{Bmatrix} \tag{4.6}$$

Displacement rate vector $\{\dot{u}\}$ and nodal displacement rate $\{\dot{u}^*\}$ are

$$\{\dot{u}\} = \begin{Bmatrix} \dot{u}_x \\ \dot{u}_y \end{Bmatrix}, \quad \{\dot{u}^*\} = \begin{Bmatrix} \dot{u}^*_x \\ \dot{u}^*_y \end{Bmatrix} \tag{4.7}$$

Pore water pressure rate vector $\{\dot{u}_w\}$ is

$$\{\dot{u}_w\} = \begin{Bmatrix} \dot{u}_w \\ \dot{u}_w \\ 0 \end{Bmatrix} \tag{4.8}$$

Eq.(4.5) can be written in matrix form as

$$\int_V \{\delta\dot{\varepsilon}\}^T \{\dot{\sigma}\}\, dV = \int_V \{\delta\dot{\varepsilon}\}^T \{\dot{\sigma}'\}\, dV + \int_V \{\delta\dot{\varepsilon}\}^T \{\dot{u}_w\}\, dV = \int_\Gamma \{\delta\dot{u}\}^T \left\{\dot{\bar{T}}_i\right\} d\Gamma \tag{4.9}$$

Displacement rate vector $\{\dot{u}\}$ in the element is defined with the shape function $[N]$ as

$$\{\dot{u}\} = [N]\{\dot{u}^*\}, \quad \{\delta\dot{u}\} = [N]\{\delta\dot{u}^*\} \tag{4.10}$$

Strain rate vector $\{\dot{\varepsilon}\}$ and volumetric strain rate $\{\dot{\varepsilon_v}\}$ in the element are given as

$$\{\dot{\varepsilon}\} = [B]\{\dot{u}^*\}, \quad \{\delta\dot{\varepsilon}\} = [B]\{\delta\dot{u}^*\} \tag{4.11}$$

$$\dot{\varepsilon}_v = \{B_v\}^T\{\dot{u}^*\}, \quad \delta\dot{\varepsilon}_v = \{B_v\}^T\{\delta\dot{u}^*\} \tag{4.12}$$

where $[B]$ is the matrix which transforms the nodal displacement into strain, and $\{B_v\}$ is the vector which transforms the nodal displacement into the volumetric strain.

In Eq.(4.9), the following is approved:

$$\int_V \{\delta\dot{\varepsilon}\}^T\{\dot{u}_w\}\,dV = \int_V \{\delta\dot{\varepsilon}_{xx}, \delta\dot{\varepsilon}_{yy}, \delta\dot{\gamma}_{xy}\}\begin{Bmatrix}\dot{u}_w\\ \dot{u}_w\\ 0\end{Bmatrix} dV = \dot{u}_w\int_V \delta\dot{\varepsilon}_v dV \tag{4.13}$$

The relation between effective stress rate vector $\{\dot{\sigma}'\}$ and strain rate vector $\{\dot{\varepsilon}\}$ for an elasto-viscoplastic model is given by

$$\{\dot{\sigma}'\} = [D]\{\dot{\varepsilon}\} - \{\dot{\sigma}^*\} \tag{4.14}$$

in which $[D]$ is the matrix of the elastic modulus and $\{\dot{\sigma}^*\}$ is the relaxation stress vector given as

$$\{\dot{\sigma}^*\} = [D]\{\dot{\varepsilon}^{vp}\} \tag{4.15}$$

Substituting Eqs.(4.10)$\sim$(4.14) into Eq.(4.9) and dividing by $\{\delta\dot{u}^*\}^T$ produce

$$[K]\{\dot{u}^*\} + \dot{u}_w\{K_v\} = \int_V [B]^T\{\dot{\sigma}^*\}\,dV + \left\{\dot{F}\right\} \tag{4.16}$$

$$[K] = \int_V [B]^T[D][B]\,dV \tag{4.17}$$

$$\{K_v\} = \int_V \{B_v\}\,dV \tag{4.18}$$

$$\left\{\dot{F}\right\} = \int_\Gamma [N]^T\left\{\dot{\bar{T}}_i\right\} d\Gamma \tag{4.19}$$

The pore water pressure is described by the following finite difference scheme.

$$\dot{u}_w = \frac{u_{w,t+\Delta t} - u_{w,t}}{\Delta t} \tag{4.20}$$

Finally, the discretization of the weak form of the equilibrium equation is obtained as follows:

$$[K]\{\Delta u^*\} + u_{w,t+\Delta t}\{K_v\} = u_{w,t}\{K_v\} + \{\Delta Q\} \tag{4.21}$$

where

$$\{\Delta Q\} = \Delta t \int_V [B]^T \{\dot{\sigma}^*\}\, dV + \Delta t \left\{\dot{F}\right\} \tag{4.22}$$

in which $\{\Delta u^*\}$ is the displacement increment vector at nodes ($\{\Delta u^*\} = \Delta t \{\dot{u}^*\}$).

Next, the equation of continuity is derived from the equation of the balance of mass and the equation of the motion of fluid as

$$\dot{\varepsilon}_v = -\frac{k}{\gamma_w} u_{w,ii} \tag{4.23}$$

in which k is the coefficient of permeability and γ_w is the density of the pore water. The implicit backward finite difference scheme is used in the approximation of Eq.(4.23).

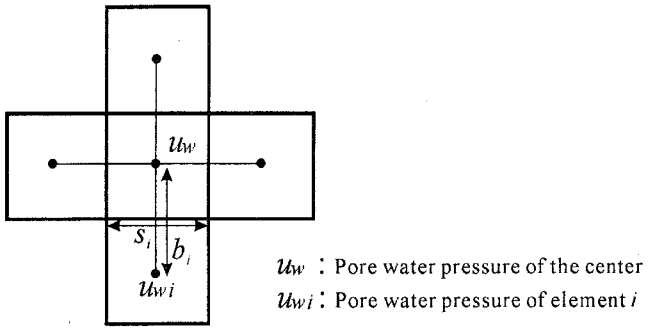

Figure 4.4: Discritization of pore water pressure

Referring to Fig.4.4,

$$\{K_v\}^T \{\Delta u^*\} = -\beta u_{w,t+\Delta t} + \sum_{i=1}^{4} \beta_i u_{wi,t+\Delta t} \tag{4.24}$$

$$\beta_i = -\frac{k\Delta t b_i}{\gamma_w s_i}, \quad \beta = \sum_{i=1}^{4} \beta_i \tag{4.25}$$

is obtained by the discretization of the continuity equation (4.23).

Combining Eqs.(4.21) and (4.24) yields the force-stiffness formulation for the element as

$$\begin{pmatrix} [K] & \{K_v\} \\ \{K_v\}^T & \beta \end{pmatrix} \begin{Bmatrix} \{\Delta u^*\} \\ u_{w,t+\Delta t} \end{Bmatrix} = \begin{Bmatrix} \{K_v\}\, u_{w,t} + \{\Delta Q\} \\ \sum_{i=1}^{4} \beta_i u_{wi,t+\Delta t} \end{Bmatrix} \tag{4.26}$$

4.3 One-Dimensional Consolidation Analysis

The behavior of sensitive clay during one-dimensional consolidation is numerically examined by the finite element analysis. As shown in Fig.4.5, the initial thickness of the soil

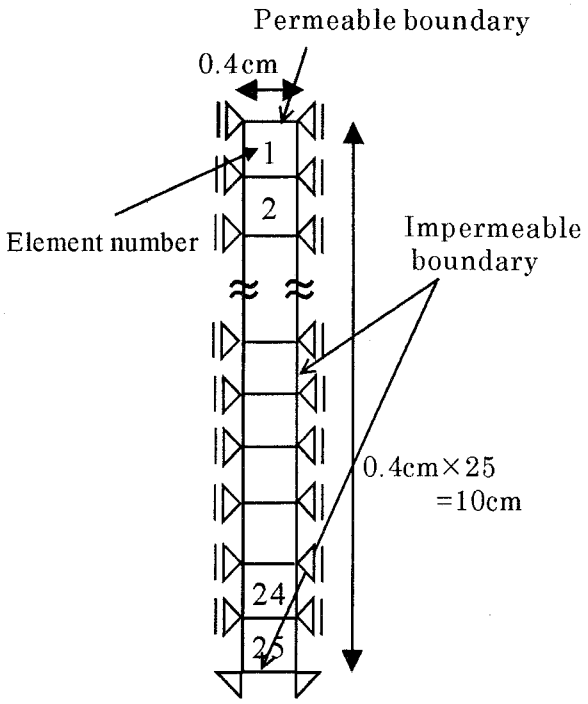

Figure 4.5: Finite element meshes and boundary conditions

sample is 10 cm with twenty five elements, the top of which is set to be permeable while the bottom is set to be impermeable.

The coefficient of permeability is given by

$$k = k_0 \exp\{(e - e_0)/C_k^*\} \tag{4.27}$$

Calculations are performed for normally consolidated (NC) clay and overconsolidated clay (OCR=2.0). The initial conditions of the calculations are shown in Table 4.1. An excess pore pressure level of 1160 kPa, which is twice as large as the compression yield stress, is applied as the initial loading for all the analyses.

Table 4.1: Initial conditions of the simulations

Initial value	**NC**	**OCR=2.0**
Initial mean effective stress $\sigma'_{m(0)}$ (kPa)	580	294
Coefficient of earth pressure K_0	0.5	
Initial pore pressure $u_{w(0)}$ (kPa)	1160	

The material parameters for the Tsurumi Pleistocene clay are used in the analyses, as listed in Table 4.2. For comparison, calculations with $\beta = 0$, corresponding to the original

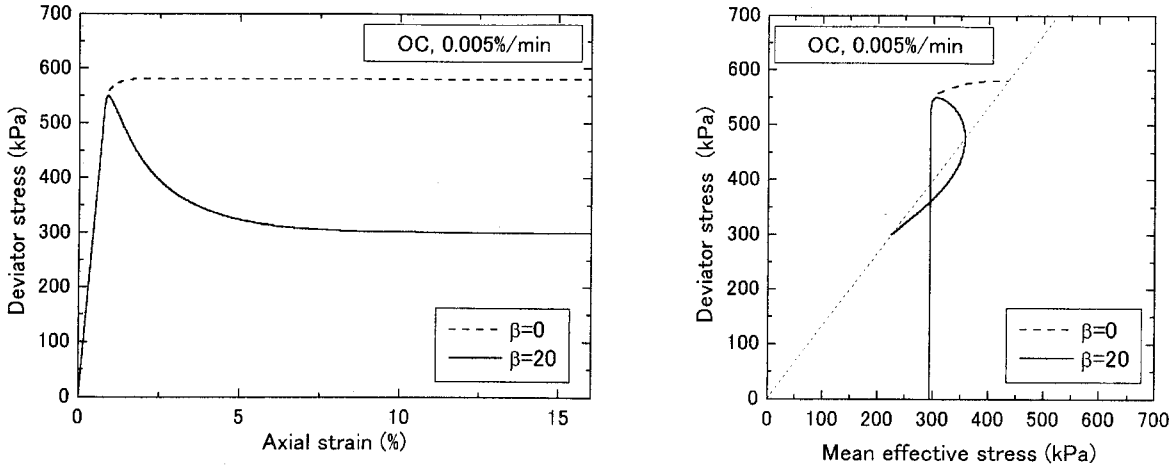

(a) Stress-strain relations (b) Stress paths

Figure 4.6: Simulations of undrained triaxial tests for OC clay

model without considering structural changes, are conducted for both NC and OC clays. Simulations of undrained triaxial compression tests for NC clay have been already shown in Fig.2.7, and simulations of undrained triaxial tests for OC clay are shown in Fig.4.6 to evaluate the material parameters.

Let us begin with NC clay. The vertical settlement vs. time and the vertical strain rate vs. time curves are shown in Figs.4.7 and 4.8. The vertical strain rate exhibits a sudden increase at around 2000 seconds after loading when structural changes are considered, namely, $\beta = 20$, while it exhibits a monotonous decreases when $\beta = 0$ (see Fig.4.8). Consequently, the displacement at the end of the calculation, when β=20, is almost three times as large as that when $\beta = 0$ (see Fig.4.7).

The generation of excess pore water pressure for element 25, namely, the bottom of the clay layer, is shown in Fig.4.9, which confirms that the pore water pressure temporarily increases after 2000 seconds with an increasing strain rate in the case of $\beta = 20$. The stress path of the elements at the center of the clay layer for $\beta = 0$ is shown in Fig.4.10. The average e-logσ'_m relation for all the elements is shown in Fig.4.11(a), and the e-logσ'_m relations for the top, the center, and the bottom of the elements are shown in Fig.4.11(b) in the case of $\beta = 0$. Similarly, the stress paths, the average e-logσ'_m relation, and e-logσ'_m relations for each element in the case of $\beta = 20$, are shown in Figs.4.12 and 4.13(a) and (b), respectively. When β=20, the mean effective stress decreases once and then increases again along the K_0 line, as shown in Figs.4.12, while it continuously increases when $\beta = 0$, as shown in Fig.4.10. Figs.4.13(a) and (b) demonstrate a temporary decrease in the mean

Table 4.2: Material parameters used in the simulations

Parameters	**NC**	**OCR=2.0**
Coefficient of permeability $k_0(m/s)$	0.8×10^{-9}	
Permeability change index C_k^*	0.1	
Elastic shear modulus G_0(kPa)	36100	22500
Compression index λ	0.508	
Swelling index κ	0.0261	
Initial void ratio e_0	1.70	
Compression yield stress σ'_{mbi} (kPa)	580	
Stress ratio at maximum compression M_m^*	1.09	
Viscoplastic parameter m'	18.5	
Viscoplastic parameter C_0 (1/s)	1.3×10^{-13}	4.0×10^{-13}
Structural parameter σ'_{maf} (kPa)	300	290
Structural parameter β	20	45

effective stress for the average e-logσ'_m curve. Similar tendency is observed for the test embankment shown in Fig.4.3 (Leroueil 1988)

The distributions of axial strain, pore water pressure, and mean effective stress during consolidation are presented in Figs.4.14, 4.15, and 4.16 for $\beta = 0$. In the same way, distributions are presented in Figs.4.17, 4.18, and 4.19 for $\beta = 20$. It is seen from Fig.4.14 that the axial strain is almost homogeneously distributed at the early stage of the calculations, while its distribution provide apparent inhomogeneity just after an increase in strain rate in the case of $\beta = 20$, as shown in Fig.4.17. The axial strain for element 1, namely, at the top of the clay layer denotes 1.7% and that for element 13, namely, at the center of the clay layer denotes 1.2% at 5000 s when β=0 (see Fig.4.14). On the contrary, the axial strain denotes 12% at the top and 2% at the center of the clay layer at 5000 s when β=20 (see Fig.4.17). The localization of axial strain, that is, compressive deformation in this case, is promoted by the structural changes. The pore water pressure decreases at the beginning of the consolidation, then temporarily increases, and finally dissipates at the end of the consolidation (Fig.4.18).

Next, let us see the results for the OC clay. Similar tendencies are obtained for the differences between $\beta = 0$ and $\beta = 20$. The vertical settlement-time and the vertical

strain rate-time curves and the pore water generation with time are shown in Figs.4.20, 4.21, and 4.22. The vertical strain rate suddenly increases after stagnation at around 20000 seconds; the excess pore pressure also shows a temporary increase when structural changes are taken into account, in other words, $\beta = 20$, as shown in Figs.4.21 and 4.22.

The stress path, the average e-logσ'_m relation, and e-logσ'_m relations for each element for $\beta = 0$ are shown in Figs.4.23 and 4.24(a) and (b). Similarly, they are shown for $\beta = 45$ in Figs.4.25 and 4.26. For the stress path in Fig.4.25, the point marked by * denotes the point at which the stress path goes out of the overconsolidation boundary surface. The mean effective stress decreases once along the K_0 line, takes the value at around 900 kPa, and then returns to the maximum value of 1100 kPa, as shown in Figs.4.25. Figs.4.26 (a) and (b) show a temporary decrease in the mean effective stress for the e-logσ'_m relation. This is the similar tendency obtained for the NC clay. The distributions of axial strain, pore water pressure, and mean effective stress are shown in Figs.4.27, 4.28, and 4.29 for $\beta = 0$, and in Figs.4.30, 4.31, and 4.32 for $\beta = 45$, respectively. As is seen for the NC clay, the strain distribution shows a higher degree of inhomogenity when structural changes are considered.

Furthermore, the calculations are conducted using the elasto-viscoplastic constitutive model with material function Φ_2, proposed by Adachi, Oka, and Mimura (1987a), which is introduced in the previous chapter. Material function Φ_2 describes strain-softening when the stress reaches the failure line. M_f^* is the failure stress rate and G_2^* is the viscoplastic parameter. Simulations of the undrained triaxial test for $G_2^* = 10$ and $M_f^* = 1.09$ have already been shown in Fig.3.5. The remaining parameters are the same as those listed in Table 4.2 for the NC clay. The results of the consolidation analysis cannot describe unstable behavior, and they are almost the same as those of the original model, as shown in Figs.4.33$\sim$4.35. The model with material function Φ_2 describes instability just around the failure stress ratio line, and cannot predict unstable behaviors during consolidation.

4.4 Summary

In this chapter, one-dimensional consolidation analyses were conducted using the elasto-viscoplastic constitutive model considering the structural changes proposed in Chapter 2. The computed results were compared using the proposed model, the original model, and the model with softening term Φ_2.

The proposed model considering structural changes can reproduce types of unstable behaviors during consolidation such as a sudden increase in the strain rate and the temporary increase in pore pressure after stagnation for both NC and OC clay, while the original model and the model with Φ_2 cannot reproduce those types of behavior. Moreover, the distributions of axial strain, when we take into account structural changes in the constitutive model, exhibit apparent inhomogenity. Specifically, the deformation is concentrated on the upper part of the clay layer. This phenomenon of the compressive strain localization due to the collapse of the structure is associated with compaction bands which may cause a large displacement.

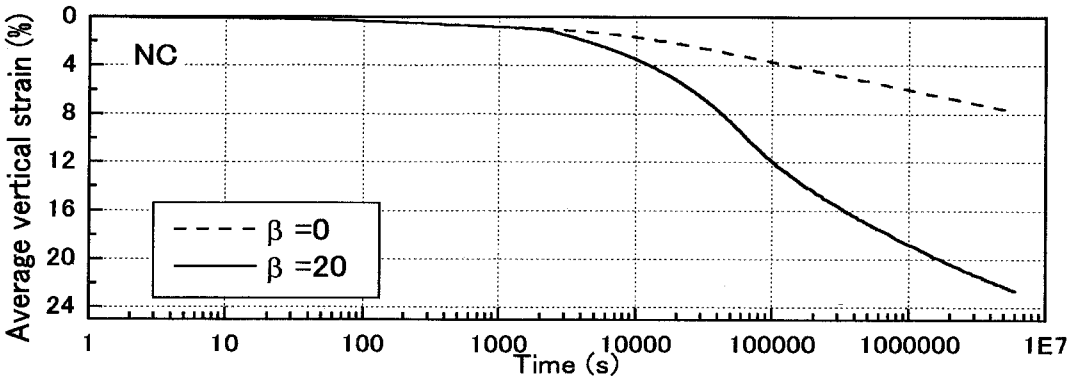

Figure 4.7: Average vertical strain during consolidation for NC clay

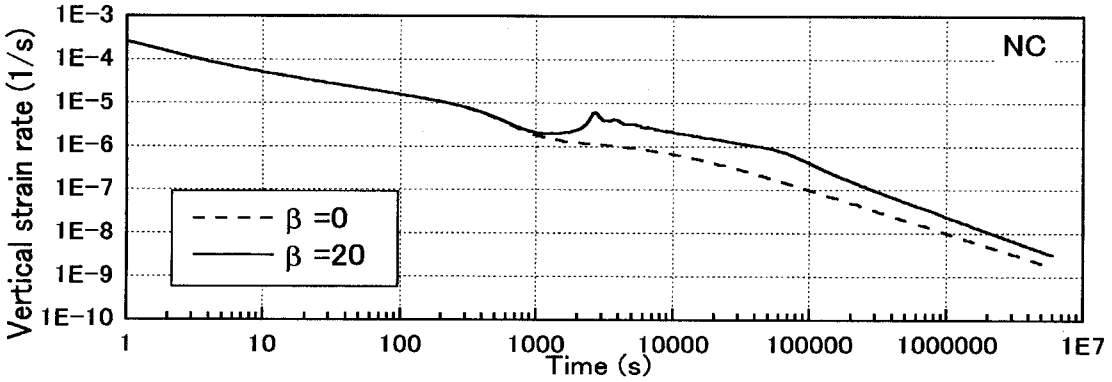

Figure 4.8: Vertical strain rate during consolidation for NC clay

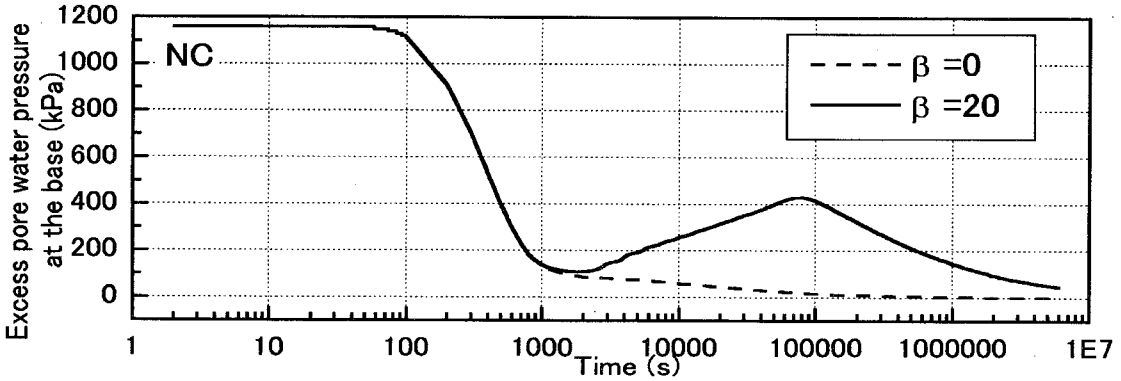

Figure 4.9: Generated pore water pressure for NC clay

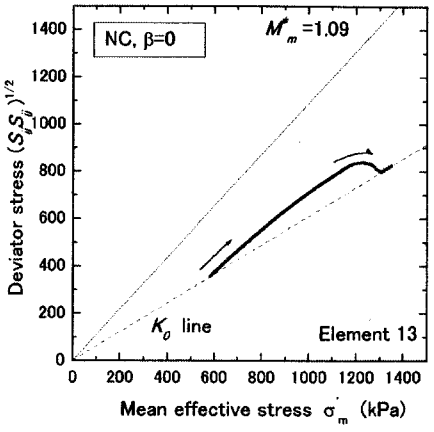

Fig.4.10

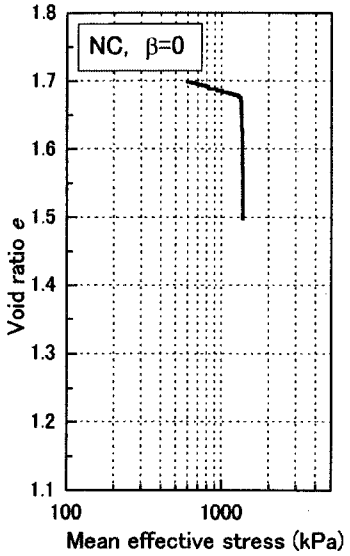

Fig.4.11 (a)

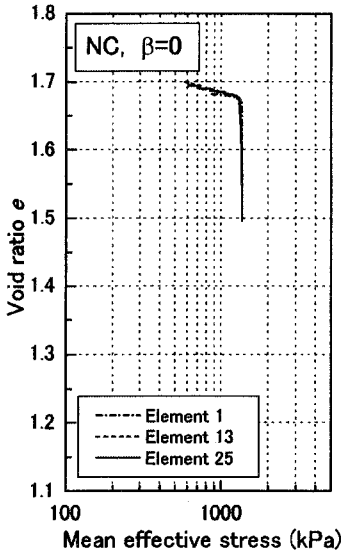

Fig.4.11 (b)

Figure 4.10: Stress path at the center of the clay layer for NC clay (β=0)

Figure 4.11: (a) Average e-logσ'_m curve for NC clay (β=0)

(b) e-logσ'_m curve of the elements for NC clay (β=0)

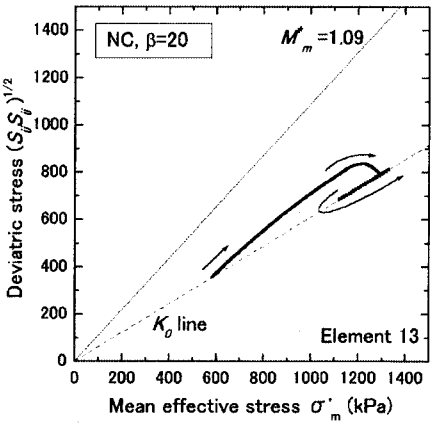

Fig.4.12

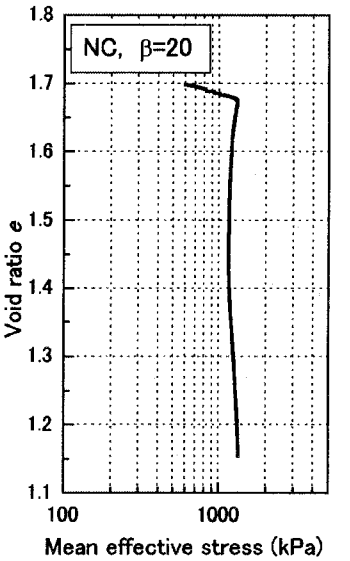

Fig.4.13 (a)

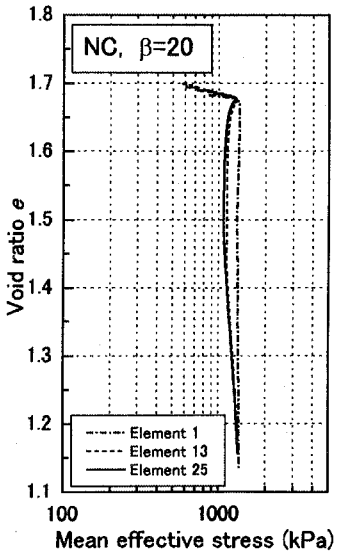

Fig.4.13 (b)

Figure 4.12: Stress path at the center of the clay layer for NC clay (β=20)

Figure 4.13: (a) Average e-logσ'_m curve for NC clay (β=20)

(b) e-logσ'_m curve of the elements for NC clay (β=20)

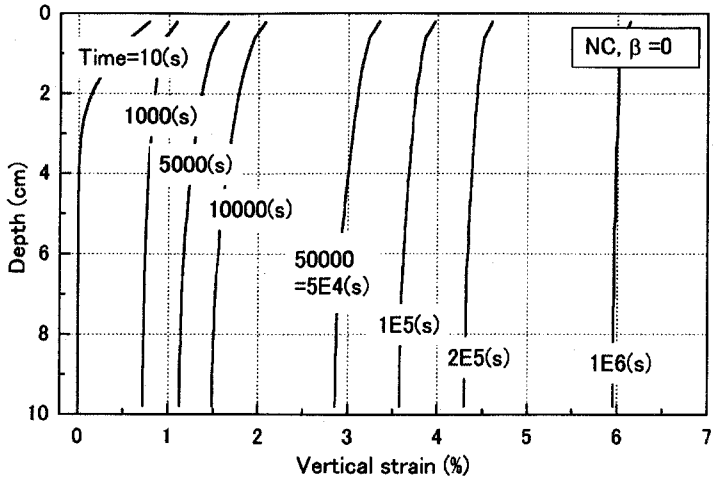

Figure 4.14: Distribution of axial strain with time for NC clay (β=0)

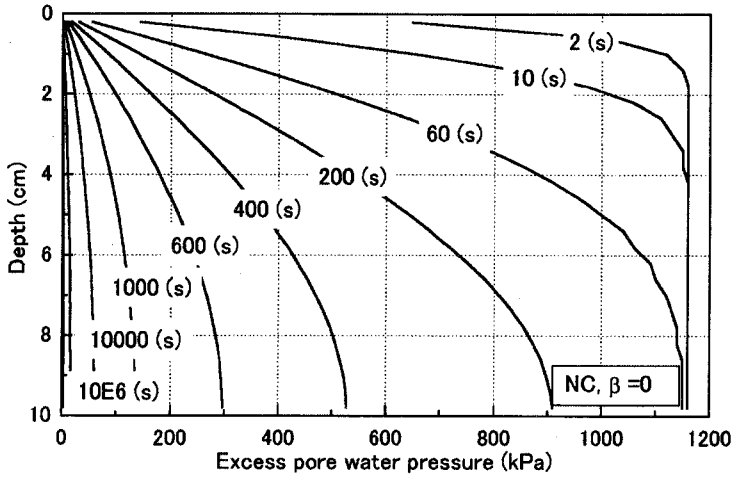

Figure 4.15: Distribution of pore water pressure with time for NC clay (β=0)

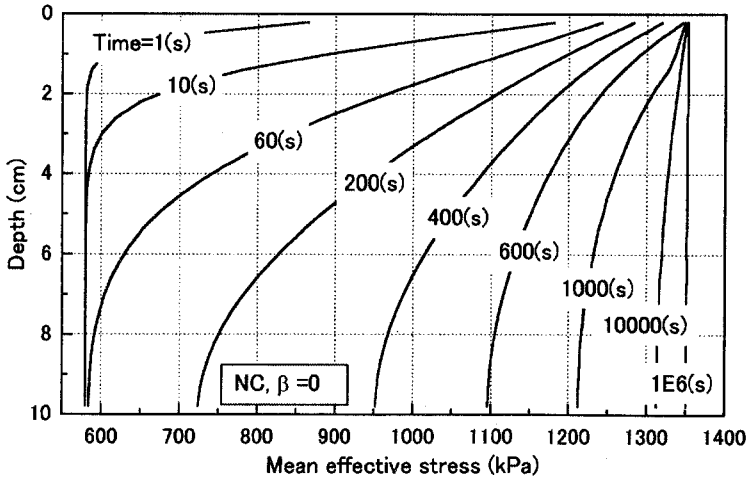

Figure 4.16: Distribution of mean effective stress with time for NC clay (β=0)

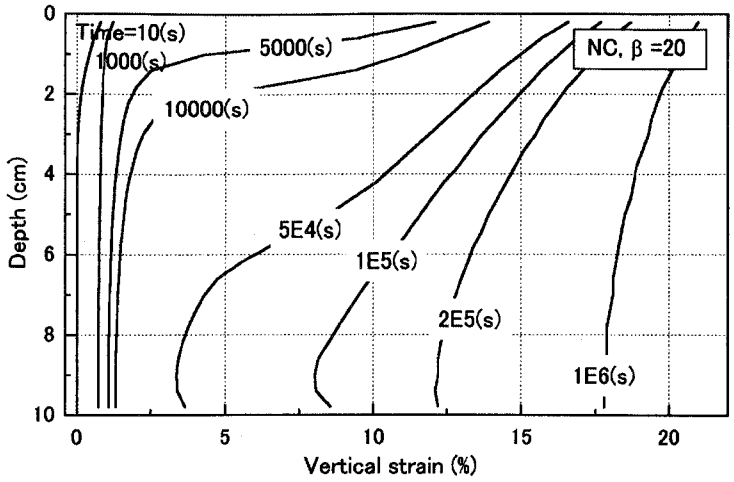

Figure 4.17: Distribution of axial strain with time for NC clay (β=20)

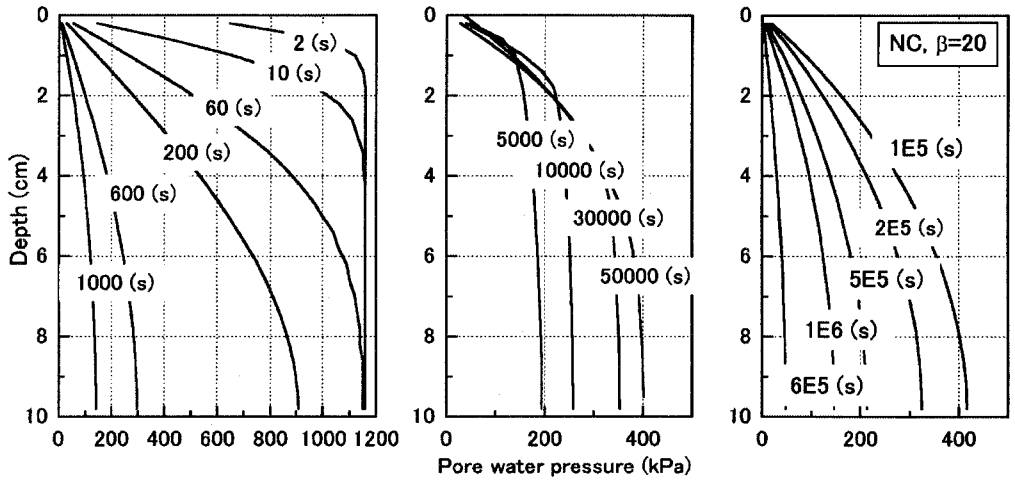

Figure 4.18: Distribution of pore water pressure with time for NC clay (β=20)

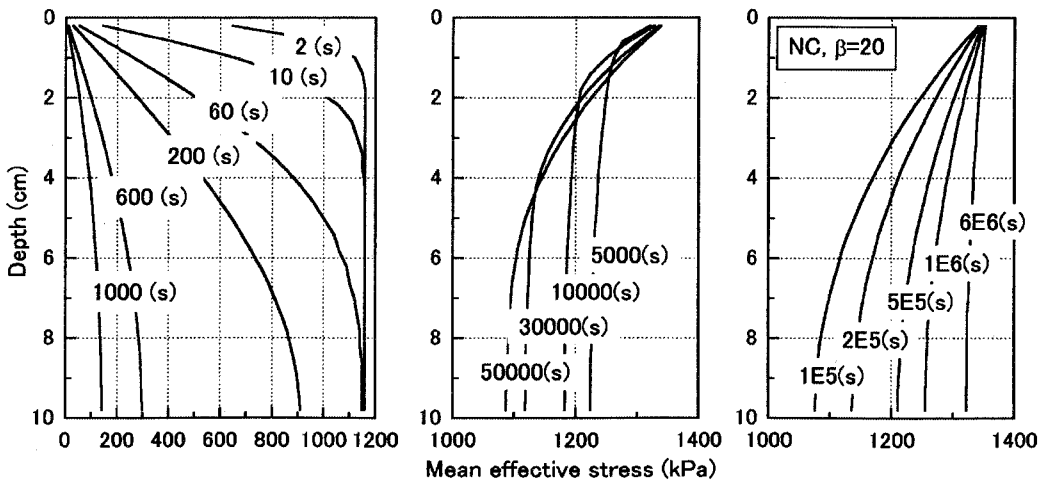

Figure 4.19: Distribution of mean effective stress with time for NC clay (β=20)

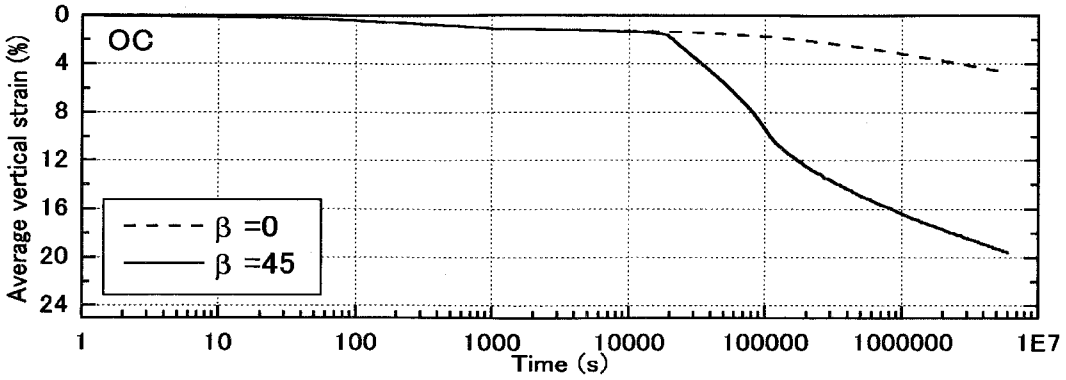

Figure 4.20: Average vertical strain during consolidation for OC clay

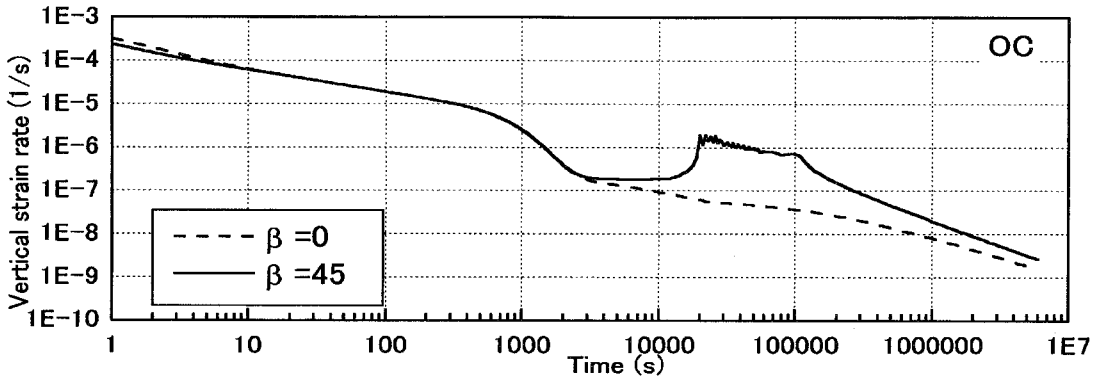

Figure 4.21: Vertical strain rate during consolidation for OC clay

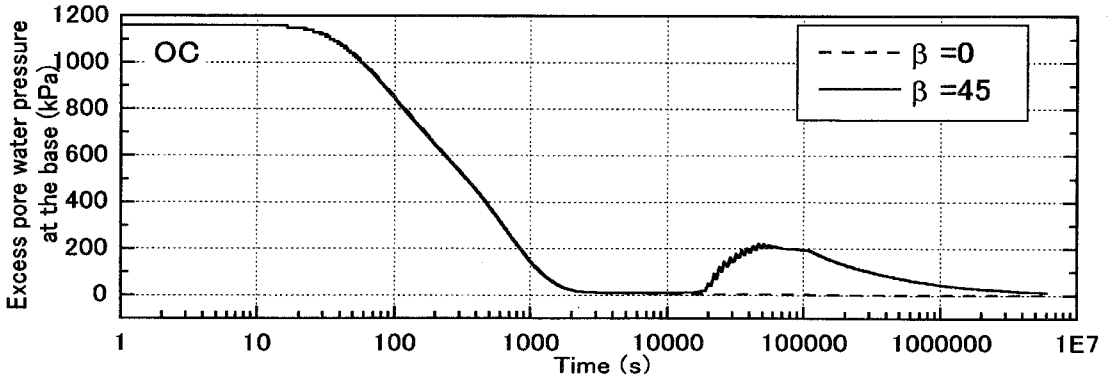

Figure 4.22: Generated pore water pressure for OC clay

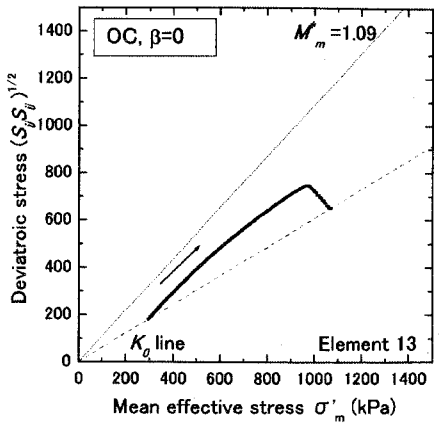

Fig.4.23

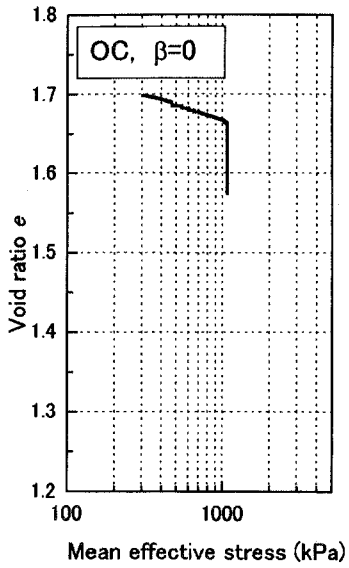

Fig.4.24 (a)

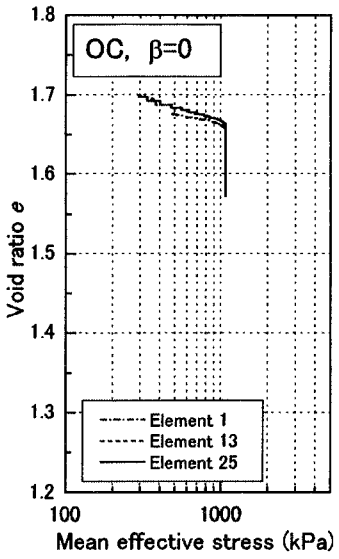

Fig.4.24 (b)

Figure 4.23: Stress path at the center of the clay layer for OC clay (β=0)

Figure 4.24: (a) Average e-logσ'_m curve for OC clay (β=0)
(b) e-logσ'_m curve of the elements for OC clay (β=0)

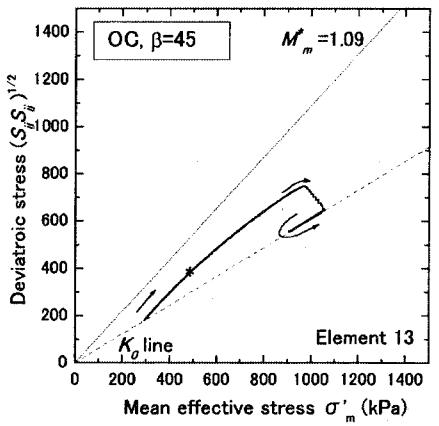

Fig.4.25

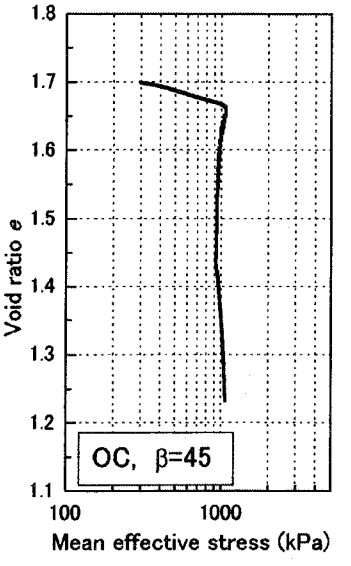

Fig.4.26 (a)

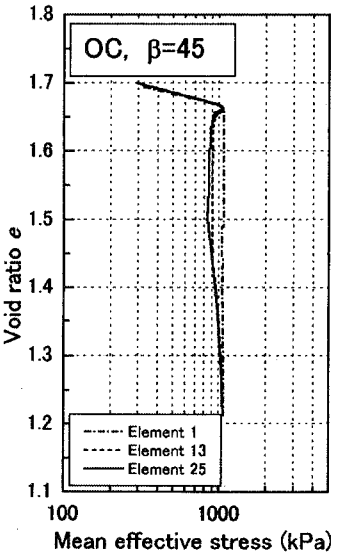

Fig.4.26 (b)

Figure 4.25: Stress path at the center of the clay layer for OC clay (β=45)

Figure 4.26: (a) Average e-logσ'_m curve for OC clay (β=45)
(b) e-logσ'_m curve of the elements for OC clay (β=45)

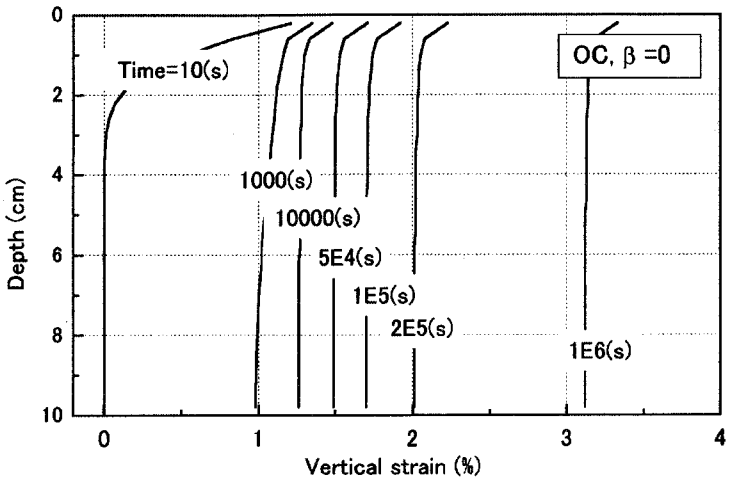

Figure 4.27: Distribution of axial strain with time for OC clay (β=0)

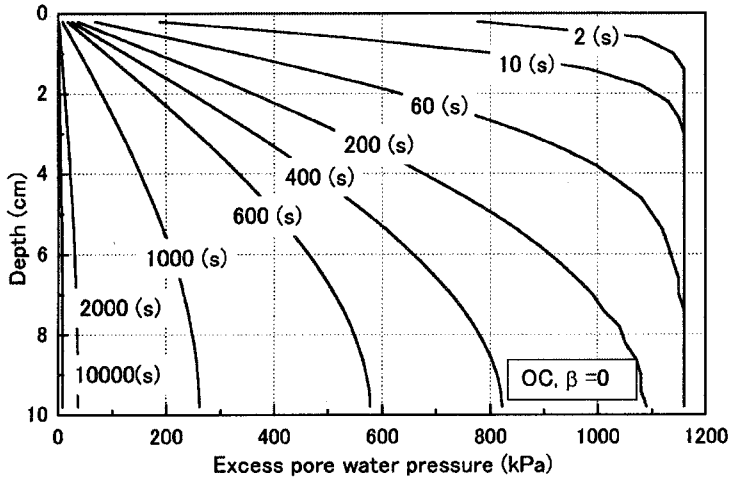

Figure 4.28: Distribution of pore water pressure with time for OC clay (β=0)

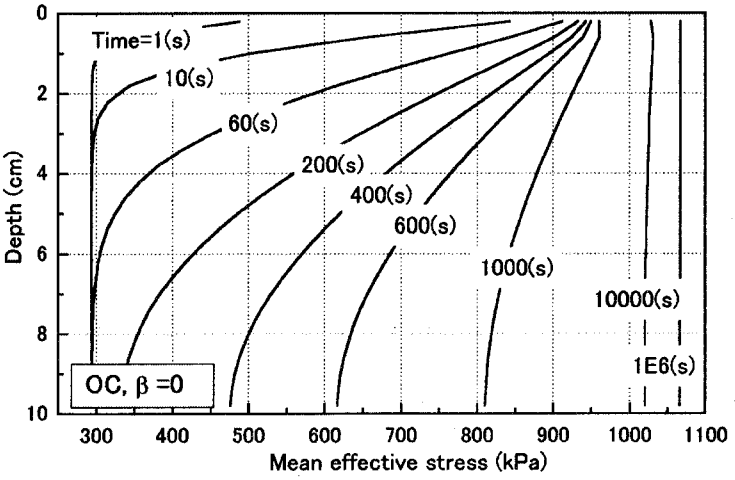

Figure 4.29: Distribution of mean effective stress with time for OC clay (β=0)

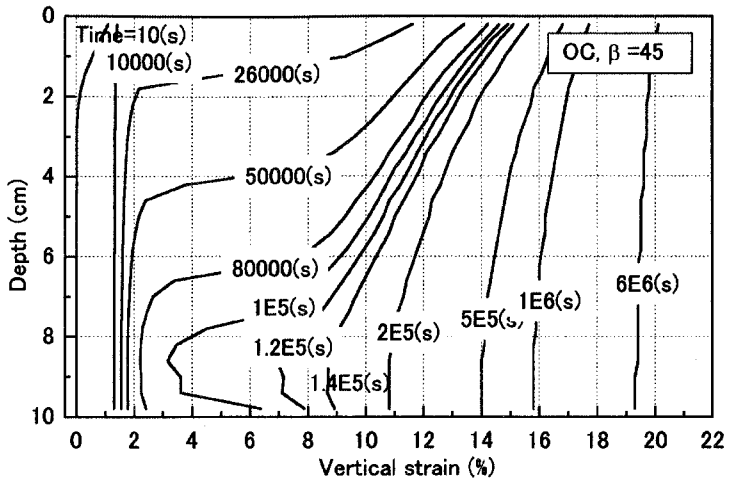

Figure 4.30: Distribution of axial strain with time for OC clay (β=45)

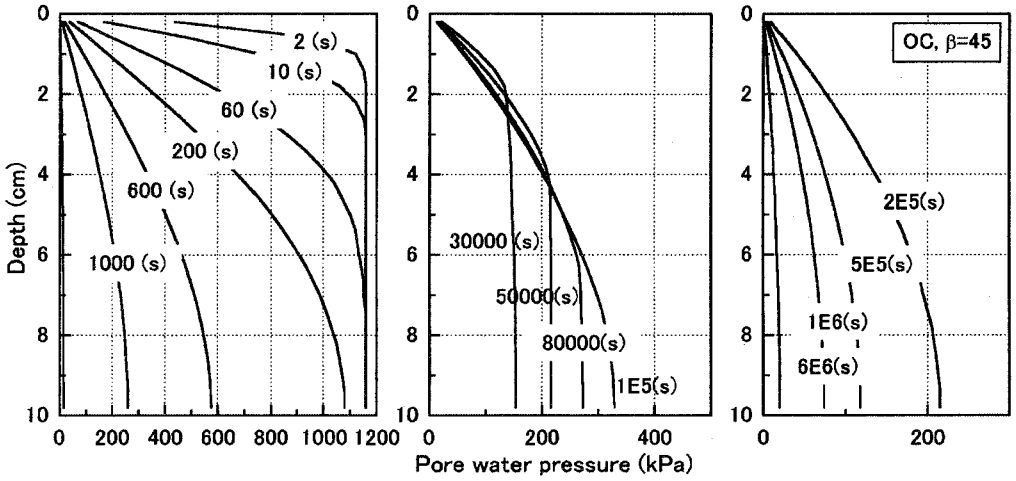

Figure 4.31: Distribution of pore water pressure with time for OC clay (β=45)

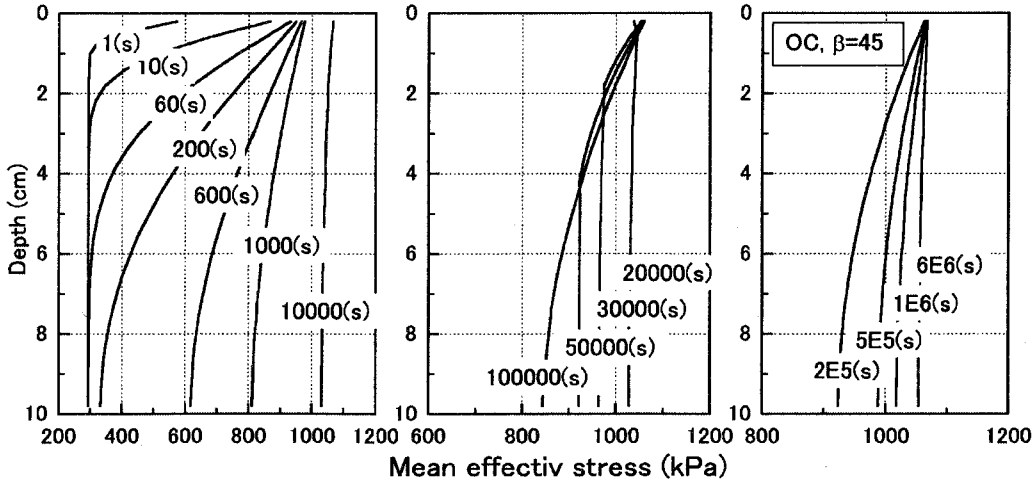

Figure 4.32: Distribution of mean effective stress with time for OC clay (β=45)

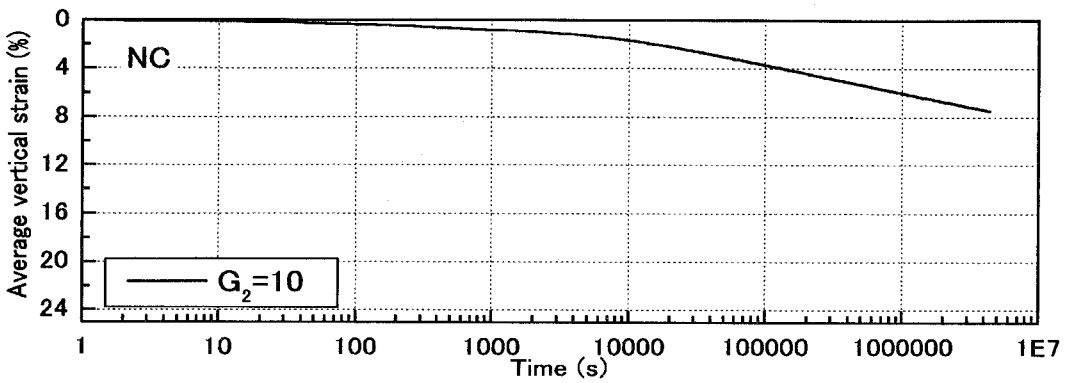

Figure 4.33: Average vertical strain during consolidation for NC clay (with Φ_2)

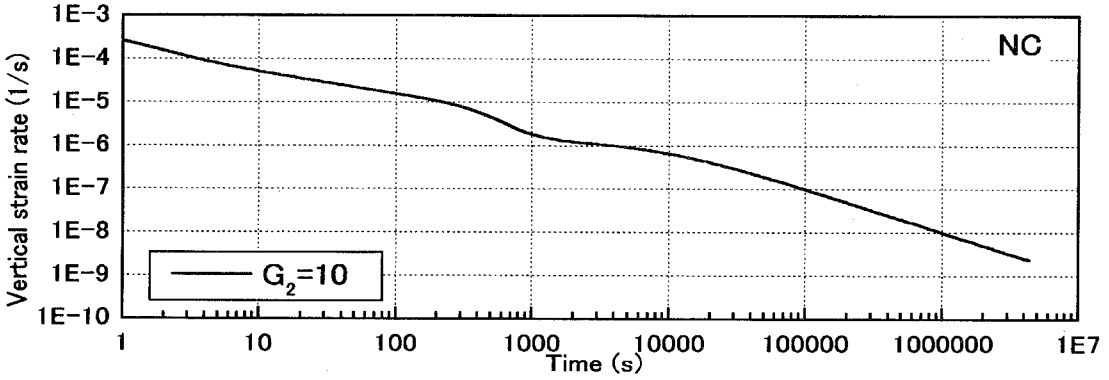

Figure 4.34: Vertical strain rate during consolidation for NC clay (with Φ_2)

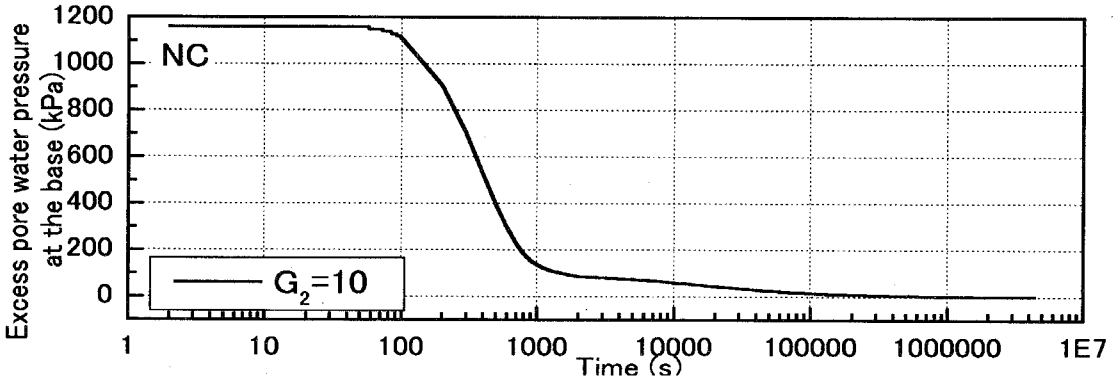

Figure 4.35: Generated pore water pressure for NC clay (with Φ_2)

Chapter 5

ELASTO-PLASTIC CONSTITUTIVE MODEL FOR SOFT ROCK CONSIDERING INITIAL STRUCTURAL ANISOTROPY

5.1 Introduction

It is well known that the mechanical behavior of most natural deposits is anisotropic due to the growth of anisotropic microstructure formed during the sedimentation process. Tavenas and Leroueil (1977), Ohtsuki et al. (1981), and Leroueil and Vaughan (1990) showed that the shape of the yield curve for overconsolidated clay and weak rock indicates that the material is anisotropic. Boehler and Sawczuk (1977) showed that sand, clay and stratified rock have the directional character of mechanical properties in the load - deformation relations and in the conditions of failure. They remarked that diversity in the mechanical response with orientation or in the privileged plane of transverse isotropy can be seen. Another investigation in the deformation and the strength properties of oriented rock was carried out by Lo and Hori (1979). They analyzed the deformation behavior of soft rock in terms of the cross-anisotropic elastic theory.

In this chapter, we propose an elasto-plastic constitutive model for soft rock considering initial structural anisotropy and discuss a performance of proposed model by applying

the model for the triaxial test results of soft sedimentary rock sampled in the different directions.

In order to introduce the initial structural anisotropy to the constitutive model, the tensor products of the vector which specifies a privileged direction are used following Boehler and Sawczuck (1977). In the present study, the isotropic constitutive model with strain-softening, proposed by Adachi and Oka (1995), is extended to an anisotropic model which can describe not only strain-softening behavior and dilatancy, but also the anisotropic behavior of soft rock. As for the direction dependent plastic deformation, Boehler's anisotropic theory is adopted to formulate the constitutive model. In the derivation of the model, the Cauchy stress tensor components are replaced by transformed stress tensor components which are expressed by a function of the stress tensor and the structure tensor that describes the direction of the sedimentation plane. The validity of the proposed model for soft rock is verified through comparisons between simulated results of triaxial tests and the experimental data.

5.2 Modeling of Anisotropy

In general, anisotropy of geomaterials is considered to be divided into two components, namely, stress induced anisotropy and inherent anisotropy. It is difficult, however, to distinguish between the two components for natural deposits. We consider the anisotropy of soft sedimentary rock to be structural anisotropy which contains both induced and inherent anisotropy. Although anisotropy may change with loading and other factors, for simplicity, only the initial structural anisotropy is taken into account in the present study. In other words, the structural anisotropy of soft rock, formed in the sedimentation process, is assumed not to change with loading.

Several methods have been proposed to describe the anisotropy of natural deposits by the constitutive model. In most of those models, natural deposits have been assumed to be transversely isotropic, sometimes called cross-anisotropic. Soft rock is also assumed to be transversely isotropic body in this model; the mechanical behavior would be isotropic in the bedding plane.

It has been pointed out that the behavior of natural deposits is characterized by the characteristic plane. Oda and Nakayama (1989) used a fabric tensor to formulate

the anisotropic constitutive model for soils. Boehler and Sawczuk (1977) explained the directional strength of solids through the use of a structural tensor. A similar manner is adopted and the isotropic model for soft rock proposed by Adachi and Oka (1995) is extended to an anisotropic one.

It is well known that soils exhibit anisotropy in both the plastic deformation and the elastic regions (Graham, Nooman and Lew (1983)). In the case of transversely isotropic elastic materials, five independent parameters are required for the formulation, which is a generalized Hooke's law (Love 1927). Graham and Houlsby (1983) proposed a convenient parameter which expresses the ratio between the horizontal and the vertical stiffness for the modified elastic matrix. Lo and Hori (1979) discussed how to determine the five elastic parameters by performing uniaxial compression tests. Kirkgard and Lade (1991) obtained undrained test results from triaxial tests on cubical sampled clay in both vertical and horizontal directions, and determined the elastic parameters from the test results. Shinjo and Komiya (1984) presented a method for determining the five parameters from triaxial compression tests on variously oriented samples.

In this model, a generalized Hooke's law is adopted for elastic deformation and Boehler's theory is used for plastic deformation; an anisotropic constitutive model is proposed for soft sedimentary rock. In the constitutive model, the total strain increment is the sum of the elastic strain increment and the plastic strain increment.

$$d\varepsilon_{ij} = d\varepsilon^e_{ij} + d\varepsilon^p_{ij} \tag{5.1}$$

In the following section, the formulation of anisotropy for elastic strain and plastic strain values will be summarized, respectively.

5.2.1 Anisotropy of Elastic Stain

The generalized Hooke's law is given as follows:

$$\{\sigma\} = [D]\{\varepsilon\} \tag{5.2}$$

$$\{\varepsilon\} = [D]^{-1}\{\sigma\} \tag{5.3}$$

where $[D]$ is the elastic stiffness matrix which is symmetric.

The generalized Hooke's law for the transversely isotropic elastic body is given as

follows:

$$\begin{bmatrix} \varepsilon_{xx} \\ \varepsilon_{yy} \\ \varepsilon_{zz} \\ \varepsilon_{xy} \\ \varepsilon_{yz} \\ \varepsilon_{zx} \end{bmatrix} = \begin{bmatrix} 1/E_x & -\nu_{yx}/E_y & -\nu_{xz}/E_x & 0 & 0 & 0 \\ -\nu_{yx}/E_y & 1/E_y & -\nu_{yx}/E_y & 0 & 0 & 0 \\ -\nu_{xz}/E_x & -\nu_{yx}/E_y & 1/E_x & 0 & 0 & 0 \\ 0 & 0 & 0 & 1/2G_{yx} & 0 & 0 \\ 0 & 0 & 0 & 0 & 1/2G_{yx} & 0 \\ 0 & 0 & 0 & 0 & 0 & (1+\nu_{xz})/E_x \end{bmatrix} \begin{bmatrix} \sigma_{xx} \\ \sigma_{yy} \\ \sigma_{zz} \\ \sigma_{xy} \\ \sigma_{yz} \\ \sigma_{zx} \end{bmatrix} \tag{5.4}$$

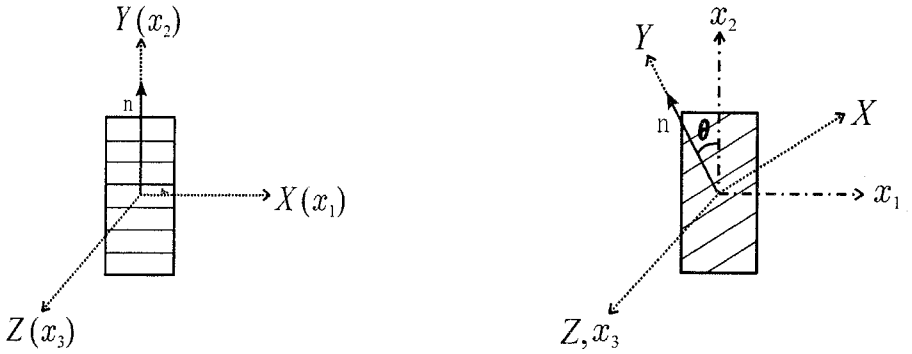

(a) When θ=0 (b) When $\theta \neq 0$

Figure 5.1: Structural tensor

There are five independent elastic moduli, namely, E_x, E_y, ν_{xz}, ν_{yx}, and G_{yx}. Eq.(5.4) gives the stress-strain relationship for the case in which the normal to sedimentation plane coincides with the major principal stress axis, in other words, angle θ is equal to 0°, as shown in Fig.5.1(a). If angle θ is not equal to 0°, as shown in Fig.5.1(b), the axis of stiffness matrix $[D]$ must be rotated. Considering a sedimentation plane which inclines θ degrees from the horizontal surface around the $Z(=Z')$ axis, $[D]$ must be defined by the (x_1, x_2, x_3) coordinate which corresponds to principal stress directions. Stiffness matrix $\left[\hat{D}\right]$ is expressed by rectangular coordinate (x_1, x_2, x_3) as follows:

$$\left[\hat{D}\right] = [Q]^T [D] [Q] \tag{5.5}$$

$$[Q] = \begin{bmatrix} l_1^2 & l_2^2 & l_3^2 & l_1 l_2 & l_2 l_3 & l_3 l_1 \\ m_1^2 & m_2^2 & m_3^2 & m_1 m_2 & m_2 m_3 & m_3 m_1 \\ n_1^2 & n_2^2 & n_3^2 & n_1 n_2 & n_2 n_3 & n_3 n_1 \\ 2l_1 m_1 & 2l_2 m_2 & 2l_3 m_3 & l_1 m_2 + m_1 n_2 & l_2 m_3 + m_2 n_3 & l_3 m_1 + m_3 n_1 \\ 2m_1 n_1 & 2m_2 n_2 & 2m_3 n_3 & m_1 n_2 + m_1 n_2 & m_2 n_3 + m_2 n_3 & l_3 m_1 + m_3 n_1 \\ 2n_1 l_1 & 2n_2 l_2 & 2n_3 l_3 & n_1 l_2 + n_1 l_2 & n_2 l_3 + n_2 l_3 & n_3 l_1 + n_3 l_1 \end{bmatrix}$$

$$l_1 = \cos\theta, \quad l_2 = \sin\theta, \quad l_3 = 0$$
$$m_1 = -\sin\theta, \quad m_2 = \cos\theta, \quad m_3 = 0$$
$$n_1 = 0, \quad n_2 = 0, \quad n_3 = 1$$

As a result, the anisotropic elastic strain increment is given by the following equation.

$$\{d\varepsilon^e\} = \left[\hat{D}\right]^{-1} \{d\sigma\} \tag{5.6}$$

There are five independent elastic moduli, E_x, E_y, ν_{xz}, ν_{yx}, and G_{yx}. Following the work of Shinjo and Komiya (1984), these parameters can be determined from the results of drained triaxial compression tests for three kinds of specimens with different θ, namely, $\theta = 0^\circ$ (vertical), $\theta = 90^\circ$ (horizontal), and $0^\circ < \theta < 90^\circ$ (inclined).

5.2.2 Anisotropy of Plastic Strain

Boehler's theory is adopted for the formulation of the plastic anisotropic deformation. In that theory, stress tensor σ_{ij} is replaced by transformed stress tensor $\hat{\sigma}_{ij}$.

The transformed stress tensor is expressed by the function of stress tensor σ_{ij} and structural tensor M_{ij} which describes the effect of anisotropy. Structural tensor M_{ij} is defined as a tensor product of unit vector n_i which is normal to the sedimentation plane.

$$M_{ij} = n_i \otimes n_j, \quad (i, j = 1, 2, 3) \tag{5.7}$$

As shown in Fig.5.1(a), when the sedimentation plane coincides with the $X - Z$ plane, namely, angle $\theta = 0^\circ$, components of the structural tensor can be expressed by the (X, Y, Z) coordinate which corresponds to the $(x_1, x_2, x_3,)$ coordinate, as follows:

$$\left[\ M\ \right] = \begin{bmatrix} 0 \\ 1 \\ 0 \end{bmatrix} \otimes \begin{bmatrix} 0 \\ 1 \\ 0 \end{bmatrix} = \begin{bmatrix} 0 & 0 & 0 \\ 0 & 1 & 0 \\ 0 & 0 & 0 \end{bmatrix} \tag{5.8}$$

where $\otimes$ denotes the tensor product.

If $\theta \neq 0^\circ$, as shown in Fig.5.1(b), structural tensor M_{ij} must be expressed in the (x_1, x_2, x_3) coordinate which corresponds to principal stress direction as

$$\begin{aligned} \left[\hat{M}\right] &= [R]\,[M]\,[R]^T \\ &= \begin{bmatrix} \cos\theta & -\sin\theta & 0 \\ \sin\theta & \cos\theta & 0 \\ 0 & 0 & 1 \end{bmatrix} \begin{bmatrix} 0 & 0 & 0 \\ 0 & 1 & 0 \\ 0 & 0 & 0 \end{bmatrix} \begin{bmatrix} \cos\theta & \sin\theta & 0 \\ -\sin\theta & \cos\theta & 0 \\ 0 & 0 & 1 \end{bmatrix} \end{aligned} \tag{5.9}$$

$$= \begin{bmatrix} \sin^2\theta & -\sin\theta\cos\theta & 0 \\ -\sin\theta\cos\theta & \cos^2\theta & 0 \\ 0 & 0 & 0 \end{bmatrix}$$

in which $[R]$ is the matrix of the orthogonal tensor components that expresses the rotation $(-\theta)$ around the Z axis.

$$[R] = \begin{bmatrix} \cos(-\theta) & \sin(-\theta) & 0 \\ -\sin(-\theta) & \cos(-\theta) & 0 \\ 0 & 0 & 1 \end{bmatrix} = \begin{bmatrix} \cos\theta & -\sin\theta & 0 \\ \sin\theta & \cos\theta & 0 \\ 0 & 0 & 1 \end{bmatrix} \tag{5.10}$$

The transformed stress tensor needs to satisfy the objectivity, and it is assumed to be expressed by a linear form of the stress tensor σ_{ij}. Furthermore, it can be expressed by a linear form of structure tensor $\hat{M}_{ij}$ since $\hat{M}_{ik}\hat{M}_{kj} = \hat{M}_{ij}$ is satisfied. Following Boehler's theory (1977), a simplified form of the transformed stress tensor $\hat{\sigma}_{ij}$ is given as

$$\hat{\sigma}_{ij} = (\alpha + \gamma - 2\beta)(\hat{M}_{mn}\sigma_{mn})\hat{M}_{ij} + \gamma\sigma_{ij} + (\beta - \gamma)(\hat{M}_{ik}\sigma_{kj} + \sigma_{ik}\hat{M}_{kj}) \tag{5.11}$$

in which α, β, and γ are three independent plastic anisotropic parameters. Although, in general, five parameters are necessary for transversely isotropic material, only three parameters are employed to satisfy the condition that $\hat{\sigma}_{ij} = \gamma\sigma_{ij}$ for isotropic materials (Boehler and Sawczuk 1970).

The components of $\hat{\sigma}_{ij}$ is expressed as follows:

$$\begin{aligned}
\hat{\sigma}_{11} &= (\alpha + \gamma - 2\beta)(\hat{M}_{mn}\sigma_{mn})\sin^2\theta + \gamma\sigma_{11} + (\beta - \gamma)(2\sigma_{11}\sin^2\theta - 2\sigma_{12}\sin\theta\cos\theta) \\
\hat{\sigma}_{12} &= (\alpha + \gamma - 2\beta)(\hat{M}_{mn}\sigma_{mn})(-\sin\theta\cos\theta) + \gamma\sigma_{12} + (\beta - \gamma)\{\sigma_{12} - (\sigma_{11} + \sigma_{22})\sin\theta\cos\theta\} \\
\hat{\sigma}_{13} &= \gamma\sigma_{13} + (\beta - \gamma)(\sigma_{13}\sin^2\theta - \sigma_{23}\sin\theta\cos\theta) \\
\hat{\sigma}_{21} &= \hat{\sigma}_{12} \\
\hat{\sigma}_{22} &= (\alpha + \gamma - 2\beta)(\hat{M}_{mn}\sigma_{mn})\cos^2\theta + \gamma\sigma_{22} + (\beta - \gamma)(2\sigma_{22}\cos^2\theta - 2\sigma_{12}\sin\theta\cos\theta) \\
\hat{\sigma}_{23} &= \gamma\sigma_{23} + (\beta - \gamma)(\sigma_{23}\cos^2\theta - \sigma_{13}\sin\theta\cos\theta) \\
\hat{\sigma}_{31} &= \hat{\sigma}_{13} \\
\hat{\sigma}_{32} &= \hat{\sigma}_{23} \\
\hat{\sigma}_{33} &= \gamma\sigma_{33}
\end{aligned} \tag{5.12}$$

in which

$$\hat{M}_{mn}\sigma_{mn} = \sigma_{11}\sin^2\theta + \sigma_{22}\cos^2\theta - 2\sigma_{12}\sin\theta\cos\theta \tag{5.13}$$

Adachi and Oka (1995) proposed a constitutive equation for soft rock with both strain-hardening and strain-softening based on the elasto-plastic constitutive equation

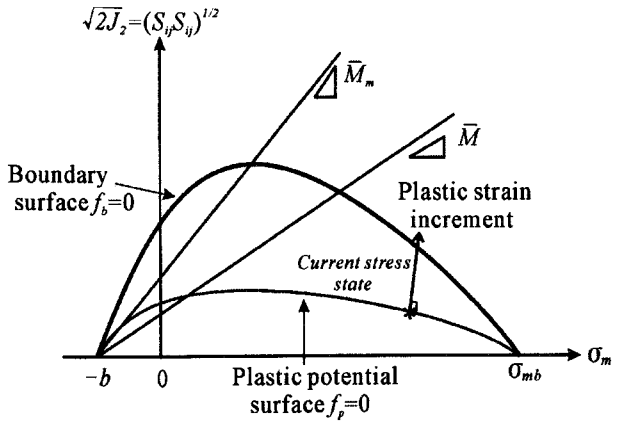

Figure 5.2: Plastic potential and overconsolidation boundary surface

with memory and internal variables. The anisotropic plastic strain increment is given by replacing the stress tensor with the transformed tensor in both the yield function and the plastic potential function. The evolutional equation is introduced for the plastic deformation on the basis of the non-associated flow rule.

$$d\varepsilon_{ij}^{p} = H\frac{\partial f_p}{\partial \hat{\sigma}_{ij}}df_y \tag{5.14}$$

in which f_y is the yield function, f_p is the plastic potential function, and H is the strain hardening - strain softening function.

An overconsolidation boundary surface that defines the boundary between the overconsolidated ($f_b < 0$) and the normally consolidated ($f_b \geq 0$) regions, shown in Fig.5.2, is defined. The boundary surface is expressed as

$$f_b = \hat{\bar{\eta}} + \bar{M}_m \ln\frac{\hat{\sigma}_m + b}{\sigma_{mb} + b} = 0 \tag{5.15}$$

where b and σ_{mb} are the material parameters, and $\hat{\bar{\eta}}$ is the stress ratio invariant given as

$$\hat{\bar{\eta}} = \left(\frac{\hat{S}_{ij}\hat{S}_{ij}}{(\hat{\sigma}_m + b)^2}\right)^{\frac{1}{2}} \tag{5.16}$$

in which $\hat{S}_{ij}$ is a deviatoric component and $\hat{\sigma}_m$ is a spherical component of transformed stress tensor $\hat{\sigma}_{ij}$.

In the proposed model, a stress history tensor which denotes a memory of stress with respect to the strain measure, was introduced. Stress history tensor σ_{ij}^{*} is expressed by an exponential type of kernel function as

$$\sigma_{ij}^{*} = \frac{1}{\tau}\int_0^z \exp\left[-\left(z - z'\right)/\tau\right]\ \left[\sigma_{ij}\left(z'\right) - \sigma_{ij}(0)\right]\ dz' + \sigma_{ij}(0) \tag{5.17}$$

in which $\sigma_{ij}(0)$ is the stress tensor when z is equal to zero. Here, z is a strain measure defined by the second invariant of deviatoric strain increment de_{ij} as

$$dz = (de_{ij}de_{ij})^{\frac{1}{2}} \tag{5.18}$$

Stress history tensor σ^*_{ij} is also transformed to $\hat{\sigma}^*_{ij}$ by Eq.(5.11). The yield function can be written as

$$f_y = \hat{\eta}^* - \kappa = 0 \tag{5.19}$$

where η^* is a stress history ratio invariant given by

$$\hat{\eta}^* = \left(\hat{\eta}^*_{ij}\hat{\eta}^*_{ij}\right)^{\frac{1}{2}} = \left(\frac{\hat{S}^*_{ij}\hat{S}^*_{ij}}{\hat{\sigma}^{*2}_m}\right)^{\frac{1}{2}} \tag{5.20}$$

in which $\hat{S}^*_{ij}$ is a deviatoric component and $\hat{\sigma}^*_m$ is a spherical component of transformed stress history tensor $\hat{\sigma}^*_{ij}$. Strain hardening - softening parameter κ is assumed to increase with the progress of the plastic deviatoric strain invariant as

$$d\kappa = \frac{G'(M^*_f - \kappa)^2}{M^*_f} d\gamma^p \tag{5.21}$$

In the above equation, M^*_f is a value of the stress ratio at the large strain strength state and γ^p is an accumulated plastic strain invariant, namely,

$$\gamma^p = \int d\gamma^p, \quad d\gamma^p = \left(de^p_{ij}de^p_{ij}\right)^{\frac{1}{2}} \tag{5.22}$$

where de^p_{ij} is the plastic deviatoric strain increment tensor.

The following plastic potential function is used.

$$f_p = \hat{\bar{\eta}} + \bar{M} \ln \frac{\hat{\sigma}_m + b}{\sigma_{mb} + b} = 0 \tag{5.23}$$

In the overconsolidated region ($f_b < 0$), $\bar{M}$ is obtained by

$$\bar{M} = -\frac{\hat{\bar{\eta}}}{\ln \frac{\hat{\sigma}_m + b}{\sigma_{mb} + b}} \tag{5.24}$$

After the stress state has reached the normally consolidated region ($f_b \geq 0$),

$$\bar{M} = \bar{M}_m \tag{5.25}$$

is always valid. Here, $\bar{M}_m$ is the value of $\bar{\eta}$ at which maximum compression takes place.

Taking account of the above relations, the plastic strain increment tensor is given as follows:

$$d\varepsilon^p_{ij} = \Lambda \left[\frac{\hat{\bar{\eta}}_{ij}}{\hat{\bar{\eta}}} + \left(\bar{M} - \hat{\bar{\eta}}\right)\frac{\delta_{ij}}{3}\right]\left[\frac{\hat{\eta}^*_{kl}}{\hat{\eta}^*} - \hat{\eta}^*\frac{\delta_{kl}}{3}\right]\frac{d\hat{\sigma}^*_{kl}}{\hat{\sigma}^*_m}, \quad \Lambda = \frac{M^{*2}_f}{G'\left(M^*_f - \hat{\eta}^*\right)^2} \tag{5.26}$$

5.3 Application to Soft Sedimentary Rock

In order to discuss the performance of the proposed model, we apply the model to soft sedimentary rock, called Tomuro stone. Firstly, we present the experimental results of drained triaxial compression tests on variously oriented samples, performed by Kobayashi (2000), Oka et al. (2002), and Adachi et al. (2002). Secondary, numerical simulations using the proposed model are presented, and finally, we compare the experimental results with numerical simulations.

5.3.1 Drained Triaxial Compression Tests of Tomuro Stone

Tomuro stone is a tuffaceous soft rock and a kind of Ohya stone which is produced in the Tomuro district of Ohya Town in Tochigi Prefecture located in north eastern part of Japan. In Ohya Town, tuffaceous soft rock layers of volcanic origin, called green tuff, exist. The sedimentation of these layers occurred 20 million years ago in the sea. The layers are inclined at 8-9 degrees with respect to the horizontal plane. Tomuro stone has fewer black or dark brown spots that contain montmorillonite and zeolite, etc. (Sudo and Shimada 1978). A block sample was vertically sampled from the Tomuro district; it is assumed that the plane of sedimentation mostly coincides with the horizontal plane in this location. As shown in Fig.5.3, the plane normal to vertical axis Y is called the sedimentation plane in the following. The specimens for the triaxial tests were cut in several directions from the block sample. Angle θ is defined as an angle between normal to sedimentation plane and the symmetrical axis of cylindrical specimen.

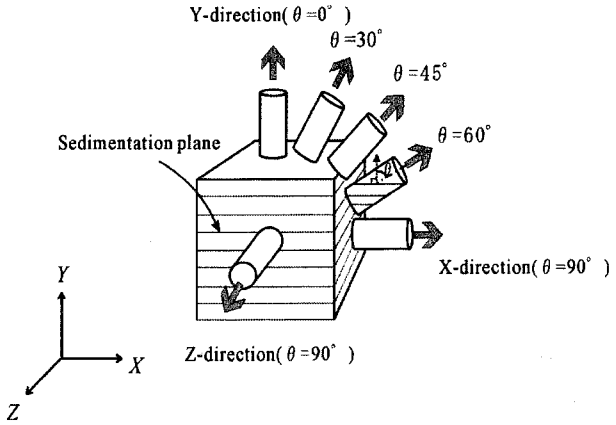

Figure 5.3: Sampling directions

The results obtained from drained triaxial compression tests are summarized as follows.

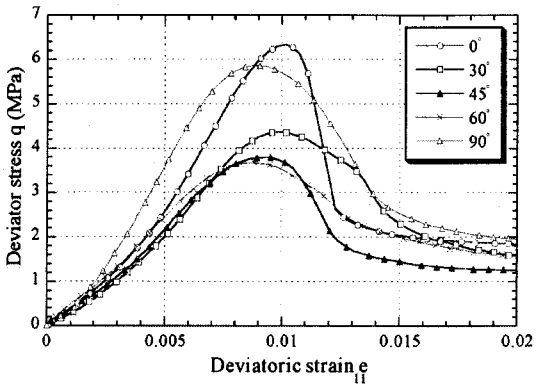

(a) Stress-strain relations

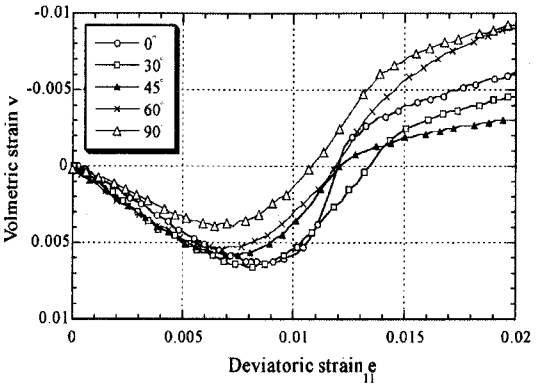

(b) Volumetric strain - deviatoric strain relations

Figure 5.4: Experimental results (Kobayashi 2000)

Relationships between deviator stress $q(=\sigma_1 - \sigma_3)$ and deviatoric strain e_{11} for confining pressure of 0.19 kPa are shown in Fig.5.4(a). Typical strain-softening behavior is observed, in other words, the stress increases at an early stage of shearing, reaches a peak stress, and then decreases and approaches a residual strength. The peak strength changes with angle θ and the minimum value is found to be around θ=60° in all cases. In addition to peak strength, the initial rigidity also changes with angle θ.

Fig.5.4(b) shows the relationships between volumetric strain v and deviatoric strain e_{11}. the volumetric strain is compressive at the early stage of shearing, thereafter, it starts to expand before reaching the peak strength. Dilatancy characteristics also depend on the angle of θ, and volumetric compression at the early stage of shearing decreases when angle θ becomes larger. The volumetric expansion at a large level of strain differs from θ=0° to θ=90° , and the minimum amount of volumetric expansion occurs around θ=45 ° , as seen in Fig.5.4(b).

5.3.2 Simulation of Drained Triaxial Tests

Four different models, namely, (I) an isotropically elastic - plastic model which is a perfectly isotropic model, (II) an anisotropically elastic - isotropically plastic model in which the anisotropy of the elastic strain is considered, (III) an isotropically elastic - anisotropically plastic model in which the anisotropy of the plastic strain is considered, and (IV) an anisotropically elastic - plastic model in which the anisotropy of both the

elastic strain and the plastic strain are considered, are used in the simulation of drained triaxial compression tests.

Constant strain rate drained triaxial compression tests under a confining pressure of 0.19 MPa are simulated using each constitutive model. The material parameters used in the analyses were determined from the vertical cut specimen (θ=0 $^\circ$); they are given in Table 5.1. The elastic anisotropic parameters are determined from drained triaxial compression tests in different direction and listed in Table 5.2. The plastic anisotropic parameters α, β, and γ were determined from the relations between peak strength and the angle of sampling direction as listed in Table 5.3.

Table 5.1: Material parameters for soft rock

Strain softening-hardening parameter G'	6000.0
Strain softening-hardening parameter M_f^*	1.90
Plastic potential parameter b (MPa)	1.96
Overconsolidation surface parameter $\bar{M}_m$	0.50
Overconsolidation surface parameter σ_{mb} (MPa)	8.82
Stress history parameter τ	0.017

Table 5.2: Anisotropic elastic parameters

E_y (MPa)	900
E_x (MPa)	1020
ν_{yx}	0.0613
ν_{xz}	0.267
G_{yx} (MPa)	190

Table 5.3: Anisotropic plastic parameters

α	0.90
β	1.05
γ	1.0

(1)Analysis I (Isotropically elastic - plastic model)

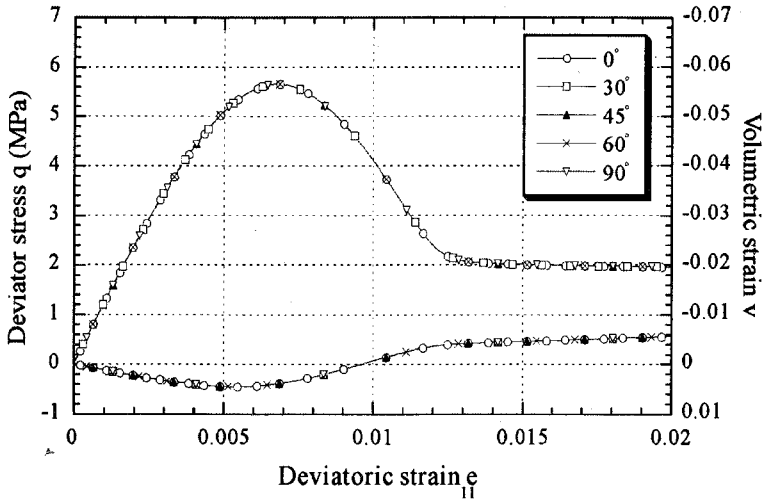

Figure 5.5: Analysis I (Isotropically elastic - plastic model)

The calculated results of the deviator stress q - deviatoric strain e_{11} relations and the volumetric strain v - deviatoric strain e_{11} relations are shown in Fig.5.5. Naturally the isotropic model cannot describe the angle θ-dependent material properties, although it can describe the experimental results of the vertical specimen ($\theta = 0^\circ$) well.

(2)Analysis II (Anisotropically elastic - isotropically plastic model)

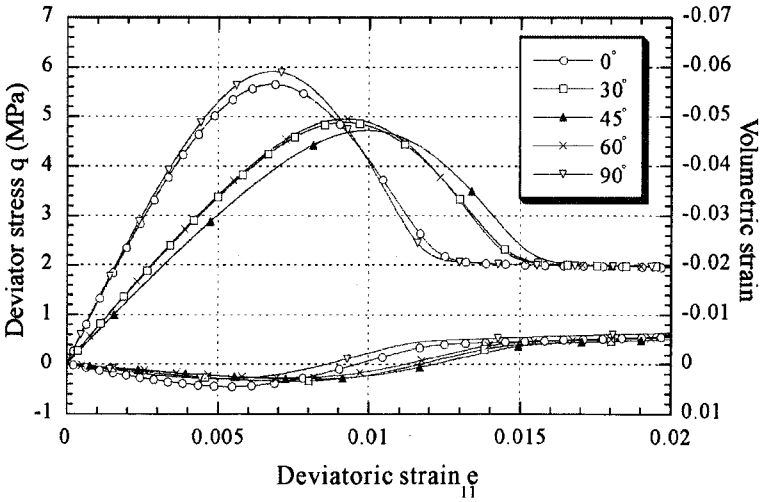

Figure 5.6: Analysis II (Anisotropically elastic - isotropically plastic model)

The relations between deviator stress q and deviatoric strain e_{11} as well as volumetric strain v and deviatoric strain e_{11} are shown in Fig.5.6. The anisotropic elastic parameters

are listed in Table 5.2. The model can simulate the experimental findings that the initial rigidity as well as the peak strength changes with angle θ, defined as the angle between the sedimentation plane and the direction of the major principal effective stress, and that they take their minimum values around θ=45 ° . It can more or less describe the stress-strain relationship and dilatancy behavior at the early stage of shearing. However, it cannot express the behavior during the softening process up to the residual strength, nor can it describe the anisotropy of the residual strength.

(3)Analysis Ⅲ (Isotropically elastic - anisotropically plastic model)

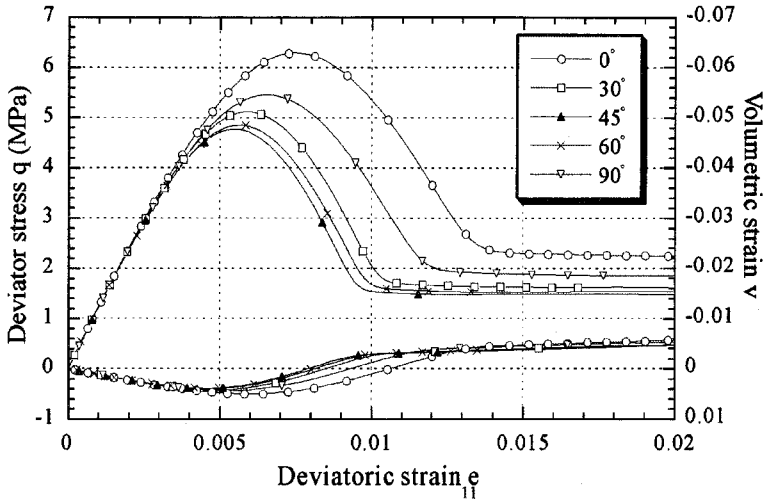

Figure 5.7: Analysis Ⅲ (Isotropically elastic - anisotropically plastic model)

The relations between deviator stress q and deviatoric strain e_{11} as well as volumetric strain v and deviatoric strain e_{11} are shown in Fig.5.7. The elastic parameters are Young's modulus E=900 MPa and Poisson's ratio ν=0.0613. The anisotropic plastic parameters are listed in Table 5.3. The model can simulate the angle θ dependency of the stress-strain relations as well as the dilatancy characteristics; it also can express changes in both peak and residual strengths according to the changes in angle θ. However, it cannot describe the angle θ dependency of the initial rigidity.

(4)Analysis Ⅳ (Anisotropically elastic - plastic model)

Fig.5.8 displays the relations between deviator stress q and deviatoric strain e_{11} as well as volumetric strain v and deviatoric strain e_{11}. The anisotropic elastic parameters and the anisotropic plastic parameters are the same as those used in Analyses Ⅱ and Ⅲ. Variations in initial rigidity, peak strength, residual strength, and dilatancy characteristics with respect to angle θ, are simulated well in Fig.5.8. The model can accurately describe

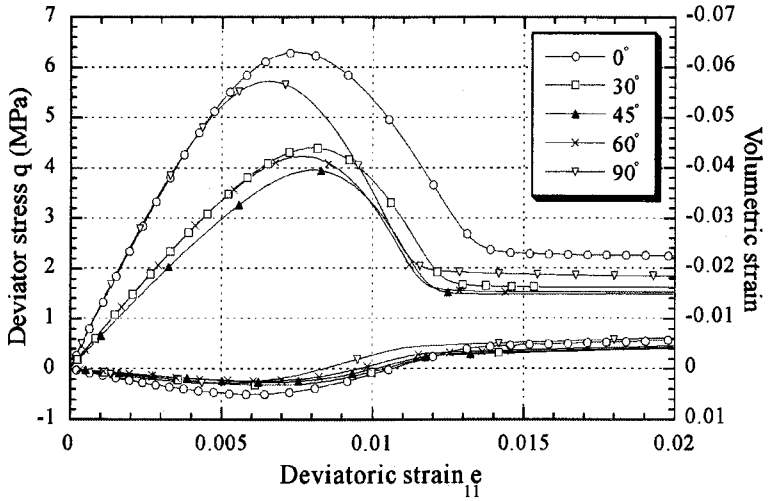

Figure 5.8: Analysis IV (Anisotropically elastic - plastic model)

the experimental results, except for that it underestimates the amount of volumetric strain during the residual stage.

5.3.3 Comparisons and Evaluation of the Four Models

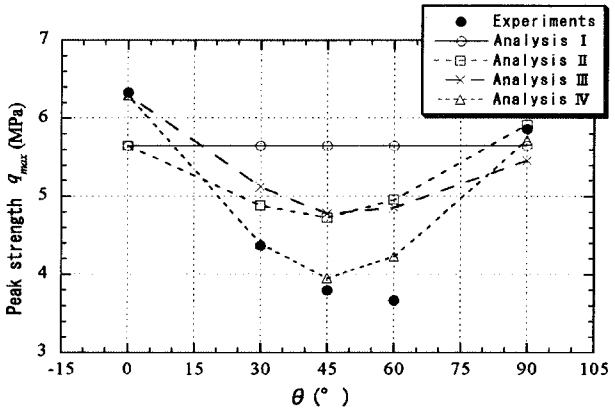

Figure 5.9: Change in peak strength with respect to angle θ

In order to find the most appropriate constitutive model, the analytical and the experimental results are compared with respect to peak strength q_{max}, residual strength q_{res}, maximum volumetric strain v_{max}, and Young's modulus E.

The relationships between peak strength q_{max} and angle θ are shown in Fig.5.9. From the comparison, it is obvious that Analysis IV is superior in regard to explaining the experimental results. Analyses II and III overestimate the peak and the residual strengths, and they show that the strengths take their minimum values at $\theta = 45^\circ$ while the

experimental results take their minimum values at $\theta = 60^\circ$.

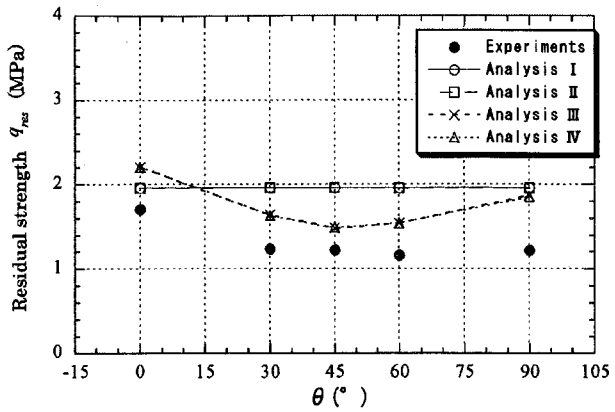

Figure 5.10: Change in residual strength with respect to angle θ

Fig.5.10 shows the relations between residual strength q_{res} and angle θ. In cases of anisotropic plasticity, namely, Analyses III and IV, the residual strength takes its minimum value at around $\theta = 45^\circ$. On the other hand, if anisotropic plasticity is not taken into account, such as with Analyses I and II, the residual strength has a constant value.

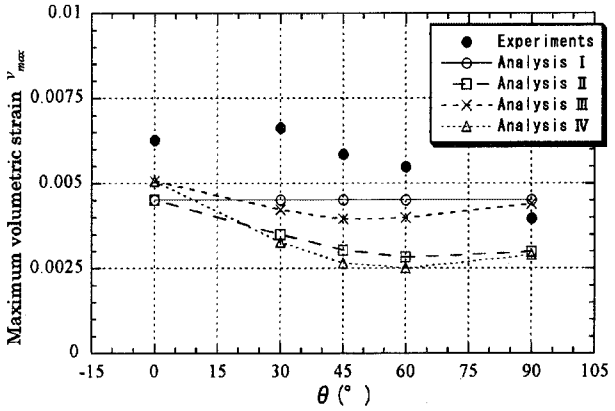

Figure 5.11: Change in maximum volumetric strain with respect to angle θ

Fig.5.11 shows the relations between maximum volumetric strain v_{max} and angle θ. All the analyses underestimate the amount of maximum volumetric strain v_{max}. Analyses II and IV quantitatively explain the decrease in v_{max} with an increase in θ.

Fig.5.12 illustrates the relations of Young's modulus E and angle θ. In cases where anisotropic elasticity is introduced, namely, Analyses II and IV, the elastic aspect of the

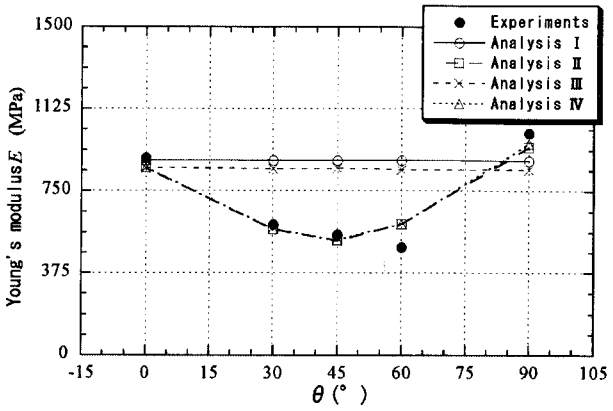

Figure 5.12: Change in Young's modulus with respect to angle θ

experimental results can be well explained.

From the above discussions, it can be concluded that Analysis IV is superior in regard to explaining the experimental findings, and that the anisotropic elasticity describes anisotropic deformation up to the peak strength, while anisotropic plasticity mainly controls the behavior after peak to residual strength.

5.4 Summary

An elasto-plastic constitutive model for soft rock has been extended to an anisotropic model based on the transformed stress concept. The proposed model was then applied to the anisotropic behavior of soft rock, and a comparison was made between the analytical results of the isotropic model and those of the anisotropic model. An extended elasto-plastic model in which anisotropy is considered in both elastic and plastic deformations can reproduce transversely anisotropic characteristics, namely, the angle θ dependency on soft rock obtained by the triaxial tests, except for that it underestimates the amount of volumetric strain during the residual stage.

Chapter 6

EFFECT OF INITIAL STRUCTURAL ANISOTROPY OF CLAY ON STRAIN LOCALIZATION

6.1 Introduction

Studies on the anisotropy of natural clays have shown that they exhibit anisotropic stress-strain and strength behavior, but the anisotropy varies for different soils. Mitchell (1972) conducted triaxial tests on one-dimensionally consolidated clay which is sampled horizontally and vertically, and found that the strength is about 10% greater for the vertical specimen than for the horizontal one. Kirkgard and Lade (1991) performed undrained triaxial tests on intact specimens of San Francisco Bay mud clay trimmed in horizontal and vertical directions, and showed that the undrained shear strength is greater for the horizontal specimens at a higher confining pressure. Dunkan (1966) has summarized the data of the variation of compressive strength with orientation of the sample, and showed that the relationship between strength and the sampling direction was different for each clay. Furthermore, Adachi et al. (1991) conducted triaxial tests on Eastern Osaka clay sampled at different angles of 0°, 30°, 60°, and 90° from the sedimentation plane. They observed that the maximum strength is obtained with the 0° angle, and the minimum strength is obtained with the 60° or the 90° angle (see Fig.6.1).

In this chapter, the effect of the anisotropy on strain localization is studied. Undrained

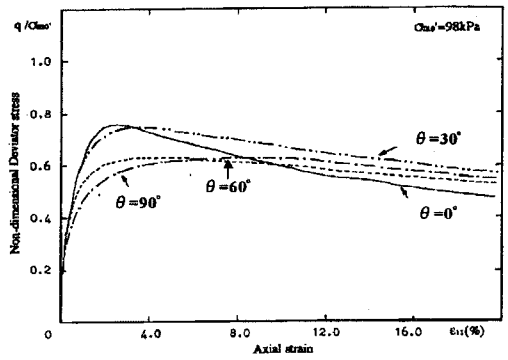

(a) Stress-strain relations

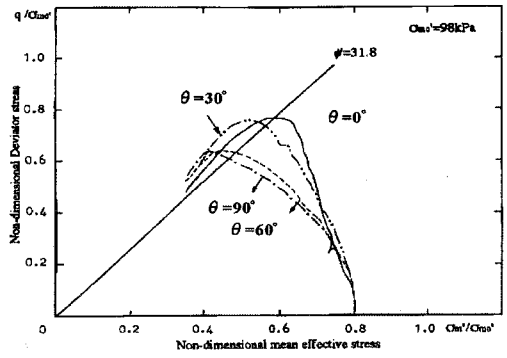

(b) Stress paths

Figure 6.1: Experimental results of Eastern Osaka clay sampled in different directions (Adachi et al. 1991)

compression tests for a specimen with different angles of the sedimentation plane are simulated using the elasto-viscoplastic constitutive model which is extended to describe the anisotropy of the viscoplastic strain. Simulations are conducted under plane strain conditions with displacement control. The way to express anisotropy in the constitutive model is similar to that of the elasto-plastic model for soft rock proposed in Chapter 5; the transformation stress concept by Boehler and Sawczuk (1977) is used for viscoplastic strain. We evaluate the effect of anisotropy on strain localization as well as the stress-strain relation and the stress path. Since the shape of shear bands strongly depend on the anisotropic viscoplastic parameters, parametric studies on the anisotropic parameters are conducted.

6.2 Anisotropy of Viscoplastic Strain

It should be noted that the anisotropy of the viscoplastic strain is considered, and the anisotropy of the elastic strain is disregarded in this chapter in order to evaluate the effect of the viscoplastic anisotropy on shear localization.

Based on Boehler's theory, stress tensor σ_{ij} is replaced by transformed stress tensor $\hat{\sigma}_{ij}$. The transformed stress tensor is given in the previous chapter as

$$\hat{\sigma}_{ij} = (\alpha + \gamma - 2\beta)(\hat{M}_{mn}\sigma_{mn})\hat{M}_{ij} + \gamma\sigma_{ij} + (\beta - \gamma)(\hat{M}_{ik}\sigma_{kj} + \sigma_{ik}\hat{M}_{kj}) \qquad (6.1)$$

in which $\hat{M}_{ij}$ is the structural tensor which describes the direction of the symmetrical axis for the transversely isotropic body, and which is defined as a tensor product of the unit

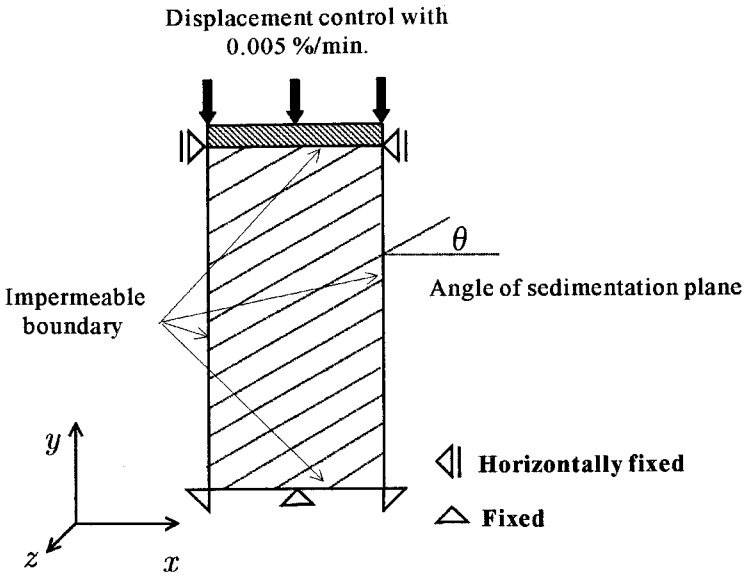

Figure 6.2: Definition of angle θ and boundary conditions

vector which is normal to the sedimentation plane. α, β, and γ are three independent plastic anisotropic parameters.

In the analysis under plane strain conditions, stress components σ_{xx}, σ_{xy}, σ_{yy}, and σ_{zz} are used. Hence, the components of the transformed stress tensor $\hat{\sigma}_{xx}$, $\hat{\sigma}_{xy}$, $\hat{\sigma}_{yy}$, and $\hat{\sigma}_{zz}$, are considered here as follows:

$$\begin{aligned}
\hat{\sigma}_{xx} &= (\alpha+\gamma-2\beta)(\hat{M}_{mn}\sigma_{mn})\sin^2\theta+\gamma\sigma_{xx}+(\beta-\gamma)(2\sigma_{xx}\sin^2\theta-2\sigma_{xy}\sin\theta\cos\theta)\\
\hat{\sigma}_{xy} &= (\alpha+\gamma-2\beta)(\hat{M}_{mn}\sigma_{mn})(-\sin\theta\cos\theta)+\gamma\sigma_{xy}+(\beta-\gamma)\{\sigma_{xy}-(\sigma_{xx}+\sigma_{yy})\sin\theta\cos\theta\}\\
\hat{\sigma}_{yy} &= (\alpha+\gamma-2\beta)(\hat{M}_{mn}\sigma_{mn})\cos^2\theta+\gamma\sigma_{yy}+(\beta-\gamma)(2\sigma_{yy}\cos^2\theta-2\sigma_{xy}\sin\theta\cos\theta)\\
\hat{\sigma}_{zz} &= \gamma\sigma_{zz}
\end{aligned} \tag{6.2}$$

in which

$$\hat{M}_{mn}\sigma_{mn}=\sigma_{xx}\sin^2\theta+\sigma_{yy}\cos^2\theta-2\sigma_{xy}\sin\theta\cos\theta \tag{6.3}$$

Angle θ is determined as the angle between the normal to the sedimentation plane and the $y-$direction in the $x-y$ plane, in other words, the angle of inclination of the sedimentation plane from the horizontal plane, namely, the $x-z$ plane, as shown in Fig.6.2.

The finite element formulation for the strain localization analysis was already presented in Chapter 3. Numerical simulations of undrained compression tests under plane

strain conditions with displacement control were conducted, using the elasto-viscoplastic constitutive model considering both structural changes and viscoplastic anisotropy. It should be noticed that structural changes are considered, in other words, structural parameter β_s, which is represented as β in Chapter 2, is set to be 20 in all the calculations, in order to obtain the apparent shear localization. Structural changes do not of course effect the anisotropic behavior. Stress components are replaced by the transformed stress components to obtain the viscoplastic strain, namely, the overconsolidation boundary surface, the static yield function, and the plastic potential surface are expressed by the transformed stress in the elasto-viscoplastic constitutive equation.

The finite element mesh and the boundary surface are the same as those used in the simulations of undrained compression tests in Chapter 3 as shown in Fig.6.2. The specimen is 10 cm in height and 5 cm in width with two hundred elements. The constant axial displacement is set to be 0.005%/min. Simulations are performed for NC clay at different angles of the sedimentation plane, namely, θ=0 $^\circ$, 30 $^\circ$, 60 $^\circ$, and 90 $^\circ$. The material parameters are shown in Table 6.1.

Table 6.1: Material parameters used in the analysis

Parameters	**NC**
Coefficient of permeability $k_0(m/s)$	0.8 $\times 10^{-9}$
Elastic shear modulus G_0(kPa)	36100
Compression index λ	0.508
Swelling index κ	0.0261
Initial void ratio e_0	1.70
Compression yield stress σ'_{mbi} (kPa)	580
Stress ratio at maximum compression M^*_m	1.09
Viscoplastic parameter m'	18.5
Viscoplastic parameter C_0 (1/s)	1.3 $\times 10^{-13}$
Structural parameter σ'_{maf} (kPa)	300
Structural parameter β_s	20

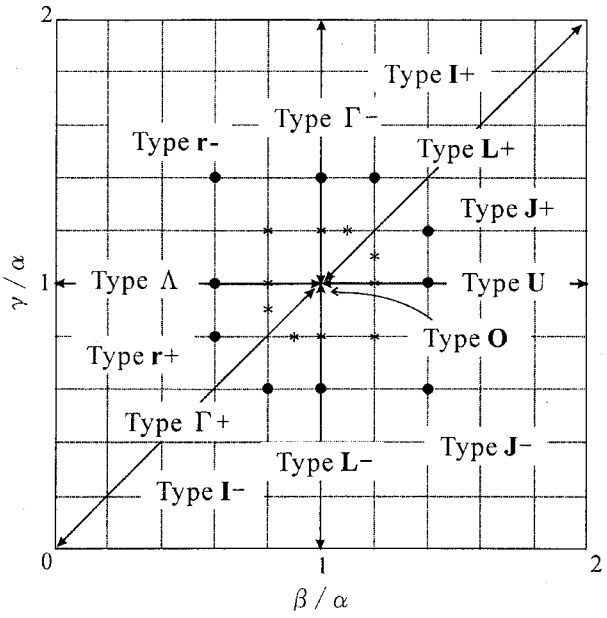

Figure 6.3: Classification of anisotropic parameters of α, β, and γ

6.3 Anisotropic Parameters α, β, and γ

In a previous study, the effect of anisotropic parameters α, β, and γ on the peak strength in the elasto-plastic model was evaluated in simulations of triaxial compression tests. We have confirmed that the effect of the anisotropic parameters on the peak strength are the same for both the elasto-plastic model and the elasto-viscoplastic model.

From the relationship between the peak strength and angle θ, sets of parameters α, β, and γ can be classified into thirteen groups, namely, Type **I**+, Type **L**+, Type **J**+, Type **U**, Type **J**-, Type **L**-, Type **I**-, Type Γ+, Type **r**+, Type Λ, Type **r**-, Type Γ-, and Type **O**, as shown in Fig.6.3. Changes in peak strength with respect to angle θ for each type are illustrated in Fig.6.4. The effect on the strength depends on the ratio of the anisotropic parameters. For Types Γ-, **I**+, **L**+, and **J**+, the peak strength reaches the maximum value when angle θ=0 ° . For Types **J**-, **L**-, **I**-, and Γ+, the peak strength yields the maximum value when angle θ=90 ° . For Type **U**, the maximum values for the peak strength are reached at angles of θ=0 ° and 90 ° . For Type Λ, the minimum value for the peak strength are obtained at angles of θ=0 ° and 90 ° . Type **O** gives the isotropic model, in which the transformed stress tensor coincides with the stress tensor.

Based on this study, we conducted numerical analyses on ten sets of anisotropic pa-

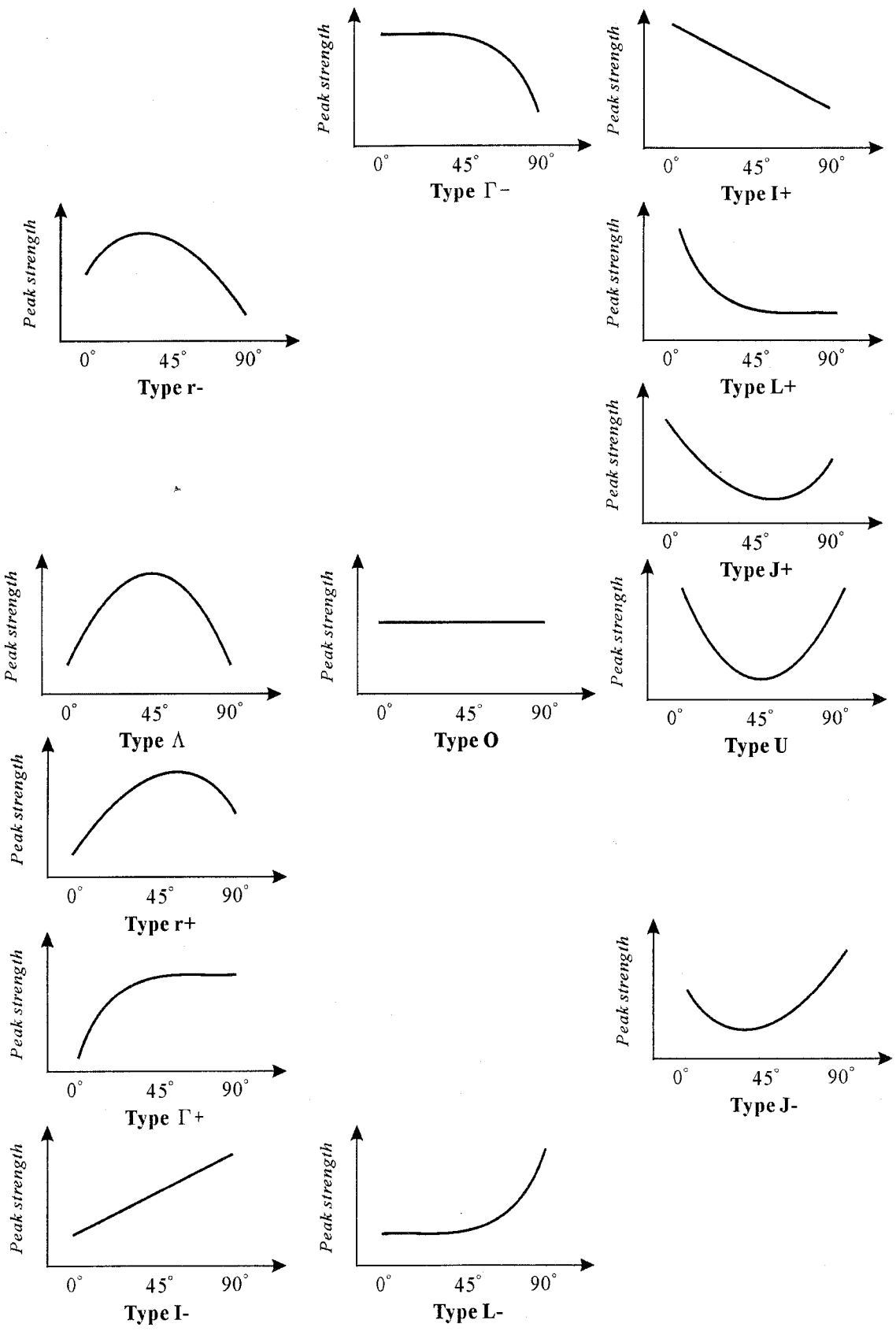

Figure 6.4: Changes in peak strength with angle θ for each type

rameters which are denoted by • in Fig.6.3 for sedimentation angles of θ=0 ° , 30 ° , 60 ° , and 90 ° . The values are listed in Table 6.2. Parameter α is set at 1.0 in all analyses.

Table 6.2: Sets of anisotropic parameters used in the analysis

Type	**I+**	**J+**	**U**	**J-**	**L-**	**I-**	**r+**	**Λ**	**r-**	**Γ-**	**O**
β	1.2	1.4	1.4	1.4	1.0	0.8	0.6	0.6	0.6	1.0	1.0
γ	1.4	1.2	1.0	0.6	0.6	0.6	0.8	1.0	1.4	1.4	1.0

Let us see the simulation results for each type of angle θ=0 ° . Figs.6.5(a) and (b) show the distribution of viscoplastic deviatoric strain at axial strains of 0.6%, 1.0%, 2.0% and 5.0%, and deformed meshes at an axial strain of 5.0% for the specimen of angle θ=0 ° . Shear bands are formed symmetrically in all the simulations. The angles of the shear bands are obtained from the distribution of viscoplastic deviatoric strain at an axial strain of 5.0% as shown in Fig.6.6. The angles of the shear bands are slightly different for each type, and a minimum value of 41 ° is obtained for Type **J-**.

Figs.6.7(a) and (b) show the distribution of the viscoplastic deviatoric strain with axial strain and deformed meshes for the specimen with an angle θ=30 ° . The shear localization strongly depends on the anisotropic parameters. For Types **r+**, Λ, and **r-**, the shear localization occurs at the edge of the specimen, and an apparent band is formed. Fig.6.8 compares the angle of shear bands determined from the distribution of viscoplastic deviatoric strain at an axial strain of 5.0%. A shear band forms in the direction across the sedimentation plane for Types Γ-, **I+**, **J+**, and **U**, while it forms in the direction along the sedimentation plane in other cases. The angles of shear bands decrease from Type **I+** to **J+** to **U** and to **J-**. Next, they increase from Type **J-** to **L-** to **I-** and to **r+**. Then, they decrease again to Type Γ-. The maximum value of a shear band is obtained at 57 ° for Type **r+**, and the minimum value is obtained for Type **J-**.

Figs.6.9(a) and (b) show the distribution of viscoplastic deviatoric strain with axial strain and deformed meshes for the specimen with an angle θ=60 ° . Fig.6.10 compares the angles of the shear bands. Apparent shear bands form in Types **J-**, **L-**, **I-**, Λ, and **r-**. The angles of the shear bands increase from Type **J+** to **U** and to **J-**. Next, they decrease to **L-** to **I-** and to **r+**. Then, that increase again to Type **r-**. This tendency is opposite to that of the 30 ° angle. A maximum value of 58 ° is obtained for Type **r-**, while a minimum value of 39 ° is obtained for Type **J+**.

Figs.6.11(a) and (b) show the distribution of viscoplastic deviatoric strain with axial strain and deformed meshes for the specimen with an angle θ=90°. The shear localization forms symmetrically in all cases. The geometry of the shear bands at an axial strain of 5.0% is compared in Fig.6.12. For Types **J-**, **L-**, and **I-**, two shear bands are formed, while in the other cases, four bands are formed. A minimum value of 38° is obtained for Type **r+**.

For comparison, simulations with other sets of anisotropic parameters are performed in the case of an angle θ=30°. Parameters are denoted with $*$ in Fig.6.3 and are listed in Table 6.3. The distribution of the viscoplastic deviatoric strain with axial strain and

Table 6.3: Sets of anisotropic parameters used in the analysis

Type	**I+**	**J+**	**U**	**J-**	**L-**	**I-**	**r+**	Λ	**r-**	Γ-
β	1.1	1.2	1.2	1.2	1.0	0.9	0.8	0.8	0.8	1.0
γ	1.2	1.1	1.0	0.8	0.8	0.8	0.9	1.0	1.2	1.2

deformed meshes are shown in Figs.6.13(a) and (b), and the angles of the shear bands are demonstrated in Fig.6.14. Let us compare Fig.6.14 and Fig.6.8 which shows the previous results. Although the obtained angles of the shear bands are larger for all types in Fig.6.14, similar tendencies can be seen except for Types **r+**, Λ, and **r-**. The largely different values between β and γ provide the large values for the angles of the shear bands, and an apparent shear band is formed when an angle is large enough.

Next, let us see the obtained results from another respect. Fig.6.15$\sim$6.25 demonstrate the stress-strain relations and the stress paths with the distribution of viscoplastic deviatoric strain for each type. These figures are for comparing the results of different angle θ values. The distribution of the viscoplastic volumetric strain, mean effective stress, and the pore water pressure are shown for Type **J-** in Fig.6.17.

We start with the results of Type **O**, an isotropic model. This calculation has already been performed in Chapter 3 in the simulation of undrained compression tests for structured soil. The results for angles of θ=0°, 45°, 60°, 90° are naturally the same, as shown in Fig.6.15. Let us see the case of Type **I+** shown in Fig.6.16. From the previous work (Adachi et al. 1991, see Fig.6.1), Eastern Osaka clay is classified in this type from

the changes in peak strength with angle θ. In this type, the peak strength obtains the maximum value at θ=0 $^\circ$ and the minimum value at θ=90 $^\circ$.

The characteristics of Tomuro Stone can be classified into Type **J+** from the experimental results presented in the previous chapter. The maximum value for the peak strength is obtained at θ=0 $^\circ$, and the minimum value is obtained at θ=60 $^\circ$. Shear localization occurs across the sedimentation plane in the simulation for angle θ=30 $^\circ$, as shown in Fig.6.17. It should be noted that the simulation is conducted under plane strain conditions, while the experiments were performed under triaxial stress state. Hence, simulations should not be simply compared with experimental results.

In the case of Types **U** and Λ, shown in Figs.6.18 and 6.23, the stress-strain relations and the stress paths coincide between 0 $^\circ$ and 90 $^\circ$, and 30 $^\circ$ and 60 $^\circ$, respectively. Shear bands form symmetrically in the case of 30 $^\circ$ and 60 $^\circ$. For Types **J-**, **L-**, and **I-**, the strength of angle θ=90 $^\circ$ is much larger than that for other angles.

When an apparent shear band is formed, namely, angle θ=60 $^\circ$ for Type **J-** (see Fig.6.19), angle θ=60 $^\circ$ for Type **L-** (see Fig.6.20), angle θ=30 $^\circ$ for Type **r+** (see Fig.6.22), angle θ=30 $^\circ$ and 60 $^\circ$ for Type Λ (see Fig.6.23), and angle θ=30 $^\circ$ and 60 $^\circ$ for Type **r-** (see Fig.6.24), a sudden decrease in the average vertical stress is observed in the average stress-strain relation.

From Fig.6.19, we confirm that the distribution of mean effective stress and the pore water pressure also show anisotropy. The difference of the pore water pressure in the specimen is, however, less than 1.0 kPa.

6.4 Summary

In this chapter, the effect of anisotropy on the strain localization was evaluated. The characteristics of shear localization strongly depend on the angles of the sedimentation plane. Shear bands form symmetrically in the case of the isotopic model, while they form asymmetrically in the case of the anisotropic model, except for angles of θ=0 $^\circ$ and 90 $^\circ$. The form of the shear bands depend on the set of anisotropic parameters, namely, α, β, and γ, and there is a tendency for each type classified by the relationship between the peak strength and angle θ. Concerning the average stress-strain relation, the average

vertical stress decreases suddenly after the peak stress when an apparent shear band is formed.

In future studies, further investigation into the development of shear bands in anisotropic structural clay are necessary.

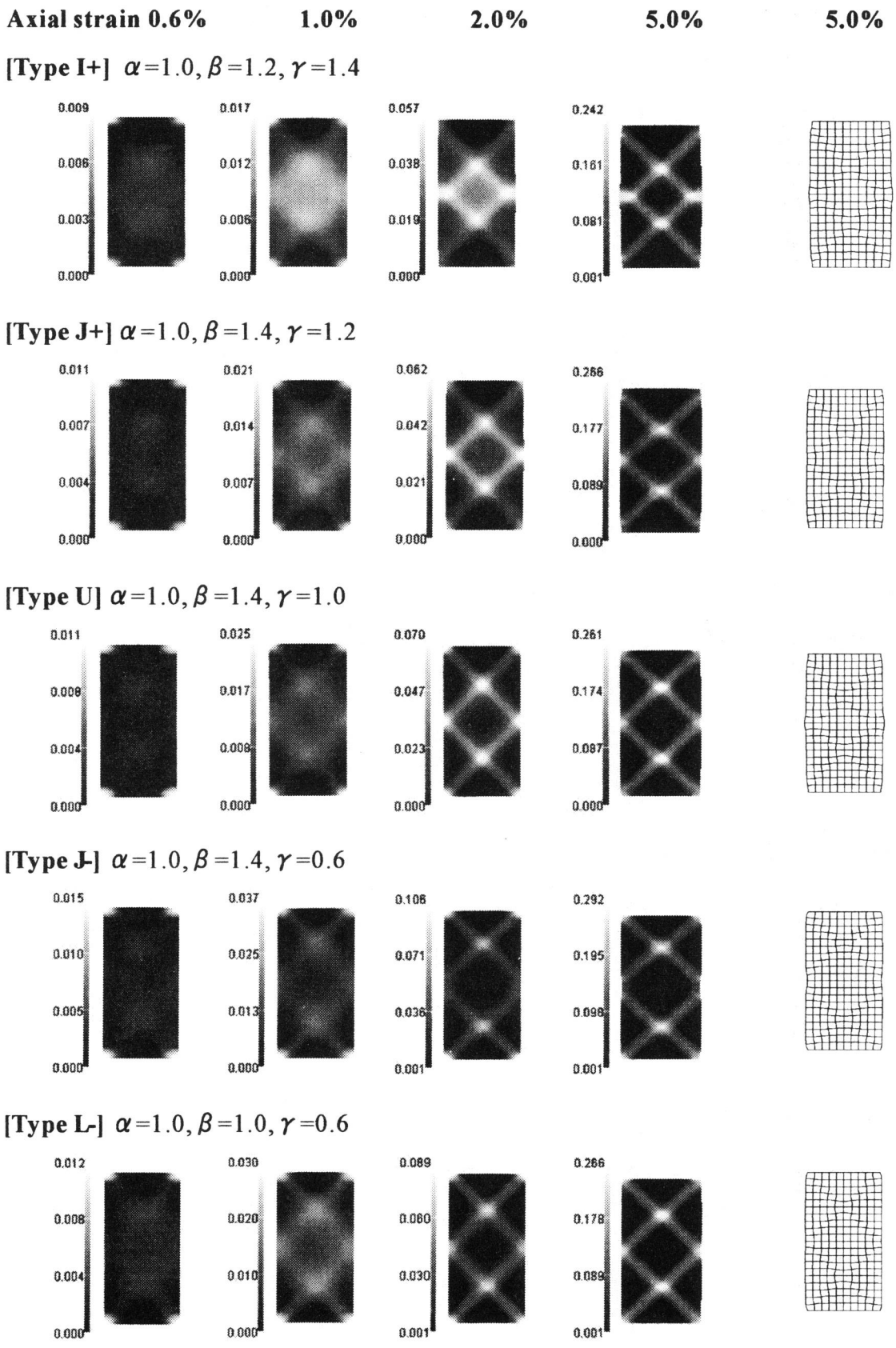

Figure 6.5: (a)Distribution of viscoplastic deviatoric strain and deformed meshes (θ =0°)

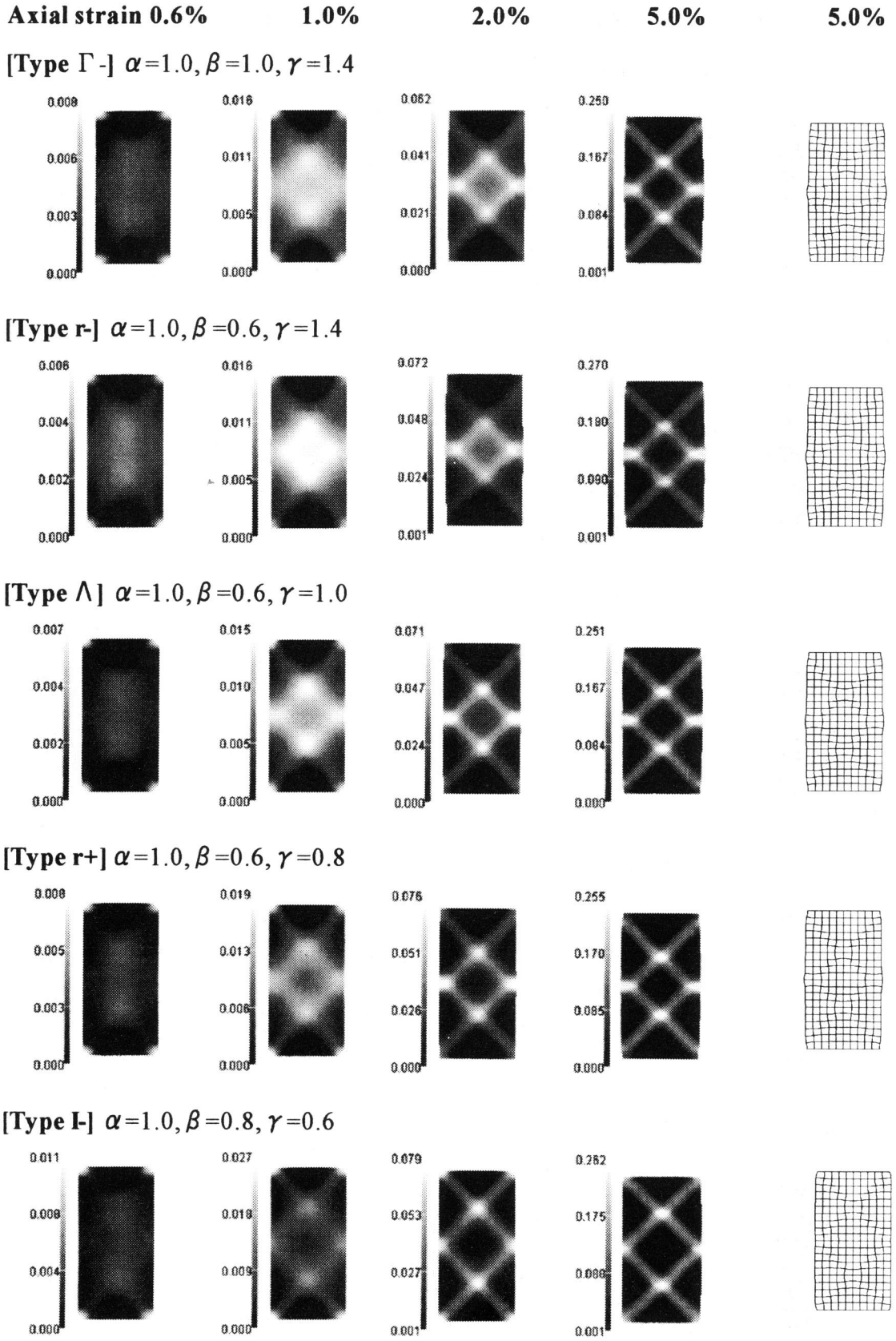

Figure 6.5: (b)Distribution of viscoplastic deviatoric strain and deformed meshes (θ =0°)

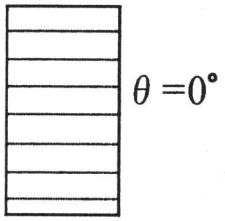

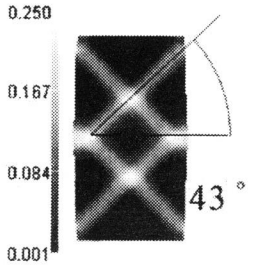

[Type Γ-] α=1.0, β=1.0, γ=1.4

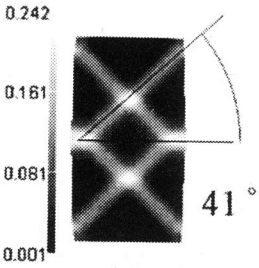

[Type I+] α=1.0, β=1.2, γ=1.4

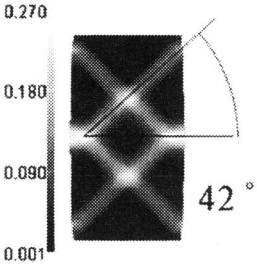

[Type r-] α=1.0, β=0.6, γ=1.4

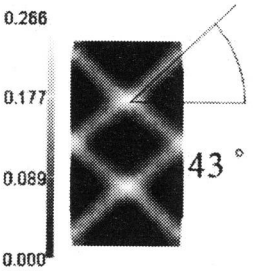

[Type J+] α=1.0, β=1.4, γ=1.2

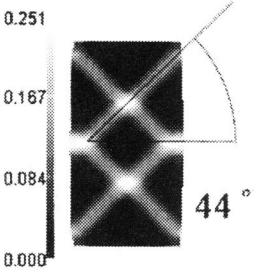

[Type Λ] α=1.0, β=0.6, γ=1.0

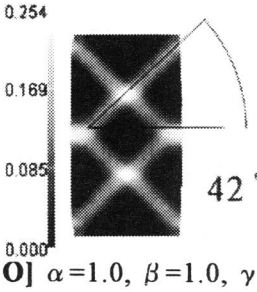

[Type O] α=1.0, β=1.0, γ=1.0

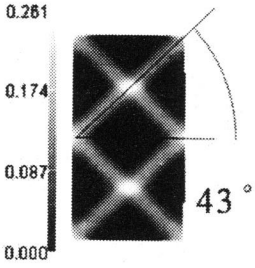

[Type U] α=1.0, β=1.4, γ=1.0

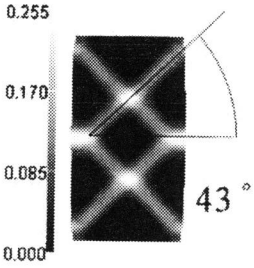

[Type r+] α=1.0, β=0.6, γ=0.8

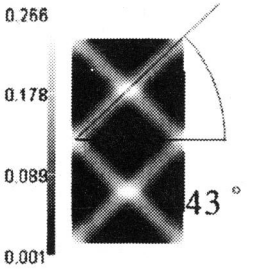

[Type L-] α=1.0, β=1.0, γ=0.6

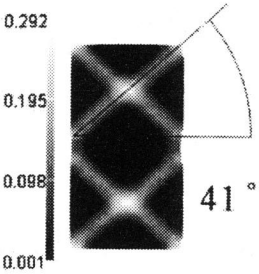

[Type J-] α=1.0, β=1.4, γ=0.6

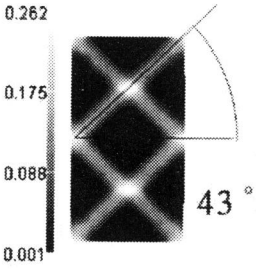

[Type I-] α=1.0, β=0.8, γ=0.6

Figure 6.6: Angles of shear bands for specimen (θ=0 °)

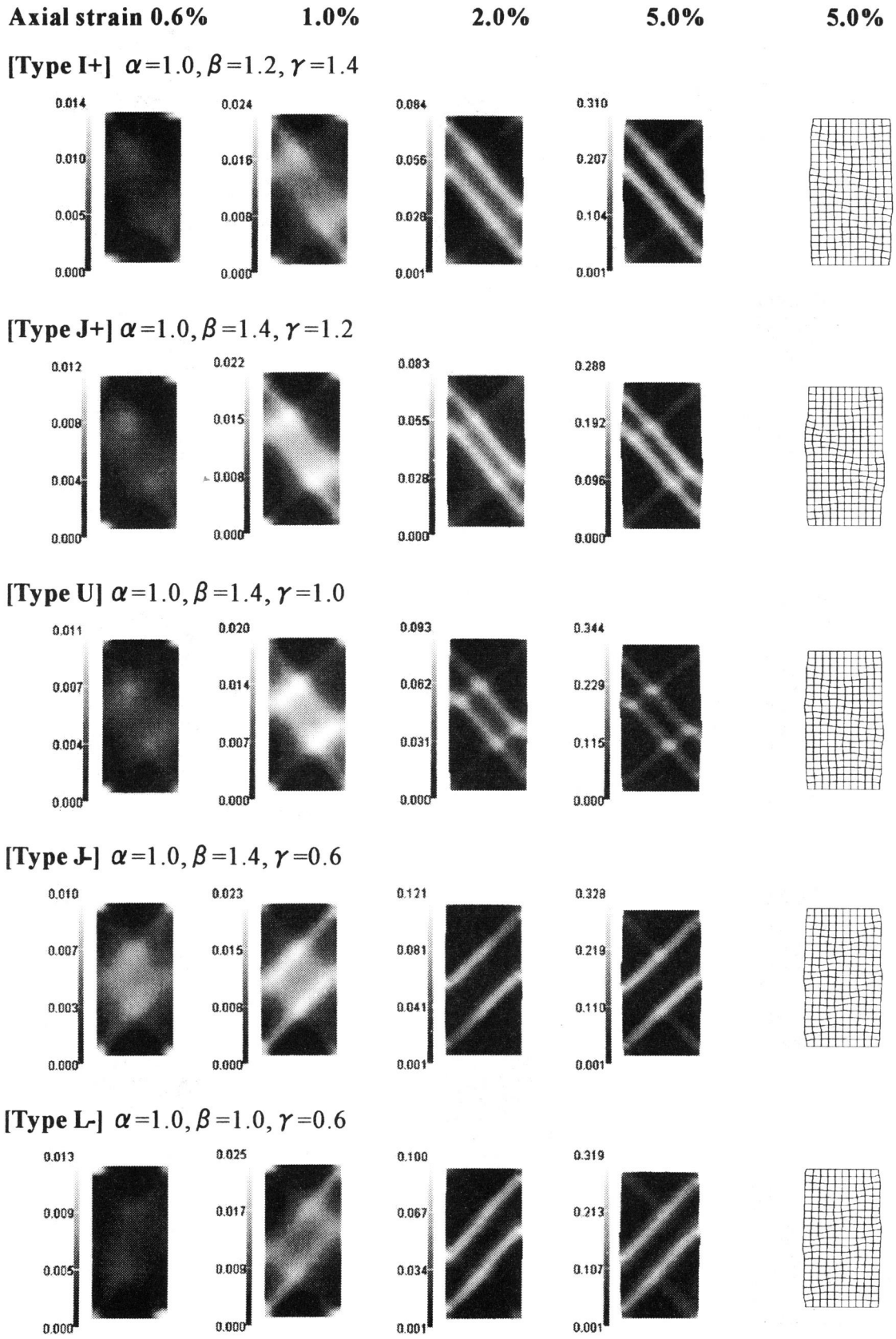

Figure 6.7: (a)Distribution of viscoplastic deviatoric strain and deformed meshes (θ =30°)

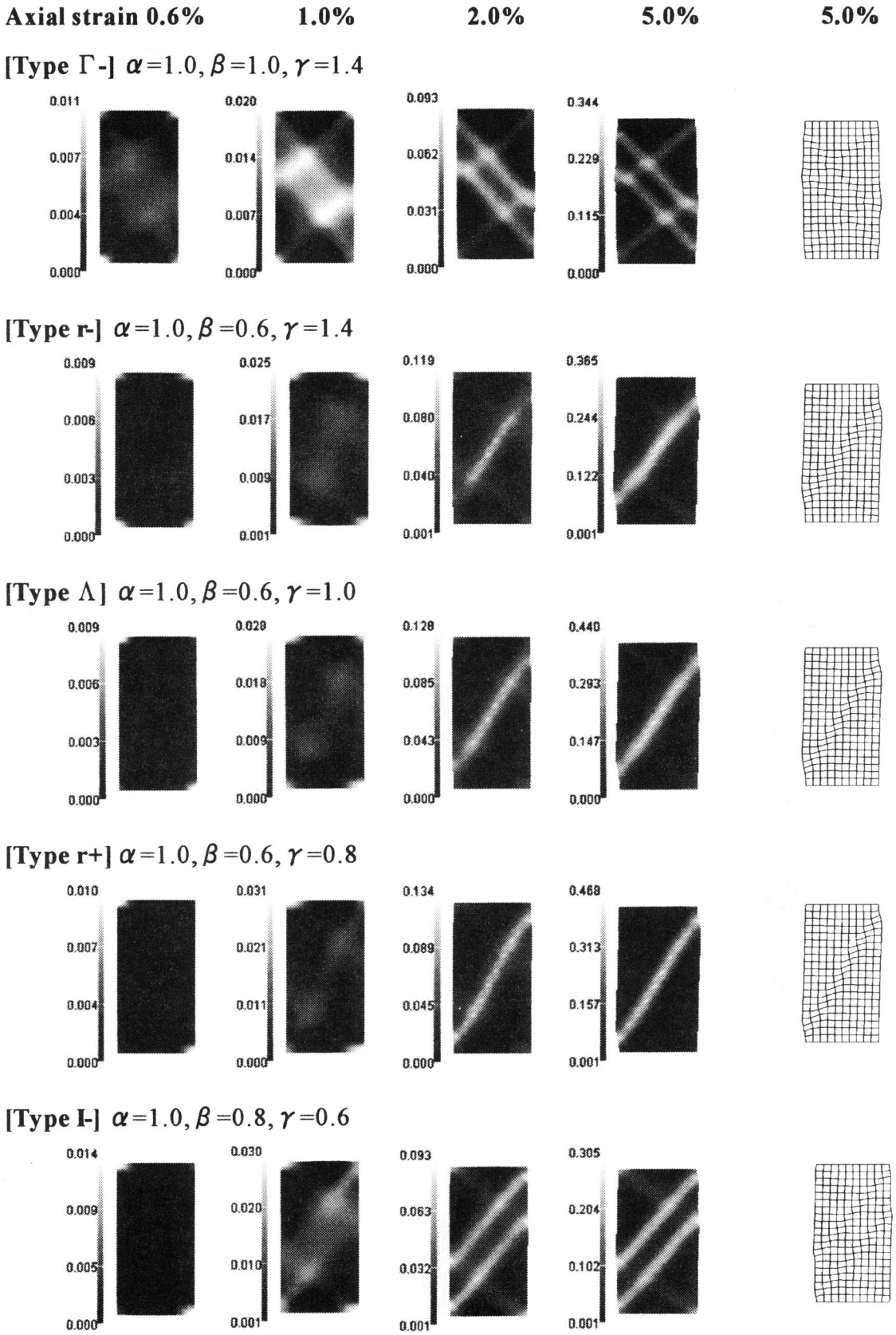

Figure 6.7: (b)Distribution of viscoplastic deviatoric strain and deformed meshes (θ =30°)

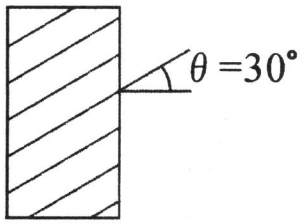

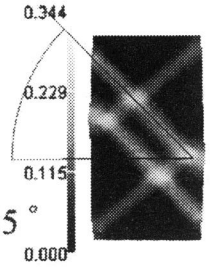

[Type Γ-] α=1.0, β=1.0, γ=1.4

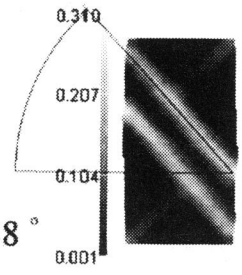

[Type I+] α=1.0, β=1.2, γ=1.4

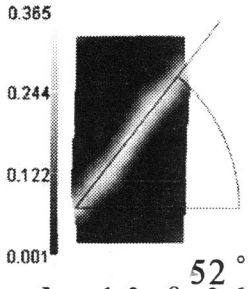

[Type r-] α=1.0, β=0.6, γ=1.4

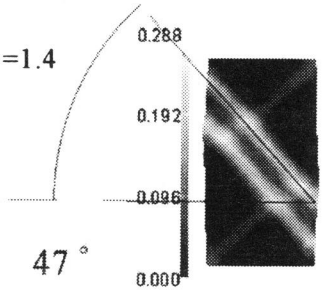

[Type J+] α=1.0, β=1.4, γ=1.2

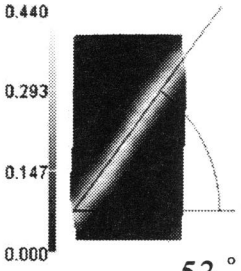

[Type Λ] α=1.0, β=0.6, γ=1.0

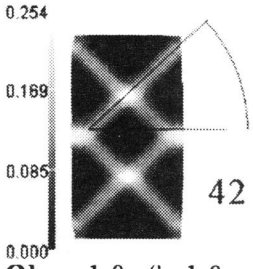

[Type O] α=1.0, β=1.0, γ=1.0

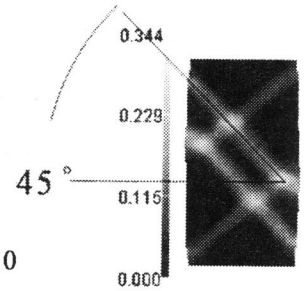

[Type U] α=1.0, β=1.4, γ=1.0

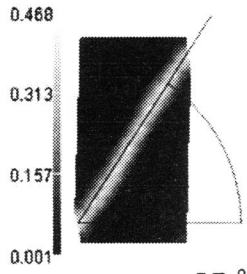

[Type r+] α=1.0, β=0.6, γ=0.8

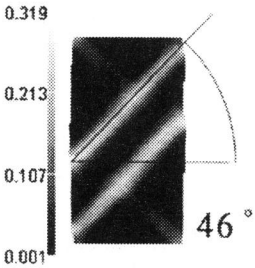

[Type L-] α=1.0, β=1.0, γ=0.6

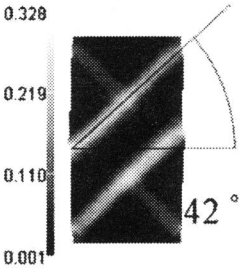

[Type J-] α=1.0, β=1.4, γ=0.6

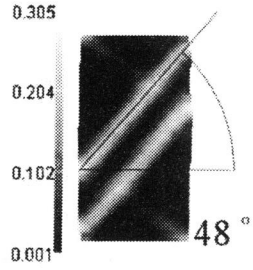

[Type I-] α=1.0, β=0.8, γ=0.6

Figure 6.8: Angles of shear bands for specimen (θ=30 °)

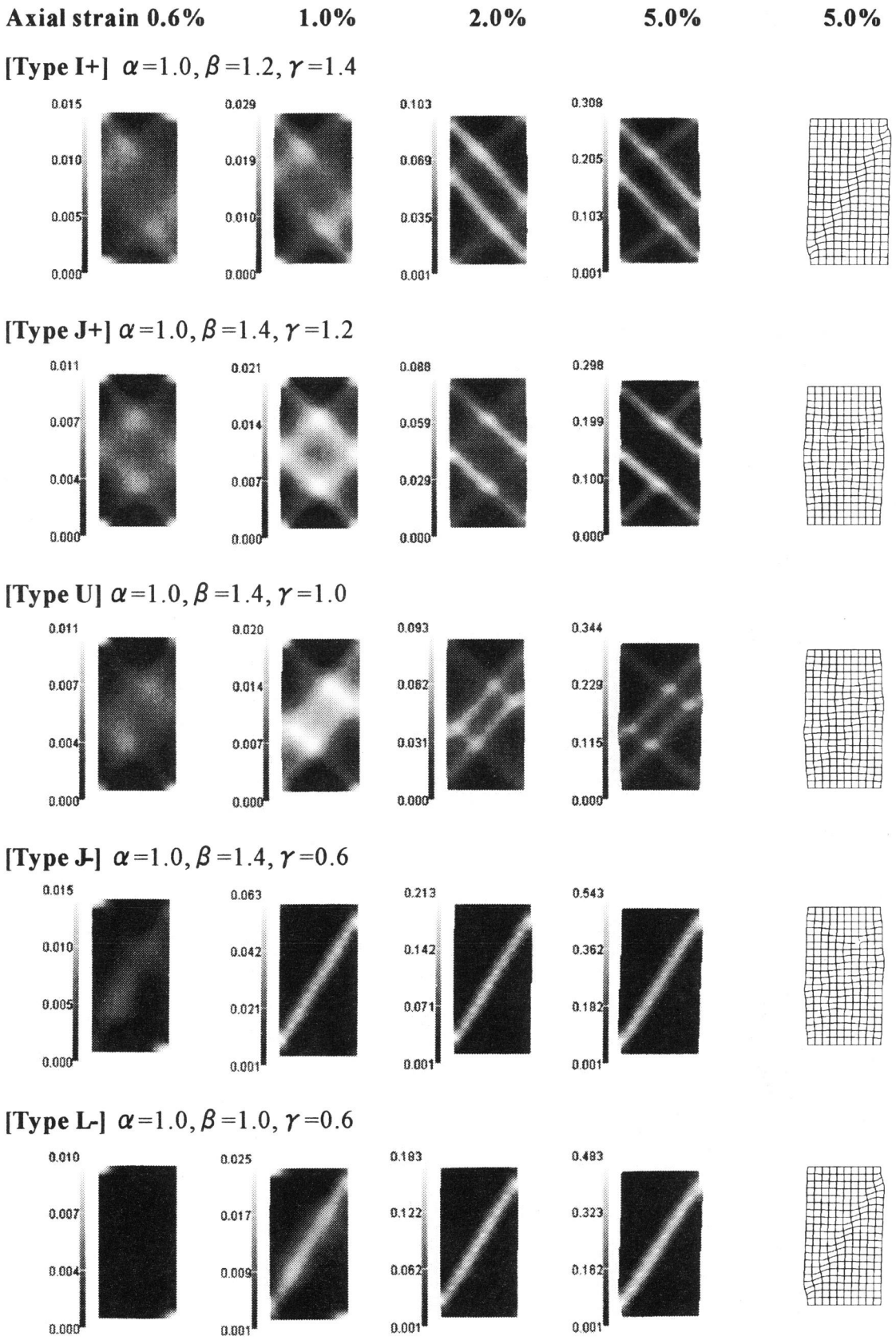

Figure 6.9: (a)Distribution of viscoplastic deviatoric strain and deformed meshes (θ =60°)

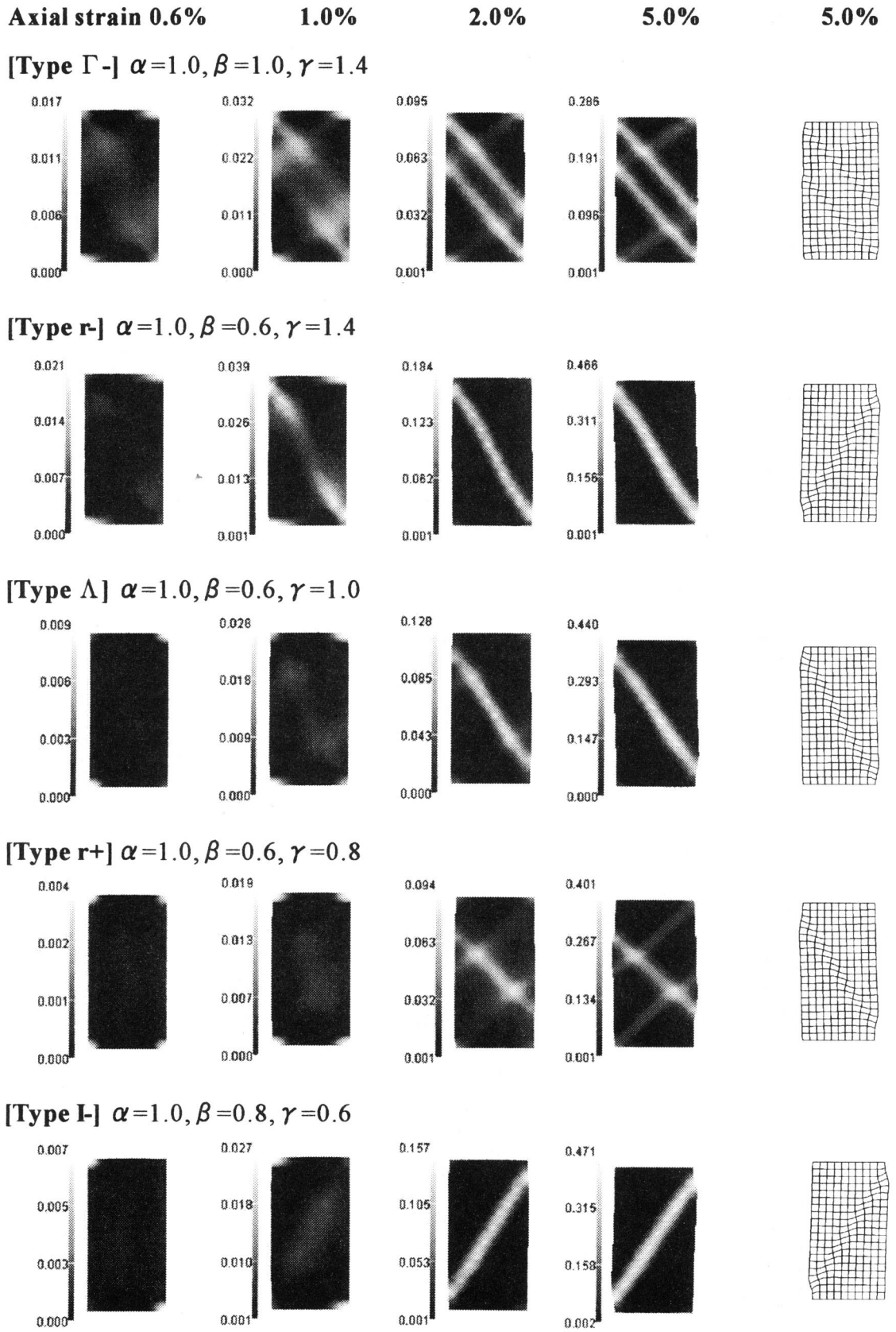

Figure 6.9: (b)Distribution of viscoplastic deviatoric strain and deformed meshes (θ =60°)

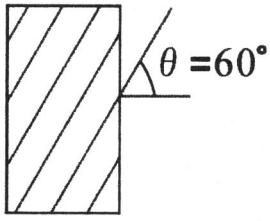

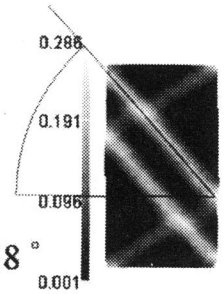

[Type Γ-] α=1.0, β=1.0, γ=1.4

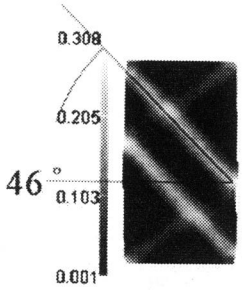

[Type I+] α=1.0, β=1.2, γ=1.4

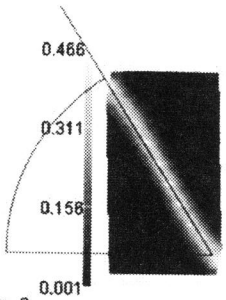

[Type r-] α=1.0, β=0.6, γ=1.4

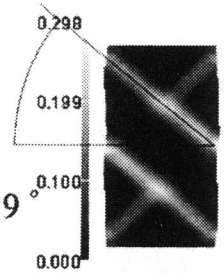

[Type J+] α=1.0, β=1.4, γ=1.2

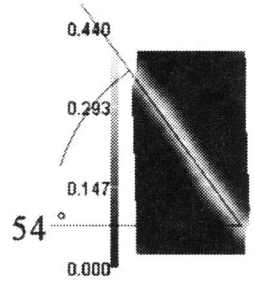

[Type Λ] α=1.0, β=0.6, γ=1.0

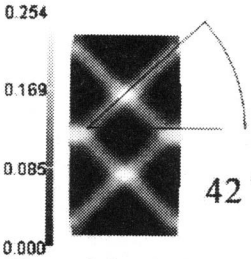

[Type O] α=1.0, β=1.0, γ=1.0

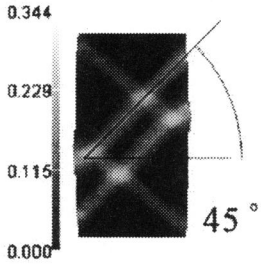

[Type U] α=1.0, β=1.4, γ=1.0

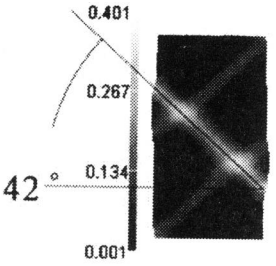

[Type r+] α=1.0, β=0.6, γ=0.8

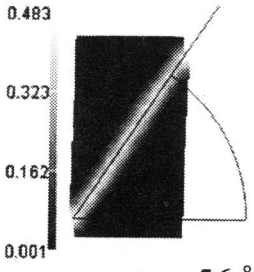

[Type L-] α=1.0, β=1.0, γ=0.6

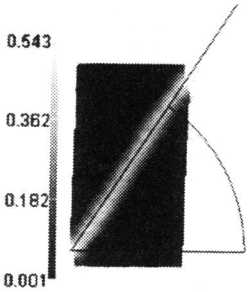

[Type J-] α=1.0, β=1.4, γ=0.6

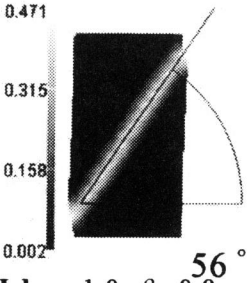

[Type I-] α=1.0, β=0.8, γ=0.6

Figure 6.10: Angles of shear bands for specimen (θ=60°)

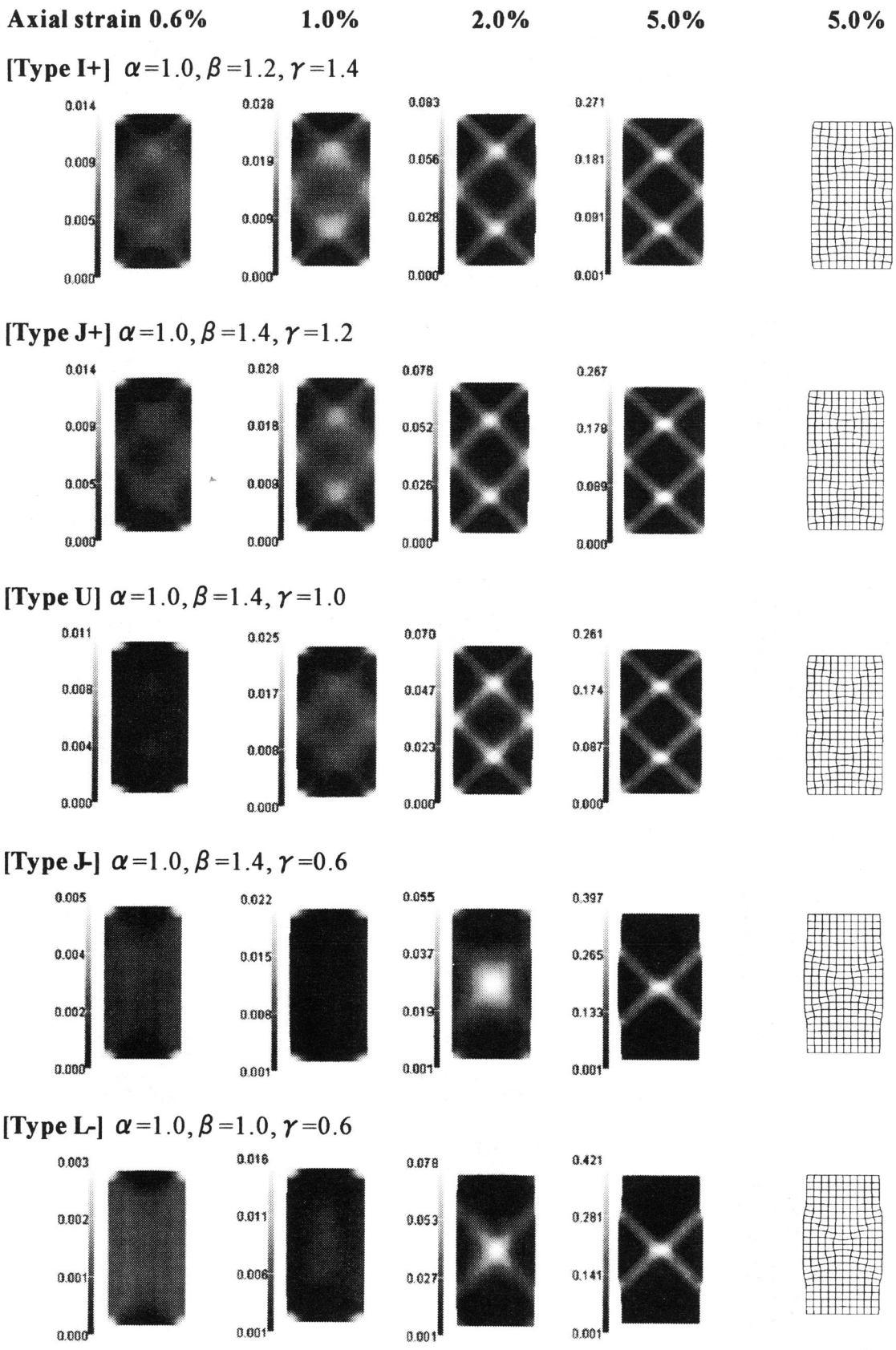

Figure 6.11: (a)Distribution of viscoplastic deviatoric strain and deformed meshes (θ =90°)

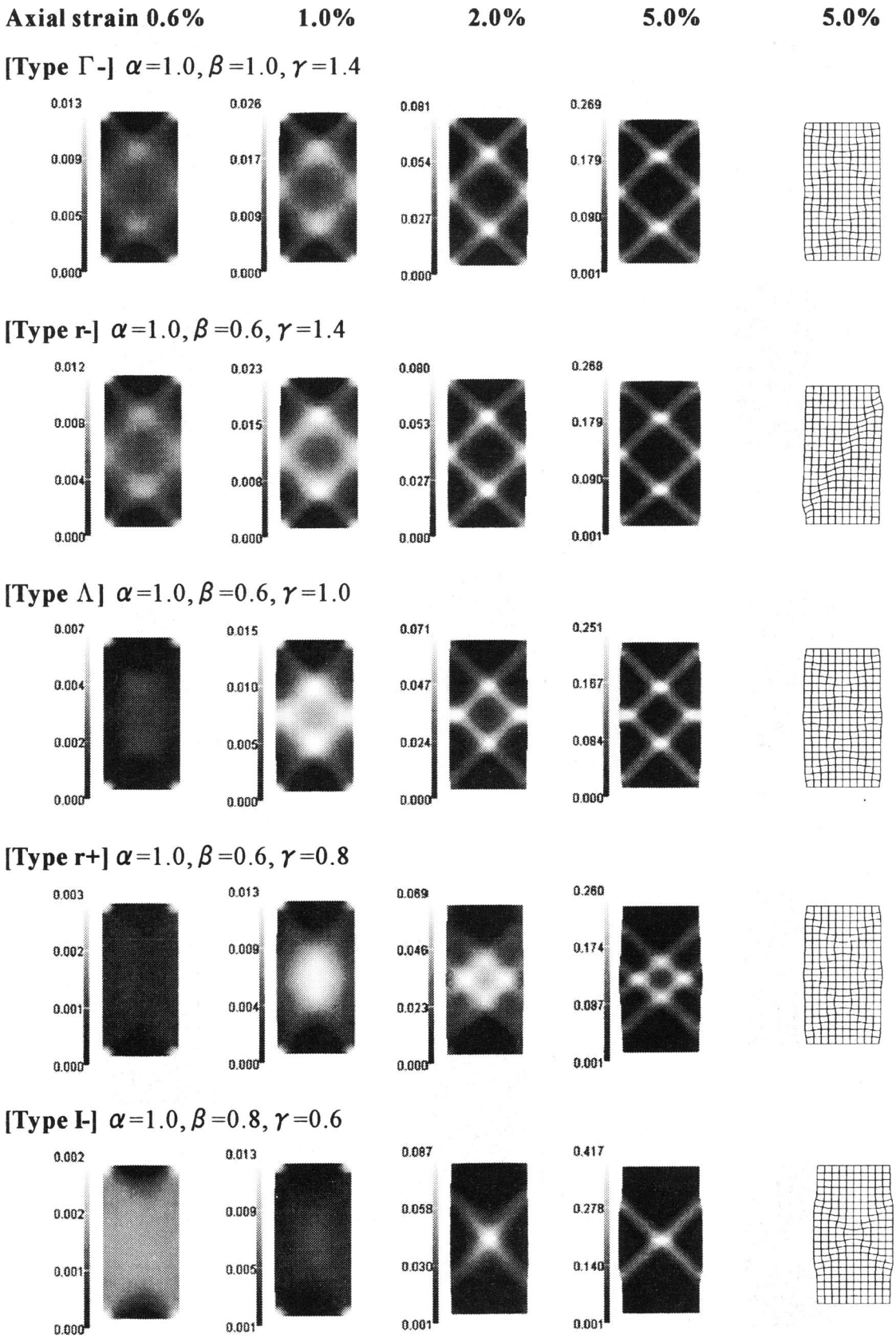

Figure 6.11: (b)Distribution of viscoplastic deviatoric strain and deformed meshes (θ =90°)

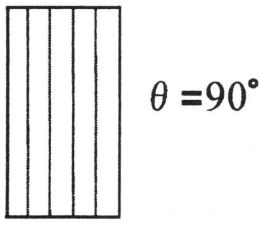

θ =90°

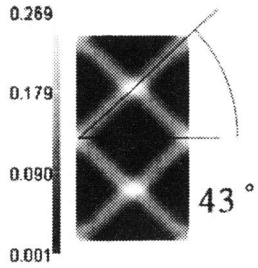

[Type Γ-] α=1.0, β=1.0, γ=1.4

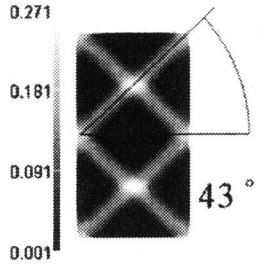

[Type I+] α=1.0, β=1.2, γ=1.4

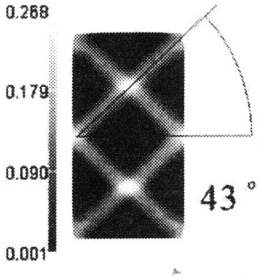

[Type r-] α=1.0, β=0.6, γ=1.4

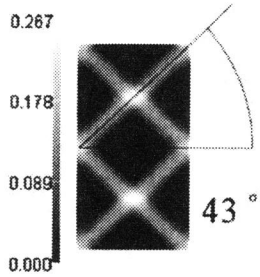

[Type J+] α=1.0, β=1.4, γ=1.2

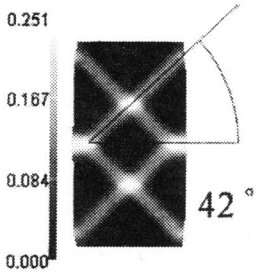

[Type Λ] α=1.0, β=0.6, γ=1.0

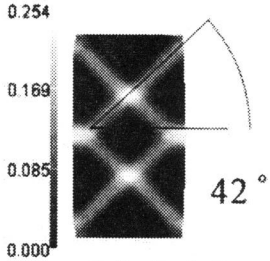

[Type O] α=1.0, β=1.0, γ=1.0

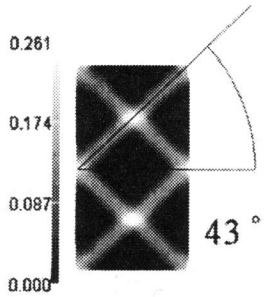

[Type U] α=1.0, β=1.4, γ=1.0

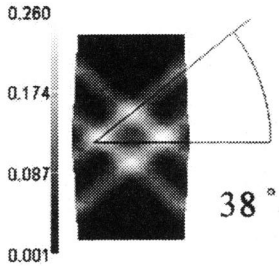

[Type r+] α=1.0, β=0.6, γ=0.8

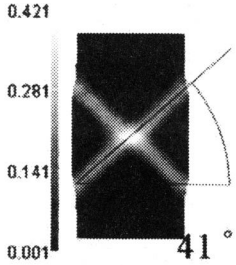

[Type L-] α=1.0, β=1.0, γ=0.6

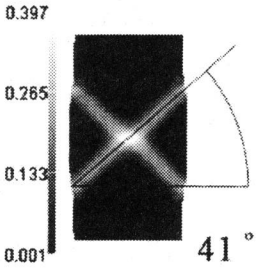

[Type J-] α=1.0, β=1.4, γ=0.6

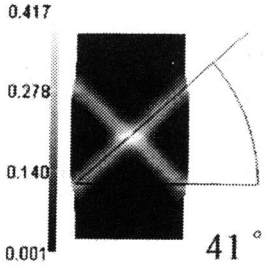

[Type I-] α=1.0, β=0.8, γ=0.6

Figure 6.12: Angles of shear bands for specimen (θ=90 °)

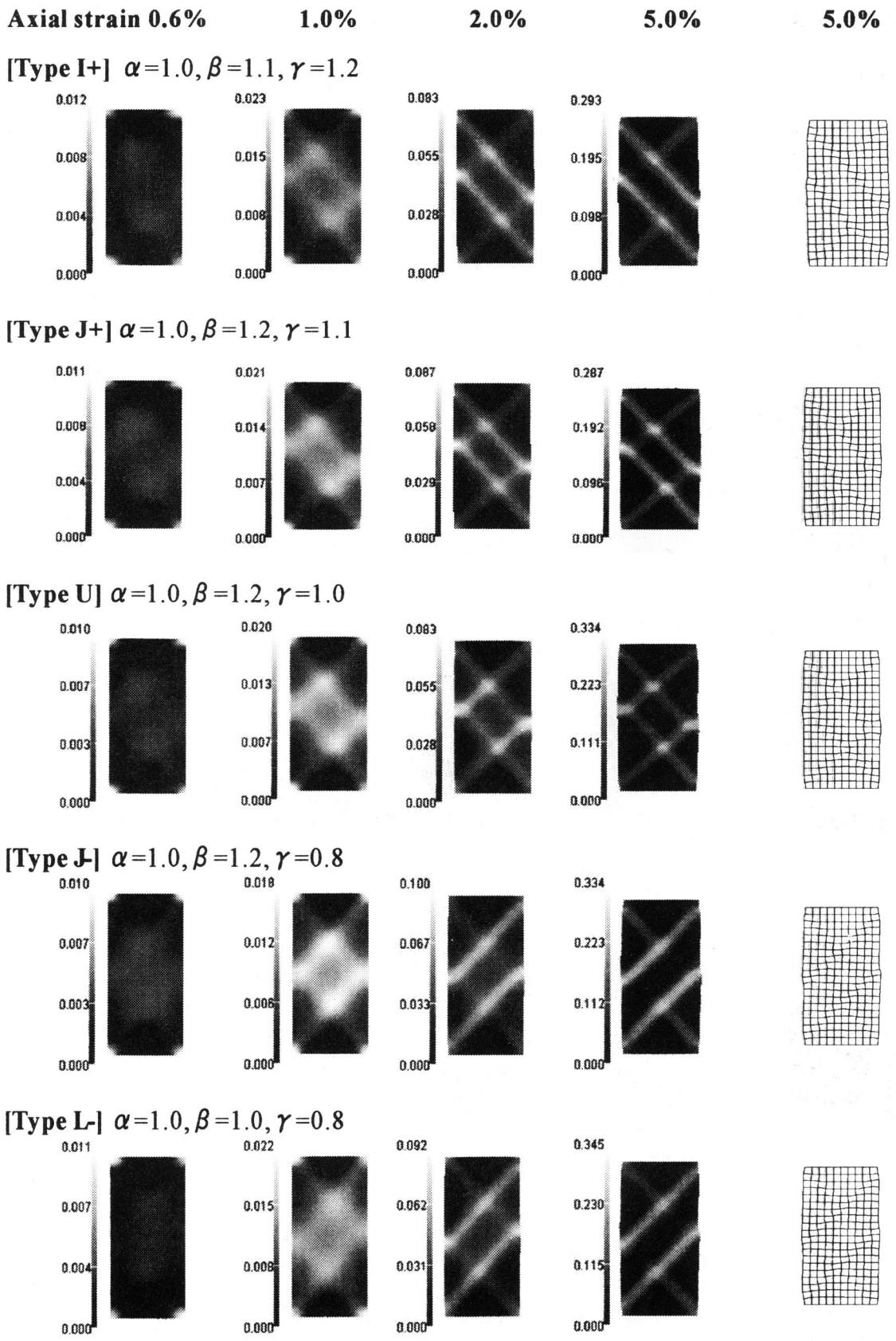

Figure 6.13: (a)Distribution of viscoplastic deviatoric strain and deformed meshes (θ =30°)

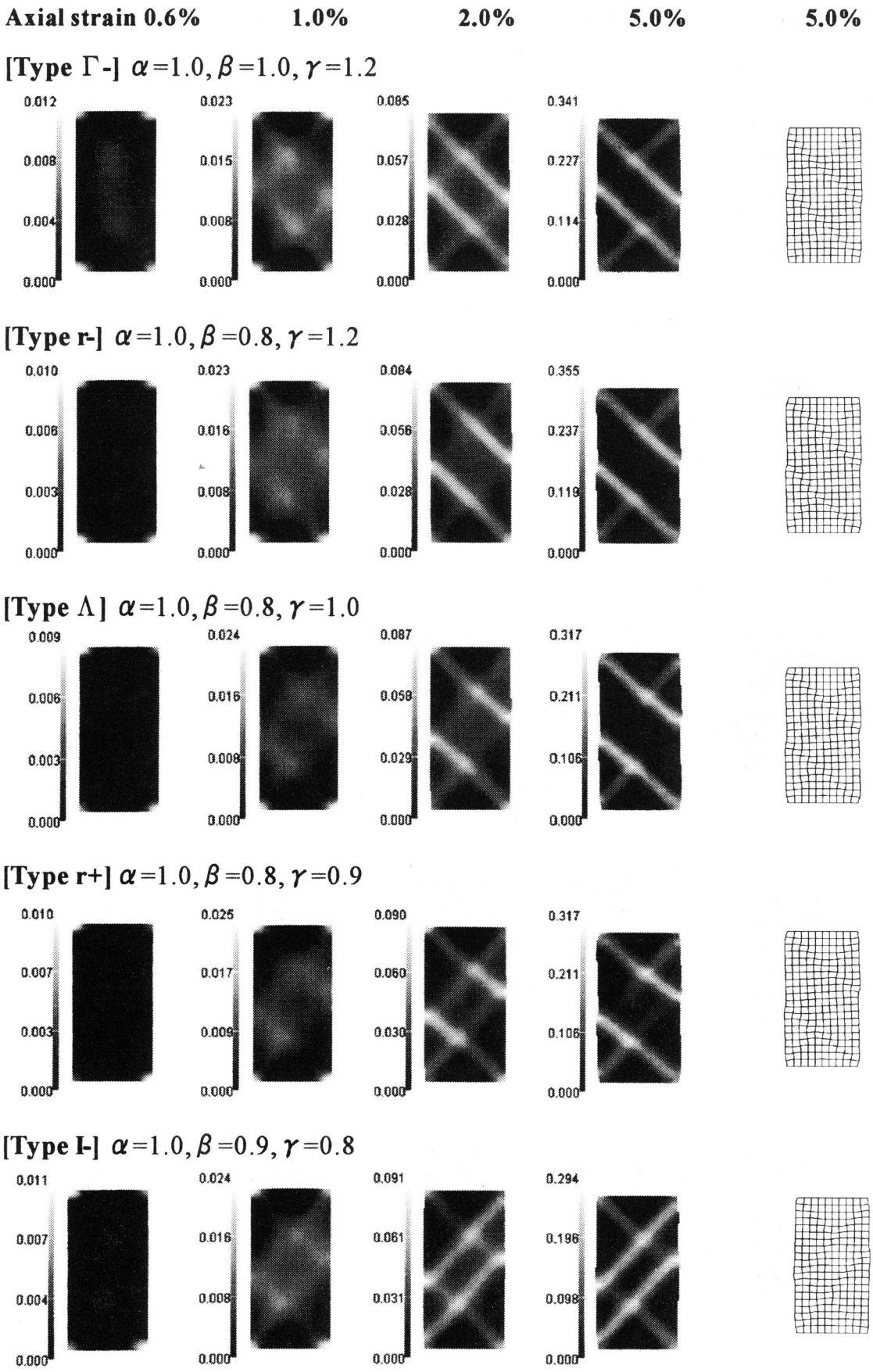

Figure 6.13: (b)Distribution of viscoplastic deviatoric strain and deformed meshes (θ =30°)

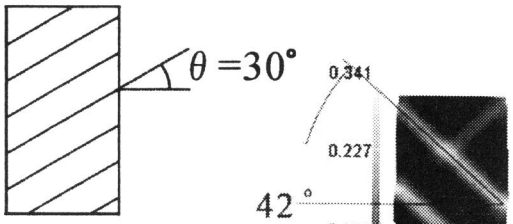

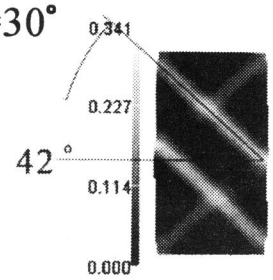

[Type Γ-] α=1.0, β=1.0, γ=1.2

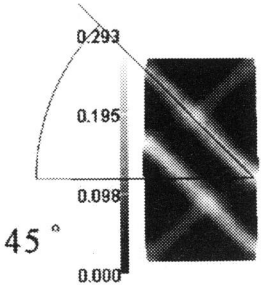

[Type I+] α=1.0, β=1.1, γ=1.2

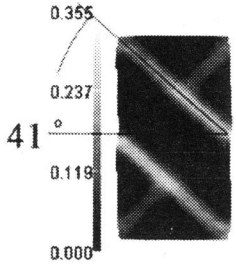

[Type r-] α=1.0, β=0.8, γ=1.2

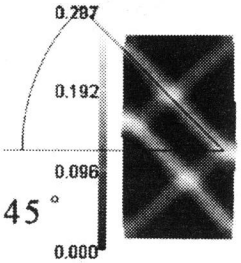

[Type J+] α=1.0, β=1.2, γ=1.1

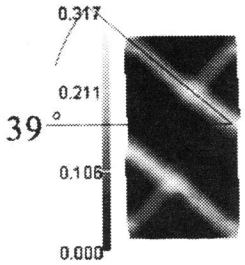

[Type Λ] α=1.0, β=0.8, γ=1.0

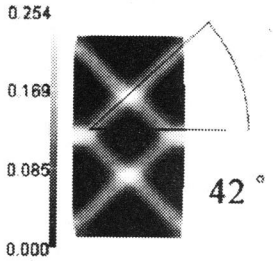

[Type O] α=1.0, β=1.0, γ=1.0

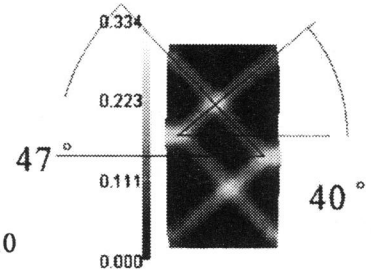

[Type U] α=1.0, β=1.2, γ=1.0

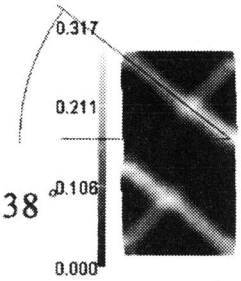

[Type r+] α=1.0, β=0.8, γ=0.9

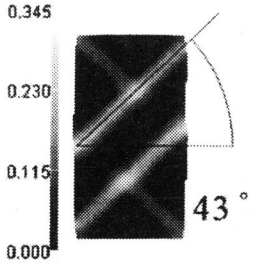

[Type L-] α=1.0, β=1.0, γ=0.8

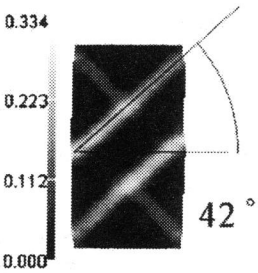

[Type J-] α=1.0, β=1.2, γ=0.8

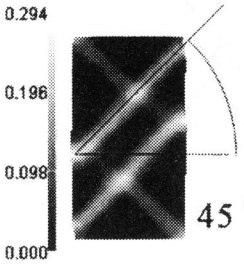

[Type I-] α=1.0, β=0.9, γ=0.8

Figure 6.14: Angles of shear bands for specimen (θ=30 °)

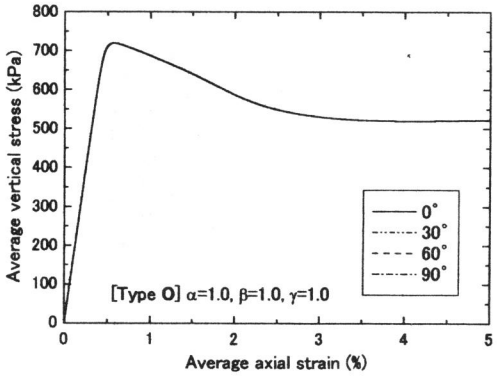

(a) Stress-strain relations

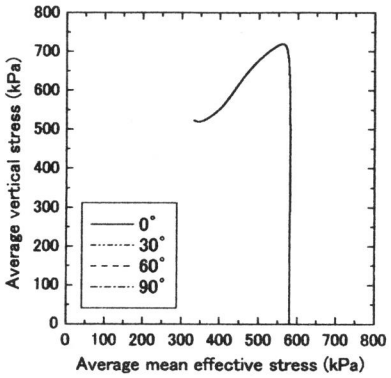

(b) Stress paths

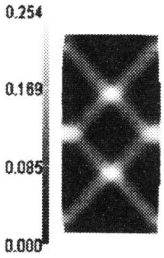

Distribution of γ^p (at axial strain of 5%)

Figure 6.15: Simulation results for Type **O**

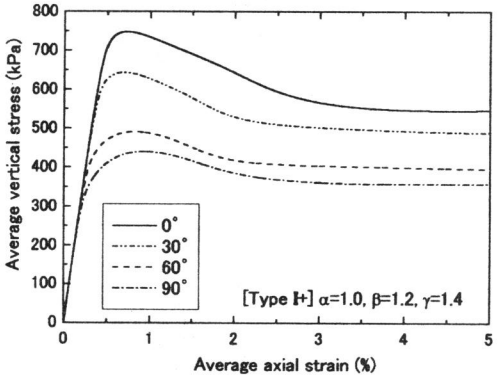

(a) Stress-strain relations

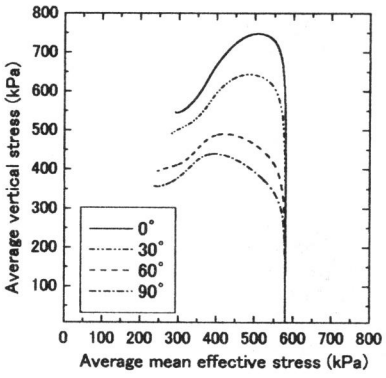

(b) Stress paths

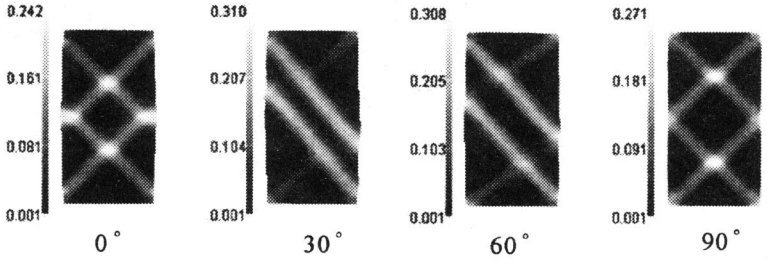

0° 30° 60° 90°

Distribution of γ^p at axial strain of 5%

Figure 6.16: Simulation results for Type **I+**

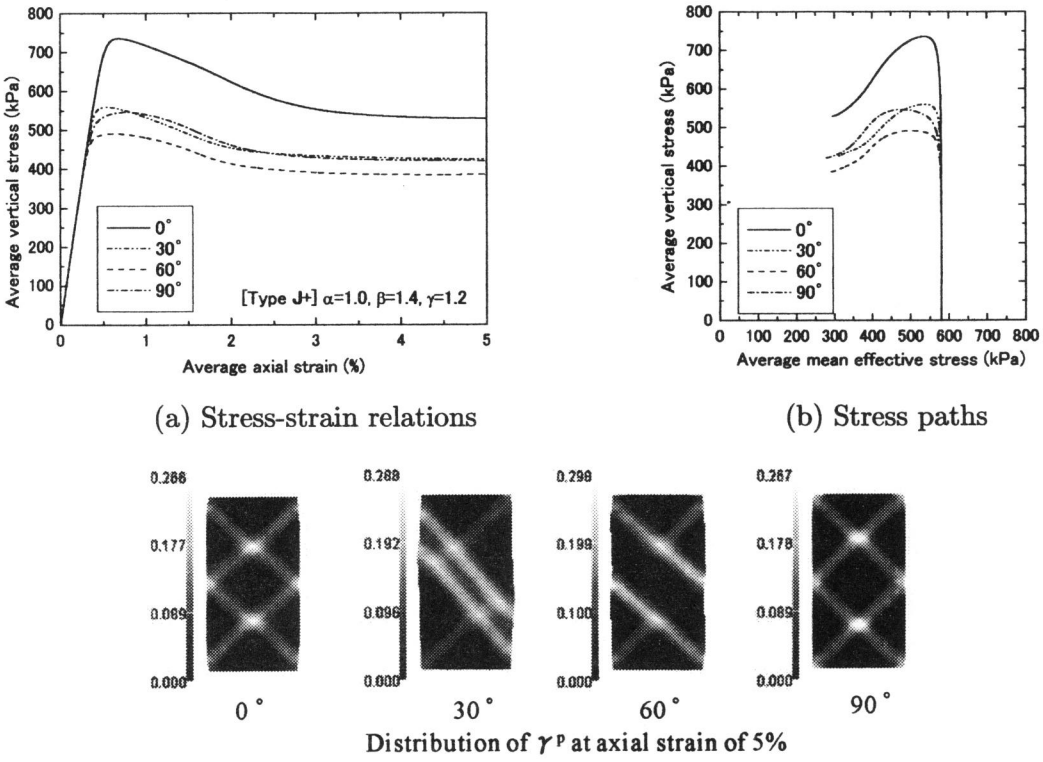

(a) Stress-strain relations (b) Stress paths

Figure 6.17: Simulation results for Type **J+**

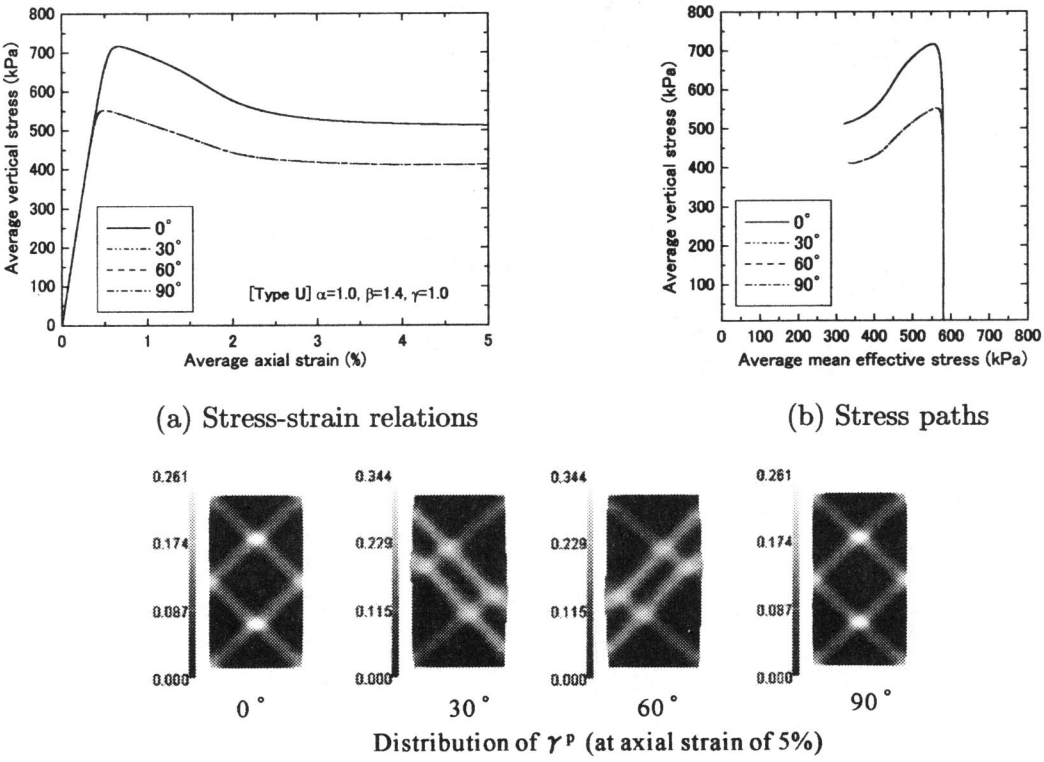

(a) Stress-strain relations (b) Stress paths

Figure 6.18: Simulation results for Type **U**

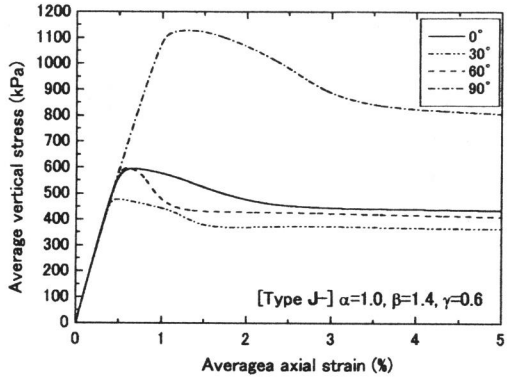

(a) Stress-strain relations

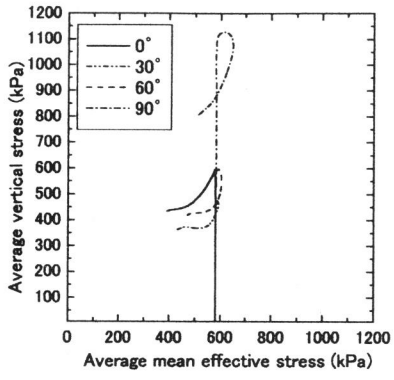

(b) Stress paths

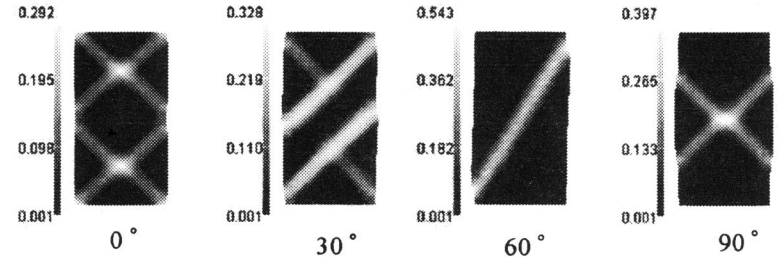

Distribution of γ^p at axial strain of 5%

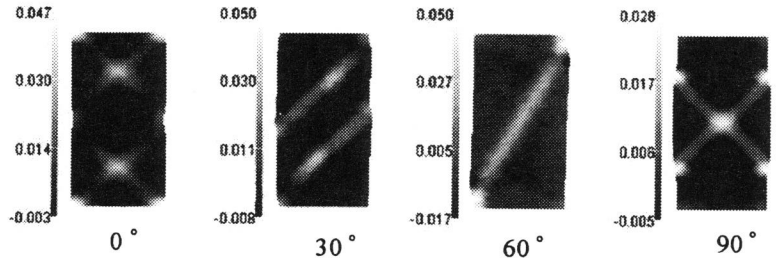

Distribution of viscoplastic volumetric strain at axial strain of 5%

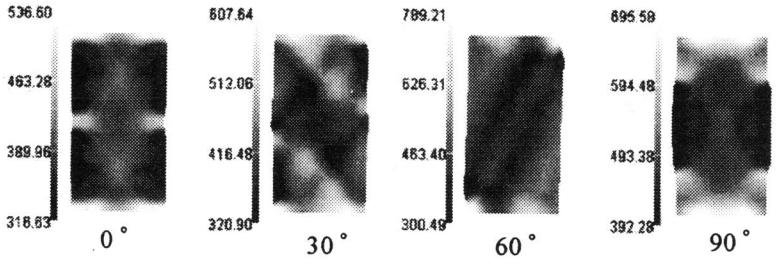

Distribution of mean effective stress at axial strain of 5%

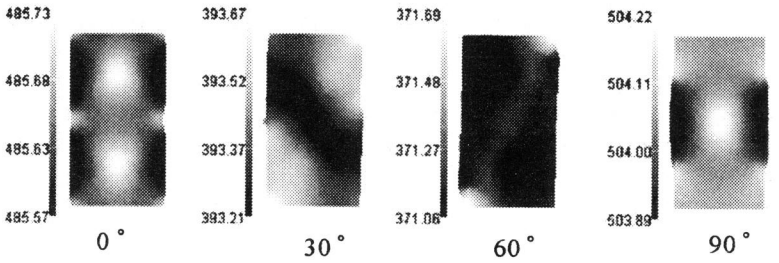

Distribution of pore water pressure at axial strain of 5%

Figure 6.19: Simulation results for Type J-

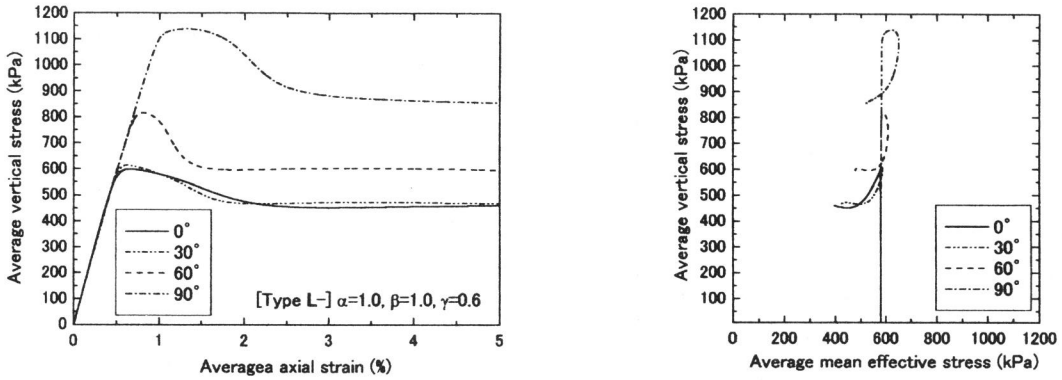

(a) Stress-strain relations (b) Stress paths

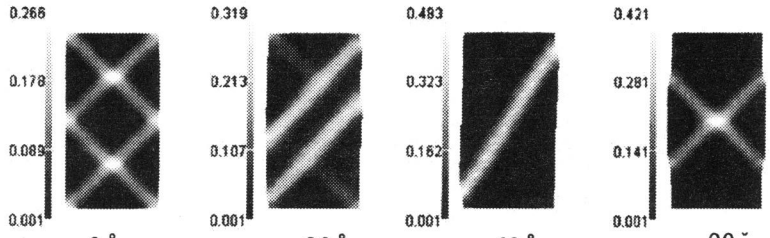

Distribution of γ^p (at axial strain of 5%)

Figure 6.20: Simulation results for Type **L-**

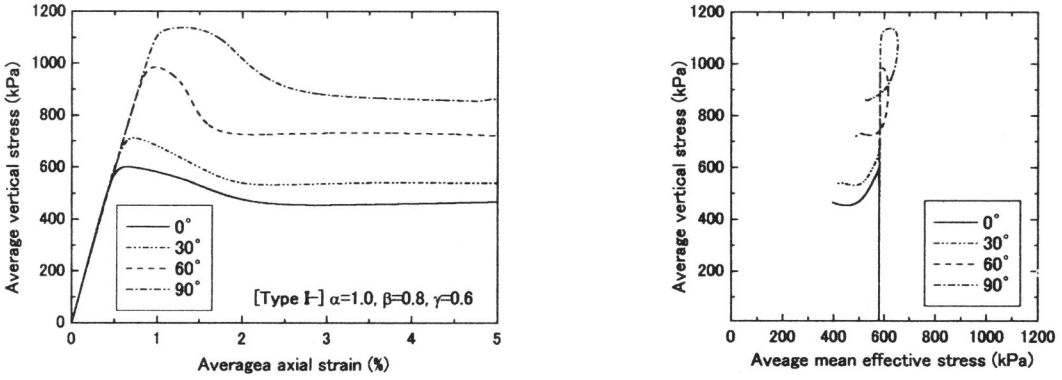

(a) Stress-strain relations (b) Stress paths

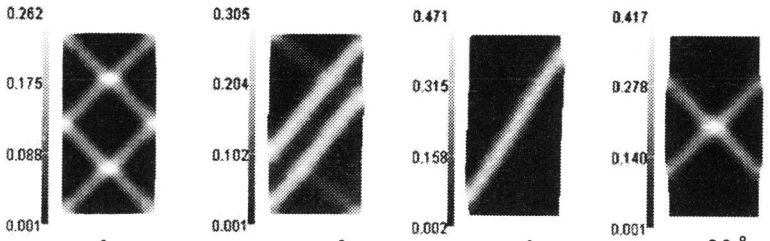

Distribution of γ^p at axial strain of 5%

Figure 6.21: Simulation results for Type **I-**

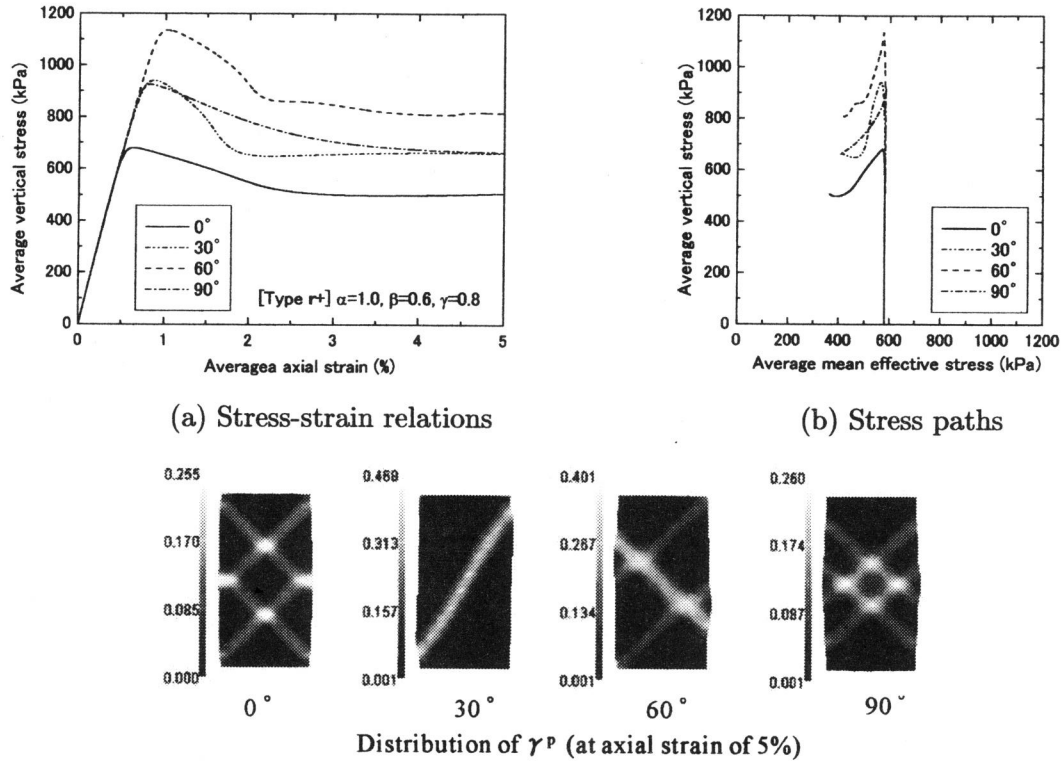

(a) Stress-strain relations (b) Stress paths

Figure 6.22: Simulation results for Type r+

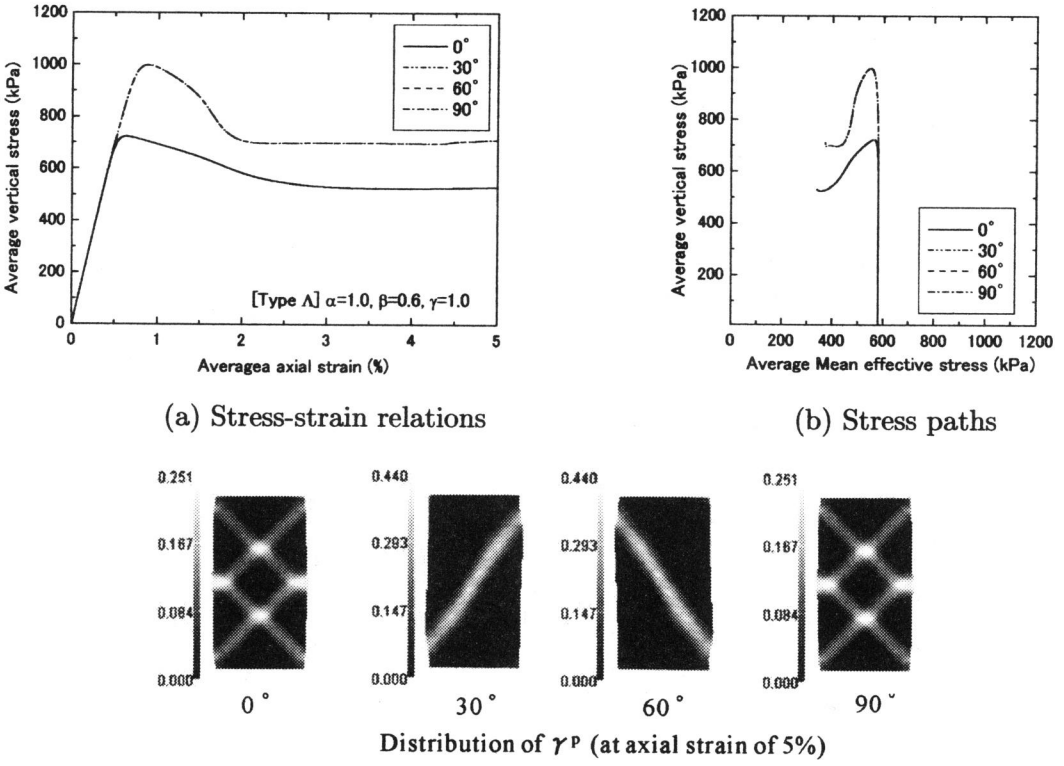

(a) Stress-strain relations (b) Stress paths

Figure 6.23: Simulation results for Type Λ+

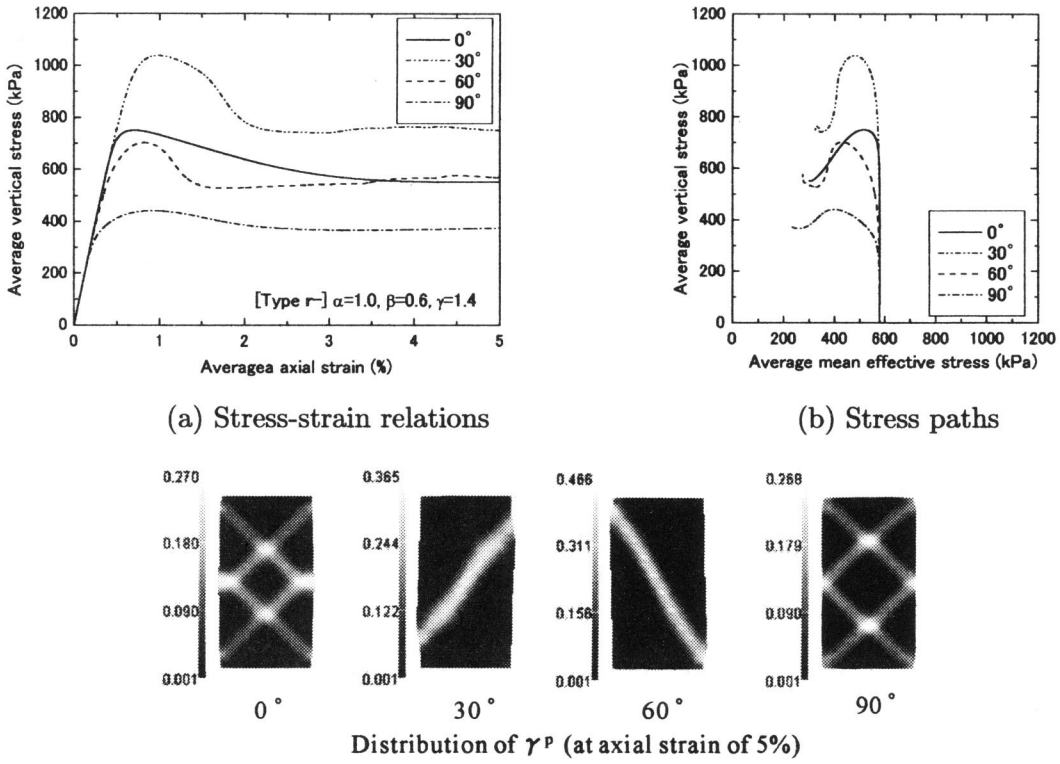

(a) Stress-strain relations (b) Stress paths

Figure 6.24: Simulation results for Type r-

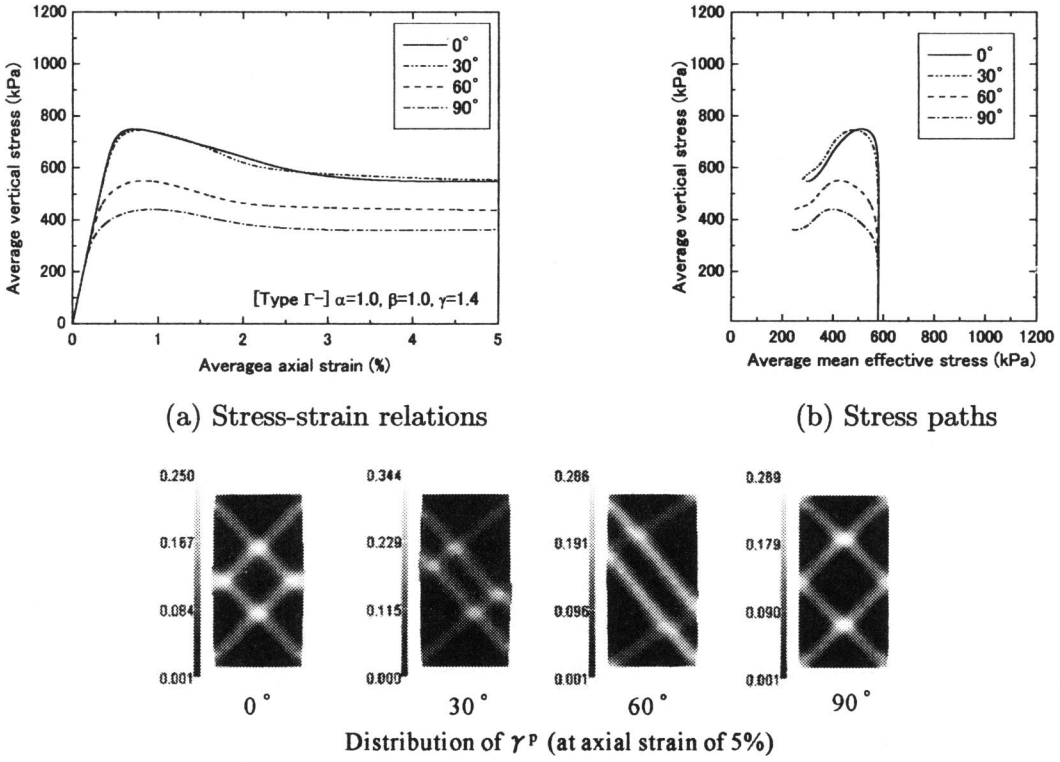

(a) Stress-strain relations (b) Stress paths

Figure 6.25: Simulation results for Type Γ-

Chapter 7

CONCLUSIONS AND FUTURE WORK

7.1 Summary and Conclusion

In the present study, the effect of structural changes and anisotropy were introduced to an elasto-viscoplastic constitutive model for clay and an elasto-plastic constitutive model for soft rock. The proposed models for clay were applied to numerical simulations of strain localization and also to a one-dimensional consolidation. The following conclusions were obtained from the present study.

In Chapter 2, the effect of structural changes, namely, the collapse of the microstructure, was introduced to the elasto-viscoplastic model proposed by Adachi and Oka (1982). Structural changes were described as the shrinking of the overconsolidation boundary surface and the static yield function, with an increasing viscoplastic strain. The proposed model was applied to undrained triaxial tests on Tsurumi clay, and compared to experimental results with reference to stress-strain relations and stress paths. It was determined that the model can well reproduce the mechanical behavior of structured clay. In the slightly overconsolidated region, however, the stress path cannot describe the actual behavior well. The instability of the proposed model was evaluated during both undrained creep and secondary consolidation. The model can be unstable around the failure stress ratio line in both NC and OC regions. Moreover, during secondary consolidation, namely, under a constant stress, the model exhibited instability depending on the set of structural parameters. It should be noted that the unstable region in this model depended not only on the current stress state, but also on the strain history.

In Chapter 3, the effect of structural changes in the constitutive model on strain localization was examined by a numerical simulation of the shear tests with displacement control under plane strain conditions. Simulations were performed for both undrained and partially drained conditions. From comparisons of the proposed model and the original model, the shear localization was more apparent in the proposed model, considering structural changes than that obtained from the original model. Under drained conditions, the deformation was concentrated on the upper parts of the specimen for the NC clay and on the lower parts for the OC clay. This is a phenomenon of the localization of compressive strain. As for the angles of shear bands, larger values for structural parameter β, which describes the rate of degradation of the structure, provided smaller values for the angles of shear bands.

In Chapter 4, an unstable behavior during consolidation was reproduced using the proposed model by a numerical simulation of a one-dimensional consolidation. According to the simulation results, types of unstable behavior such as pore water generation and a temporary increase in the strain rate can be described. The distribution of axial strain in the clay layer exhibited higher inhomogeneity, which corresponds to a compaction band, than that of the original model.

In Chapter 5, an elasto-plastic constitutive model for soft rock has been extended to an anisotropic model based on the transformed stress concept. The proposed model was applied to drained triaxial tests on Tomuro stone sampled in different directions. From comparisons of the experimental results and the simulations, an extended model considering both elastic and plastic anisotropy can well reproduce the anisotropic behavior of soft rock, namely, the angle dependency on the deformation.

In Chapter 6, the transformed stress concept was applied to the elasto-viscoplastic constitutive model, and then extended to the anisotropic model. Undrained compression tests with different angles for the sedimentation plane were performed using the extended model in order to evaluate the effect of anisotropy on strain localization. The shape of the shear bands strongly depended on the angle of the sedimentation plane. The tendency of shear localization also depended on the anisotropic parameters. If the difference between the anisotropic parameters was large, an apparent shear band formed with a large angle, nearly 60°, when the sedimentation plane inclined at 30° and 60° from the horizontal

plane.

The proposed model, which considers the soil structure, can indeed reproduce unstable behavior concerning compressive deformation as well as shear failure, while the original model, with material function Φ_2, cannot describe instability during the consolidation process. The extended anisotropic model for soft rock and clay can describe the diverse anisotropy of geomaterials well.

7.2 Recommendation for Future Work

Topics for future research are suggested based on the findings of this work. Subjects that deserve future investigation include the following.

The present model for clay is based on the elasto-viscoplastic theory. Since it is known that the behavior of clay is viscoelastic for small levels of strain, it is necessary to consider the viscoelasticity in order to explain more accurately the deformation characteristics of clay.

The effect of structural changes on strain localization was analytically studied in Chapter 3. To complete the development of the constitutive model and to reveal the mechanism of the localization, further experimental research on structured soils with respect to strain localization is required. In addition, these studies can be applied to practical problems such as slope failure.

In the proposed anisotropic model, only the initial structural anisotropy is considered. To describe real behavior, however, anisotropy induced by stress and/or strain should also be taken into account. Furthermore, the actual behavior of the shear localization for specimens sampled with different angles is needed in order to evaluate the proposed model. In particular, the direction of the shear band to the sedimentation plane should be investigated.

References

[1] Adachi, T. and Oka, F. (1982): Constitutive equations for normally consolidated clay based on elasto-viscoplasticity, *Soils and Foundations*, **22** (4), 55-70.

[2] Adachi, T. and Oka, F. (1984): Constitutive equations for sands and overconsolidated clays and assigned works for sand, *Proc. Int. Workshop on Constitutive Relations for soils* (ed. by Gudehus, G., Darve, F. and Vardoulakis, I.), 6-8 September 1982, Grenoble, Balkema, 141-157.

[3] Adachi, T., Oka, F. and Mimura, M. (1987a): An elasto-viscoplastic theory for clay failure, *Proc. 8th Asian Regional Conf. on Soil Mechanics and Foundation Engrg.*, Kyoto, Japan, JSSMFE, **1**, 5-8.

[4] Adachi, T., Oka, F. and Mimura, M. (1987b): Mathematical structure of an overstress elasto-viscoplastic model for clay, *Soils and Foundations*, **27** (3), 31-42.

[5] Adachi, T., Oka, F., Hirata, T., Hashimoto, T., Pradhan, T.B.S., Nagaya, J. and Mimura, M. (1991): Triaxial and torsional hollow cylinder tests of sensitive natural clay and an elasto-viscoplastic constitutive model, Deformation of Soils and Displacements of Structures, *Proc. 10th European Conf. on Soil Mechanics and Foundation Engrg.*, Florence, Italian Geotechnical Association, Balkema, **1**, 3-6.

[6] Adachi, T. and Oka, F. (1995): An elasto-plastic constitutive model for soft rock with strain-softening, *Int. J. Numerical and Analytical Methods in Geomechanics*, **19**, 233-247.

[7] Adachi, T., Oka, F., Hirata, T., Hashimoto, T., Nagaya, J. and Mimura, M. and Pradhan, T.B.S. (1995): Stress-strain behavior and yielding characteristics of Eastern Osaka clay, *Soils and Foundations*, **35** (3), 1-13.

[8] Adachi, T., Kimoto, S., Oka, F. and Kobayashi, H. (2002): A constitutive model of anisotropic behavior of soft sedimentary rock, *Proc. 8th Int. Symp. on Numerical Models in Geomechanics* (ed. by G.N. Pande and S. Pietruszczak), 10-12 April, Rome, Italy, 75-78.

[9] Akai, K. and Tamura, T. (1978): Numerical analysis of multi-dimensional consolidation accompanied with elasto-plastic constitutive equation, *Tans. of JSCE*, **269**, 95-104 (in Japanese).

[10] Asaoka, A., Nakano, M. and Noda, T.(2000): Superloading yield surface concept for highly structured soil behavior, *Soils and Foundations*, **40** (2), 99-110.

[11] Asaoka, A., Nakano, M., Noda, T. and Kaneda, K. (2000): Delayed compression/consolidation of natural clay due to degradation of soil structure, *Soils and Foundations*, **40** (3), 75-85.

[12] Biot, M.A. (1962): Mechanics of deformation and acoustic propagation in porous media, *J. Appl. Phys.*, **33** (4), 1482-1498.

[13] Bishop, A.W. and Lovenbury, H.T. (1969): Creep characteristics of two undisturbed clays, *Proc. 7th Int. Conf. on Soil Mechanics and Foundation Engrg.*, Mexico City, **1**, 29-37.

[14] Boehler, J.P. and Sawczuk, A. (1970): *Équilibre limite des sols anisotropes*, *J. de Mécanique*, **9** (1), 5-33 (in French).

[15] Boehler, J.P. and Sawczuk, A. (1977): On yielding of oriented solids, *Acta Mechanica*, **27**, 185-206.

[16] Di Prisco, C., Matiotti, R. and Nova, R. (1992): A mathematical model of grouted sand allowing for strength degradation, *Proc. 4th Int. Symp. on Numerical Models in Geomechanics* (ed. by Pande, G.N. and Pietruszczak, S.), 24-27 August, Swansea, UK, Balkema, **1**, 25-35.

[17] Duncan, J.M. and Seed, H.B. (1966): Anisotropy and stress reorientation in clay, *J. Soil Mechanics and Foundations Div. Proc. ASCE*, **92** (SM5), 21-50.

[18] Graham, J. and Houlsby, G.T. (1983): Anisotropic elasticity of a natural clay, *Géotechnique*, **33** (2), 165-180.

[19] Graham, J., Nooman, J.L. and Lew, K.V. (1983): Yield states and stress-strain relationships in a natural plastic clay, *Can. Geotechnical, J.*, **20** (2), 502-516.

[20] Issen, K.A. and Rudnicki, J.W. (2000): Conditions for compaction bands in porous rock, *J. Geophy. Res.*, **105** (B9), 21,529-21,536.

[21] Kabbaj, M., Oka, F., Leroueil, S. and Tavenas, F. (1985): Consolidation of natural clays and laboratory testing, *Consolidation of Soils: Testing and Evaluation, ASTM Special Technical Publication 892* (ed. by Yong, R.N. and Townsend, F.C.), 378-404.

[22] Kabbaj, M., Tavenas, F. and Leroueil, S. (1988): In situ and laboratory stress-strain relationships, *Géotechnique*, **38** (1), 83-100.

[23] Kirkgard, M.M. and Lade, P.V. (1991): Anisotropy of normally consolidated San Francisco Bay Mud, *Geotech. Testing J.*, GTJODJ, **14** (3), 231-246.

[24] Kobayashi, H. (2000): Strain-softening elasto-plastic constitutive model considering anisotropy and its application to slope stability, Master thesis, Kyoto University, Japan (in Japanese).

[25] Leroueil, S., Kabbaj, M., Tavenas, F. and Bouchard, R. (1985): Stress-strain-strain rate relation for the compressibility of sensitive natural clays, *Géotechnique*, **35** (2), 159-180.

[26] Leroueil, S. (1988): Recent developments in consolidation of natural clays, Tenth Canadian Geotechnical Colloquium, *Can. Geotech. J.*, **25**, 85-107.

[27] Leroueil, S. and Vaughan, P.R. (1990): The general and congruent effects of structure in natural soils and weak rocks, *Géotechnique*, **40** (3), 467-488.

[28] Lo, K.Y. and Hori, M. (1979): Deformation and strength properties of some rocks in southern Ontario, *Can. Geotech. J.*, **16**, 108-120.

[29] Love, A.E.H. (1927): A treatise on the mathematical theory of elasticity, Cambridge University Press.

[30] Mitchell, J.K. (1972): Some deviations from isotropy in a lightly overconsolidated clay, *Géotechnique*, **22** (3), 459-467.

[31] Mitchell, J.K. (1986): Practical problems from surprising soil behavior, 20th Terzaghi Lecture, ASCE, *J. Geotech. Engrg.*, **112** (3), 259-289.

[32] Oda, M. and Nakayama, H. (1989): Yield function for soil with anisotropic fabric, *J. Engrg. Mechanics*, ASCE, **115** (1), 89-104.

[33] Ohtsuki, H., Nishi, K., Okamoto, T. and Tanaka, S. (1981): Time-dependent characteristics of strength and deformation of a mudstone, *Proc. Int. Symp. on Weak Rock*

(ed. by K. Akai, M. Hayashi, and Y. Nishimatsu), 21-24 September, Tokyo, Balkema, **1**, 119-124.

[34] Oka, F. (1981): Prediction of time-dependent behaviour of clay, *Proc. 10th Int. Conf. on Soil Mech. and Foundation Engrg.*, 15-19 June, Stockholm, Balkema, **1**, 215-218.

[35] Oka, F., Tavenas, F. and Leroueil, S. (1991): An elasto-viscoplastic FEM analysis of sensitive clay foundation beneath embankment, *Proc. 7th Int. Conf. on Computer Method and Advances in Geomechanics* (ed. by Beer, G., Booker, J.R. and Carter, J.P.), 6-10 May, Cairns, Balkema, **2**, 1023-1028.

[36] Oka, F. (1992): A cyclic elasto-viscoplastic constitutive model for clay based on the non-linear-hardening rule, *Proc. 4th Int. Symp. on Numerical Models in Geomechanics* (ed. by Pande, G.N. and Pietruszczak, S.), 24-27 August, Swansea, UK, Balkema, **1**, 105-114.

[37] Oka, F. (1993): Anisotropic and pseudo-anisotropic elasto-viscoplastic constitutive models for clay, *Modern approaches to plasticity, Proc. workshop held in Horton* (ed. by D. Kolymbas), June 1992, Elsevier Sci. Pub., 505-526.

[38] Oka, F., Adachi, T. and Yashima, A. (1994): Instability of an elasto-viscoplastic constitutive model for clay and strain localization, *Mechanics of Materials*, **18**, 119-129.

[39] Oka, F., Adachi, T. and Yashima, A. (1998): A constitutive model for soft rock with both strain softening and negative dilatancy, *The Geotechnics of Hard Soils-Soft Rocks, Proc. 2nd Int. Symp. on Hard Soils-Soft rocks* (ed. by Evangelista, A. and Picarelli, L.), Naples, Italy, Balkema, **2**, 737-744.

[40] Oka, F., Yashima, A., Tateishi, A., Taguchi, Y. and Yamashita, S. (1999): A cyclic elasto-plastic constitutive model for sand considering a plastic-strain dependence of the shear modulus, *Géotechnique*, **49** (5), 661-680.

[41] Oka, F., Higo, Y. and Kimoto, S. (2001a): Effect of dilatancy on strain localization of elasto-viscoplastic soil, *Mechanical Properties of Advanced Engrg. Materials, Proc. 5th IMMM* (ed. by Tokuda, M. and Xu, B.), 27-31 May, Mie, Japan, Mie University Press, 57-62.

[42] Oka, F., Higo, Y. and Kimoto, S. (2001b): Effect of dilatancy on strain localization of water saturated cohesive soil based on an elasto-viscoplastic model, *Computational*

Mechanics, Proc. first Asian-Pacific Congress on Computational Mechanics (ed. by S. Valliappan and N. Khalili), 20-23 Nov., Sydney, Australia, Elsevier, **1**, 1147-1154.

[43] Oka, F., Higo, Y. and Kimoto, S. (2002a): Effect of dilatancy on the strain localization of water-saturated elasto-viscoplastic soil, *Int. J. Solids and Structures*, **39**, 3625-3647.

[44] Oka, F., Higo, Y. and Kimoto, S. (2002b): Instability and strain localization analysis of elasto-viscoplastic normally and overconsolidated clays, *Proc. 8th Int. Symp. on Numerical Models in Geomechanics* (ed. by G.N. Pande and S. Pietruszczak), 10-12 April, Rome, Italy, Balkema, 185-190.

[45] Oka, F., Kimoto, S., Kobayashi, H. and Adachi, T. (2002): Anisotropic behavior of soft sedimentary rock and a constitutive model, *Soils and Foundations*, **42** (5), 59-70.

[46] Olsson, W.A. (1999): Theoretical and experimental investigation of compaction bands, *J. Geophys. Res.*, **104** (B4), 7219-7228.

[47] Perzyna, P. (1963): The constitutive equations for work-hardening and rate sensitive plastic materials, *Proc. Vibrational Problems*, Warsaw, **4** (3), 281-290.

[48] Pusch, R. (1970): Microstructural changes in soft quick clay at failure, *Can. Geotech. J.*, **7** (1), 1-7.

[49] Rice, J. R. (1976): The localization of plastic deformation, *Theoretical and Applied Mechanics* (ed. by W.T. Koiter), North-Holland Publishing Company, 207-220.

[50] Rudnicki, J.W. and Rice, J.R. (1975): Conditions for the localization of deformation in pressure-sensitive dilatant materials, *J. Mech. Phys. Solids*, **23**, 371-394.

[51] Shigematsu, H. (2002): Study on the microstructure and mechanical behavior of natural sedimentary soils with aging effect, Doctoral thesis, Gifu University, Japan (in Japanese).

[52] Shinjo, T. and Komiya, Y. (1984): Anisotropic elastic deformations and strength properties of mudstone, *Tsuchi-to-Kiso JSSMFE*, **32** (11), 49-54 (in Japanese).

[53] Sudo, T. and Shimada, S. (1978): *Clays and clay minerals of Japan, Developments in Sedimentology* 26, Elsevier Scientific Publishing Company (Kodansha, printed in Japan).

[54] Tavenas, F. and Leroueil, S. (1977): Effects of stresses and time on yielding of clays, *Proc. 9th ICSMFE*, Tokyo, **1**, 319-326.

[55] Technical Committee on Indurated Soils and Soft Rocks (TC22), ISSMFE (1994): Testing methods of indurated soils and soft rocks (ed. by K. Akai), JGS.

[56] Yashima, A., Shigematsu, H., Oka, F. and Nagaya, J. (1999): Mechanical behavior and micro-structure of Osaka upper-most Pleistocene marine clay, *J. Geotech. Engrg.*, **624** (III-47), 217-229 (in Japanese).